

**UNIVERSIDADE FEDERAL DE SANTA MARIA  
CENTRO DE TECNOLOGIA  
POST-GRADUATION PROGRAM IN ELECTRICAL  
ENGINEERING**

**Lucas Sangoi Mendonça**

**MODELING OF AN ELECTRO-MECHANICAL-ACOUSTIC  
CONTACTLESS ENERGY TRANSFER SYSTEM BASED ON  
MULTIPHYSICS NETWORKS AND RESONANT  
TOPOLOGIES**

**Santa Maria, Brazil  
2021**



Lucas Sangoi Mendonça

**MODELING OF AN ELECTRO-MECHANICAL-ACOUSTIC  
CONTACTLESS ENERGY TRANSFER SYSTEM BASED ON  
MULTIPHYSICS NETWORKS AND RESONANT TOPOLOGIES**

Thesis presented to the Doctorate Course of the Post-Graduation Program in Electrical Engineering, concentration area in Power Processing, of Universidade Federal de Santa Maria (UFSM), as a partial requirement to obtain the degree of **Doctor in Electrical Engineering**.

**Advisor: Prof. Dr.-Ing. Fábio Ecke Bisogno**

**Santa Maria, Brazil  
2021**

Ficha catalográfica elaborada através do Programa de Geração Automática da Biblioteca Central da UFSM, com os dados fornecidos pelo(a) autor(a).

Mendonça, Lucas Sangoi

Modeling of an electro-mechanical-acoustic contactless energy transfer system based on multiphysics networks and resonant topologies / Lucas Sangoi Mendonça – 2021

244 p.; 30cm

Orientador: Fábio Ecke Bisogno

Tese (doutorado) – Universidade Federal de Santa Maria, Centro de Tecnologia, Programa de Pós-Graduação em Engenharia Elétrica, RS, 2021

1. Contactless energy transfer systems
2. Multiphysics networks, resonant power conversion I. Bisogno, Fábio Ecke. II. Título.

---

© 2021

All copyrights reserved to Lucas Sangoi Mendonça. Reproduction of parts or all of this work can only be done with written authorization from the author.

Address: Av. Roraima, N° 1000, Bairro Camobi, Santa Maria, RS, Brasil, CEP: 97105-900;

Phone: +55 55 999635563;

E-mail: [lucassangoi1993@gmail.com](mailto:lucassangoi1993@gmail.com)

---

Lucas Sangoi Mendonça

**MODELING OF AN ELECTRO-MECHANICAL-ACOUSTIC  
CONTACTLESS ENERGY TRANSFER SYSTEM BASED ON  
MULTIPHYSICS NETWORKS AND RESONANT TOPOLOGIES**

Thesis presented to the Doctorate Course of the Post-Graduation Program in Electrical Engineering, concentration area in Power Processing, of Universidade Federal de Santa Maria (UFSM), as a partial requirement to obtain the degree of **Doctor in Electrical Engineering**.

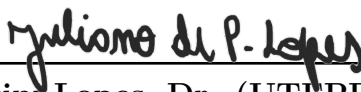
Approved on 17 of May of 2021:



\_\_\_\_\_  
Fábio Ecke Bisogno, Dr.-Ing. (UFSM) - Videoconference  
(Chairman/ Advisor)



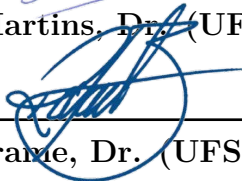
\_\_\_\_\_  
José Marcos Alonso Álvarez, Ph.D. (UNIOVI) - Videoconference



\_\_\_\_\_  
Juliano de Pelegrini Lopes, Dr. (UTFPR) - Videoconference



\_\_\_\_\_  
Mário Lúcio da Silva Martins, Dr. (UFSM) - Videoconference



\_\_\_\_\_  
Rafael Concatto Beltrame, Dr. (UFSM) - Videoconference

Santa Maria, Brazil  
2021



## AGRADECIMENTOS (ACKNOWLEDGMENTS)

Ao professor Dr.-Ing. Fábio Ecke Bisogno, por me orientar durante minha graduação, mestrado e doutorado. Por transmitir os conhecimentos técnicos e orientação científica. Por motivar-me e confiar no meu trabalho e ser um exemplo de profissional e ser humano.

Aos meus pais, Roseane Sangoi Mendonça e Worney Dellani Mendonça pelo apoio incondicional, por terem me oportunizado o estudo e me ensinarem, entre tantos valores, sempre enxergar o lado positivo dos desafios.

Ao meu irmão gêmeo Matheus Sangoi Mendonça por me inspirar a ser íntegro e disciplinado em todas tarefas.

Aos meus avós Armando Pereira Mendonça, Celeste Benedito Sangoi, Orlanda Leal Sangoi e Tereza Dellani Mendonça pelo carinho e amizade.

À minha amada Caroline Ozorio Escobar pelo incentivo, por me entender e pelo companheirismo eterno.

A todos os meu familiares, os quais sempre torceram por mim.

À Universidade Federal de Santa Maria (UFSM), onde tive oportunidade de estudar e me desenvolver profissionalmente e pessoalmente.

À Coordenação de Aperfeiçoamento de Pessoal de Nível Superior - Brasil (CAPES/PROEX) - Código de Financiamento 001, pelo apoio científico, financeiro e tecnológico.

Ao Conselho Nacional de Desenvolvimento Científico e Tecnológico - CNPq (315101/2018-0), pelo apoio científico, financeiro e tecnológico.

Aos professores membros da minha banca de qualificação, Dr. Mário Lúcio S. Martins, Dr. Alysson R. Seidel, Dr. Rafael C. Beltrame e Dr. Juliano P. Lopes pelas contribuições para o meu trabalho.

Aos amigos e colegas da Engenharia de Controle e Automação e Mestrado em Engenharia Elétrica, Leandro T. Martins, Matheus N. Medeiros, André J. Ramos, Mauro M. Mello Júnior e Thiago Cattani Naidon.

Ao Fraunhofer IIS, ao Dr.-Ing. Matthias Radecker e ao Dr.-Ing. Klaus Meyer pelo apoio técnico e científico durante o período realizado na Alemanha de desenvolvimento deste trabalho.

Aos amigos e colegas do Fraunhofer IIS, Vinícius Trentin, Ricardo J. Jacobs, Felipe L. Albanio, Marcelo H. Fracaro, Marcelo B. de Araujo, Leonardo C. Bach, Adriele S. Carvalho, Giancarlo Daros, Igor B. Barboza, João Pedro S. Cipriani, Gabriel Alli, Eduardo M. Viera, Matheus F. Gonçalves, Marcelo S. Costa, Vinícius C. Cassanego, Helga U. Dornelas, Wilmar C. Ossa, Pedro Zamuner, Juan Santanna e Vadim Pozhidaev.

Aos amigos de longa data, Bruno G. Silva, Pedro S. Ramos e Rodrigo S. Bender.  
A Deus.





“...much more than me, much more than you, and things that the eyes can see. Thou gave me the blood. Thou gave me the roots. Thy essence in my heart, I will always keep...

**Unknown author”**



**ABSTRACT**

**MODELING OF AN  
ELECTRO-MECHANICAL-ACOUSTIC  
CONTACTLESS ENERGY TRANSFER SYSTEM  
BASED ON MULTIPHYSICS NETWORKS AND  
RESONANT TOPOLOGIES**

AUTHOR: LUCAS SANGOI MENDONÇA  
ADVISOR: FÁBIO ECKE BISOGNO

This doctoral thesis shows a modeling methodology for an electro-mechanical-acoustic contactless energy transfer system and the analysis and design of its power conversion circuits. Contactless energy transfer systems (CET) are mainly divided into acoustic, inductive, capacitive and optical, which main applications related to biomedical and wireless chargers. The electro-mechanical-acoustic CET system is composed of: an ultrasound transmitter and a receiver based on piezoelectricity, a transfer media and a power conversion circuit. Due to the multi-domains, like as electrical, mechanical and acoustical, a multiphysics scenario is depicted. Modeling of such system requires a well-defined methodology. In this sense, this work presents an analytical multiphysical model based on lumped parameters. The model is based on the geometry and properties of the materials. By means of a decomposition into unit-less parameters scheme, the system is represented by a normalized state-space model. The model leads to solutions that do not depend on design specifications and do not rely on real system parameters. This work shows an equivalent electrical model that can be converted into a piezoelectric transformer model, which is used as part of the resonant tank in resonant topologies. This allows the design of power conversion circuits in order to manage the transferred electrical power. Furthermore, an augmented-order multiphysical model is proposed as an enhancement of the previous models. The models are evaluated for different scenarios and an error analysis is conducted based on the comparison between the experimental response of the physical system and the theoretical results. Resonant topologies are used as representation of the system and the generalized averaged dynamic modeling is performed for the Class-E<sup>2</sup> resonant converter. A practical demonstrator including the piezoelectric ultrasound transmitter and receiver, solid transfer media, and the power conversion circuitry was assembled in order to evaluate the feasibility of the system for practical applications.

**Keywords:** contactless energy transfer systems, multiphysics networks, resonant power conversion.



## RESUMO

# MODELAGEM DE UM SISTEMA ELETRO-MECÂNICO-ACÚSTICO DE TRANSFERÊNCIA DE ENERGIA WIRELESS BASEADO EM CIRCUITOS MULTIFÍSICOS E TOPOLOGIAS RESSONANTES

AUTOR: LUCAS SANGOI MENDONÇA  
ORIENTADOR: FÁBIO ECKE BISOGNO

Esta tese de Doutorado apresenta uma metodologia de modelagem para um sistema eletro-mecânico-acústico de transferência de energia sem fio/*wireless* e a análise e projeto dos conversores estáticos do sistema. Sistemas de transferência de energia sem contato (CET) são divididos principalmente em acústico, indutivo, capacitivo e óptico, com aplicações relacionadas à biomedicina e carregadores sem fio. O sistema eletro-mecânico-acústico CET é composto de: transmissor e receptor ultrassônicos baseados em piezoelectricidade, um meio de transferência de energia e os circuitos de conversão de energia. Devido aos multidomínios, como o elétrico, mecânico e acústico, um cenário multifísico é apresentado. A modelagem deste tipo de sistema requer uma metodologia muito bem definida. Neste âmbito, este trabalho apresenta um modelo analítico multifísico baseado em parâmetros concentrados. O modelo é baseado na geometria e nas propriedades dos materiais. Por meio de uma decomposição em parâmetros adimensionais, o sistema é representado em um modelo de espaço de estados normalizado. O modelo gera soluções que são independentes de especificações de projeto e não necessitam do conhecimento dos parâmetros reais do sistema. Ademais, este trabalho mostra um modelo elétrico equivalente que pode ser convertido em um modelo do transformador piezoelétrico que é usado como parte do circuito ressonante em topologias de conversores ressonantes. Esta técnica permite o projeto dos circuitos de conversão de energia que gerenciam a transferência de potência. Além disso, um modelo multifísico de ordem aumentada é proposto como melhoramento dos modelos supracitados. Os modelos são avaliados para diferentes cenários e uma análise de erro é usada para comparar a resposta experimental do sistema físico com os resultados teóricos. Topologias ressonantes são utilizadas neste trabalho como representação do sistema e um modelo dinâmico médio generalizado é aplicado no conversor ressonante Classe-E<sup>2</sup>. Um protótipo que inclui, transmissor/receptor ultrassônico, meio de transferência sólido e os circuitos de conversão de energia, foi construído visando avaliar a viabilidade do sistema para aplicações práticas.

**Palavras-chave:** sistemas de transferência de energia sem contato, circuitos multifísicos, conversão ressonante de energia.



## LIST OF FIGURES

Figure 1.1	– Contactless energy transfer system. ....	29
Figure 1.2	– Multiphysics understanding for electro-mechanical-acoustic contactless energy transfer systems. ....	31
Figure 1.3	– Electro-mechanical-acoustic CET system based on resonant DC/DC topology. ....	32
Figure 2.1	– Classification and applications of contactless energy transfer systems. ....	40
Figure 2.2	– General block diagram of an acoustic contactless energy transfer system. ....	41
Figure 2.3	– General block diagram of an inductively contactless energy transfer system. ....	42
Figure 2.4	– Class-E <sup>2</sup> wireless power transfer system. ....	43
Figure 2.5	– Wireless electric vehicle charging system. ....	44
Figure 2.6	– General block diagram of a capacitive contactless energy transfer system. ....	45
Figure 2.7	– General block diagram of an optical contactless energy transfer system. ....	47
Figure 2.8	– Ultrasonic transducer based on piezoelectricity. ....	48
Figure 3.1	– Overview of the modeling and methodology. ....	56
Figure 3.2	– Electro-mechanical-acoustic contactless energy transfer system. ....	59
Figure 3.3	– Multiphysical representation based on lumped components. ....	60
Figure 3.4	– Acoustical network by discrete components. ....	62
Figure 3.5	– Voltage gain ( <i>dB</i> ) as function of frequency ( <i>Hz</i> ) obtained from the multiphysical model based on lumped components. ....	67
Figure 3.6	– Voltage gain ( <i>dB</i> ) as function of frequency ( <i>Hz</i> ) obtained from the multiphysical model based on lumped components for different transducers frequencies. ....	69
Figure 3.7	– Decomposition into unit-less parameters scheme for multiphysics networks. ....	71
Figure 3.8	– Decomposition into unit-less parameters for the multiphysical model. ....	79
Figure 3.9	– Normalized gain curves for the multiphysical model based on lumped parameters (Voltage gain as function of the normalized operating frequency): (a) $Q_{el} = 1.0$ for different values of $\zeta_{1,2}$ . (b) $Q_{el} = 10$ for different values of $\zeta_{1,2}$ . (c) $Q_{el} = 1.0$ for different values of $\gamma_{1,2}$ . (d) $Q_{el} = 10$ for different values of $\gamma_{1,2}$ . (e) $\zeta_{1,2} = 0.01$ for different values of $\Lambda_1$ . (f) $\zeta_{1,2} = 0.05$ for different values of $\Lambda_1$ . ....	84
Figure 3.10	– Normalized gain curves for the multiphysical model based on lumped parameters (Voltage gain as function of the normalized operating frequency): (a) $Q_{el} = 0.1$ for different values of $O_1$ . (b) $Q_{el} = 1.0$ for different values of $O_1$ . (c) $\zeta_{1,2} = 0.1$ for different values of $O_1$ . (d) $\zeta_{1,2} = 0.3$ for different values of $O_1$ . (e) $\Lambda_1 = 0.01$ for different values of $O_1$ . (f) $\Lambda_1 = 0.03$ for different values of $O_1$ . ....	85
Figure 3.11	– Equivalent electrical model. ....	86
Figure 3.12	– Piezoelectric transformer model. ....	88
Figure 3.13	– Voltage gain ( <i>dB</i> ) as function of frequency ( <i>Hz</i> ) for different models. ....	89
Figure 3.14	– Augmented-order multiphysical model based on lumped parameters. ....	90
Figure 3.15	– Voltage gain as function of normalized operating frequency. ....	95
Figure 4.1	– Multiphysics network connected to resonant power conversion systems. ....	100

Figure 4.2	– Class-E <sup>2</sup> resonant power conversion system. (a) Class-E <sup>2</sup> resonant converter. (b) Electro-mechanical-acoustic CET system based on Class-E <sup>2</sup> topology. ....	102
Figure 4.3	– Class-E <sup>2</sup> resonant DC-DC converter model. ....	103
Figure 4.4	– Class-E <sup>2</sup> resonant converter - Operating mode <i>I</i> : <i>S</i> on and <i>D</i> off. ..	104
Figure 4.5	– Class-E <sup>2</sup> resonant converter - Operating mode <i>II</i> : <i>S</i> on and <i>D</i> on. ..	104
Figure 4.6	– Class-E <sup>2</sup> resonant converter - Operating mode <i>III</i> : <i>S</i> off and <i>D</i> on. ....	105
Figure 4.7	– Class-E <sup>2</sup> resonant converter - Operating mode <i>IV</i> : <i>S</i> off and <i>D</i> off. ....	105
Figure 4.8	– Decomposition into unit-less parameters scheme for the Class-E <sup>2</sup> resonant converter. ....	111
Figure 4.9	– Flowchart to solve the Class-E <sup>2</sup> resonant DC-DC converter model. .	114
Figure 4.10	– Normalized waveforms for the Class-E <sup>2</sup> resonant DC-DC converter for $D_c = 0.4$ . (a) Resonant current. (b) Resonant voltage. (c) Inverter's capacitor voltage. (d) Rectifier's capacitor voltage. (e) Switch <i>S</i> current. (f) Diode <i>D</i> current. ....	116
Figure 4.11	– Normalized waveforms for the Class-E <sup>2</sup> resonant DC-DC converter for $D_c = 0.5$ . (a) Resonant current. (b) Resonant voltage. (c) Inverter's capacitor voltage. (d) Rectifier's capacitor voltage. (e) Switch <i>S</i> current. (f) Diode <i>D</i> current. ....	117
Figure 4.12	– Normalized waveforms for the Class-E <sup>2</sup> resonant DC-DC converter for $D_c = 0.6$ . (a) Resonant current. (b) Resonant voltage. (c) Inverter's capacitor voltage. (d) Rectifier's capacitor voltage. (e) Switch <i>S</i> current. (f) Diode <i>D</i> current. ....	118
Figure 4.13	– Normalized gain and component stress curves for the Class-E <sup>2</sup> converter: (a) Current transfer function <i>S</i> as function of $D_c$ . (b) Quality factor $Q_L$ as function of $D_c$ . (c) Time $T_1$ as function of $D_c$ . (d) Time $T_2$ as function of $D_c$ . (e) Peak switch current $I_{S_{peak}}/I_{in}$ as function of $D_c$ . (f) Peak switch voltage $V_{S_{peak}}/V_{in}$ as function of $D_c$ . (g) Peak diode current $I_{D_{peak}}/I_{in}$ as function of $D_c$ . (h) Peak diode voltage $V_{D_{peak}}/V_{in}$ as function of $D_c$ . (i) Transfer power ratio $T_{POT}$ as function of transformation ratio $\alpha$ . ....	119
Figure 4.14	– Phase diagram of the Class-E <sup>2</sup> converter for $D_c = 0.5$ considering $i_{L_r}/I_{in}$ and $v_{C_1}/V_{in}$ : (a) ZVS. (b) Non-ZVS. ....	120
Figure 4.15	– Phase diagram of the Class-E <sup>2</sup> converter for $D_c = 0.5$ considering $i_{L_r}/I_{in}$ and $v_{C_2}/V_{in}$ : (a) ZDVS. (b) Non-ZDVS. ....	120
Figure 4.16	– Electro-mechanical-acoustic CET system based on Class-D <sup>2</sup> topology. ....	128
Figure 4.17	– Electro-mechanical-acoustic CET system based on Class-DCW topology. ....	129
Figure 4.18	– Cockcroft-Walton AC-DC rectifier. ....	130
Figure 5.1	– Switching function described by Fourier series for the switch <i>S</i> behavior. (a) $k = 0..1$ . (b) $k = 0..3$ . (c) $k = 0..9$ . (d) $k = 0..50$ . ....	135
Figure 5.2	– Switching function described by Fourier series for the diode <i>D</i> behavior. (a) $k = 0..1$ . (b) $k = 0..3$ . (c) $k = 0..9$ . (d) $k = 0..50$ . ....	136
Figure 5.3	– Class-E <sup>2</sup> resonant DC-DC converter. ....	137
Figure 5.4	– Choke inductor current, $i_{L_c}(t)$ . (a) Time window: 9.5 – 12 $\mu s$ . (b) Time window: 11 – 11.4 $\mu s$ . ....	147
Figure 5.5	– Inverter capacitor voltage, $v_{C_1}(t)$ . (a) Time window: 9.5 – 12 $\mu s$ . (b) Time window: 11 – 11.4 $\mu s$ . ....	147
Figure 5.6	– Resonant current, $i_{L_r}(t)$ . (a) Time window: 9.5 – 12 $\mu s$ . (b) Time window: 11 – 11.4 $\mu s$ . ....	148
Figure 5.7	– Resonant voltage, $v_{C_r}(t)$ . (a) Time window: 9.5 – 12 $\mu s$ . (b) Time window: 11 – 11.4 $\mu s$ . ....	148



Figure 5.8	– Rectifier capacitor voltage, $v_{C_2}(t)$ . (a) Time window: $9.5 - 12 \mu s$ . (b) Time window: $11 - 11.4 \mu s$ . . . . .	149
Figure 5.9	– Output filter inductor current, $i_{L_f}(t)$ . (a) Time window: $9.5 - 12 \mu s$ . (b) Time window: $11 - 11.4 \mu s$ . . . . .	149
Figure 5.10	– Output filter capacitor voltage, $v_{C_f}(t)$ . (a) Time window: $9.5 - 12 \mu s$ . (b) Time window: $11 - 11.4 \mu s$ . . . . .	150
Figure 5.11	– Harmonic content of the Class-E <sup>2</sup> resonant converter. (a) Inverter capacitor $C_1$ voltage, $v_{C_1}$ . (b) Resonant current, $i_{L_r}$ . (c) Rectifier capacitor $C_2$ voltage, $v_{C_2}$ . (d) Output voltage, $v_{C_f}$ . . . . .	151
Figure 5.12	– Output filter capacitor voltage, $v_{C_f}(t)$ with disturbance in the input voltage, $\hat{v}_{in} = 1 V$ (Time window: $200 - 440 \mu s$ ). . . . .	154
Figure 5.13	– Resonant current, $i_{L_r}(t)$ with disturbance in the input voltage, $\hat{v}_{in} = 1 V$ (Time window: $200 - 400 \mu s$ ). . . . .	154
Figure 5.14	– Output filter capacitor voltage, $v_{C_f}(t)$ with disturbance in the frequency (Time window: $100 - 440 \mu s$ ). . . . .	154
Figure 6.1	– Experimental x Theoretical: Gain ( $dB$ ) as function of frequency ( $Hz$ ) for $f = 738 Hz$ considering aluminium ( $l = 100 mm$ ; $R = 15 mm$ ) as transfer media. . . . .	159
Figure 6.2	– Experimental x Theoretical: Gain ( $dB$ ) as function of frequency ( $Hz$ ) for $f = 738 Hz$ considering aluminium ( $l = 100 mm$ ; $R = 15 mm$ ) as transfer media. . . . .	160
Figure 6.3	– Experimental x Theoretical: Gain ( $dB$ ) as function of frequency ( $Hz$ ) for $f = 738 Hz$ considering aluminium ( $l = 200 mm$ ; $R = 15 mm$ ) as transfer media. . . . .	161
Figure 6.4	– Experimental x Theoretical: Gain ( $dB$ ) as function of frequency ( $Hz$ ) for $f = 738 Hz$ considering steel ( $l = 100 mm$ ; $R = 15 mm$ ) as transfer media. . . . .	161
Figure 6.5	– Experimental x Theoretical: Gain ( $dB$ ) as function of frequency ( $Hz$ ) for $f = 738 Hz$ considering steel ( $l = 200 mm$ ; $R = 15 mm$ ) as transfer media. . . . .	162
Figure 6.6	– Experimental x Theoretical: Gain ( $dB$ ) as function of frequency ( $Hz$ ) for $f = 1040 Hz$ considering aluminium ( $l = 100 mm$ ; $R = 15 mm$ ) as transfer media. . . . .	163
Figure 6.7	– Experimental x Theoretical: Gain ( $dB$ ) as function of frequency ( $Hz$ ) for $f = 1040 Hz$ considering aluminium ( $l = 200 mm$ ; $R = 15 mm$ ) as transfer media. . . . .	164
Figure 6.8	– Experimental x Theoretical: Gain ( $dB$ ) as function of frequency ( $Hz$ ) for $f = 1040 Hz$ considering steel ( $l = 100 mm$ ; $R = 15 mm$ ) as transfer media. . . . .	164
Figure 6.9	– Experimental x Theoretical: Gain ( $dB$ ) as function of frequency ( $Hz$ ) for $f = 1040 Hz$ considering steel ( $l = 200 mm$ ; $R = 15 mm$ ) as transfer media. . . . .	165
Figure 6.10	– Developed power conversion circuit. (a) AC-DC converter based on Cockcroft-Walton multiplier. (b) AC-DC converter based on Class-E resonant rectifier. . . . .	172
Figure 6.11	– Experimental setup. (a) Electro-mechanical-acoustic CET system connected to power conversion circuits. (b) Developed printed circuit board. . . . .	173
Figure 6.12	– Experimental results for the electro-mechanical-acoustic CET system with resonant Class-E rectifier considering load variation ( $P_{in} = 0.318 W$ ). (a) Output voltage $V_o$ . (b) Output current $I_o$ . (c) Output power $P_o$ . (d) Efficiency $\eta$ . . . . .	174

Figure 6.13 – Waveforms for the Class-E resonant rectifier - $v_{C_2}$ . (a) Theoretical. (b) Simulation. (c) Experimental. ....	175
Figure 6.14 – Waveforms for the Class-E resonant rectifier - $V_o$ . (a) Theoretical. (b) Simulation. (c) Experimental. ....	175
Figure 6.15 – Experimental results for the electro-mechanical-acoustic CET system with Cockcroft-Walton multiplier considering load variation ( $P_{in} = 0.24 W$ ). (a) Output voltage $V_o$ . (b) Output current $I_o$ . (c) Output power $P_o$ . (d) Efficiency $\eta$ . ....	177
Figure 6.16 – Experimental results for the electro-mechanical-acoustic CET system with Cockcroft-Walton multiplier. (a) $R_L = 1.2 k\Omega$ . (b) $R_L = 6.6 k\Omega$ . (c) $R_L = 11 k\Omega$ . (d) $R_L = 26 k\Omega$ . ....	178
Figure A.1 – Decomposition into unit-less parameters for the transfer media representation. ....	202
Figure C.1 – Class-D <sup>2</sup> resonant power conversion system. (a) Class-D <sup>2</sup> resonant converter. (b) Electro-mechanical-acoustic CET system based on Class-D <sup>2</sup> topology. ....	207
Figure C.2 – Assumption for the input source of the Class-D <sup>2</sup> resonant DC-DC converter. ....	208
Figure C.3 – Assumption for the output capacitor of the Class-D <sup>2</sup> resonant DC-DC converter. ....	208
Figure C.4 – Class-D <sup>2</sup> resonant DC-DC converter model. ....	209
Figure C.5 – Class-D <sup>2</sup> resonant DC-DC converter - Operating mode I: $S_1$ and $D_1$ on; $S_2$ and $D_2$ off. ....	209
Figure C.6 – Class-D <sup>2</sup> resonant DC-DC converter - Operating mode II: $S_1$ and $D_2$ on; $S_2$ and $D_1$ off. ....	210
Figure C.7 – Class-D <sup>2</sup> resonant DC-DC converter - Operating mode III: $S_2$ and $D_2$ on; $S_1$ and $D_1$ off. ....	211
Figure C.8 – Class-D <sup>2</sup> resonant DC-DC converter - Operating mode IV: $S_2$ and $D_1$ on; $S_1$ and $D_2$ off. ....	211
Figure C.9 – Normalized waveforms for the Class-D <sup>2</sup> resonant DC-DC converter for $D_c = 0.25$ . (a)-(f) Circuit variables. ....	219
Figure C.10 – Normalized waveforms for the Class-D <sup>2</sup> resonant DC-DC converter for $D_c = 0.5$ . (a)-(f) Circuit variables. ....	220
Figure C.11 – Phase diagrams for the Class-D <sup>2</sup> resonant DC-DC converter. (a) $D_c = 0.3$ . (b) $D_c = 0.35$ . (c) $D_c = 0.4$ . (d) $D_c = 0.45$ . (e) $D_c = 0.5$ . (f) $D_c = 0.55$ . (g) $D_c = 0.6$ . (h) $D_c = 0.65$ . (i) $D_c = 0.7$ . ....	221
Figure C.12 – Normalized gain and component stress curves for the Class-D <sup>2</sup> converter: (a) Transfer power ratio $T_{POT}$ as function of $D_c$ . (b) Switch $S_1$ peak current $I_{S_{1_{peak}}}/I_{in}$ as function of $D_c$ . (c) Switch $S_2$ peak current $I_{S_{2_{peak}}}/I_{in}$ as function of $D_c$ . (d) Diode $D_1$ peak voltage $V_{D_{1_{peak}}}/V_{in}$ as function of $D_c$ . (e) Diode $D_2$ peak voltage $V_{D_{2_{peak}}}/I_{in}$ as function of $D_c$ . (f) Output voltage - rms $V_{or_{rms}}/V_{in}$ as function of $D_c$ . (g) Ripple in the output voltage $\Delta V_o/V_{in}$ as function of $D_c$ . (h) Transfer power ratio $T_{POT}$ as function of $Q_L$ . (i) Output voltage - rms $V_{or_{rms}}/V_{in}$ as function of $Q_L$ . ....	222
Figure D.1 – Main events of the genetic algorithm. ....	224
Figure E.1 – Driving circuits considering the piezoelectric components as resonant tank. ....	228
Figure E.2 – Driving circuits based on external electrical components. ....	228
Figure E.3 – Driving circuits based on function generator, power amplifier and MPPT circuit. ....	229

## LIST OF TABLES

Table 1.1	– Comparison among modeling approaches. ....	35
Table 2.1	– Overview of contactless energy transfer systems. ....	39
Table 2.2	– Literature review on acoustic contactless energy transfer systems. ..	42
Table 2.3	– Literature review on inductive contactless energy transfer systems. ..	45
Table 2.4	– Literature review on capacitive contactless energy transfer systems. ....	46
Table 2.5	– Literature review on optical contactless energy transfer systems. ....	47
Table 3.1	– List of components for multiphysics networks. ....	57
Table 3.2	– List of sources for multiphysics networks. ....	58
Table 3.3	– Parameters for the piezoelectric components. ....	68
Table 3.4	– Parameters for the transfer media - Aluminium. ....	68
Table 3.5	– Parameters for the transfer media - Steel. ....	68
Table 3.6	– Parameters for the transfer media - PVC. ....	69
Table 3.7	– Relationships among unit-less, electromechanical, piezoelectric, acous- tical and transfer media parameters. ....	93
Table 3.8	– Design specifications for the example of denormalization procedure. ....	94
Table 3.9	– Designed system based on the normalized model. ....	97
Table 4.1	– Unit-less parameters for the Class-E <sup>2</sup> resonant converter considering $\alpha = 1.0$ , $A_2 = 0.55$ and $A_3 = 1.25$ . ....	121
Table 4.2	– Unit-less parameters for the Class-E <sup>2</sup> resonant converter considering $\alpha = 1.0$ , $A_2 = 0.75$ and $A_3 = 1.25$ . ....	121
Table 4.3	– Design specifications for the electro-mechanical-acoustic CET system based on Class-E <sup>2</sup> topology. ....	124
Table 4.4	– Unit-less parameters for the electro-mechanical-acoustic CET system based on Class-E <sup>2</sup> topology. ....	124
Table 4.5	– Components for the electro-mechanical-acoustic CET system based on Class-E <sup>2</sup> topology. ....	125
Table 5.1	– Parameters to numerically solve the large-signal model. ....	146
Table 6.1	– Properties of the aluminium. ....	157
Table 6.2	– Properties of the steel. ....	158
Table 6.3	– Parameters for the $f = 738 \text{ kHz}$ piezoelectric transducers. ....	158
Table 6.4	– Parameters for the $f = 1040 \text{ kHz}$ piezoelectric transducers. ....	163
Table 6.5	– Parameters for the models: $f = 738 \text{ kHz}$ piezoelectric transducers considering aluminium ( $l = 100 \text{ mm}$ ; $R = 15 \text{ mm}$ ) as transfer media. ....	166
Table 6.6	– Parameters for the models: $f = 738 \text{ kHz}$ piezoelectric transducers considering aluminium ( $l = 200 \text{ mm}$ ; $R = 15 \text{ mm}$ ) as transfer media. ....	166
Table 6.7	– Parameters for the models: $f = 738 \text{ kHz}$ piezoelectric transducers considering steel ( $l = 100 \text{ mm}$ ; $R = 15 \text{ mm}$ ) as transfer media. ....	167
Table 6.8	– Parameters for the models: $f = 738 \text{ kHz}$ piezoelectric transducers considering steel ( $l = 200 \text{ mm}$ ; $R = 15 \text{ mm}$ ) as transfer media. ....	167
Table 6.9	– Parameters for the models: $f = 1040 \text{ kHz}$ piezoelectric transducers considering aluminium ( $l = 100 \text{ mm}$ ; $R = 15 \text{ mm}$ ) as transfer media. ....	168
Table 6.10	– Parameters for the models: $f = 1040 \text{ kHz}$ piezoelectric transducers considering aluminium ( $l = 200 \text{ mm}$ ; $R = 15 \text{ mm}$ ) as transfer media. ....	168
Table 6.11	– Parameters for the models: $f = 1040 \text{ kHz}$ piezoelectric transducers considering steel ( $l = 100 \text{ mm}$ ; $R = 15 \text{ mm}$ ) as transfer media. ....	169
Table 6.12	– Parameters for the models: $f = 1040 \text{ kHz}$ piezoelectric transducers considering steel ( $l = 200 \text{ mm}$ ; $R = 15 \text{ mm}$ ) as transfer media. ....	169
Table 6.13	– Error analysis for the comparison experimental x theoretical. ....	171

*LIST OF TABLES*

---

Table 6.14	– Specification and components for the designed Class-E resonant rectifier. ....	173
Table 6.15	– Designed Cockcroft-Walton multiplier. ....	176
Table 6.16	– Comparison with related works. ....	180
Table D.1	– Evolutionary genetic algorithm to design Cockcroft-Walton AC-DC multipliers. ....	225
Table F.1	– Automatic AC Model Construction Algorithm ....	231
Table G.1	– Matrix $\mathbf{A}_{\mathbf{L}}$ elements - Pt. I. ....	234
Table G.2	– Matrix $\mathbf{A}_{\mathbf{L}}$ elements - Pt. II. ....	235
Table G.3	– Matrix $\mathbf{A}_{\mathbf{L}}$ elements - Pt. III. ....	236
Table G.4	– Matrix $\mathbf{A}_{\mathbf{L}}$ elements - Pt. IV. ....	237
Table G.5	– Matrix $\mathbf{A}_{\mathbf{L}}$ elements - Pt. V. ....	238
Table G.6	– Matrix $\mathbf{A}_{\mathbf{L}}$ elements - Pt. VI. ....	239
Table G.7	– Matrix $\mathbf{A}_{\mathbf{L}}$ elements - Pt. VII. ....	240
Table G.8	– Matrix $\mathbf{A}_{\mathbf{L}}$ elements - Pt. VIII. ....	241
Table G.9	– Matrix $\mathbf{A}_{\mathbf{L}}$ elements - Pt. IX. ....	242
Table H.1	– Matrix $\mathbf{B}_{\mathbf{S}}$ elements. ....	244

## ABBREVIATIONS

AC	<i>Alternating Current</i>
CET	<i>Contactless Energy Transfer System</i>
CMOS	<i>Complementary-Metal-Oxide-Semiconductor</i>
CPT	<i>Capacitive Contactless Power Transfer</i>
DC	<i>Direct Current</i>
EM	<i>Electromagnetic Waves</i>
EV	<i>Electric Vehicle</i>
FEM	<i>Finite Element Method</i>
FFT	<i>Fast Fourier Transform</i>
GAM	<i>Generalized Averaged Model</i>
IPT	<i>Inductive Power Transfer</i>
LED	<i>Light-Emitting Diodes</i>
MPPT	<i>Maximum Power Point Tracking</i>
PZT	<i>Piezoelectric Component, Piezoelectric Transformer</i>
SPICE	<i>Simulation Program with Integrated Circuit Emphasis</i>
SSHI	<i>Synchronized Switch Harvesting on Inductor</i>
UAV	<i>Unmanned Aerial Vehicles</i>
V2G	<i>Vehicle to Grid</i>
WPT	<i>Wireless Power Transfer</i>
ZCS	<i>Zero Current Switching</i>
ZDCS	<i>Zero Derivative Current Switching</i>
ZDS	<i>Zero Derivative Switching</i>
ZDVS	<i>Zero Derivative Voltage Switching</i>
ZVS	<i>Zero Voltage Switching</i>



## SYMBOLS

$a$	Inverse transfer power ratio
$A_{FFT}$	Amplitude of the normalized harmonic content
$\mathbf{A}_L$	Large-signal model state matrix
$\mathbf{A}_k$	State matrix
$A_j$	Normalized electrical resonant frequency
$\overline{\mathbf{A}}_k$	State matrix related to $\mathbf{e}(t)$
$A_r$	Piezoelectric component area
$Ar$	Area of the transducer
$\mathbf{A}_S$	Small-signal model state matrix
$b$	Term in $\overline{\mathbf{B}}_k$ that is different from 0 or 1
$\mathbf{B}_L$	Large-signal model input matrix
$\mathbf{B}_k$	Input matrix
$\overline{\mathbf{B}}_k$	Input matrix related to $\mathbf{e}(t)$
$\mathbf{B}_S$	Small-signal model input matrix
$\mathbf{C}_k$	Output matrix
$\overline{\mathbf{C}}_k$	Output matrix related to $\mathbf{e}(t)$
$C_L$	Wave velocity
$C_n$	Capacitor
$C_{TOT}$	Total capacitance
$c_{33}^E$	Piezoelectric stiffness
$D$	Diode
$D_c$	Duty cycle
$\mathbf{D}_k$	Transmission matrix
$\overline{\mathbf{D}}_k$	Transmission matrix related to $\mathbf{e}(t)$
$D_l$	Mechanical damper
$\mathbf{e}$	New state vector, new vector space
$\overline{\mathbf{E}}_k$	Unit-less state matrix
$E_{nc}$	Storage element
$Exp(f)$	Function related to the experimental response of a model
$e_{33}^E$	Piezoelectric coupling constant
$f$	Frequency, mechanical force
$f_a$	Anti-resonant frequency
$F_{in}$	Mechanical input force
$\overline{\mathbf{F}}_k$	Unit-less input matrix
$f_{1,2}(t)$	Force, switching function
$G_k$	Genotype in the genetic algorithm
$\overline{\mathbf{G}}_k$	Unit-less output matrix
$\overline{\mathbf{H}}_k$	Unit-less transmission matrix
$i$	Electrical current
$i_c$	Convolution index

## SYMBOLS

---

$I_{in}$	Current input source
$k$	Harmonic
$K_n$	Mechanical stiffness
$l$	Length of the transfer media
$L_m$	Inductor
$l_n$	Length of a finite element
$M_{a,m}$	Acoustical mass
$M_m$	Mechanical mass
$N_{a,n}$	Acoustical compliance
$MRE$	Mean relative error
$n_{A_j}$	Number of normalized electrical resonant frequencies
$nc$	Number of storage elements
$n_C$	Number of capacitors in the genetic algorithm
$NF$	Near field
$nf$	Number of families for the first generation in the genetic algorithm
$ni$	Number of main iterations in the genetic algorithm
$n_o$	System order
$n_{O_j}$	Number of normalized acoustical resonant frequencies
$n_{Q_l}$	Number of quality factors
$n_{S_{V,I}}$	Number of AC-to-DC transfer functions
$nv$	Number of state variables
$n_{vr}$	Number of variables
$n_{\Lambda_\kappa}$	Number of electromechanical gains
$n_{\Omega_l}$	Number of normalized mechanical resonant frequencies
$n_{\zeta_h}$	Number of dampings
$O_j$	Normalized acoustical resonant frequency
$p$	Acoustic sound pressure
$\mathbf{P}$	Equivalence transformation
$P_{in}$	Acoustical input sound pressure, input power
$q$	Acoustical sound velocity
$\bar{q}$	Quadratic error
$Q_a$	Acoustical quality factor
$Q_{el}$	Electrical quality factor
$Q_{in}$	Acoustical input sound velocity
$Q_{mech}$	Mechanical quality factor
$r$	Radius of the piezoelectric component
$R$	Radius of the transfer media
$R_l$	Resistor
$s_{1,2}$	Fourier coefficient
$S$	Transfer function, switch
$S_I$	AC-to-DC current transfer function
$S_V$	AC-to-DC voltage transfer function
$Theo(f)$	Function related to the theoretical response of a model



## SYMBOLS

---

$T_m$	Generated set by the fitness function
$t_p$	Piezoelectric component thickness
$T_{POT}$	Transfer power ratio
$T_{1,2}$	Diode switching time
$u(t)$	Input source
$\hat{\mathbf{u}}_d(t)$	Small-signal model state vector
$U_o$	Amplitude of a generic input source $u(t)$
$U_\kappa$	Mechanical-acoustic gain
$v$	Electrical voltage
$\hat{v}_{in}$	Small variation in the input source
$V_D$	Diode voltage drop
$V_{in}$	Voltage input source
$Vol$	Volume of the transfer media
$V_{pp}$	Peak-to-peak voltage
$w_{1,2}$	Constants for the augmented-order multiphysical model, weights
$\mathbf{x}$	State vector, vector space
$x_i$	Element related to index $i$ in the standard deviation equation, experimental values in the quadratic error equation
$\hat{\mathbf{x}}$	Small-signal model state vector
$\hat{x}_i$	Theoretical values in the quadratic error equation
$\mathbf{X}$	Large-signal model equilibrium solution
$y$	Mechanical velocity
$y_i$	Large-signal model state variable
$\hat{y}$	Small variation in the state variables
$\mathbf{y}(t)$	Output vector
$Y$	Large-signal model equilibrium solution
$z$	Mechanical displacement
$Z_{a,l}$	Acoustical friction
$Z_{in}$	Mechanical input displacement
$\alpha$	Transformer ratio
$\alpha_\nu$	Electro-mechanical coupling factor
$\gamma_\nu$	Mechanical-acoustic coupling factor
$\Gamma$	Correction factor
$\delta V_o$	Voltage ripple
$\Delta V_o$	Voltage drop
$\epsilon_{33}^E$	Permittivity of the piezoelectric layer
$\varepsilon_{nc}$	System variable
$\zeta_h$	Damping
$\eta$	Efficiency
$\Lambda_\kappa$	Electro-mechanical gain
$\mu$	Mean of the values in the standard deviation equation
$\mu_L$	Material friction coefficient
$\Xi$	Selection factor

## *SYMBOLS*

---

$\rho$	Density of the transfer media material
$\sigma$	Standard deviation
$\omega$	Angular frequency
$\omega_a$	Angular acoustical resonant frequency
$\omega_s$	Angular operating frequency
$\hat{\omega}_s$	Small variation in the angular frequency
$\Omega_s$	Operating frequency
$\Omega_l$	Normalized mechanical resonant frequency
$\mathcal{A}$	Force factor
$\langle \rangle_k$	Notation that represents an evaluated function considering harmonic $k$

## APPENDICES

Appendix A– Generic Transfer Media Decomposition into Lumped Components .....	199
Appendix B– Proofs .....	205
Appendix C– Class-D <sup>2</sup> Resonant Converter .....	207
Appendix D– Evolutionary Genetic Algorithm for Design of Cockcroft-Walton Circuits .....	223
Appendix E– Discussion about the Practical Implementation of the Driving Circuits .....	227
Appendix F– Automatic AC Model Construction Algorithm .....	231
Appendix G– Large-Signal Model of the Class-E <sup>2</sup> Resonant Converter .	233
Appendix H– Small-Signal Model of the Class-E <sup>2</sup> Resonant Converter .	243



# TABLE OF CONTENTS

<b>1 INTRODUCTION</b> .....	29
1.1 STATE-OF-ART .....	33
1.2 HYPOTHESIS .....	36
1.3 OBJECTIVES .....	37
1.4 SUMMARY .....	38
<b>2 CONTACTLESS ENERGY TRANSFER SYSTEMS</b> .....	39
2.1 TYPES OF CONTACTLESS ENERGY TRANSFER SYSTEMS .....	39
2.1.1 Acoustic .....	40
2.1.2 Inductive .....	42
2.1.3 Capacitive .....	45
2.1.4 Optical .....	46
2.2 ACOUSTIC CONTACTLESS ENERGY TRANSFER SYSTEMS .....	47
2.2.1 Ultrasonic transducers .....	48
2.2.2 Energy transfer through air .....	49
2.2.3 Energy transfer through living tissue .....	49
2.2.4 Energy transfer through solids .....	50
2.3 POWER CONVERSION CIRCUITRY .....	51
2.4 CONCLUSION .....	54
<b>3 SYSTEM MODELING</b> .....	55
3.1 METHODOLOGY .....	55
3.2 MULTIPHYSICS NETWORKS .....	56
3.3 MULTIPHYSICAL MODEL BASED ON LUMPED PARAMETERS .....	58
3.4 NORMALIZED MODELING OF MULTIPHYSICS NETWORKS BASED ON UNIT- LESS PARAMETERS .....	70
3.4.1 Real system parameters and unit-less parameters .....	70
3.4.2 Equivalence transformation .....	75
3.4.3 Decomposition into unit-less parameters .....	79
3.4.4 Normalized state-space model based on unit-less parameters .....	81
3.5 EQUIVALENT ELECTRICAL MODEL .....	86
3.6 PIEZOELECTRIC TRANSFORMER MODEL .....	87
3.7 AUGMENTED-ORDER MULTIPHYSICAL MODEL BASED ON LUMPED PARAME- TERS .....	89
3.8 DENORMALIZATION PROCEDURE .....	92
3.9 CONCLUSION .....	98
<b>4 ANALYSIS AND DESIGN OF THE MULTIPHYSICAL SYSTEM BASED ON RESONANT TOPOLOGIES</b> .....	99

4.1 ELECTRO-MECHANICAL-ACOUSTIC CET BASED ON RESONANT TOPOLOGIES	99
4.2 CLASS-E <sup>2</sup> RESONANT CONVERTER	101
4.2.1 State-space model based on real system parameters	106
4.2.2 Normalized state-space model based on real system parameters	108
4.2.3 Normalized state-space model based on unit-less parameters	110
4.3 DESIGN METHODOLOGY	121
4.4 DESIGN OF THE POWER CIRCUITRY FOR THE ELECTRO-MECHANICAL-ACOUSTIC CET SYSTEM BASED ON CLASS-E <sup>2</sup> RESONANT CONVERTER	125
4.5 OTHER TOPOLOGIES	128
4.5.1 Class-D <sup>2</sup> resonant converter	128
4.5.2 Cockcroft-Walton-based converters	129
4.6 CONCLUSION	131
<b>5 GENERALIZED AVERAGED DYNAMIC MODEL</b>	<b>133</b>
5.1 SWITCHING FUNCTION	134
5.2 NON-LINEAR DIFFERENTIAL EQUATIONS	136
5.3 CONVOLUTION BETWEEN SWITCHING FUNCTIONS AND STATE VARIABLES	140
5.4 LARGE-SIGNAL MODEL	141
5.5 SMALL-SIGNAL MODEL	152
5.6 CONCLUSION	154
<b>6 RESULTS</b>	<b>157</b>
6.1 COMPARISON BETWEEN MODELS AND EXPERIMENTAL RESPONSE	157
6.1.1 Results for aluminium - 100 mm length and 15 mm radius considering 738 kHz piezoelectric transducers	158
6.1.2 Results for aluminium - 200 mm length and 15 mm radius considering 738 kHz piezoelectric transducers	160
6.1.3 Results for steel - 100 mm length and 15 mm radius considering 738 kHz piezoelectric transducers	160
6.1.4 Results for steel - 200 mm length and 15 mm radius considering 738 kHz piezoelectric transducers	162
6.1.5 Results for aluminium - 100 mm length and 15 mm radius considering 1040 kHz piezoelectric transducers	162
6.1.6 Results for aluminium - 200 mm length and 15 mm radius considering 1040 kHz piezoelectric transducers	163
6.1.7 Results for steel - 100 mm length and 15 mm radius considering 1040 kHz piezoelectric transducers	164
6.1.8 Results for steel - 200 mm length and 15 mm radius considering 1040 kHz piezoelectric transducers	165
6.2 ERROR ANALYSIS	170
6.3 POWER CONVERSION CIRCUITRY	171

6.3.1 Evaluation of the electro-mechanical-acoustic CET system with Class-E resonant rectifier .....	172
6.3.2 Evaluation of the electro-mechanical-acoustic CET system with Cockcroft-Walton multiplier .....	176
6.4 COMPARISON WITH RELATED WORKS .....	179
6.5 CONCLUSION .....	181
<b>7 CONCLUSION</b> .....	183
7.1 PUBLISHED WORKS .....	184
7.2 FUTURE WORKS .....	185
<b>REFERENCES</b> .....	187
<b>APPENDICES</b> .....	197
A.1 GENERIC TRANSFER MEDIA DECOMPOSITION INTO LUMPED COMPONENTS	199
B.1 PROOF OF LEMMA 1 .....	205
B.2 PROOF OF THEOREM 1 .....	206
C.1 CLASS-D <sup>2</sup> RESONANT CONVERTER .....	207
D.1 EVOLUTIONARY GENETIC ALGORITHM FOR DESIGN OF COCKCROFT-WALTON CIRCUITS .....	223
E.1 DISCUSSION ABOUT THE PRACTICAL IMPLEMENTATION OF THE DRIVING CIRCUITS .....	227
F.1 AUTOMATIC AC MODEL CONSTRUCTION ALGORITHM .....	231
G.1 LARGE-SIGNAL MODEL OF THE CLASS-E <sup>2</sup> RESONANT CONVERTER .....	233
H.1 SMALL-SIGNAL MODEL OF THE CLASS-E <sup>2</sup> RESONANT CONVERTER .....	243





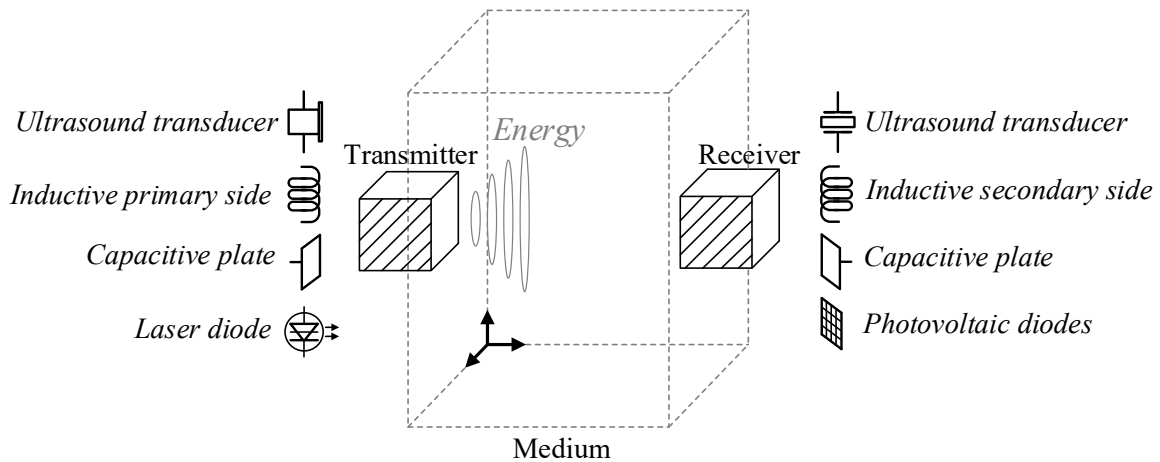
# 1 INTRODUCTION

From the first ideas on the understanding of the physical nature of electricity to cutting-edge technologies, the modern world was molded by the comprehension of energy and its ways of conversion. Energy is still one of today's human challenges.

Envisaging sustainability and environmental concerns, renewable sources are widely used as input sources for electronics systems in order to obtain usable electrical energy. In its low power level, renewable energy systems are well-known as energy harvesting systems, in which energy is extracted from the environment in order to supply a low power device. Considering electricity generation, low power energy harvesting systems, automation of the industrial sector, growth expectations in electric mobility and high demand for portable devices, development of efficient electrical systems becomes mandatory (NEWELL; DUFFY, 2019).

Usually, energy transfer systems are related to wires in electrical circuits or mechanical moving parts. However, aiming to eliminate cables and connectors, transfer energy through physical boundaries and charge non-accessible devices, contactless energy transfer systems (CET) are revealed as solutions. A contactless energy transfer system is a concept in which a transmitter device sends energy through a medium and a receiver catches the energy. The general concept is depicted in Figure 1.1.

Figure 1.1 – Contactless energy transfer system.



Source: Author.

In the search for an ideal switch that can convert raw electrical energy into a controlled flow of electrons, switching technology has evolved from vacuum tube to transistors and in the 1970's and 1980's, the silicon transistor allowed the rise of integrated circuits (EPC, 2017). This evolution on switching technology is leading to improvements in several applications, including contactless energy transfer systems. One example is the use

of a powered work desk as battery charger. A 300 W is capable of power several devices, such as smart-phones, notebooks, watches and desk lamps (EPC, 2017).

In a low power energy harvesting system, a transducer is used to capture energy from different sources, like as solar light, heat, vibration and radio-waves. The energy has to be converted into electrical power and then, an efficient power monitoring and energy storage system should be developed to meet some design specifications. Combining the features of energy harvesting systems and CET, a potential solution for medical applications can be considered. Implanted medical devices that use batteries, such as pacemakers, can have expected lifetime of about ten years, which is fundamentally important the development of a CET system for open surgery avoidance (HOANG; LEE; LEE, 2014).

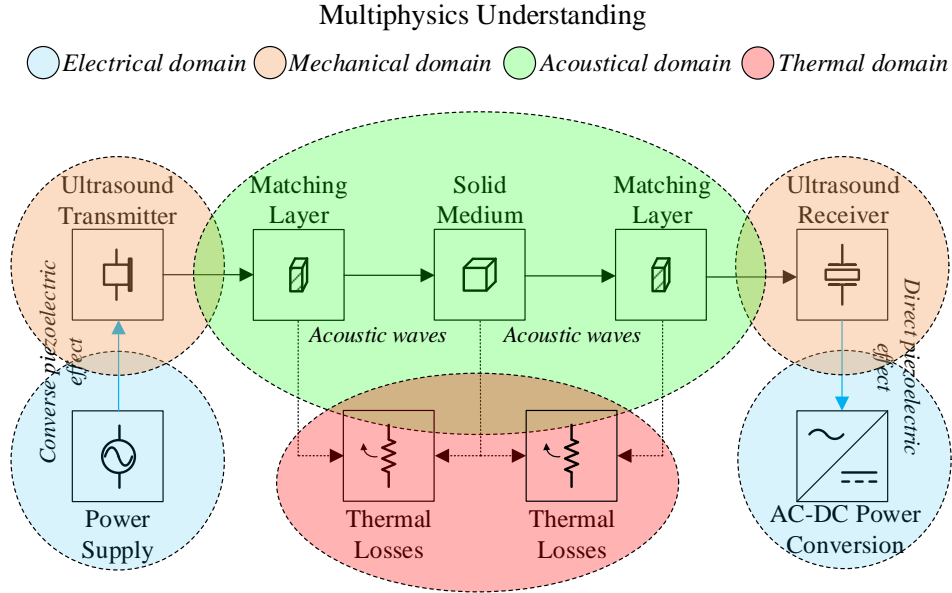
Different types of CET have been emerging, such as acoustic, inductive, capacitive and optical. Acoustic CET has great potential to be used in applications in which electromagnetic waves are not allowed. In addition, reasonable distance between the transmitter and the receiver and honest efficiency put acoustic CET in the same footing of the widely accepted inductive CET.

By transferring power through metal barriers (known as through-wall), acoustic CET can be used in industrial applications. For instance, machine tool sensors can be charged without stopping the operating process. Also, batteries surrounded by metal enclosures, sensors in pipe-lines, nuclear plants and vacuum chambers are cited as applications (BAR-COHEN et al., 2008; YANG et al., 2018a; MENG et al., 2015). Furthermore, considering the thriving evolution of mechatronics and expected space applications, electrical parts bypass solid structures, which is a fitting environment for acoustic CET when wires and electromagnetic waves are not allowed.

Through-wall acoustic CET is divided into five main parts: an ultrasonic transmitter, the transfer media, an ultrasonic receiver, the power conversion circuitry and a load. The ultrasonic transducers can use piezoelectricity in order to convert electrical into mechanical energy and vice-versa. The constructive characteristics of the transducers allow them to send / receive ultrasonic waves. When ultrasound transducers based on piezoelectricity are used in acoustic CET, it can be also named as *electro-mechanical-acoustic CET system*. As long as electrical, mechanical and acoustical domains appear on the CET system, a multiphysics scenario is depicted as shown in Figure 1.2. Modeling of such system can be a complicated task and requires a well-defined methodology. In this sense, this work is founded. The thermal domain was included in Figure 1.2. However, such domain is out of the scope of this work.

Considering the front-to-end block diagram in Figure 1.2, it can be seen that a two electrical ports system is drawn. It is because an electrical source supplies the ultrasound transmitter and an AC-DC power conversion system is used to convert the AC signal from the transducer into a DC signal to supply a specific load.

Figure 1.2 – Multiphysics understanding for electro-mechanical-acoustic contactless energy transfer systems.



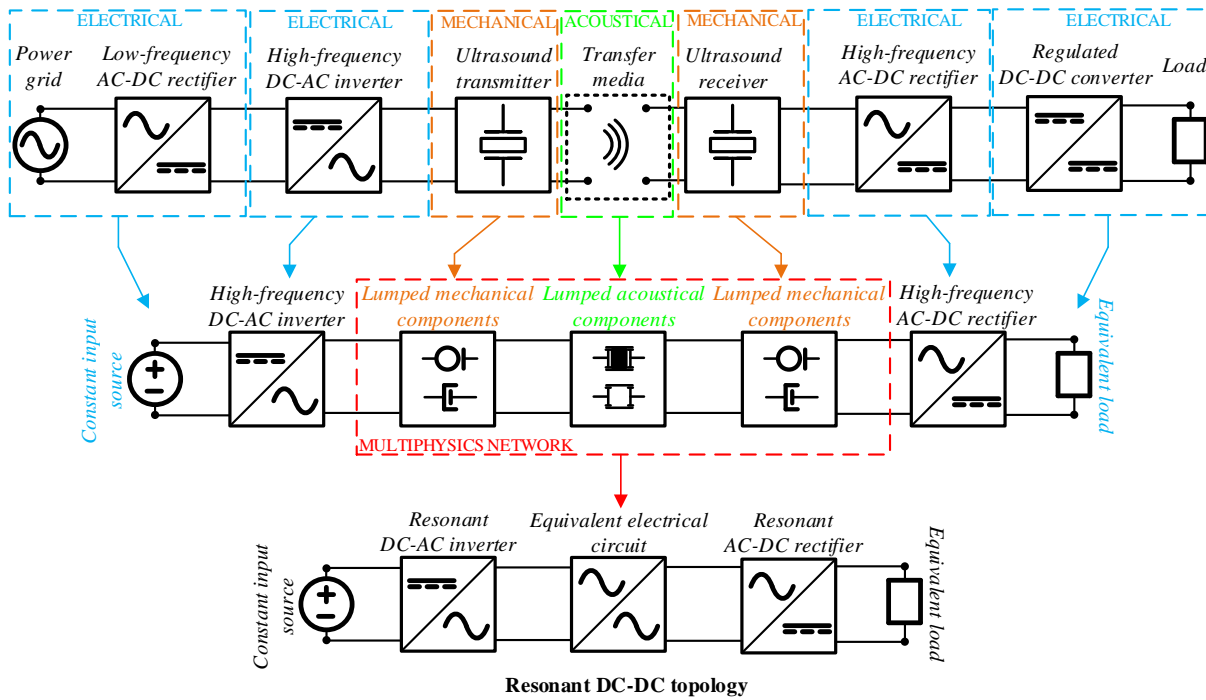
Source: Author.

Considering a grid-connected application, a low-frequency AC-DC rectifier is used to provide a constant voltage source. A high-frequency DC-AC inverter generates the alternate signal to supply the ultrasound transmitter. Figure 1.3 depicts the electro-mechanical-acoustic CET system considering all required power converters for a grid-connected application. The purpose of this illustration is to show the obtainment of an equivalent electrical circuit representation for a multiphysics system in a high-level of abstraction.

It can be seen in Figure 1.3 that the ultrasound transducers can be represented by lumped components, as well as the transfer media. In this sense, analogies among electrical, mechanical and acoustical components should be used. By using lumped components, the mechanical and acoustical systems can be easily connected to the power converters.

The power grid and the low-frequency AC-DC rectifier can be simplified by a constant input source, which supplies the high-frequency DC-AC inverter. The regulated DC-DC converter and the load can be represented as an equivalent load for the AC-DC rectifier. By using networks theory, the multiphysics network can be represented by an equivalent electrical circuit. As shown in Figure 1.3, the final representation has DC input and DC output. However, there is an AC power conversion required for the CET system. In this work, resonant topologies are considered to drive the system. It is because,

Figure 1.3 – Electro-mechanical-acoustic CET system based on resonant DC/DC topology.



Source: Author.

resonant converters shape the waveforms in a sinusoidal way. In addition, switching losses are reduced by means of soft-switching operating conditions.

This Doctorate Thesis presents a modeling methodology for an electro-mechanical-acoustic contactless energy transfer system and the analysis and design of the power conversion circuits. The main idea is to represent the system as a multiphysical model based on lumped parameters. This model uses components to describe the behavior of the electrical, mechanical and acoustical parts. From the multiphysical model, an equivalent electrical model is derived, which is suitable for SPICE simulations. In addition, a piezoelectric transformer model is developed in order to have a simpler configuration that can be topologically connected to other converters without causing a very complex system. The multiphysical model based on lumped parameters can be considered a novelty in the literature because it puts together all the power conversions, electrical-to-mechanical, mechanical-to-acoustical, acoustical-to-mechanical and mechanical-to-electrical into a single state-space representation. Even though there are some works that represent the CET system by lumped parameters, literature shows that usually, impedance matrices are used as methodology. However, real physical components are omitted into a unknown representation block that is submitted to signals in order to obtain the transfer parameters (YANG et al., 2018b; BAO et al., 2007).

Furthermore, this Thesis proposes a normalized state-space model based on unit-

less (dimensionless) parameters for the electro-mechanical-acoustic CET system, which leads to generalized solutions that do not depend on specifications, such as input power, frequency, input voltage, etc.; and do not depend on real system parameters, such as inductors, capacitors, mechanical stiffness, acoustical mass and so on. An equivalence transformation is used on the modeling in order to systematize the method. A decomposition in unit-less parameters is applied on the multiphysics network to extract unit-less parameters.

An analysis and design methodology for multiphysics systems is proposed based on resonant topologies. The main idea is to use a representation for the multiphysical model in a way that it can be connected to resonant circuits. By means of this concept, the power conversion circuits can be designed in order to manage the transferred power while considering the behavior of the multiphysical system.

The Class-E<sup>2</sup> DC-DC resonant converter is used as topological representation of the multiphysical system. Similar idea was performed by Nagashima et al. (2015) for inductive wireless power transfer systems. In this work, the resonant tank of Class-E<sup>2</sup> converter is used to represent the multiphysical energy conversion, while the components of the inverter and rectifier stages can be designed to manage the electrical power. In order to perform the dynamic model of the converter, the generalized averaged model is applied to develop the large-signal and small-signal models. A practical demonstrator combining the ultrasonic transducers, transfer media and AC-DC rectifier is assembled in order to experimentally investigate the electro-mechanical-acoustic CET system.

## 1.1 STATE-OF-ART

Contactless energy transfer systems have been used based on acoustic, inductive, capacitive and optical types. Inductive CET shows higher efficiency but when the distance between transmitter and receiver is increased, efficiency is drastically reduced. Optical CET appears as a solution when longer distances are needed, varying from meters to kilometers. However, efficiency is low and it is confined to applications that radiation is allowed. Capacitive CET has reduced electromagnetic interference and is suitable for integrated circuits. However, output power is low and the distance between plates is very limited. Acoustic CET affirms its place as candidate solution for wireless power transfer (WPT) because through-wall applications can be considered. Distance is reasonable and efficiency varies from 1-90 % depending on the application (KAZMIERKOWSKI; MORADEWICZ, 2012; TAALLA et al., 2019).

Considering through-wall applications, Yang et al. (2018b) has shown an acoustic CET by means of ultrasonic transducers based on piezoelectricity. The transducers are bonded on the opposite sides of the metal wall and a full-bridge rectifier cascaded with a

regulated DC-DC power converter performs the electrical power conversion. The methodology used by Yang et al. (2018b) is based on Lawry et al. (2012). The main idea is to consider the acoustic part as a “black-box” and relate the electromechanical parts by means of impedance matrices. In other words, a two-port network is used. In addition, a normalized smith chart is used to design the matching networks. Overall efficiency was 27.7 % by considering a 40-mm-thick stainless steel plate.

Three main approaches of acoustic CET modeling are highlighted:

1. *Analytical 3D wave equation*;
2. *Multiphysics networks*;
3. *Finite element methods*.

*Analytical 3D wave equation* is a representation of a wave in a three-dimensional environment by partial differential equations. Although its solution is a closed-form elegant expression, it is valid for specific boundary conditions (SINGH; CHANDRA; SINGH, 2015). Practical applications lead to complex boundary conditions in order to define the transfer media geometry. In addition, the task becomes harder if both shear and longitudinal waves are included in the mathematical representation. Another question mark about this approach is how to connect such solution to a 1D-based representation of power conversion circuit for power transfer applications.

*Multiphysics networks* deal with systems that are interconnected by different domains, like as electrical, mechanical and acoustical. The main areas of study are microtechnology and mechatronics (MARSCHNER; WERTHSCHUTZKY, 2015). By using discrete building blocks, the different domains are represented by networks (circuits) (LENK et al., 2011). Most of the analysis techniques can be used in such networks, such as Kirchhoff’s laws, Newton’s laws of motion, state-space models, frequency domain response, and so on. As a drawback, in order to validate the models for different resonant frequencies, several discrete components should be used to approximate the representation as a distributed parameters system, which can lead to high computational effort to solve the multiphysics networks. In such approximation, it is difficult to match the real system properties with the discrete components (GASSMANN, 2007).

At this point, it is important to differentiate multiphysics networks to finite element method for multiphysics simulation. The first one is related to a representation by lumped components, such as inductors, capacitors, acoustical mass, mechanical stiffness, and so on; and their interactions. Also, multiphysics networks are represented by differential equations and usually solved by iterative numerical methods or semi-analytical solutions. For instance, mathematical software are used, such as MATLAB® and Mathematica®; in some cases, SPICE® software are more suitable.

On the other hand, *finite element method* (FEM) for multiphysics simulation is a

numerical method for solving problems of coupled systems. A large system is subdivided into simpler parts called finite elements (ZIMMERMAN, 2006). The finite element method is suitable for applied engineering problems. The main advantages are that complex geometry and irregular shapes can be designed, material properties can be included (usually in a friendly interface) and it can easily represent different domains. However, the finite element method requires a large amount of data as input to realize the meshing and a longer execution is performed to solve only one problem. For this reason, it is difficult to have an understanding of the system's behavior in a generalized way (DUDHAL; UPADHYE; AGASHE, 2016; ZHANG, 2017; ABDULLAHI; OYADIJI, 2018).

The three main approaches for acoustic CET are summarized in Table 1.1:

Table 1.1 – Comparison among modeling approaches.

Method	Advantage	Disadvantage
3D wave equation	3D perception	Hard multi-domain interactions
	Closed-form solution	Defining geometries
Multiphysics networks	Circuit theory	No 3D perception
	Multi-domain interactions	Trade-off: complex/accuracy
FEM	3D perception	Number of inputs
	Geometries	Longer execution

As long as the output from the receiver is an AC signal in CET, it must be converted into a DC signal to supply a load. In this case, rectifiers circuits should be used. There are several options for rectifying circuits; highlighted here is the full-bridge cascaded with a regulated DC-DC converter reported by Yang et al. (2018b). In a high-level of abstraction, design methodologies use the design-oriented architecture, which can be summarized by the following steps:

1. Starting from a system or technical task, a rough concept is drawn toward to solve an engineering's task;
2. Design specifications are defined, such as input voltage, output voltage, output power and operating frequency;
3. Proposition of a converter by means of general guidelines or the choice of classical topologies;
4. Design-oriented analysis, in which the converter is analyzed by means of computational tools and empirical methods in order to achieve a mathematical model;
5. Circuit design considering previous specifications;

6. Iterative circuit-level simulations;
7. Results;
8. Experimental tests.

This type of architecture aims to solve a specific application. It can be seen that the second step already defines the specifications and the remaining procedure will be confined to the initial requirements. An alternative for this procedure was proposed by Bisogno (2006), Mendonça (2017) and Mendonça et al. (2018), which is referred as result-oriented architecture and can be described by the following steps:

1. Starting from a system or technical task, a rough concept is drawn toward to solve an engineering's task;
2. A result-oriented analysis is performed by converting real system parameters into unit-less parameters;
3. Normalized results in relation to the specifications are achieved;
4. A database is created with the results for any operating point;
5. Design specifications are defined, such as input voltage, output voltage, output power and operating frequency;
6. Choice of one or more suitable topologies;
7. Design based on the unit-less parameters;
8. Experimental tests.

The result-oriented architecture suggests that the results are previously obtained and the converter design ensues in the same. The condition imposed for it is that the obtained results are normalized, meaning that they are valid for any operating point and specification.

The result-oriented architecture can be referred as a normalized approach. It was explored in PWM (pulse-width modulation) converters and resonant inverters.

Based on the aforementioned state-of-art related to acoustic contactless energy transfer systems and analysis and design methodologies for power converters, the hypothesis for this work are going to be described in the next section.

## 1.2 HYPOTHESIS

1. It is possible to include the required multiphysical power conversions in electro-mechanical-acoustic contactless energy transfer systems, like as electrical-to-mechanical,



mechanical-to-acoustic, acoustic-to-mechanical and mechanical-to-electrical into a single state-space representation by means of coupling devices that linearly connect the different domains;

2. It is possible to design the transfer media geometry and the piezoelectric transducers of a contactless energy transfer system by means of a normalized state-space model that includes, not only electrical circuits, but also multiphysics networks. For instance, the development of a modeling methodology for coupled systems (electrical, mechanical and acoustical) can be interesting to contribute on the understanding of multiphysics systems in a generalized way. In other words, it is possible to convert the real system parameters into unit-less parameters in order to represent the system in a mathematical format that is independent of specifications;
3. It is possible to analysis and design power converters for a contactless energy transfer system by including an equivalent electrical model for multiphysics systems as part of the resonant tank in resonant converters.

### 1.3 OBJECTIVES

The general objective of this work is the development of a modeling methodology for systems composed of coupled electrical, mechanical and acoustic domains. The specific objectives of this work are described as follows:

- Representation of an electro-mechanical-acoustic contactless energy transfer system by means of a multiphysical state-space model based on lumped components that includes all the required power conversions: electrical-to-mechanical, mechanical-to-acoustic, acoustic-to-mechanical and mechanical-to-electrical;
- Development of a modeling methodology for multiphysics networks based on unit-less parameters;
- Normalized analysis of resonant converters including the models for the electro-mechanical-acoustic CET system;
- Dynamic modeling of the Class-E<sup>2</sup> resonant converter;
- Assembling of a practical demonstrator that includes: ultrasonic transmitter, transfer media based on solid material, ultrasonic receiver and power conversion circuitry.

## 1.4 SUMMARY

This introduction has shown the general concept of an electro-mechanical-acoustic CET system and which aspects are interesting to be explored as scientific contributions. The hypothesis and objectives of the thesis were described in order to create a preamble for this work.

It was pointed out the multiphysics scenario in the electro-mechanical-acoustic CET system and why it is interesting to develop a model that includes all the required power conversion. Furthermore, it was highlighted the use of resonant topologies for the representation of CET systems. In this sense, normalized models were set as goals to be applied into the power conversion systems.

## 2 CONTACTLESS ENERGY TRANSFER SYSTEMS

In this section, a review of the literature in contactless energy transfer system is presented. First, the main types of CET are explained, like as acoustic, inductive, capacitive and optical. A comparison among different works is going to be shown considering operating frequency, efficiency, distance between transducers (gap) and application.

Subsequently, this work will deepen the research on acoustic CET. A theoretical background on ultrasound waves, ultrasonic transducers and acoustic CET through air, living tissue and solids is going to be presented. In addition, some industrial applications for acoustic CET are highlighted.

In the end of this chapter, a review on power conversion electrical circuits is performed. Several converters are presented as candidate solutions as power circuitry for acoustic CET systems.

### 2.1 TYPES OF CONTACTLESS ENERGY TRANSFER SYSTEMS

There are different techniques for contactless energy transfer systems, such as acoustic (sound), inductive (magnetic field), capacitive (electric field) and light (optical). An overview of CET technologies is shown in Table 2.1.

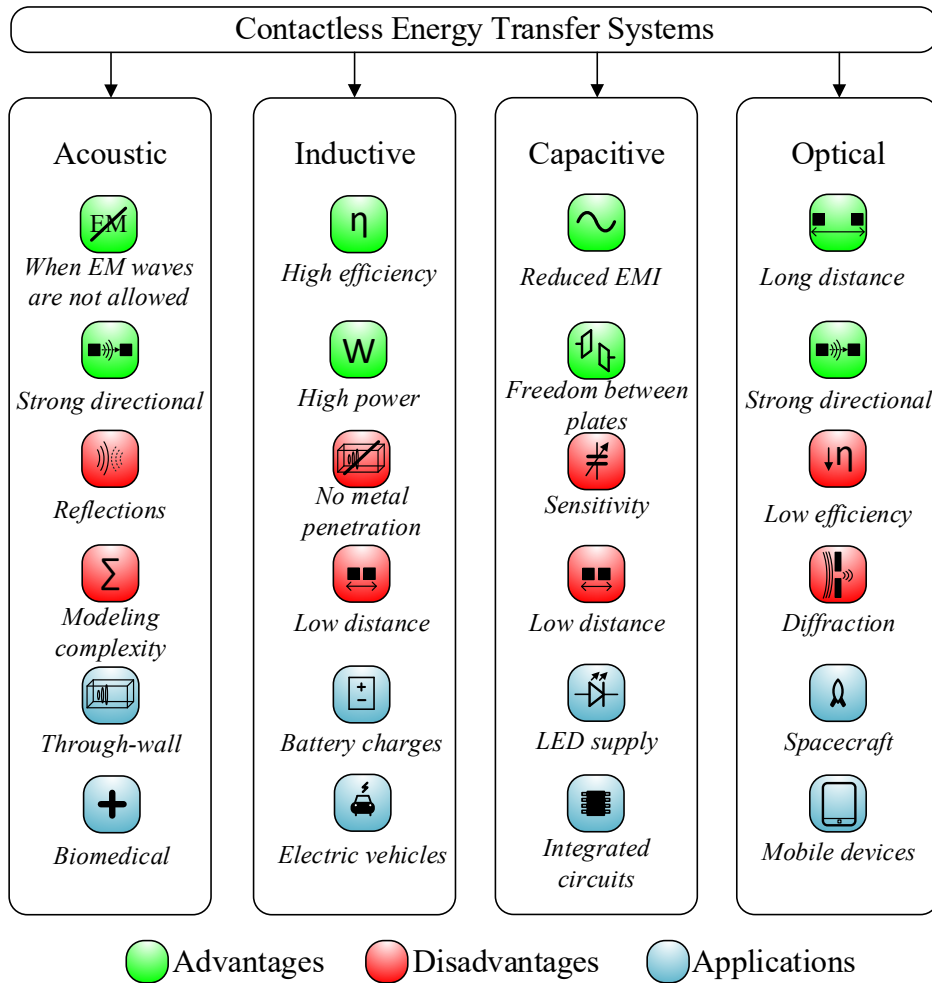
Table 2.1 – Overview of contactless energy transfer systems.

<b>Technology</b>	<b>Distance (mm)</b>	<b>Output power (W)</b>	<b>Efficiency (%)</b>
Acoustic	0.2-400	0.0001-1000	1-90
Inductive	0.2-134	1-200 kW	80-90
Capacitive	0.1-0.5	1-50	50-80
Optical	(m to km)	1-100	20-30

Source: Adapted from (KAZMIERKOWSKI; MORADEWICZ, 2012).

Besides the quantitative features of CET technologies, the properties and typical applications should be taken into account when selecting a CET system. In Figure 2.1, the classification and main applications of CET systems are shown.

Figure 2.1 – Classification and applications of contactless energy transfer systems.



Source: Author.

### 2.1.1 Acoustic

Acoustic CET is suitable when electromagnetic waves (EM) are not allowed. In addition, when high directionality is required, these systems can be designed with smaller dimensions. In general, a transducer is a device that converts one type of energy into another. Ultrasound transducers are used for acoustic CET applications. In acoustic CET, a transducer is used to convert electrical energy into a pressure wave that is transferred through a medium. Another transducer is used as receiver to perform the inverse process, in other words, to convert the sound wave into electrical energy. In this chapter, it is considered the nomenclature *acoustic CET* because many considered works in this literature review are related to that. However, in the development of this work, it is going to be considered as *electro-mechanical-acoustic CET system* in order to highlight that

ultrasound transducers based on piezoelectricity are used.

Three types of acoustic CET are found in the literature and industrial applications:

- Propagation through living tissue;
- Propagation through air;
- Propagation through solids (through-wall).

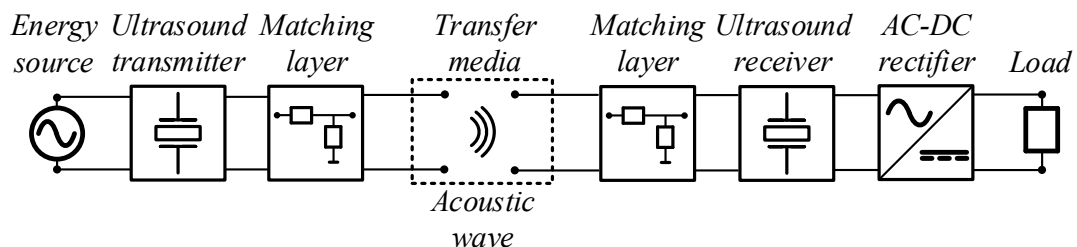
In order to charge implants, like pacemakers, acoustic CET has been extensively explored. Cochran et al. (1985) used a piezoelectric material with an internal fixation device and self-generated electrical stimulation to improve bone healing. It can be considered one of the first applications of acoustic CET for biomedical applications. The energy is harvested from body movement or externally applied ultrasonic energy.

Amar, Kouki & Cao (2015) presented recent methodologies to transfer and harvest energy in implantable medical devices. In general, power approaches for implantable devices are divided into independent systems and systems with a transferring mechanism. The first class is divided into onetime batteries and environmental harvesting, which includes several energy sources, like as biofuel cells, thermoelectricity, piezoelectricity, electrostatics and electromagnetics. Systems with a transferring mechanism are classified as optical charging, inductive coupling or ultrasonic transducers.

Mano, Maio & Heller (2003) presented a bio-full cell implanted in a grape. A power of  $2.4\mu W$  at  $0.52V$  was generated with this miniaturized device. Melodie et al. (2018) reported the piezoelectric properties of materials found inside the body and how they are used in medical implants. In this sense, it is highlighted the use of the ultrasonic lancet for operations aiming to preserve the surrounding tissue.

A general acoustic contactless energy transfer system is portrayed in Figure 2.2.

Figure 2.2 – General block diagram of an acoustic contactless energy transfer system.



Source: Author.

A sinusoidal electrical energy source supplies an ultrasound transmitter that sends an acoustic wave through a transfer media. An ultrasound receiver captures the signal and a rectifier is used to convert the AC signal into DC signal. Matching layers should

be used between the transducers and the transfer media. This is because the acoustic impedance of the transducers, in general, is very different from the transducers. Many types of transfer media can be used, like as air, solids (metals, plastic, etc.) and living tissues, which is going to be explained in details in the next section (TAALLA et al., 2019).

A summarized literature review of acoustic contactless energy transfer systems is presented in Table 2.2. The system features, such as frequency, efficiency  $\eta$ , gap and application are indicated in Table 2.2 for each reference.

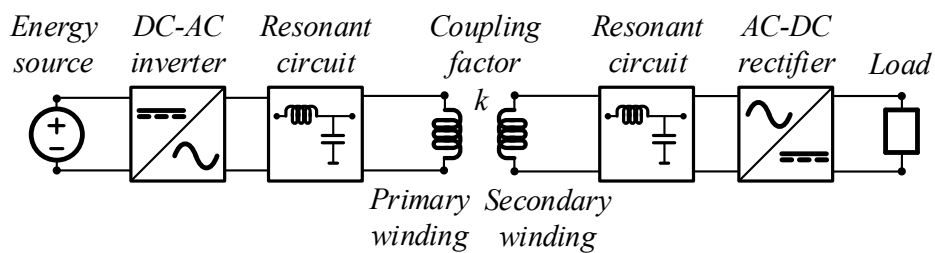
Table 2.2 – Literature review on acoustic contactless energy transfer systems.

Reference	Freq. (kHz)	$\eta$ (%)	Gap (mm)	Application
Denisov & Yeatman (2010)	1000	39	10	Biomedical
Ozeri & Shmilovitz (2010)	673	39.1	40	Biomedical
Shih & Shih (2010)	35	-	15	Biomedical
Lawry et al. (2012)	4000	-	63.5	Through-wall
Zaid et al. (2016)	40.75	-	20	Through-air
Yang et al. (2018b)	944.4	27.7	40	Through-wall
Mahmood, Mohammed & Gharghan (2019)	40	69.4	40	Biomedical

### 2.1.2 Inductive

In inductively coupled CET, a primary side DC-AC power converter transfers AC energy to a secondary side AC-DC power converter with a specific inductive coupling factor. The general block diagram of an inductively contactless energy transfer system is depicted in Figure 2.3.

Figure 2.3 – General block diagram of an inductively contactless energy transfer system.



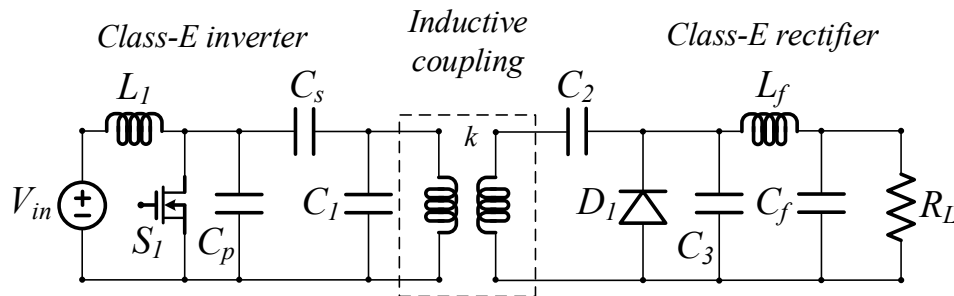
Source: Author.

This system is also named inductive power transfer (IPT). Trautmann et al. (2016)

developed a robust inductive plug for energy and transfer data. By using coupling coils, a contactless transmission channel for low data rate operation between the primary and secondary sides at a frequency of 8  $kHz$  was demonstrated. The main result is a system with 3000  $W$  delivered power at 1  $kbit/s$  data rate. Such system is interesting to be used in harsh environments, in which plug connectors should be resistant to pollutants, like as oil and dust (TRAUTMANN et al., 2016).

As it can be seen in Figure 2.3, a DC-AC inverter and an AC-DC rectifier are necessary to perform the IPT. In this sense, some works deal with the analysis and design of such power converters. Nagashima et al. (2015) analyzed a Class-E resonant inverter and a Class-E resonant rectifier for wireless power transfer systems. By cascading the inverter and the rectifier, the Class-E<sup>2</sup> DC-DC resonant converter is obtained. The advantage of such system is that the inverter switch turns-on under zero voltage switching (ZVS) and zero derivative switching (ZDS). In addition, at the turn-off transition of the rectifier diode, both the diode voltage and its derivative are zero. These features reduce losses and improve the overall system efficiency. The Class-E<sup>2</sup> DC-DC resonant converter for IPT is shown in Figure 2.4.

Figure 2.4 – Class-E<sup>2</sup> wireless power transfer system.



Source: Adapted from (NAGASHIMA et al., 2015).

By applying coupled coils in IPT systems for charging electrical vehicles, cables and wires can be avoided. For such applications, full-bridge inverters were reported in the literature. Lu & Ngo (2018) shows a design approach based on normalized electrical parameters and decouples equations for IPT system based on full-bridge inverter and rectifier. The normalized parameters are described as the quality factor, normalized impedance, normalized switching frequency, coupling coefficient and turns ratio. They are used to perform a systematical design for series-series IPT systems based on given specifications. The design procedure leads to a practical implementation of a 98.9 % of coils efficiency at 100  $kHz$ .

The automotive market is an attractive field for inductive power transfer. However, efficiency and cost are challenges to be faced in electric vehicle (EV) charging system. A typical EV or vehicle to grid (V2G) system is shown in Figure 2.5.

By increasing the operating frequency to MHz, challenges in the power electronics

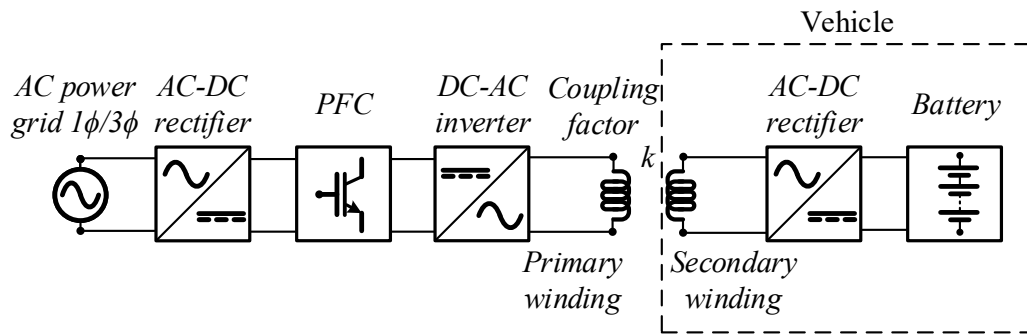


Figure 2.5 – Wireless electric vehicle charging system.

devices are relevant. Furthermore, when an air-core coil is attached to a vehicle, the magnetic flux goes inside the chassis. This leads to significant changes in the coil parameters (NAGATSUKA et al., 2010). Ning et al. (2013) assembled a system for EV with tested efficiency of 90 % for 7 kW power delivery. Recently, a technology of dynamic wireless power transfer with vehicular detection system for vehicle misalignment and speed detection was proposed by Azad et al. (2019). The main parts of the system are a magnetic coupler composed of a transmitter system mounted on the road or in the vehicle and multiple receiver detection coils installed underground to sense the induced voltage. In this case, the contactless energy transfer system is used to sense the voltage, which is processed in order to extract the vehicle misalignment and speed information.

Arteaga et al. (2019) implemented an unmanned aerial vehicle (UAV) with a Husban H107L X4 quadcopter. The standard lithium polymer battery was replaced by an IPT receiver. The drone was able to operate without any energy storage system while near to the IPT transmitter. The selected frequency was 13.56 MHz in order to match the design of the coils regarding size, weight and shape. As the drone changes its alignment with the transmitting coil, the misalignment is one of the main challenges that must be considered in the design methodology. Wireless transfer can be also used in simultaneous power and data transfer, and charging battery applications (YAO et al., 2020; NAMADMALAN; ALONSO; IQBAL, 2021). A summarized literature review of inductive contactless energy transfer systems is described in Table 2.3.



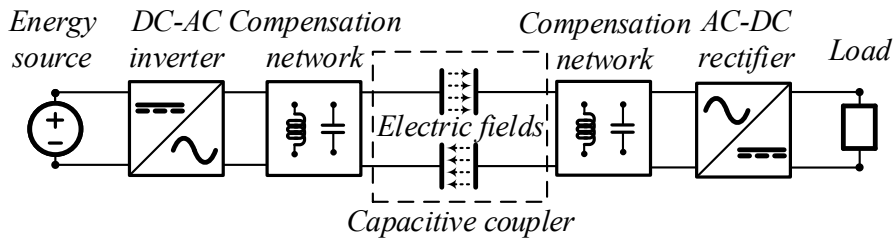
Table 2.3 – Literature review on inductive contactless energy transfer systems.

Reference	Freq. (kHz)	$\eta$ (%)	Gap (mm)	Application
Laskovski & Yuce (2010)	27000	80	15	Biomedical
Sample, Meyer & Smith (2011)	7650	50	700	WPT
Wu et al. (2012)	20	90	246	EV
Calder, Lee & Lorenz (2013)	3540	80	300	WPT
Zhang et al. (2016)	-	77	1100	Smart grid
Arteaga et al. (2019)	13560	60	75	UAV

### 2.1.3 Capacitive

Following the same general concept of CET in Figure 1.1, the capacitive contactless power transfer (CPT) is conceived. Nonetheless, the transmitter and receiver devices are based on metal plates. In general, two plates are used at the primary side as a power transmitter, and two plates at the secondary side as a power receiver, ensuring in at least two coupling capacitors to provide the power flow (LU; ZHANG; MI, 2017). The typical block diagram of a CPT system is shown in Figure 2.6.

Figure 2.6 – General block diagram of a capacitive contactless energy transfer system.



Source: Author.

The main applications of CPT systems are biomedical devices, light-emitting diodes (LED) lighting and mobile device charging. Furthermore, CPT systems have been used to realize dynamic charging while the vehicle is moving along the roadway as demonstrated by Sakai et al. (2016).

Erfani et al. (2018) have reported the modeling and experimental investigation of a CPT system for biomedical implants. A  $400 \text{ mm}^2$  capacitive pads on printed-circuit boards were used for a series-resonant capacitive link. A  $5 \text{ mm}^2$ -thick tissue layer was used along with two  $100 \mu\text{H}$  inductors resulting in resonance frequencies of 115 and 127 kHz. Measurements were performed for different distances between the metal plates.

When the capacitive link is excited by 1  $W$  of power, the maximum specific absorption rate averaged (biosafety-imposed limitations) over 10  $g$  of tissue was reported to be 1.63  $W/kg$ , which is below the safety limit for this kind of application.

In comparison to IPT systems, the CPT technology has the following advantages:

- Good misalignment performance;
- Low cost;
- Low weight;
- Negligible eddy-current loss.

In the IPT system, the coils work as a loosely coupled transformer. In this sense, it is necessary to increase the circulating current in the coils due to very small coupling coefficient. In contrast, only several pieces of metal plates are used to build the capacitive coupler and the system performance is not greatly affected by the thickness of the plates. Considering recent studies, a CPT system with 610  $mm \times 610 mm$  metal plates maintained 89.4 % of the power considering 300  $mm$  misalignment (LU et al., 2015). On the other hand, a IPT system with 600  $mm \times 800 mm$  inductive coupler reduces to 56 % of the well-aligned value with 310  $mm$  misalignment (LI et al., 2015). A summarized literature review of capacitive contactless energy transfer systems is described in Table 2.4.

Table 2.4 – Literature review on capacitive contactless energy transfer systems.

Reference	Freq. ( $kHz$ )	$\eta$ (%)	Gap (mm)	Application
Kline et al. (2011)	4200	80	0.13	WPT
Theodoridis (2012)	1000	>80	-	WPT
Dai & Ludois (2016)	530	90	0.25	EV
Minnaert & Stevens (2018)	300	-	2.5	WPT
Zhu et al. (2019)	2170	66	2.5	Mobile
Abramov, Zeltser & Peretz (2019)	1500	75	30	WPT

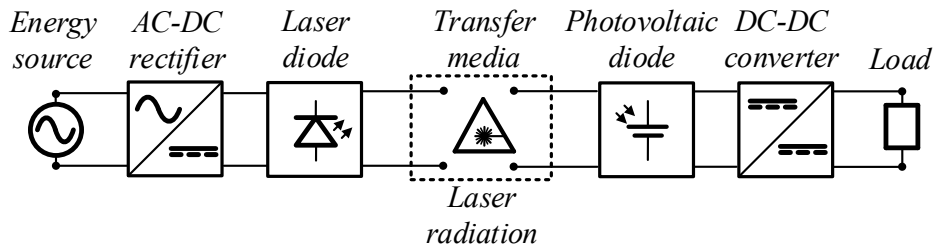
#### 2.1.4 Optical

In optical or light contactless energy transfer systems, laser diodes generate a optical power beam and photovoltaic diodes convert it back into electrical energy. An optical CET system operates similar to far-field electromagnetic or microwave energy transfer systems (KAZMIERKOWSKI; MORADEWICZ, 2012).

A light beam is collimated for maximum overlap with the active region of a photovoltaic with free space in between. The main advantage is long distance (m to km) transmission. In addition, it is easy to control the direction of energy propagation (SAHAI; GRAHAM, 2011), (STONE; HOGAN, 1988).

The optical CET is used in mobile devices and space applications (EDWARDS, 2000). The typical block diagram of an optical CET system is portrayed in Figure 2.7 and a summarized literature review in Table 2.5.

Figure 2.7 – General block diagram of an optical contactless energy transfer system.



Source: Author.

Table 2.5 – Literature review on optical contactless energy transfer systems.

Reference	Freq. (kHz)	$\eta$ (%)	Gap (mm)	Application
Fakidis (2017)	-	3.2	3600	EH
Kim & Rhee (2018)	-	12.1	500000	WPT
Lim, Khwaja & Ha (2019)	-	-	1000	WPT

## 2.2 ACOUSTIC CONTACTLESS ENERGY TRANSFER SYSTEMS

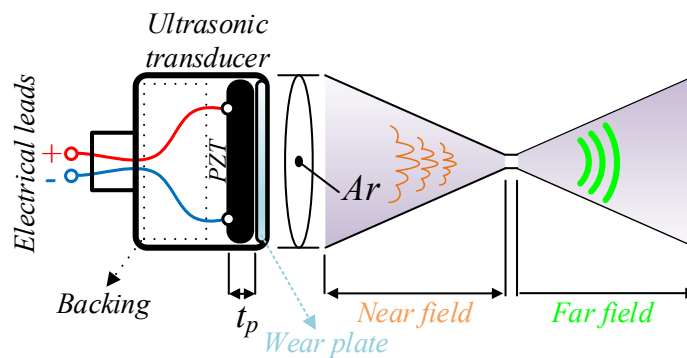
This work thematizes the acoustic contactless energy transfer systems. In this sense, this section presents the basics about ultrasound waves, ultrasonic transducers and a review of the state-of-art on energy transfer through air, living tissue and solids. Furthermore, industrial applications are highlighted for through-wall acoustic CET.

The acoustic contactless energy transfer systems use ultrasound waves, which are sound waves with higher frequencies than the upper audible limit of human hearing ( $\geq 20$  kHz).

### 2.2.1 Ultrasonic transducers

An ultrasonic transducer is a device that converts electrical energy into acoustical waves (transmitter) or vice-versa (receiver). The ultrasonic transmitter is supplied by an electrical power source and by means of a piezoelectric component, a mechanical vibration is generated, then, due to the constructive characteristics of the device, acoustical sound pressure is transmitted in the form of ultrasound waves (LENK et al., 2011). A representation of an ultrasonic transducer based on piezoelectricity is shown in Figure 2.8.

Figure 2.8 – Ultrasonic transducer based on piezoelectricity.



Source: Author.

The piezoelectric component (PZT) has a thickness  $t_p$ . The sound field of the transducer is composed of two regions: the near field and the far field.

The region directly in front of the transducer is the near field. In this region, the amplitude goes through a series of maxima and minima. Beyond the near field, is the region called far field, in which the ultrasonic beam is more uniform (OLYMPUS, 2006).

The near field  $NF$  can be calculated by

$$NF = \frac{Arf}{\pi C_L}, \quad (2.1)$$

being,  $Ar$  the area of the transducer,  $C_L$  the wave velocity and  $f$  the frequency.

A highly attenuative, high density material is the backing. It controls the vibration of the transducer by absorbing the energy radiating from the back face of the piezoelectric component. A compromise between the acoustic impedance matching of the backing material and the PZT must be taken into account when designing ultrasonic transducers. If the impedances are matching, the transducer resolution is high, on the other hand, it may be lower in signal amplitude. However, if there is an impedance mismatching, more sound energy will be reflected forward into the test material (OLYMPUS, 2006).

### 2.2.2 Energy transfer through air

Ishiyama et al. (2003) demonstrated a wireless power transfer system based on ultrasonic air transducers for mobile applications. By measuring the sound pressure level and the output voltage, the characteristics of the system were experimentally described. Around  $0.05\text{ mW}$  were achieved over a distance of  $0.3\text{ m}$  at  $20\text{ V}_{pp}$  as input source (peak to peak). The same work concludes that enclosed-type transducers are suitable for ultrasound contactless energy transfer systems. It is interesting to note that the used frequency was  $28\text{ kHz}$ , which is relatively low for such applications considering commercial uses.

The use of ultrasound waves for wireless communication is performed in the work of Jiang & Wright (2013). The transmitted data were encoded and modulated using a specific computer program in MATLAB with an interface to a waveform generator. The modulated data were sent through air by means of a capacitive ultrasonic transmitter. The characters  $Q$ ,  $W$ ,  $E$ ,  $R$ ,  $T$  and  $Y$  are represented by different frequencies encoded in the ultrasound wave. The work shows that it is feasible to transmit the data through air. However, the delay when changes occur in the binary values leads to errors between  $1.8\%$  to almost  $50\%$ .

A wireless sensor system for power and data transmission was reported by Lin, Chiang & Chen (2017). Commercial ultrasound transmitters and receivers operating at  $40\text{ kHz}$  are used to send energy through air. A micro-controller performs the signal manipulation in order to modulated a specific signal that is sent back by means of a pair of ultrasound transmitter and receiver. This micro-controller requires  $10\text{ }\mu\text{A}$  under sleep mode and  $1.8\text{ V}$  as minimum operating voltage. It was shown that the system operates correctly over a distance of  $14\text{ cm}$ . The efficiency was not presented.

### 2.2.3 Energy transfer through living tissue

One of the most common application of acoustic contactless energy transfer system is related to bio-implantable devices. Several publications deal with biomedical applications, in which the acoustic energy transfer is used to charge implants (FRAUNHOFER-IBMT-THERANOSTISCHE-PROJEKT, 2011).

Denisov & Yeatman (2010) investigated the power transmission efficiency of ultrasonic and inductive energy transfer system for wireless charging of implanted microdevices. Different receiver sizes and distance between the transducers were evaluated. The inductive system is better for small distances between transmitter and receiver (less than  $1\text{ cm}$ ), in which the simulation results have shown  $81\%$  of efficiency when considering inductive systems and  $39\%$  for ultrasonic. However, by increasing the distance between the transducers, the ultrasonic system outperforms the inductive one ( $0.02\%$  vs.  $0.00002\%$ ).

In the work of Radziemski, S. & Makini (2017), an ultrasound charging system for implanted medical devices is demonstrated. The proposed system consists of an ultrasound transmitter and an implanted receiver that converts acoustic to electrical energy. A  $1\text{ cm}$  of length tissue was used as transfer media inside a water tank. The overall system efficiency and the ratio of acoustic input power to the electrical charging available power were evaluated at a selected frequency of  $1\text{ MHz}$ . The overall system efficiency was  $15 - 25\%$ , the transmitter efficiency was  $50 - 70\%$ , the receiver efficiency was  $50 - 70\%$  and the charging circuit efficiency was about  $55\%$ .

Shih & Shih (2010) developed an ultrasonic wireless power transfer for an implantable biomedical device with fully packaged power receivers with dimensions of  $10\text{ mm} \times 10\text{ mm} \times 5.5\text{ mm}$ . It was shown that the device is able to recharge a  $25\text{ }\mu\text{J}$  battery in 18.1 minutes with  $1.23\text{ mW}$ .

Rosa & Yang (2016) reported a implantable device that is wirelessly activated in order to enable ultrasound emissions for computing biological tissue parameters, such as pH, concentration of electrolytes and thermal gradients. By using  $3\text{ cm}$  as distance between the receiver and the source, the device consumes  $60\text{ }\mu\text{A}$  with  $0.8\text{ V}$ .

#### 2.2.4 Energy transfer through solids

Yang et al. (2018b) recently reported a interesting work about through-metal energy transfer by means of ultrasound waves. The selected ultrasonic transducers are based on commercial PZT-5 piezoelectric discs. The transfer media is a steel plate with dimensions  $300\text{ mm} \times 300\text{ mm} \times 40\text{ mm}$ . The transmitter is driven by a cascaded combination of a continuous-wave signal source and a  $100\text{ W}$  linear power amplifier. Matching networks are analytically analyzed in order to improve the impedance matching related to the piezoelectric transducers. They are designed by using a normalized Smith chart, which is characterized by different regions that show different topologies. Yang et al. (2018b) have not included the effects of changing the transfer media geometry. However, the transducers are designed to achieve maximum efficiency on the proposed scenario. Furthermore, an AC-DC rectifier is designed to perform regulated DC output current. The rectifier topology is a full-bridge circuit with input inductor and filter capacitor designed to increase the conduction angle of the input current and a DC-DC converter is used to stabilize the operating point of the rectifier. The system generates  $5\text{ V}$ ,  $15.7\text{ W}$  and overall power transfer efficiency of  $27.7\%$ .

Lawry et al. (2012) presented an analytical model for a sandwiched plate piezoelectric transformer. This system is composed of a metallic barrier between two piezoelectric disk transducers. The authors described a model based on a representation by a set of two-port network parameters. The analogy force as voltage and velocity as current is

used. Under the assumptions that all interfaces are parallel with zero surface roughness, large diameter-to-thickness ratio of the transducers and considering that all mechanical layers of the sandwiched plate piezoelectric transformer are represented by slabs of homogeneous elastic materials with finite thicknesses, the ultrasound wave is modeled by the one-dimensional wave equation for particle displacement in order to describe the linear dilatation elastic wave propagation in the material. The model is interesting because it includes the media properties (thickness, density, speed of sound and attenuation coefficient), transducers parameters and matching networks parameters in a elegant telegrapher's equations. The evaluated transfer media is a steel barrier with thickness of  $63.5\text{ mm}$ . It is important to note that the authors mention that the model was enhanced by systematically adjustment based on the measurements. The measured power transfer function shows good agreement with the developed analytical model.

### 2.3 POWER CONVERSION CIRCUITRY

The electro-mechanical-acoustic CET system has an electrical input and an electrical output. A DC-AC inverter can be used to drive the system and an AC-DC rectifier can be used to convert the AC signal of the piezoelectric transducer into a DC signal to supply a load.

In a general way, an AC-DC rectifier is a system that converts an AC signal into a DC signal by means of reactive components and switches. In low power applications, three families of rectifiers are highlighted, full-bridge topologies, resonant rectifiers and voltage multipliers.

The first family, full bridge topologies, is mainly represented by four diodes and an output filter capacitor. However, several synchronized switching circuit topologies were proposed in the literature in order to enhance the system operation (CHEN, 2013).

A standard full-bridge rectifier is used as interfacing circuit for a multiple piezoelectric patch energy harvesters in Aghakhani & Basdogan (2017). Analytical closed-form solution for the response of the system is provided. The model gathers the equivalent impedance of the harvesting circuit into a distributed-parameter electroelastic model of the plate with multiple harvesters.

In Chen (2013) two techniques to improve the full-bridge rectifier operation for piezoelectric energy harvesters were presented: the synchronized switching harvesting on inductor in parallel (SSHI-parallel) and the synchronized switching harvesting on inductor in series (SSHI-series). The SSHI-parallel makes use of a bi-directional switch and an inductor is connected in parallel with the AC input source. It was shown in Chen (2013) that the energy stored in the piezoelectric capacitance is extracted by its resonance in relation to the inductor of SSHI-parallel circuit. The resonant circuit increases the mag-

nitude of the voltage across the piezoelectric capacitance, which leads to more extracted energy from the vibration source. On the other hand, the SSHI-series uses an inductor and a switch in series with the input source. It was shown that both interfacing circuits can be used for piezoelectric energy harvesters.

Voltage multipliers are composed of diodes and capacitors and increase the voltage while performing AC-to-DC power conversion. They are commonly referred to as voltage rectifiers. The main advantage is that higher DC output voltage can be obtained from small AC input voltage. On the other hand, the high-voltage stress on the diodes and output capacitor is considered as a drawback (FOROUZESH et al., 2017).

There are several arrangements of diodes and capacitors that characterize a voltage multiplier. For instance, Greinacher voltage doubler (ZUMBAHLEN, 2008), improved Greinacher voltage doubler (FOROUZESH et al., 2017), voltage quadrupler (LIN et al., 2014), voltage doubler rectifier (WANG et al., 2010), voltage quadrupler rectifier (SHANG; WANG, 2018), basic switched capacitor (SCHMID; HUBER, 2018), Dickson charge pump (TANZAWA; TANAKA, 1997) and Cockcroft-Walton multiplier (COCKCROFT; WALTON, 1932). Furthermore, voltage multipliers can be combined to DC-DC switched converters (ANDRADE et al., 2018) and to resonant converters (WU et al., 2015).

The third type of AC-DC rectifiers under study in this work is related to the resonant rectifiers. Essentially, resonant circuits allow shaping the power converters waveforms in a sinusoidal fashion ensuring soft-switching conditions (KAZIMIERCZUK; CZARKOWSKI, 1995). In general a DC-DC resonant converter is obtained by cascading a DC-AC resonant inverter with an AC-DC resonant rectifier. For some applications, these two subsystems should be used separately. Recently, Class-E based rectifiers have been used with complementary-metal-oxide-semiconductor (CMOS) technology aiming to battery avoidance in wireless sensors (DEHGHANI; JOHNSON, 2016). The resonant rectifiers can be divided into Class-D or Class-E; zero-current soft switching (ZCS), zero-voltage soft switching (ZVS) and zero-derivative switching (ZDCS / ZDVS); and current-driven or voltage-driven.

Topologies based on full-bridge rectifiers are commonly found in the literature and by designing the synchronized switch the overall efficiency can be improved. However, the high stress on the switches is a drawback.

Voltage multipliers can be easily implemented and high AC-to-DC transfer power ratio can be achieved. Nevertheless, components design aiming improvement are not a straightforward task.

Resonant rectifiers can achieve high efficiency due to their soft-switching mechanisms (JOZWIK; KAZIMIERCZUK, 1990; KAZIMIERCZUK; TOMESCU; IVASCU, 1994). Notwithstanding, the complexity of such circuits is high due to the resonance features; it is necessary a well-defined methodology in order to achieve the optimum



behavior (zero-derivative voltage/current switching).

One of the advantages of the resonant rectifiers over the SSHI full-bridge topologies, is that the first ones do not need gate-drivers for the switches. In addition, the soft-switching characteristics allow to reduce losses.

The DC-AC inverter converts a continuous input source into an alternating signal. Considering grid-connected applications, half-bridge and full-bridge topologies with a resonant tank are commonly used (BABAEI; ASL; BABAYI, 2016; KISHORE; BHIMASINGU, 2017; PHADUNGTHIN, 2017).

In Tebianian J. Quaiocoe (2016), a Class-D inverter operating at  $13.56\text{ MHz}$  is used for wireless power transfer systems based on enhanced-mode GaN on silicon FETs. Such switches have lower on-resistance and higher band gap when compared to conventional power MOSFETS. The proposed Class-D inverter has a resonant tank composed of a  $5.2\ \mu\text{H}$  inductor and a  $26\ \text{pF}$  capacitor. The converter is designed to achieve ZVS condition and operates from  $20 - 80\ \text{V}$  input voltage range. In addition, a dynamic dead-time control is presented, in which digital potentiometers dynamically change the charging time constant as the input voltage changes based on the variation of the load.

An interesting review on resonant DC-AC inverters was conducted by Outeiro, Buja & Czarkowski (2016). A classification considering resonant tanks with two, three and multiple elements is presented. It is shown that two-element series resonant tank exhibits poor regulation of the output voltage in the case of very light loads and operates only as step-down converter. On the other hand, two-element parallel resonant tank has capability of no-load regulation and low-output ripple current. However, it is not a good solution in applications where the input voltage varies over a large range.

Class-E inverter can operate with ZVS or ZCS condition. By choosing the proper values of the resonant circuit for the Class-E ZVS inverter, the switch turns on at zero voltage. In this case, the switch current and voltage waveforms do not overlap during the switching time intervals, which increases efficiency. Switching losses are virtually zero. In the Class-E ZCS inverter the switch is turned off at zero current, yielding zero current soft-switching operation (KAZIMIERCZUK; CZARKOWSKI, 1995; LOTFI et al., 2019; AYACHIT et al., 2019; JEDI; KAZIMIERCZUK, 2018).

Not as well known as the Class-E inverter, the Class-F inverter is a modification in Class-B amplifiers, in which additional resonators are added in series with the load in order to open-circuit the transistor drain at several low-order odd harmonics (KEE et al., 2003). The inverter waveform begins to resemble a square wave because the odd voltage harmonics tend to flatten the waveform. This feature leads to a reduced voltage across the transistor during the conduction time, which increases efficiency. The Class-F inverter is commonly used as amplifier. However, its features were reported as an add-on for the Class-E inverter, which generates a topology called Class-EF<sub>2</sub> inverter or Class- $\Phi_2$  inverter. The idea is to add a resonant network related to the switching frequency

of the inverter, the voltage or current stress can be reduced, which increases efficiency (ALDHAHER; YATES; MITCHESON, 2016; JEDI et al., 2020).

By cascading a DC-AC resonant inverter to a AC-DC resonant rectifier, a DC-DC resonant converter is obtained. These converters are characterized by double soft-switching operation, which means that both inverter switch and diode rectifier operate with ZVS/ZDS or ZCS/ZDS. One example is the Class-E<sup>2</sup> DC-DC resonant converter, which has been especially used for wireless power transfer (NAGASHIMA et al., 2015).

Resonant topologies can be also integrated to hard-switching converters, like as the Flyback-Class-E converter demonstrated by Zhang et al. (2017) for LED applications. Furthermore, Almeida et al. (2015) has shown a resonant DC-DC converter integrated into a bridge-less Boost power factor correction topology aiming to reduce the bulk capacitance and increase the overall efficiency of a LED driver.

Piezoelectric transformers driven by resonant converters were explored by Alonso, Ordiz & Costa (2008), in which a control method that ensures ZVS operation is proposed. Yang et al. (2009) demonstrated a comparison between Half-bridge and Class-E resonant converters as topological representation of piezoelectric transformers.

In Pareschi et al. (2019), a through-the-barrier communication technique based on Class-E<sup>2</sup> resonant converter is proposed. The idea is based on observation of parameter changing in the secondary side (rectifier part), which leads to an easily detected parameter changing in the primary side. The converter is analyzed by means of defining soft-switching conditions for both inverter and rectifier. A proof-of-concept is performed by designing a 5 V input voltage and 5 V output voltage. The converter was designed to operate at 1 MHz and 1 Mbit/s data rate is achieved.

## 2.4 CONCLUSION

In this Chapter, the literature review on contactless energy transfer systems has been presented. The different types of CET have been highlighted considering applications, qualitative and quantitative factors.

The main applications for acoustic CET have been reported, like as energy transfer through air, living tissues and solids. In addition, some industrial applications were highlighted. The main power conversion circuits used in low power applications have been shown in order to compare different solutions for CET. It has been shown that the main circuits are: full-bridge topologies, voltage multipliers and resonant converters.

### 3 SYSTEM MODELING

This chapter shows the development of a modeling methodology for an electro-mechanical-acoustic contactless energy transfer system. The selected approach is based on multiphysics networks to represent the electrical, mechanical and acoustical domains by lumped parameters. The multiphysics building blocks are converted into unit-less parameters in order to obtain a normalized state-space model for the system.

The next section shows the overview of the methodology. Subsequently, the multiphysics networks are described by explaining their main building blocks. A representation for the system is proposed and from it, the modeling methodology is explained.

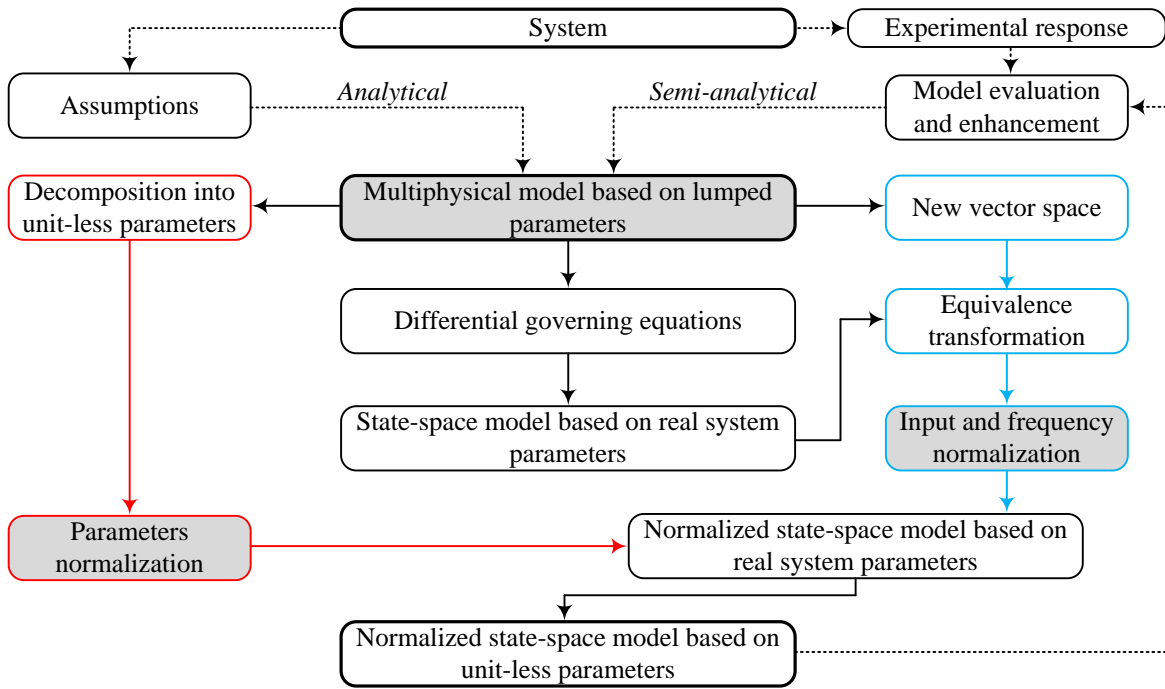
#### 3.1 METHODOLOGY

The main idea is to represent the electro-mechanical-acoustic CET system by a multiphysics network which can be mathematically equated by a state-space model. The system is analyzed by the Kirchhoff's Laws of Circuits and the Newton's Laws of Motion. Subsequently, unit-less parameters are extracted from the real system representation. A new vector space is defined in order to perform an equivalence transformation. This mathematical operation allows to easily relate real system parameters and unit-less parameters. The advantage of the proposed model is that all the required power conversions, electrical-to-mechanical, mechanical-to-acoustic, acoustic-to-mechanical and mechanical-to-electrical, are included into a single state-space model.

Based on the normalized state-space model with unit-less parameters, normalized gain curves are obtained, which represent the behaviour of the system in a general way.

An overview of the modeling methodology is portrayed in Figure 3.1. From the system, a normalized state-space model based on unit-less parameters is aimed to be achieved. For this purpose, the main used techniques are: multiphysics networks representation, parameters normalization and input and frequency normalization.

Figure 3.1 – Overview of the modeling and methodology.



Source: Author.

First, an analytical model is developed. The model can be evaluated based on real system parameters and it can be converted into a normalized model based on unit-less parameters. By evaluating the model based on the experimental response of the physical system, it is possible to determine which parts of the model should be enhanced or modified in order to achieve an adequate agreement between theoretical and experimental results.

## 3.2 MULTIPHYSICS NETWORKS

Multiphysics networks are structures composed of building blocks that represent physical components in different domains, such as electrical, mechanical and acoustical. The Kirchhoff's Laws of Circuits are well-known in electrical networks representation. In the same way, Newton's Laws of Motion are used to equate mechanical systems and their interactions. For acoustical systems, analogies can be made with the mechanical and electrical ones.

The main advantage of physical system representation by multiphysics networks based on lumped parameters is that, well-known modeling techniques can be used to mathematically analyze the system. For instance, state-space models and frequency domain response. Furthermore, the normalization procedure used for electrical circuits, is going to be extended for multiphysics networks, which is a novelty that is shown in this

work.

First of all, the components used in multiphysics networks are going to be presented. Table 3.1 shows the components and their time domain and frequency domain equations. Table 3.2 shows the sources used in multiphysics networks (LENK et al., 2011; MARSCHNER; WERTHSCHUTZKY, 2015).

Table 3.1 – List of components for multiphysics networks.






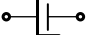






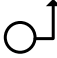
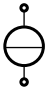
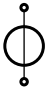
Symbol	Component	Time domain	Frequency domain
	Electrical inductor $L$	$v_L = L \frac{di_L}{dt}$	$\underline{v}_L = j\omega L \underline{i}_L$
	Electrical capacitor $C$	$i_C = C \frac{dv_C}{dt}$	$\underline{i}_C = j\omega C \underline{v}_C$
	Electrical resistor $R$	$v_R = R i_R$	$\underline{v}_R = R \underline{i}_R$
	Mechanical mass $M$	$f = M \frac{dy}{dt}$	$\underline{f} = j\omega M \underline{y}$
	Mechanical stiffness $K$	$y = \frac{1}{K} \frac{df}{dt}$	$\underline{y} = \frac{j\omega f}{K}$
	Mechanical damper $D$	$f = D y$	$\underline{f} = D \underline{y}$
	Acoustical mass $M_a$	$p = M_a \frac{dq}{dt}$	$\underline{p} = j\omega M_a \underline{q}$
	Acoustical compliance $N_a$	$q = N_a \frac{dp}{dt}$	$\underline{q} = j\omega N_a \underline{p}$
	Acoustical friction $Z_a$	$p = Z_a q$	$\underline{p} = Z_a \underline{q}$

Table 3.2 – List of sources for multiphysics networks.

Symbol	Component	Time domain	Unit
	Electrical voltage source $v(t)$	$v(t) = V \sin(\omega t)$	$V$
	Electrical current source $i(t)$	$i(t) = I \sin(\omega t)$	$A$
	Mechanical force $f$	$f(t) = F \sin(\omega t)$	$N = \frac{kg \cdot m}{s^2}$
	Mechanical velocity $y(t)$	$y(t) = \frac{dz}{dt}$	$\frac{m}{s}$
	Acoustic sound pressure $p(t)$	$p(t) = P \sin(\omega t)$	$Pa = \frac{N}{m^2}$
	Acoustic volume velocity $q(t)$	$q(t) = Q \sin(\omega t)$	$\frac{m^3}{s}$

In Table 3.1 and Table 3.2,  $v_L$  is an inductor voltage,  $i_L$  an inductor current,  $v_C$  is a capacitor voltage,  $i_C$  is a capacitor current,  $v_R$  is a resistor voltage,  $i_R$  is a resistor current,  $f$  is a mechanical force,  $y$  is a mechanical velocity,  $p$  is an acoustical sound pressure and  $q$  is an acoustical sound velocity. In addition,  $V$ ,  $I$ ,  $F$ ,  $P$  and  $Q$  are the input signals amplitudes.

### 3.3 MULTIPHYSICAL MODEL BASED ON LUMPED PARAMETERS

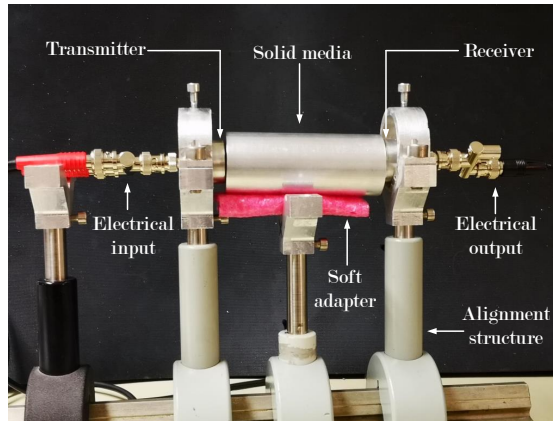
The problem is described as an electro-mechanical-acoustic CET system shown in Figure 3.2. The transducers are noted as transmitter and receiver and they are based on piezoelectricity. The acoustic medium is based on solid elements, which can be considered a material with specific geometry and material properties. The system has an electrical input and an electrical output. The solid media is the system's transfer media.

A lumped parameter can be understood as a representation of a physical system by an idealized discrete component. In this sense, a model based on lumped parameters aims to represent the behavior of a spatially distributed physical system by means of a topology based on discrete elements.

The goal is to develop a model for the system based on lumped parameters. In this sense, it is important to describe the conditions and assumptions for the modeling.

An alignment structure is shown in Figure 3.2. This is used to ensure that the transducers and the media are aligned to each other. In order to avoid undesirable me-

Figure 3.2 – Electro-mechanical-acoustic contactless energy transfer system.



Source: Author.

chanical vibration from the media to the structure, soft adapters are used between the main system components and the structure.

Ultrasound gel is used as interface between the transducers and the acoustic media. The gel enhances the coupling and leads to better power transmission.

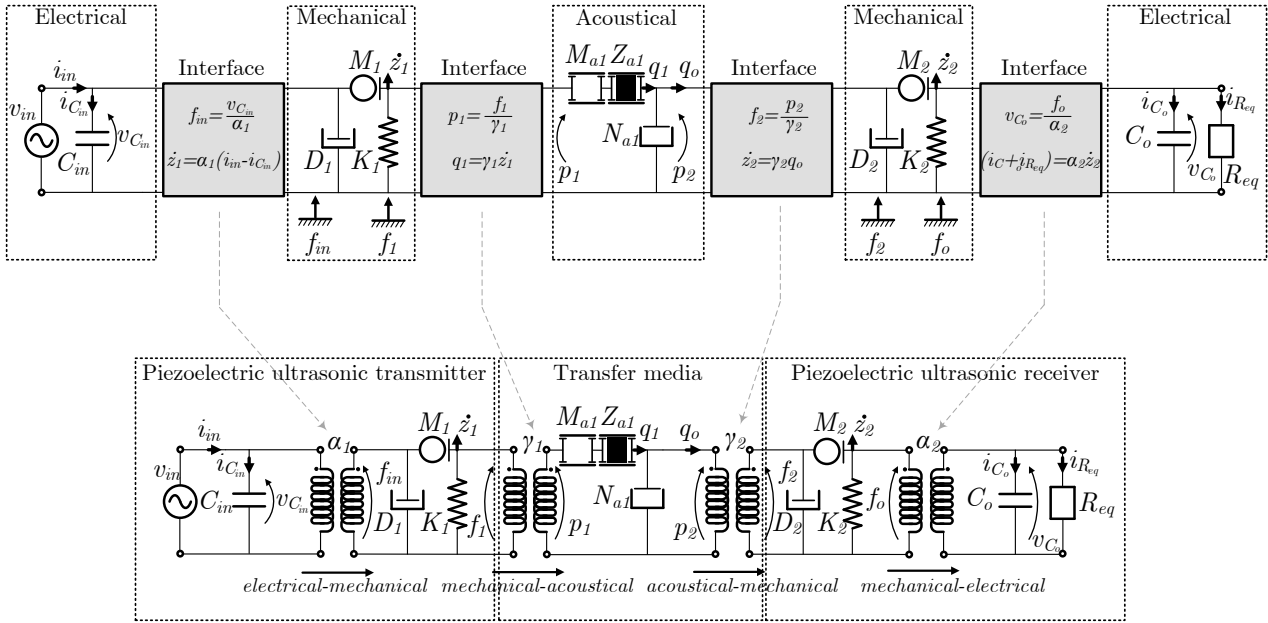
Based on the aforementioned conditions, the model is developed under the following assumptions:

1. The coupling between different domains is mathematically described by ideal transformers;
2. The piezoelectric transducers are modeled as electromechanical devices based on lumped parameters;
3. The transfer media is modeled by a network based on equivalent acoustical lumped parameters;
4. The alignment structure is neglected. It is because the soft adapters are used to avoid the undesirable mechanical vibration to the structure;
5. The ultrasound gel is neglected. It is only used to enhance the coupling. The model considers an ideal coupling between transducers and transfer media;
6. Auxiliary cables and measurements devices are not considered in the model;
7. Temperature and pressure conditions are not taken into account on the modeling.

The multiphysics network representation for the system is drawn in Figure 3.3.

The piezoelectric components have electrical and mechanical components. The system is supplied by a voltage source  $v_{in}(\omega t) = V_{in} \sin(\omega t)$ , with amplitude  $V_{in}$  and angular frequency  $\omega$ . Capacitors  $C_{in}$  and  $C_o$  are the piezoelectric capacitances. The

Figure 3.3 – Multiphysical representation based on lumped components.



Source: Author.

mechanical components are: mass  $M_1$  and  $M_2$ , dampers  $D_1$  and  $D_2$ , and stiffness  $K_1$  and  $K_2$ . Subscripts 1 and 2 in the mechanical components refer to transmitter and receiver, respectively.

The transfer media is composed of equivalent acoustical elements. They are acoustical components with analogous behavior to electrical components.  $M_{a1}$  is the equivalent acoustical mass,  $Z_{a1}$  is the equivalent acoustical friction and  $N_{a1}$  is the equivalent acoustical compliance.

It is important to note that the system has three domains: electrical, mechanical and acoustical. The domains are connected to each other by means of coupling devices, which work mathematically as ideal transformers. The electrical to mechanical conversion is given as

$$\alpha_1 = \frac{v_{C_{in}}}{f_{in}} = \frac{\dot{z}_1}{i_{in} - i_{C_{in}}}, \quad (3.1)$$

being  $\alpha_1$  the electro-mechanical coupling factor,  $v_{C_{in}}$  is the input capacitor  $C_{in}$  voltage,  $f_{in}$  is the equivalent mechanical force,  $\dot{z}_1$  is the mechanical velocity ( $z_1$  is the mechanical displacement),  $i_{in}$  is the input current and  $i_{C_{in}}$  is the capacitor  $C_{in}$  current.

The mechanical to acoustical conversion is mathematically described by

$$\gamma_1 = \frac{f_1}{p_1} = \frac{q_1}{\dot{z}_1}, \quad (3.2)$$

being  $\gamma_1$  the mechanical-acoustic coupling factor,  $f_1$  the mechanical force generated by the piezoelectric component (transmitter),  $p_1$  is the acoustic sound pressure generated by the transmitter and  $q_1$  the acoustic volume velocity.



The acoustical to mechanical conversion is related as

$$\gamma_2 = \frac{p_2}{f_2} = \frac{\dot{z}_2}{q_o}, \quad (3.3)$$

being  $\gamma_2$  the acoustical-mechanic coupling factor,  $p_2$  is the acoustic sound pressure that reaches the receiver,  $f_2$  is the equivalent mechanical force,  $\dot{z}_2$  is the mechanical velocity and  $q_o$  is the acoustic volume velocity.

The mechanical to electrical conversion is given as

$$\alpha_2 = \frac{f_o}{v_{C_o}} = \frac{i_{C_o} + i_{R_{eq}}}{\dot{z}_2}, \quad (3.4)$$

being  $\alpha_2$  the mechanical-electrical coupling factor,  $f_o$  is the mechanical force,  $v_{C_o}$  is the output voltage generated by the piezoelectric component (receiver),  $i_{C_o}$  is the output capacitance current and  $i_{R_{eq}}$  is the load current.

The representation in Figure 3.3 considers that the system is driven by a voltage source. Capacitor  $C_{in}$  is the input capacitance of the piezoelectric component on the ultrasonic transmitter. The piezoelectric component is represented by  $C_{in}$  and a mechanical part composed of  $M_1$ ,  $K_1$  and  $D_1$ . The same concept is applied for the receiver by considering an output capacitance  $C_o$  and mechanical components  $M_2$ ,  $K_2$  and  $D_2$ . This representation can be referenced as the electro-mechanical representation of the piezoelectric component (MASON, 1942; KRIMHOLTZ; LEEDOM; MATTACI, 1942; HEYWANG; LUBITZ; WERSING, 2008; CHEN, 2013).

Regarding the transfer media, the basic network is represented by an acoustic mass, an acoustic friction and an acoustic compliance. However, in order to enhance the model, several networks can be added to the system.

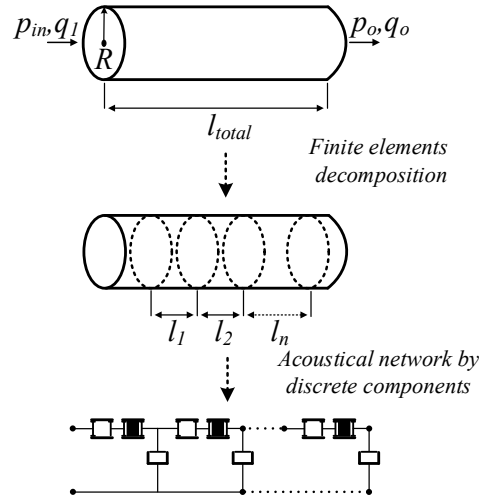
The acoustical network that represents the transfer media is derived from a geometric model. Considering a solid with cylindrical geometry as shown in Figure 3.4, it is decomposed into finite elements of length  $l_n$ , being  $n$  the index for the number of elements. The solid has a specific radius  $R$  and total length  $l_{total}$  (LENK et al., 2011). The generic transfer media decomposition into lumped parameters is shown in Appendix A.

The mentioned concepts are the fundamentals that allow to describe the system in Figure 3.2 as the representation in Figure 3.3. Based on that, the system is going to be mathematically described by a state-space representation.

A linear system can be described by a state-space model as

$$\begin{aligned} \dot{\mathbf{x}}(t) &= \mathbf{A}_I \mathbf{x}(t) + \mathbf{B}_I u(t) \\ &\vdots \\ \dot{\mathbf{x}}(t) &= \mathbf{A}_k \mathbf{x}(t) + \mathbf{B}_k u(t) \end{aligned} \quad (3.5)$$

Figure 3.4 – Acoustical network by discrete components.



Source: Author.

and

$$\begin{aligned}
 \mathbf{y}(t) &= \mathbf{C}_I \mathbf{x}(t) + \mathbf{D}_I u(t) \\
 &\vdots \\
 \mathbf{y}(t) &= \mathbf{C}_k \mathbf{x}(t) + \mathbf{D}_k u(t).
 \end{aligned} \tag{3.6}$$

where  $\mathbf{A}_k$  is the state matrix,  $\mathbf{B}_k$  is the input matrix,  $\mathbf{C}_k$  is the output matrix and  $\mathbf{D}_k$  is the transmission matrix, being  $k$  the index for the system operating mode and  $u(t)$  the input source.

The state vector  $\mathbf{x}(t)$  can be generically represented in a diagonal matrix form by

$$\mathbf{x}(t) = \begin{bmatrix} \varepsilon_1 & \cdots & 0 \\ \vdots & \ddots & \vdots \\ 0 & \cdots & \varepsilon_{nc} \end{bmatrix}, \tag{3.7}$$

where  $\varepsilon_{nc}$  represents a system variable, such as inductor current, capacitor voltage, mechanical displacement, mechanical velocity, acoustic sound pressure or acoustic volume velocity.  $nc$  is the number of storage elements.  $\mathbf{y}(t)$  is the output vector and can be described by any desirable system variable.

The electro-mechanical-acoustic system is described by the Kirchhoff's Circuit Laws and the Newton's Laws of Motion. By considering the forces in the electro-mechanical-acoustic conversion related to the ultrasonic transmitter, a governing equation can be described as

$$M_1 \frac{d^2 z_1(t)}{dt^2} + D_1 \frac{dz_1(t)}{dt} + K_1 z_1(t) + f_{in}(t) + f_1(t) = 0. \tag{3.8}$$

By means of relations (3.1) and (3.2), the governing equation is written as

$$M_1 \frac{d^2 z_1(t)}{dt^2} + D_1 \frac{dz_1(t)}{dt} + K_1 z_1(t) + \frac{v_{C_{in}}(t)}{\alpha_1} + \gamma_1 p_1(t) = 0. \quad (3.9)$$

The acoustic network can be described by a differential equations as

$$p_1(t) = M_{a1} \frac{dq_1(t)}{dt} + Z_{a1} q_1(t) + p_2(t), \quad (3.10)$$

which can be applied into (3.9), resulting on

$$M_1 \frac{d^2 z_1(t)}{dt^2} + D_1 \frac{dz_1(t)}{dt} + K_1 z_1(t) + \frac{v_{C_{in}}(t)}{\alpha_1} + \gamma_1 \left( M_{a1} \frac{dq_1(t)}{dt} + Z_{a1} q_1(t) + p_2(t) \right) = 0. \quad (3.11)$$

The acoustic sound velocity  $q_1(t)$  can be described based on the mechanical velocity  $dz_1(t)/dt$  by means of (3.2), which results on

$$M_1 \frac{d^2 z_1(t)}{dt^2} + D_1 \frac{dz_1(t)}{dt} + K_1 z_1(t) + \frac{v_{C_{in}}(t)}{\alpha_1} + \left( \gamma_1^2 M_{a1} \frac{d^2 z_1(t)}{dt^2} + \gamma_1^2 Z_{a1} \frac{dz_1(t)}{dt} + \gamma_1 p_2(t) \right) = 0. \quad (3.12)$$

Re-arranging (3.11) and considering  $v_{C_{in}}(t) = V_{in} \sin(\omega t)$ , the governing equation is described by

$$(M_1 + \gamma_1^2 M_{a1}) \frac{d^2 z_1(t)}{dt^2} + (D_1 + \gamma_1^2 Z_{a1}) \frac{dz_1(t)}{dt} + K_1 z_1(t) + \frac{V_{in} \sin(\omega t)}{\alpha_1} + \gamma_1 p_2(t) = 0, \quad (3.13)$$

which is finally written as

$$\frac{d^2 z_1(t)}{dt^2} = - \frac{(D_1 + \gamma_1^2 Z_{a1})}{(M_1 + \gamma_1^2 M_{a1})} \frac{dz_1(t)}{dt} - \frac{K_1 z_1(t)}{(M_1 + \gamma_1^2 M_{a1})} - \frac{V_{in} \sin(\omega t)}{\alpha_1 (M_1 + \gamma_1^2 M_{a1})} - \frac{\gamma_1 p_2(t)}{(M_1 + \gamma_1^2 M_{a1})}. \quad (3.14)$$

In the same way, by considering the forces in the acoustical-mechanical-electric conversion related to the ultrasonic receiver, a governing equation can be described as

$$M_2 \frac{d^2 z_2(t)}{dt^2} + D_2 \frac{dz_2(t)}{dt} + K_2 z_2(t) + f_2(t) + f_o(t) = 0. \quad (3.15)$$

By using (3.3) and (3.4), the equation is written as

$$M_2 \frac{d^2 z_2(t)}{dt^2} + D_2 \frac{dz_2(t)}{dt} + K_2 z_2(t) + \frac{p_2(t)}{\gamma_2} + \alpha_2 v_{C_o}(t) = 0, \quad (3.16)$$

which can be re-arranged as

$$\frac{d^2 z_2(t)}{dt^2} = - \frac{D_2}{M_2} \frac{dz_2(t)}{dt} - \frac{K_2}{M_2} z_2(t) - \frac{p_2(t)}{\gamma_2 M_2} - \frac{\alpha_2}{M_2} v_{C_o}(t). \quad (3.17)$$

The piezoelectric receiver is ruled by the following differential equation:

$$i_{C_o}(t) + i_{R_{eq}}(t) = \alpha_2 \frac{dz_2(t)}{dt}, \quad (3.18)$$

which is also equated as

$$\frac{dv_{C_o}}{dt} = \frac{\alpha_2}{C_o} \frac{dz_2(t)}{dt} - \frac{v_{C_o}(t)}{R_{eq}C_o}. \quad (3.19)$$

The acoustic network provides the differential equation

$$q_1(t) = N_{a1} \frac{dp_2(t)}{dt} + q_o(t), \quad (3.20)$$

which can be re-arranged by means of (3.2) and (3.3) as

$$\frac{dp_2(t)}{dt} = \frac{\gamma_1}{N_{a1}} \frac{dz_1(t)}{dt} - \frac{1}{\gamma_2 N_{a1}} \frac{dz_2(t)}{dt}. \quad (3.21)$$

Equations (3.14), (3.17), (3.19) and (3.21) describe the system. However, (3.14) and (3.17) have second-order state variables, which are not suitable for the state-space representation. In this sense, first-order state variables must be defined as

$$\mathbf{x}_1 \triangleq z_1(t), \quad (3.22)$$

$$\mathbf{x}_2 \triangleq \frac{d\mathbf{x}_1}{dt} = \frac{dz_1(t)}{dt}, \quad (3.23)$$

$$\mathbf{x}_3 \triangleq z_2(t), \quad (3.24)$$

$$\mathbf{x}_4 \triangleq \frac{d\mathbf{x}_3}{dt} = \frac{dz_2(t)}{dt}, \quad (3.25)$$

$$\mathbf{x}_5 \triangleq p_2(t) \quad (3.26)$$

and

$$\mathbf{x}_6 \triangleq v_{C_o}(t). \quad (3.27)$$

By considering the state vector as

$$\mathbf{x}(t) = [\mathbf{x}_1, \mathbf{x}_2, \mathbf{x}_3, \mathbf{x}_4, \mathbf{x}_5, \mathbf{x}_6]^T, \quad (3.28)$$

and the input as

$$u(t) = V_{in} \sin(\omega t), \quad (3.29)$$

the system can be represented by the following state and input matrices:

$$\mathbf{A} = \begin{bmatrix} 0 & 1 & 0 & 0 & 0 & 0 \\ -\frac{K_1}{(M_1+\gamma_1^2 M_{a1})} & -\frac{(D_1+\gamma_1^2 Z_{a1})}{(M_1+\gamma_1^2 M_{a1})} & 0 & 0 & -\frac{\gamma_1}{(M_1+\gamma_1^2 M_{a1})} & 0 \\ 0 & 0 & 0 & 1 & 0 & 0 \\ 0 & 0 & -\frac{K_2}{D_2} & -\frac{D_2}{M_2} & -\frac{1}{\gamma_2 M_2} & -\frac{\alpha_2}{M_2} \\ 0 & \frac{\gamma_1}{N_{a1}} & 0 & -\frac{1}{\gamma_2 N_{a1}} & 0 & 0 \\ 0 & 0 & 0 & \frac{\alpha_2}{C_o} & 0 & -\frac{1}{Req C_o} \end{bmatrix} \quad (3.30)$$

and

$$\mathbf{B} = \begin{bmatrix} 0 \\ -\frac{1}{\alpha_1(M_1+\gamma_1^2 M_{a1})} \\ 0 \\ 0 \\ 0 \\ 0 \end{bmatrix}. \quad (3.31)$$

By selecting the output vector as

$$\mathbf{y}(t) = [\mathbf{x}_1, \mathbf{x}_2, \mathbf{x}_3, \mathbf{x}_4, \mathbf{x}_5, \mathbf{x}_6]^T, \quad (3.32)$$

the output and transmission matrices are

$$\mathbf{C} = \begin{bmatrix} 1 & 0 & 0 & 0 & 0 & 0 \\ 0 & 1 & 0 & 0 & 0 & 0 \\ 0 & 0 & 1 & 0 & 0 & 0 \\ 0 & 0 & 0 & 1 & 0 & 0 \\ 0 & 0 & 0 & 0 & 1 & 0 \\ 0 & 0 & 0 & 0 & 0 & 1 \end{bmatrix} \quad (3.33)$$

and

$$\mathbf{D} = [0]_{6 \times 1}. \quad (3.34)$$

The state-space representation was built based on the electrical and mechanical parts of the piezoelectric components and in an equivalent acoustical network based on the geometry of the transfer media. Furthermore, coupling factors are used to connect the different domains.

By solving the state-space model, the frequency and time-domain responses of the system can be obtained. For this purpose, it is necessary to give values for the terms in the matrices.

The piezoelectric mass  $M_1$  and  $M_2$ , the piezoelectric dampers  $D_1$  and  $D_2$ , and the piezoelectric capacitances  $C_{in}$  and  $C_o$ , are considered as inputs given by the device

manufacturer. The piezoelectric stiffness is calculated as

$$K_1 = (2\pi f_a)^2 M_1 \quad (3.35)$$

and

$$K_2 = (2\pi f_a)^2 M_2, \quad (3.36)$$

in which,  $f_a$  is the anti-resonant frequency (YANG, 2018).

The electro-mechanical couplings  $\alpha_1$  and  $\alpha_2$  can be equated as

$$\alpha_{1,2} = \frac{\mathcal{A}}{\sqrt{K_{1,2} C_{in,o}}} = \frac{e_{33}^E}{\sqrt{c_{33}^E \epsilon_{33}^E}}, \quad (3.37)$$

being,  $\mathcal{A} = e_{33}^E A_r / t_p$  the force factor,  $A_r$  the area of the piezoelectric component,  $t_p$  the piezoelectric component thickness,  $e_{33}^E$  the piezoelectric coupling constant,  $c_{33}^E$  the piezoelectric stiffness and  $\epsilon_{33}^E$  the piezoelectric permittivity (DUTOIT; WARDLE; KIM, 2005).

The acoustical equivalent mass  $M_{a1}$ , equivalent friction  $Z_{a1}$  and equivalent compliance  $N_{a1}$  are calculated based on the geometry and material properties of the transfer media as

$$M_{a1} = \frac{1}{M_a}, \quad (3.38)$$

$$N_{a1} = \frac{Vol}{C_L^2 \rho} \quad (3.39)$$

and

$$Z_{a1} = \frac{1}{Z_a}. \quad (3.40)$$

In (3.38),  $M_a$  is the acoustical mass, in (3.40),  $Z_a$  is the acoustical friction calculated as (LENK et al., 2011; MARSCHNER; WERTHSCHUTZKY, 2015):

$$M_a = \frac{\rho l}{\pi R^2} \quad (3.41)$$

and

$$Z_a = \frac{8\mu_L l}{\pi R^4}, \quad (3.42)$$

being,  $\mu_L$  the material friction coefficient.

In (3.38),  $Vol$  is the transfer media volume. For example, for a cylinder geometry, it is calculated as  $Vol = \pi R^2 l$ .

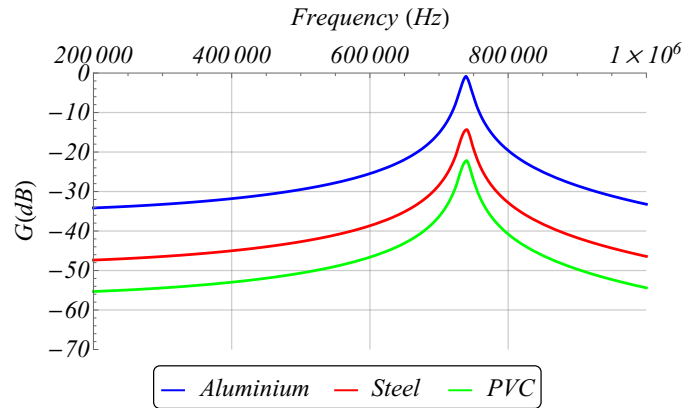
The mechanical-acoustic couplings are calculated by the relation between the areas of the piezoelectric component and the transfer media, which leads to (LENK et al., 2011):

$$\gamma_{1,2} = \frac{\pi r^2}{\pi R^2}, \quad (3.43)$$

being,  $r$  the radius of the piezoelectric component.

As an example, the multiphysical model based on lumped components is going to be evaluated for three different scenarios for the transfer media: aluminum, steel and plastic. All cases consider a cylindrical geometry. In Figure 3.5, the voltage gain ( $dB$ ) as function of the frequency ( $Hz$ ) is depicted for the three different scenarios.

Figure 3.5 – Voltage gain ( $dB$ ) as function of frequency ( $Hz$ ) obtained from the multiphysical model based on lumped components.



Source: Author.

The used parameters are shown in Table 3.3 for the piezoelectric components. For the transfer media as aluminium, steel and PVC, the parameters are shown in Tables 3.4, 3.5 and 3.6, respectively. The parameters for the piezoelectric components were given by the manufacturer and some based on the properties of the PZT-4 material. The parameters for the materials related to the transfer media were found in the literature (W.TITOW, 1990; OLYMPUS, 2006; ROSE, 2014).

One can see that, the gain is higher for aluminium and lower for PVC. In addition, in the three scenarios, the maximum voltage gain is ruled by the anti-resonant frequency of the piezoelectric component.

Table 3.3 – Parameters for the piezoelectric components.

Parameter	Description	Value	Domain
$M_1$	Piezoelectric mass	0.0075 <i>kg</i>	Mechanical
$D_1$	Piezoelectric damper	69.6373 <i>N · s · m<sup>-1</sup></i>	Mechanical
$K_1$	Piezoelectric stiffness	16.1 × 10 <sup>10</sup> <i>N · m<sup>-1</sup></i>	Mechanical
$M_2$	Piezoelectric mass	0.0075 <i>kg</i>	Mechanical
$D_2$	Piezoelectric damper	69.6373 <i>N · s · m<sup>-1</sup></i>	Mechanical
$K_2$	Piezoelectric stiffness	16.1 × 10 <sup>10</sup> <i>N · m<sup>-1</sup></i>	Mechanical
$t_p$	Thickness	0.003 <i>m</i>	Mechanical
$r$	Radius	0.01 <i>m</i>	Mechanical
$C_{in}$	Input capacitance	75 <i>pF</i>	Electrical
$C_o$	Output capacitance	75 <i>pF</i>	Electrical
$f_r$	Resonant frequency	681 <i>kHz</i>	Mechanical
$f_a$	Anti-resonant frequency	738 <i>kHz</i>	Mechanical

Table 3.4 – Parameters for the transfer media - Aluminium.

Parameter	Description	Value	Domain
$R$	Radius	0.015 <i>m</i>	Acoustical
$l$	Length	0.1 <i>m</i>	Acoustical
$\rho$	Density	2710 <i>kg/m<sup>3</sup></i>	Acoustical
$C_L$	Wave velocity	6300 <i>m/s</i>	Acoustical
$\mu_L$	Friction coefficient	1.2 <i>m · Pa · s</i>	Acoustical

Source: (ROSE, 2014; CHENG et al., 2014).

Table 3.5 – Parameters for the transfer media - Steel.

Parameter	Description	Value	Domain
$R$	Radius	0.015 <i>m</i>	Acoustical
$l$	Length	0.1 <i>m</i>	Acoustical
$\rho$	Density	7800 <i>kg/m<sup>3</sup></i>	Acoustical
$C_L$	Wave velocity	5800 <i>m/s</i>	Acoustical
$\mu_L$	Friction coefficient	4.5 <i>m · Pa · s</i>	Acoustical

Source: (ROSE, 2014; CHENG et al., 2014).



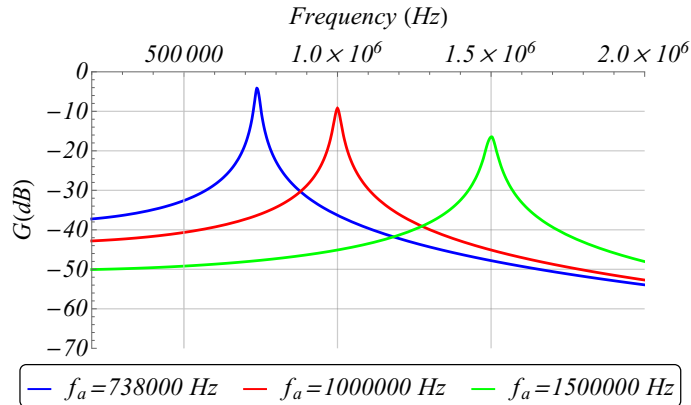
Table 3.6 – Parameters for the transfer media - PVC.

Parameter	Description	Value	Domain
$R$	Radius	$0.015\text{ m}$	Acoustical
$l$	Length	$0.1\text{ m}$	Acoustical
$\rho$	Density	$1380\text{ kg/m}^3$	Acoustical
$C_L$	Wave velocity	$2388\text{ m/s}$	Acoustical
$\mu_L$	Friction coefficient	$0.6\text{ m} \cdot \text{Pa} \cdot \text{s}$	Acoustical

Source: (ROSE, 2014; CHENG et al., 2014).

A graphic related to the voltage gain as function of the frequency obtained from the multiphysical model considering different transducers frequency is shown in Figure 3.6. The parameters are the same used for the previous graphic related to the aluminium, except for the resonant frequencies.

Figure 3.6 – Voltage gain ( $dB$ ) as function of frequency ( $Hz$ ) obtained from the multiphysical model based on lumped components for different transducers frequencies.



Source: Author.

It was possible to note that the system has several parameters to be considered, which leads to a huge number of possibilities for data plotting. For example, the length and radius of the transfer media can be analyzed by different values. Also, by changing the piezoelectric components, the anti-resonant and resonant frequencies change. Furthermore, the system can be analyzed by different materials with different properties.

In this sense, this Thesis proposes a normalized state-space representation based on unit-less parameters, which is going to be performed in the next section. By normalized, it means that the model becomes independent of the frequency and the amplitude of the input source. The unit-less parameters are used to avoid the need to know the real system parameters to understand the behavior of the system.

Subsequently, relationships among the unit-less parameters, the piezoelectric pro-

perties, the electro-mechanical components, the geometry of the transfer and the acoustic components, are going to be explained in order to clarify the conversion from real system parameters to the proposed unit-less parameters and vice-versa.

### 3.4 NORMALIZED MODELING OF MULTIPHYSICS NETWORKS BASED ON UNIT-LESS PARAMETERS

This section shows the development of a modeling methodology for multiphysics networks that normalizes the system in relation to the input source and the operating frequency. Furthermore, instead of using real system parameters, like as inductor, capacitor, resistor, mechanical mass, mechanical stiffness, mechanical damper, acoustical mass, acoustical compliance and acoustical friction, unit-less parameters are derived in order to represent the system in a normalized model.

#### 3.4.1 Real system parameters and unit-less parameters

A system decomposition scheme for multiphysics networks is depicted in Figure 3.7. Three main electrical components are represented by: resistor  $R_l$ , inductor  $L_m$  and capacitor  $C_n$ . Three main mechanical components are represented as: damper  $D_l$ , mass  $M_m$  and stiffness  $K_n$ . Three main acoustical components as: friction  $Z_{a,l}$ , mass  $M_{a,m}$  and compliance  $N_{a,n}$ .

It is important to differentiate real system parameters and unit-less parameters. Real system parameters are divided into electrical, mechanical and acoustical parameters.

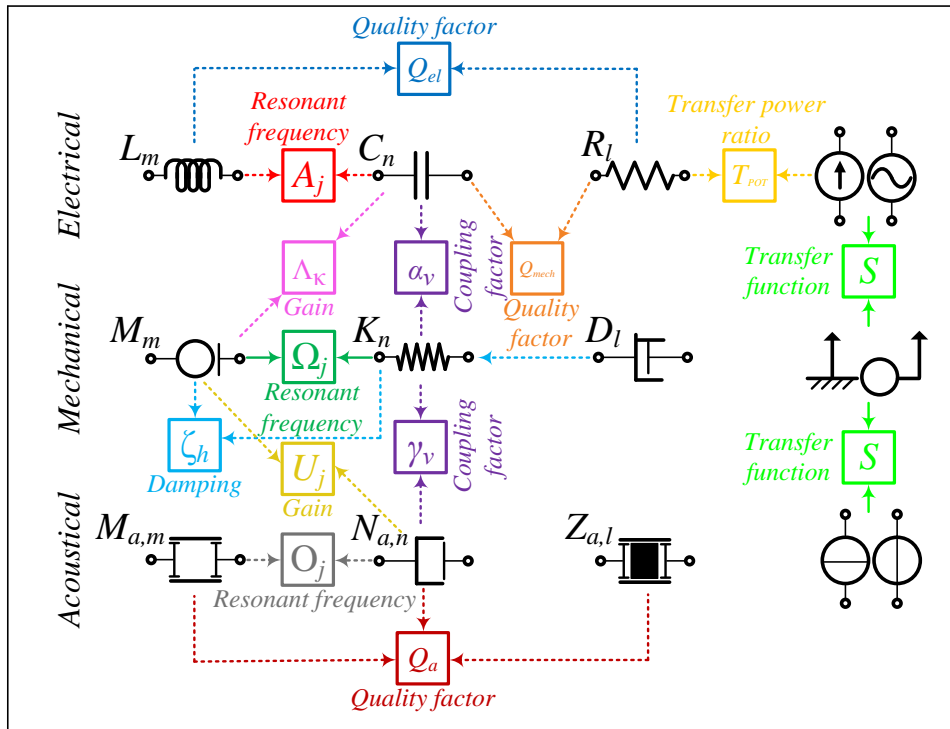
Electrical circuit parameters are described by:

- Resistors:  $R_l$ ;
- Inductors:  $L_m$ ;
- Capacitors:  $C_n$ ;
- Operating angular frequency:  $\omega$ ;
- Voltage input source:  $V_{in}$ ;
- Current input source:  $I_{in}$ .

Mechanical parameters are described by:

- Dampers:  $D_l$ ;
- Mass:  $M_m$ ;

Figure 3.7 – Decomposition into unit-less parameters scheme for multiphysics networks.



Source: Author.

- Stiffness:  $K_n$ ;
- Operating angular frequency:  $\omega$ ;
- Mechanic input force:  $F_{in}$ ;
- Mechanic displacement:  $Z_{in}$ .

Acoustical parameters are described by:

- Friction:  $Z_{a,l}$ ;
- Mass:  $M_{a,m}$ ;
- Compliance:  $N_{a,n}$ ;
- Operating angular frequency:  $\omega$ ;
- Sound pressure:  $P_{in}$ ;
- Sound velocity:  $Q_{in}$ .

Unit-less parameters are described by:

- Normalized electrical resonant frequencies:  $A_j$ ;

- Normalized mechanical resonant frequencies:  $\Omega_l$ ;
- Normalized acoustical resonant frequencies:  $O_j$ ;
- Electro-mechanical gains:  $\Lambda_\kappa$ ;
- Mechanical-acoustic gains:  $U_\kappa$ ;
- Electro-mechanical coupling factor:  $\alpha_\nu$
- Mechanical-acoustic coupling factor:  $\gamma_\nu$
- Electrical quality factor:  $Q_{el}$ ;
- Mechanical quality factor:  $Q_{mech}$ ;
- Acoustical quality factor:  $Q_a$ ;
- Damping:  $\zeta_h$ ;
- Transfer power ratio:  $T_{POT}$ ;
- Transfer function:  $S$ ;
- AC-to-DC voltage transfer function:  $S_V$ ;
- AC-to-DC current transfer function:  $S_I$ .

The indexes  $l, m, n, \kappa, j, \nu$  and  $h$  are used to indicate the number of the elements.

The normalized electrical resonant frequency is based on the relation among reactive components:

$$A_j = \frac{\omega_j}{\omega} \quad (3.44)$$

being

$$\omega_j = \frac{1}{\sqrt{L_m C_n}}. \quad (3.45)$$

The normalized mechanical resonant frequency is based on the relation among mass and stiffness:

$$\Omega_j = \frac{\omega_j}{\omega} \quad (3.46)$$

being

$$\omega_j = \frac{\sqrt{K_n}}{\sqrt{M_m}}. \quad (3.47)$$

The normalized acoustical resonant frequency is related to the acoustic mass and compliance:

$$O_j = \frac{\omega_j}{\omega} \quad (3.48)$$

being

$$\omega_j = \frac{1}{\sqrt{M_{a,m}N_{a,n}}}. \quad (3.49)$$

The electro-mechanical gain is defined as

$$\Lambda_\kappa = \frac{\omega_\kappa}{\omega} \quad (3.50)$$

being

$$\omega_\kappa = \frac{1}{\sqrt{C_n M_m}}. \quad (3.51)$$

The mechanical-acoustic gain is defined as

$$U_\kappa = \frac{\omega_\kappa}{\omega} \quad (3.52)$$

being

$$\omega_\kappa = \frac{1}{\sqrt{M_m N_{a,n}}}. \quad (3.53)$$

The mechanical quality factor is equated by:

$$Q_{mech} = R_l \omega_l C_n. \quad (3.54)$$

The electrical quality factor can be equated as function of the real system parameters as

$$Q_{el(parallel)} = \frac{R_l}{\omega_j L_m} = \omega_j C_n R_l \quad (3.55)$$

or

$$Q_{el(series)} = \frac{\omega_j L_m}{R_l} = \frac{1}{\omega_j C_n R_l}. \quad (3.56)$$

In (3.55), the relationship is used for parallel connection between the reactive components and the resistor. On the other hand, (3.56) is used for series connection.

The acoustical quality factor can be equated as function of the real system parameters as

$$Q_{a(parallel)} = \frac{Z_{a,l}}{\omega_j M_{a,m}} = \omega_j N_{a,n} Z_{a,l} \quad (3.57)$$

or

$$Q_{a(series)} = \frac{\omega_j M_{a,m}}{Z_{a,l}} = \frac{1}{\omega_j N_{a,n} Z_{a,l}}. \quad (3.58)$$

The damping combines the mechanical components in an unit-less equation described by

$$\zeta_h = \frac{D_l}{2\sqrt{M_m K_n}}. \quad (3.59)$$

The transfer power ratio is an unit-less parameter that performs the interface

between the input and the load by

$$T_{POT} = \frac{R_l I_{in}}{V_{in}} \quad (3.60)$$

or

$$T_{POT} = \frac{R_l Z_{in}}{F_{in}}. \quad (3.61)$$

The AC-to-DC transfer function  $S_{V,I}$  relates an AC input with a DC output signal. As long as an AC-DC rectifier must be used to convert the output voltage from the ultrasound receiver into a DC signal to supply a load,  $S_{V,I}$  is suitable to understand the rectifier behavior when relating the transferred energy with other circuit parameters. The AC-to-DC transfer function is equated as

$$S_V = \frac{V_o}{V_{in_{rms}}} = \frac{V_o \sqrt{2}}{V_{in}} \quad (3.62)$$

and

$$S_I = \frac{I_o}{I_{in_{rms}}} = \frac{I_o \sqrt{2}}{I_{in}} \quad (3.63)$$

being  $V_o$  and  $I_o$ , the output voltage and the output current, respectively.

The unit-less parameters should be extracted from the system to represent it in a normalized manner with respect to the input, frequency and system parameters (BI-SOGNO, 2006). The decomposition into unit-less parameters scheme for multiphysics networks are related to the following statements:

**Axiom 1.** *The combination of a mechanical mass and a mechanical stiffness generates one normalized mechanical resonant frequency.*

**Axiom 2.** *The combination of an electrical inductor and an electrical capacitor generates one normalized electrical resonant frequency.*

**Axiom 3.** *The combination of an acoustical mass and an acoustical compliance generates one normalized acoustical resonant frequency.*

**Axiom 4.** *The combination of an electrical capacitance and a mechanical mass generates one electro-mechanical gain.*

**Axiom 5.** *The combination of a mechanical mass and an acoustical compliance generates one mechanical-acoustic gain.*

**Axiom 6.** *The combination of a mechanical mass, a mechanical stiffness and a mechanical damper generates the damping factor.*

**Axiom 7.** *Each electrical resistance generates one electrical quality factor.*

**Axiom 8.** *Each acoustical friction generates one acoustical quality factor.*

**Axiom 9.** *The number of extracted normalized resonant frequencies and gains is the number of energy storage components minus 1.*

**Axiom 10.** *The number of quality factors is the number of electrical resistances and acoustical frictions.*

**Axiom 11.** *The number of damping factors is the the number of mechanical dampers.*

**Axiom 12.** *Each coupling device between electrical and mechanical domains generates one electro-mechanical coupling factor.*

**Axiom 13.** *Each coupling device between mechanical and acoustical domains generates one mechanical-acoustic coupling factor.*

**Axiom 14.** *The relation between input and load is described by the transfer power ratio.*

**Axiom 15.** *The relation between input and output is described by the transfer function.*

These axioms are the general rules that must be applied in a multiphysics network in order to obtain the normalized model. In the next subsections, the development of the normalized model for the proposed system is going to be explained in details, and the axioms are going to be applied to clarify the proposed decomposition into unit-less parameters.

### 3.4.2 Equivalence transformation

The state-space representation in (3.28)-(3.34) is dependent of real system parameters. In order to obtain a normalized model based on unit-less parameters in a systematic way, an equivalence transformation should be defined, in which, the vector space described by  $\mathbf{x}(t)$ , is converted into a new vector space  $\mathbf{e}(t)$  based on the square roots of the energy in the storage elements.

In linear systems, an equivalence transformation is a operation that allows the representation of a vector by means of other terms by multiplying it using a non-singular real matrix (CHEN, 1999). In general, the operation

$$\mathbf{e}(t) = \mathbf{P} \cdot \mathbf{x}(t) \quad (3.64)$$

is called *equivalence transformation*, in which  $\mathbf{e}(t)$  and  $\mathbf{x}(t)$  are vector spaces and  $\mathbf{P}$  is a non-singular real matrix.

The new vector space  $\mathbf{e}(t)$  is composed of the square roots of the energy in the storage elements, which can be generically defined by

$$\mathbf{e}(t) = \begin{bmatrix} \varepsilon_1 \frac{\sqrt{E_1}}{\sqrt{2}} & \cdots & 0 \\ \vdots & \ddots & \vdots \\ 0 & \cdots & \varepsilon_j \frac{\sqrt{E_{nc}}}{\sqrt{2}} \end{bmatrix}, \quad (3.65)$$

in which  $E_{nc}$  represents a storage element. By taking (3.64), matrix  $\mathbf{P}$  is written as

$$\mathbf{P} = \Gamma(\mathbf{e}(t) \cdot \mathbf{x}(t)^{-1}), \quad (3.66)$$

which gives

$$\mathbf{P} = \begin{bmatrix} \Gamma \frac{\sqrt{E_1}}{\sqrt{2}} & \dots & 0 \\ \vdots & \ddots & \vdots \\ 0 & \dots & \Gamma \frac{\sqrt{E_{nc}}}{\sqrt{2}} \end{bmatrix}. \quad (3.67)$$

Matrix  $\mathbf{P}$  is used to obtain new state-space matrices related to the new vector space  $\mathbf{e}(t)$ . Also,  $\Gamma$  is a correction factor that is going to be explained subsequently. In this sense, a new state-space model is described by

$$\begin{aligned} \dot{\mathbf{e}}(\omega t) &= \overline{\mathbf{A}}_{I[R_l, L_m, C_n, D_l, M_m, K_n, M_{a,m}, N_{a,n}, Z_{a,l}, \omega]} \mathbf{e}(\omega t) + \overline{\mathbf{B}}_I \\ &\quad \vdots \end{aligned} \quad (3.68)$$

$$\dot{\mathbf{e}}(\omega t) = \overline{\mathbf{A}}_{k[R_l, L_m, C_n, D_l, M_m, K_n, M_{a,m}, N_{a,n}, Z_{a,l}, \omega]} \mathbf{e}(\omega t) + \overline{\mathbf{B}}_k$$

$$\begin{aligned} \mathbf{y}(\omega t) &= \overline{\mathbf{C}}_{I[V_{in}, I_{in}, F_{in}, Z_{in}, P_{in}, Q_{in}, R_l, L_m, C_n, D_l, M_m, K_n, M_{a,m}, N_{a,n}, Z_{a,l}, \omega]} \mathbf{e}(\omega t) + \overline{\mathbf{D}}_I \\ &\quad \vdots \end{aligned} \quad (3.69)$$

$$\mathbf{y}(\omega t) = \overline{\mathbf{C}}_{k[V_{in}, I_{in}, F_{in}, Z_{in}, P_{in}, Q_{in}, R_l, L_m, C_n, D_l, M_m, K_n, M_{a,m}, N_{a,n}, Z_{a,l}, \omega]} \mathbf{e}(\omega t) + \overline{\mathbf{D}}_k,$$

in which,

$$\overline{\mathbf{A}}_k = \frac{1}{\omega} \mathbf{P} \mathbf{A}_k \mathbf{P}^{-1}, \quad (3.70)$$

$$\overline{\mathbf{B}}_k = \frac{1}{\omega} \mathbf{P} \mathbf{B}_k, \quad (3.71)$$

$$\overline{\mathbf{C}}_k = \mathbf{C}_k \mathbf{P}^{-1} \quad (3.72)$$

and

$$\overline{\mathbf{D}}_k = \mathbf{D}_k. \quad (3.73)$$

**Lemma 1.** *The multiplication of the state and input matrices from a generic state-space model in (3.5) and (3.6) by a linear operator, proportionally modifies the independent variable of the derivative operator and the argument of the related function.*

The proofs of Lemmas and Theorems are in the Appendix B.



A new vector space for the state-space model is defined as

$$\mathbf{e}(t) = \begin{bmatrix} x_1 \frac{\sqrt{K_1}}{\sqrt{2}} & 0 & 0 & 0 & 0 & 0 \\ 0 & x_2 \frac{\sqrt{M_1}}{\sqrt{2}} & 0 & 0 & 0 & 0 \\ 0 & 0 & x_3 \frac{\sqrt{K_2}}{\sqrt{2}} & 0 & 0 & 0 \\ 0 & 0 & 0 & x_4 \frac{\sqrt{M_2}}{\sqrt{2}} & 0 & 0 \\ 0 & 0 & 0 & 0 & x_5 \frac{\sqrt{N_{a1}}}{\sqrt{2}} & 0 \\ 0 & 0 & 0 & 0 & 0 & x_6 \frac{\sqrt{C_o}}{\sqrt{2}} \end{bmatrix}. \quad (3.74)$$

First, matrix  $\mathbf{P}$  is equated as

$$\mathbf{P} = \begin{bmatrix} \frac{\sqrt{K_1}}{\sqrt{2}} & 0 & 0 & 0 & 0 & 0 \\ 0 & \frac{\sqrt{M_1}}{\sqrt{2}} & 0 & 0 & 0 & 0 \\ 0 & 0 & \frac{\sqrt{K_2}}{\sqrt{2}} & 0 & 0 & 0 \\ 0 & 0 & 0 & \frac{\sqrt{M_2}}{\sqrt{2}} & 0 & 0 \\ 0 & 0 & 0 & 0 & \frac{\sqrt{N_{a1}}}{\sqrt{2}} & 0 \\ 0 & 0 & 0 & 0 & 0 & \frac{\sqrt{C_o}}{\sqrt{2}} \end{bmatrix}. \quad (3.75)$$

By using (3.71), the following equation is obtained as

$$\overline{\mathbf{B}} = \begin{bmatrix} 0 \\ -\frac{\sqrt{M_1}}{\sqrt{2}\omega\alpha_1(M_1+M_{a1}\gamma_1^2)} \\ 0 \\ 0 \\ 0 \\ 0 \end{bmatrix}. \quad (3.76)$$

It is necessary to check matrix  $\overline{\mathbf{B}}$  in order to ensure that all terms are 0 or 1 to normalize the system in relation to the input source. It can be seen in (3.76) that there is a term different from 0 or 1. In this case, the correction factor  $\Gamma$  is used to normalize the system as

$$\Gamma = \frac{b^{-1}}{U_o}, \quad (3.77)$$

in which,  $b$  is the term in  $\overline{\mathbf{B}}_k$  that is different from 0 or 1. If all terms in  $\overline{\mathbf{B}}_k$  are 0 or 1, then  $b = 1$ . In addition,  $U_o$  is the amplitude of the input source, which automatically normalizes the system in relation to the input.

So, from (3.76) and (3.77), the correction factor is given by

$$\Gamma = \frac{\sqrt{2}\omega\alpha_1(M_1 + M_{a1}\gamma_1^2)}{\sqrt{M_1}V_{in}}. \quad (3.78)$$

In order to normalize the system in relation to the input source, the output vector  $\mathbf{y}(t)$  is composed of any system variable divided by the input current peak value  $I_{in}$ , input

voltage peak value  $V_{in}$ , input force peak value  $F_{in}$ , input displacement peak value  $Z_{in}$ , input acoustic sound pressure peak value  $P_{in}$  or input acoustic sound velocity peak value  $Q_{in}$ . In this case, the input is a electrical source, which leads to the following:

$$\mathbf{y}(t) = \left[ \frac{\mathbf{x}_1\omega}{\mathbf{I}_{in}}, \frac{\mathbf{x}_2}{\mathbf{I}_{in}}, \frac{\mathbf{x}_3\omega}{\mathbf{I}_{in}}, \frac{\mathbf{x}_4}{\mathbf{I}_{in}}, \frac{\mathbf{x}_5}{\mathbf{V}_{in}}, \frac{\mathbf{x}_6}{\mathbf{V}_{in}} \right]^T, \quad (3.79)$$

In (3.79),  $\mathbf{x}_2$  and  $\mathbf{x}_3$  are parameterized by the input current due to analogy velocity-current.  $\mathbf{x}_1$  and  $\mathbf{x}_3$  are related to displacements, so they should be parameterized by velocity  $dx_1(\omega t)/dt = df_1(\omega t)/dt = \omega f_2(\omega t)$  and  $dx_3(\omega t)/dt = df_1(\omega t)/dt = \omega f_2(\omega t)$ , being  $f_1(\omega t)$  and  $f_2(\omega t)$  any input functions. By considering  $f_2(\omega t)$  as  $z_1(\omega t)$  or  $z_2(\omega t)$ , the displacements are parameterized by  $\omega/I_{in}$ .

At this point,  $\mathbf{P}$  is equated again by means of (3.66). By using (3.70)-(3.73), the new state-space models are found by:

$$\bar{\mathbf{A}} = \begin{bmatrix} 0 & \frac{\sqrt{K_1}}{\sqrt{M_1}\omega} & 0 & 0 & 0 & 0 \\ -\frac{\sqrt{K_1}M_1}{(M_1+\gamma_1^2M_{a1})\omega} & -\frac{(D_1+\gamma_1^2Z_{a1})}{(M_1+\gamma_1^2M_{a1})} & 0 & 0 & -\frac{\sqrt{M_1}\gamma_1}{\sqrt{N_{a1}}(M_1+\gamma_1^2M_{a1})\omega} & 0 \\ 0 & 0 & 0 & \frac{\sqrt{K_2}}{\sqrt{M_2}\omega} & 0 & 0 \\ 0 & 0 & -\frac{\sqrt{K_2}}{\sqrt{M_2}\omega} & -\frac{D_2}{M_2\omega} & -\frac{1}{\sqrt{M_2}N_{a1}\gamma_2\omega} & -\frac{\alpha_2}{\sqrt{M_2}C_o\omega} \\ 0 & \frac{\gamma_1}{\sqrt{M_1}N_{a1}\omega} & 0 & -\frac{1}{\sqrt{M_2}N_{a1}\gamma_2\omega} & 0 & 0 \\ 0 & 0 & 0 & \frac{\alpha_2}{\sqrt{M_2}C_o\omega} & 0 & -\frac{1}{R_{eq}C_o\omega} \end{bmatrix}, \quad (3.80)$$

$$\bar{\mathbf{B}} = \left[ 0 \quad -\frac{1}{V_{in}} \quad 0 \quad 0 \quad 0 \quad 0 \right]^T, \quad (3.81)$$

$$\bar{\mathbf{C}} = \begin{bmatrix} \frac{-V_{in}I_{in}^{-1}\sqrt{M_1}\alpha_1^{-1}}{\sqrt{K_1}(M_1+M_{a1}\gamma_1^2)} & 0 & 0 & 0 & 0 & 0 \\ 0 & \frac{-V_{in}I_{in}^{-1}\alpha_1^{-1}}{(M_1+M_{a1}\gamma_1^2)\omega} & 0 & 0 & 0 & 0 \\ 0 & 0 & \frac{-V_{in}I_{in}^{-1}\sqrt{M_1}\alpha_1^{-1}}{\sqrt{K_2}(M_1+M_{a1}\gamma_1^2)} & 0 & 0 & 0 \\ 0 & 0 & 0 & \frac{-V_{in}I_{in}^{-1}\sqrt{M_1}\alpha_1^{-1}}{\sqrt{M_2}(M_1+M_{a1}\gamma_1^2)\omega} & 0 & 0 \\ 0 & 0 & 0 & 0 & \frac{-\sqrt{M_1}\alpha_1^{-1}}{\sqrt{N_{a1}}(M_1+M_{a1}\gamma_1^2)\omega} & 0 \\ 0 & 0 & 0 & 0 & 0 & \frac{-\sqrt{M_1}\alpha_1^{-1}}{\sqrt{C_o}(M_1+M_{a1}\gamma_1^2)\omega} \end{bmatrix} \quad (3.82)$$

and

$$\bar{\mathbf{D}} = \left[ 0 \right]_{6 \times 1}. \quad (3.83)$$

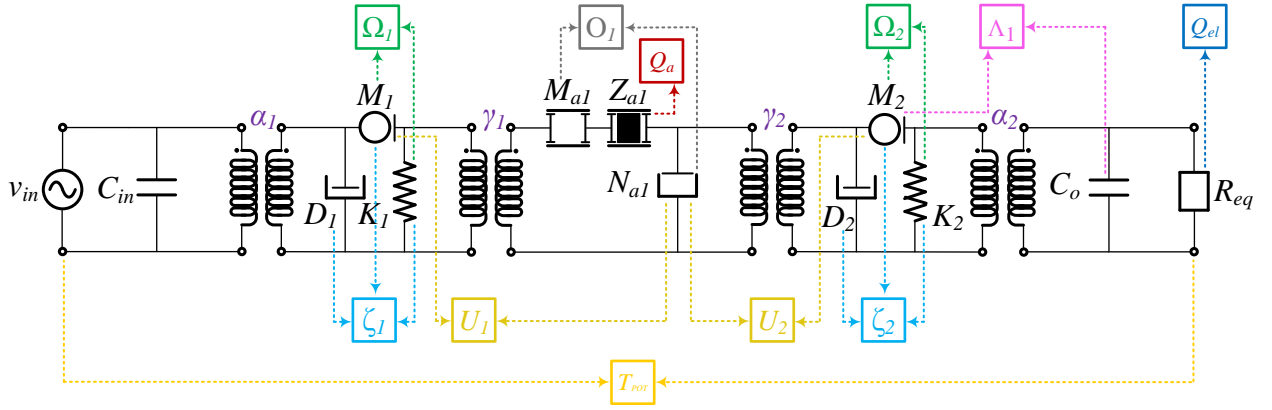
At this point, the system is normalized by the input and the frequency. However, the system is dependent of real system parameters. This configuration is suitable to convert the terms of the matrices into unit-less terms. For this purpose, the decomposition into unit-less parameters scheme for multiphysics networks is going to applied into the

system.

### 3.4.3 Decomposition into unit-less parameters

By following the defined axioms in the previous subsections, the unit-less parameters for the system under study are going to be extracted. Note that  $C_{in}$  is omitted in the decomposition because it is connected in parallel to a voltage source, which means that it does not change the dynamic of the system. The decomposition into unit-less parameters scheme for the system is depicted in Figure 3.8.

Figure 3.8 – Decomposition into unit-less parameters for the multiphysical model.



Source: Author.

The system has 7 storage elements ( $M_1$ ,  $K_1$ ,  $M_2$ ,  $K_2$ ,  $M_{a1}$ ,  $N_{a1}$  and  $C_o$ ), which means that 6 unit-less parameters related to normalized resonant frequencies and gains should be extracted (*Axiom 9*). The system has two mass and two stiffness. In this case, by following *Axiom 1*, the normalized mechanical resonant frequencies are described as

$$\Omega_1 = \frac{\omega_1}{\omega} \quad (3.84)$$

and

$$\Omega_2 = \frac{\omega_2}{\omega}, \quad (3.85)$$

in which,

$$\omega_1 = \frac{\sqrt{K_1}}{\sqrt{M_1}} \quad (3.86)$$

and

$$\omega_2 = \frac{\sqrt{K_2}}{\sqrt{M_2}}. \quad (3.87)$$

The combination of  $C_o$  and  $M_2$  generates one electro-mechanical gain  $\Lambda_1$  (*Axiom 4*):

$$\Lambda_1 = \frac{\omega_3}{\omega}, \quad (3.88)$$

being

$$\omega_3 = \frac{1}{\sqrt{M_2 C_o}}. \quad (3.89)$$

The system has one normalized acoustical resonant frequency  $O_1$  based on the acoustical mass and compliance (*Axiom 3*):

$$O_1 = \frac{\omega_4}{\omega}, \quad (3.90)$$

being

$$\omega_4 = \frac{1}{\sqrt{M_{a1} N_{a1}}}. \quad (3.91)$$

By following *Axiom 5*, the mechanical mass  $M_1$  and  $M_2$  are combined to the acoustical compliance  $N_{a1}$  to generate the mechanical-acoustic gains  $U_1$  and  $U_2$ :

$$U_1 = \frac{\omega_5}{\omega} \quad (3.92)$$

and

$$U_2 = \frac{\omega_6}{\omega}, \quad (3.93)$$

in which,

$$\omega_5 = \frac{1}{\sqrt{M_1 N_{a1}}} \quad (3.94)$$

and

$$\omega_6 = \frac{1}{\sqrt{M_2 N_{a1}}}. \quad (3.95)$$

The system has one electrical resistance as load  $R_{eq}$  and one acoustical friction  $Z_{a1}$ . This means that two quality factors are extracted (*Axiom 10*). The acoustical quality factor  $Q_a$  is given by

$$Q_a = \frac{1}{Z_{a1} N_{a1} \omega_4} = \frac{M_{a1} \omega_4}{Z_{a1}}. \quad (3.96)$$

The electrical quality factor  $Q_{el}$  is

$$Q_{el} = C_o R_{eq} \omega_2 = \frac{R_{eq}}{M_2 \omega_2}. \quad (3.97)$$

The combination of  $M_1$ ,  $K_1$  and  $D_1$  generates the damping factor  $\zeta_1$ . The combination of  $M_2$ ,  $K_2$  and  $D_2$  generates the damping factor  $\zeta_2$ . The two damping factors are extracted based on *Axiom 11*:

$$\zeta_1 = \frac{D_1}{2\sqrt{M_1 K_1}} = \frac{D_1}{2M_1 \omega_1}, \quad (3.98)$$

and

$$\zeta_2 = \frac{D_2}{2\sqrt{M_2 K_2}} = \frac{D_2}{2M_2 \omega_2}. \quad (3.99)$$

The transfer power ratio is given by (*Axiom 14*):

$$T_{POT} = \frac{1}{a} = \frac{R_{eq} I_{in}}{V_{in}}, \quad (3.100)$$

being  $a$  the inverse transfer power ratio.

#### 3.4.4 Normalized state-space model based on unit-less parameters

By means of (3.84)-(3.100), the real system terms in (3.80)-(3.83) are converted into unit-less terms by mathematical operations. The state-space model based on unit-less parameters is described in a generic way by

$$\begin{aligned} \dot{\mathbf{e}}(\omega t) &= \overline{\mathbf{E}}_{I[A_j, \Omega_i, O_j, \Lambda_\kappa, U_\kappa, Q_{mech}, Q_{el}, Q_a, \zeta_h, S_{V,I}, T_{POT}]} \mathbf{e}(\omega t) + \overline{\mathbf{F}}_I \\ &\quad \vdots \end{aligned} \quad (3.101)$$

$$\dot{\mathbf{e}}(\omega t) = \overline{\mathbf{E}}_{k[A_j, \Omega_i, O_j, \Lambda_\kappa, U_\kappa, Q_{mech}, Q_{el}, Q_a, \zeta_h, S_{V,I}, T_{POT}]} \mathbf{e}(\omega t) + \overline{\mathbf{F}}_k$$

$$\begin{aligned} \mathbf{y}(\omega t) &= \overline{\mathbf{G}}_{I[A_j, \Omega_i, O_j, \Lambda_\kappa, U_\kappa, Q_{mech}, Q_{el}, Q_a, \zeta_h, S_{V,I}, T_{POT}]} \mathbf{e}(\omega t) + \overline{\mathbf{H}}_I \\ &\quad \vdots \end{aligned} \quad (3.102)$$

$$\mathbf{y}(\omega t) = \overline{\mathbf{G}}_{k[A_j, \Omega_i, O_j, \Lambda_\kappa, U_\kappa, Q_{mech}, Q_{el}, Q_a, \zeta_h, S_{V,I}, T_{POT}]} \mathbf{e}(\omega t) + \overline{\mathbf{H}}_k,$$

in which,  $\overline{\mathbf{E}}_k$  is the unit-less state matrix,  $\overline{\mathbf{F}}_k$  is the unit-less input matrix,  $\overline{\mathbf{G}}_k$  is the unit-less output matrix and  $\overline{\mathbf{H}}_k$  is the unit-less transmission matrix. The unit-less matrices for the system under study is given by:

$$\overline{\mathbf{E}} = \begin{bmatrix} 0 & \Omega_1 & 0 & 0 & 0 & 0 \\ -\frac{\Omega_1 O_1^2}{(O_1^2 + \gamma_1^2 U_1^2)} & -\frac{(2\zeta_1 \Omega_1 O_1^2 Q_a O_1 U_1^2 \gamma_1^2)}{Q_a (O_1^2 + \gamma_1^2 U_1^2)} & 0 & 0 & -\frac{U_1 O_1^2 \gamma_1}{(O_1^2 + \gamma_1^2 U_1^2)} & 0 \\ 0 & 0 & 0 & \Omega_2 & 0 & 0 \\ 0 & 0 & -\Omega_2 & -2\zeta_2 \Omega_2 & -\frac{U_2}{\gamma_2} & -\Lambda_1 \alpha_2 \\ 0 & U_1 \gamma_1 & 0 & -\frac{U_2}{\gamma_2} & 0 & 0 \\ 0 & 0 & 0 & \Lambda_1 \alpha_2 & 0 & -\frac{\Omega_2}{Q_{el}} \end{bmatrix}, \quad (3.103)$$

$$\overline{\mathbf{F}} = [0 \ 1 \ 0 \ 0 \ 0 \ 0]^T, \quad (3.104)$$

$$\bar{\mathbf{G}} = \begin{bmatrix} \frac{-\Omega_2 U_1^2 O_1^2 Q_{el} a}{\Omega_1 U_2^2 \alpha_1 (O_1^2 + \gamma_1^2 U_1^2)} & 0 & 0 & 0 & 0 & 0 \\ 0 & \frac{-\Omega_2 U_1^2 O_1^2 Q_{el} a}{U_2^2 \alpha_1 (O_1^2 + \gamma_1^2 U_1^2)} & 0 & 0 & 0 & 0 \\ 0 & 0 & \frac{-U_1 O_1^2 Q_{el} a}{U_2 \alpha_1 (O_1^2 + \gamma_1^2 U_1^2)} & 0 & 0 & 0 \\ 0 & 0 & 0 & \frac{-\Omega_2 U_1 O_1^2 Q_{el} a}{U_2 \alpha_1 (O_1^2 + \gamma_1^2 U_1^2)} & 0 & 0 \\ 0 & 0 & 0 & 0 & \frac{-U_1 O_1^2}{\alpha_1 (O_1^2 + \gamma_1^2 U_1^2)} & 0 \\ 0 & 0 & 0 & 0 & 0 & \frac{-\Lambda_1 U_1 O_1^2}{U_2 \alpha_1 (O_1^2 + \gamma_1^2 U_1^2)} \end{bmatrix} \quad (3.105)$$

and

$$\bar{\mathbf{H}} = [0]_{6 \times 1}. \quad (3.106)$$

**Theorem 1.** *A generic system described by a state-space model  $\mathbf{x}(t) = \mathbf{A}\mathbf{x}(t) + \mathbf{B}u$  and  $\mathbf{y}(t) = \mathbf{C}\mathbf{x}(t) + \mathbf{D}u$  can be represented as a dimensionless model normalized by the input source and the operating frequency by using the transfer power ratio and the resonance among the storage elements.*

In order to solve the normalized model, a parameter sweep is performed in some of the unit-less parameters while others are defined. The frequency response of the system can be obtained by means of a mathematical software by solving the state-space matrices. The system was solved for different sets of unit-less parameters. The idea is to provide graphics based on the voltage gain as function of the normalized operating frequency. The voltage gain can be related to the gain in *dB* and to the transfer power ratio by the following relation:

$$\text{Voltage gain} = \sqrt{T_{POT}} = \frac{1}{\sqrt{a}} = 10^{\frac{\text{Gain}(dB)}{20}}. \quad (3.107)$$

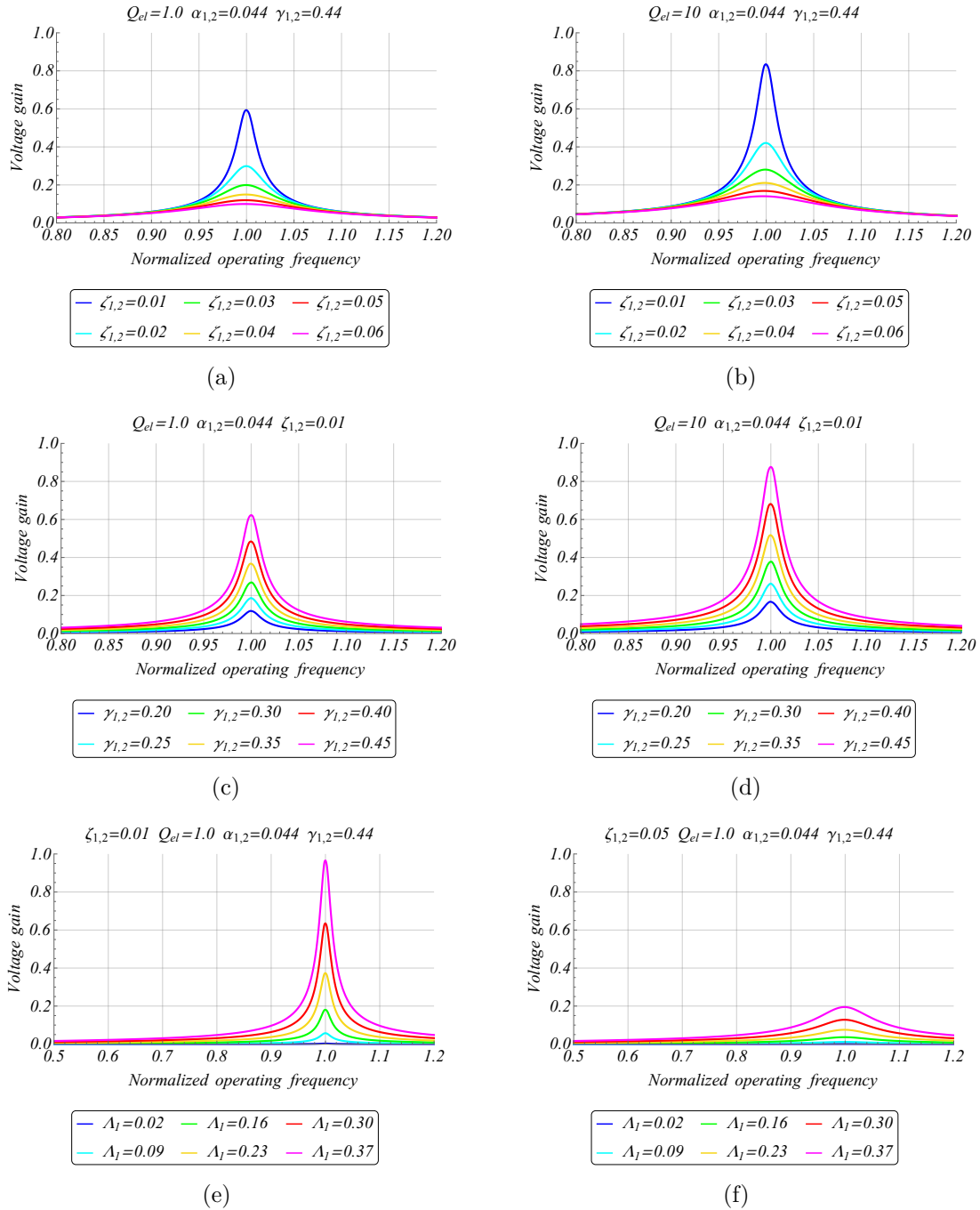
The normalized gain curves for the developed model are shown in Figure 3.9 and in Figure 3.10. Figures 3.9(a)-(b) depict the theoretical result for different values of damping  $\zeta_{1,2}$ . It can be seen that the lower the damping, higher is the voltage gain. The higher the coupling factors  $\gamma_{1,2}$ , higher the voltage gain, as shown in Figures 3.9(c)-(d). The comparison between quality factors shows the higher gain for  $Q_{el} = 10$  in Figures 3.9(a)-(d). The influence of the electromechanical gain  $\Lambda_1$  is realized in Figures 3.9(e)-(f), in which the higher  $\Lambda_1$ , higher the voltage gain. The maximum voltage gain is obtained when the normalized operating frequency is 1.0, which means that, for the chosen set of parameters, the predominant frequency is the operating frequency of the piezoelectric transducers. In Figure 3.9 and Figure 3.10, the system was evaluated considering  $\Omega_{1,2} = 1.0$ ,  $\Lambda_1 = 0.29$  (except in Figures 3.9(e)-(f)),  $1/U_{1,2} = 0.01$ ,  $Q_a = 38 \times 10^{10}$  and  $1/O_1 = 0.0002$  (except in Figure 3.10).

Figure 3.10 aims to evaluate the influence of  $O_1$  in the system. It can be seen

---

that for low values of  $1/O_1$ , the resonant frequency of the system is ruled by the resonant frequency of the piezoelectric transducers  $\Omega_{1,2}$  (note curves in blue and cyan). This means that, if  $1/O_1$  is sufficiently low when compared to the piezoelectric transducers frequency, the acoustical resonant frequency does not interfere in the system's predominant frequency. This is an important result because it highlights a condition in which the acoustic resonant frequency does not have huge impact in the transducers frequency.

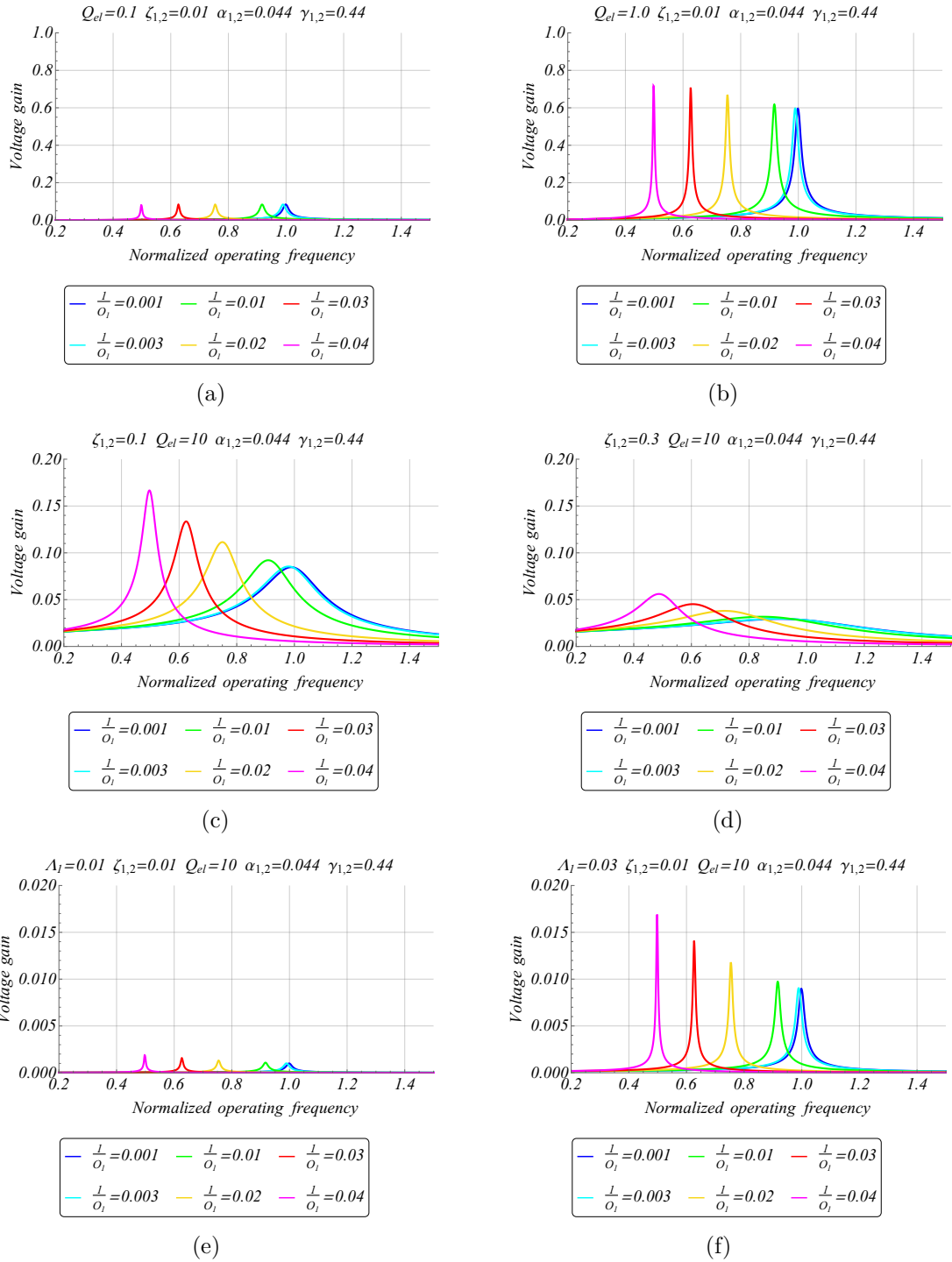
Figure 3.9 – Normalized gain curves for the multiphysical model based on lumped parameters (Voltage gain as function of the normalized operating frequency): (a)  $Q_{el} = 1.0$  for different values of  $\zeta_{1,2}$ . (b)  $Q_{el} = 10$  for different values of  $\zeta_{1,2}$ . (c)  $Q_{el} = 1.0$  for different values of  $\gamma_{1,2}$ . (d)  $Q_{el} = 10$  for different values of  $\gamma_{1,2}$ . (e)  $\zeta_{1,2} = 0.01$  for different values of  $\Lambda_1$ . (f)  $\zeta_{1,2} = 0.05$  for different values of  $\Lambda_1$ .



Source: Author.



Figure 3.10 – Normalized gain curves for the multiphysical model based on lumped parameters (Voltage gain as function of the normalized operating frequency): (a)  $Q_{el} = 0.1$  for different values of  $O_1$ . (b)  $Q_{el} = 1.0$  for different values of  $O_1$ . (c)  $\zeta_{1,2} = 0.1$  for different values of  $O_1$ . (d)  $\zeta_{1,2} = 0.3$  for different values of  $O_1$ . (e)  $\Lambda_1 = 0.01$  for different values of  $O_1$ . (f)  $\Lambda_1 = 0.03$  for different values of  $O_1$ .



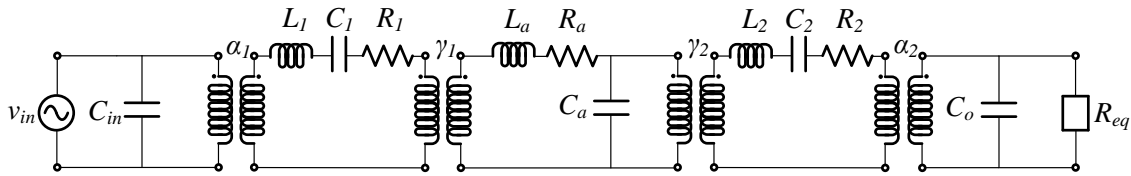
Source: Author.

## 3.5 EQUIVALENT ELECTRICAL MODEL

It is possible to derive an equivalent electrical model for the multiphysical model shown in Section 3.3. The equivalent electrical model replaces the mechanical and acoustical lumped components by equivalent electrical components. The equivalent electrical model can be used in SPICE simulation software.

The equivalent electrical model is shown in Figure 3.11.

Figure 3.11 – Equivalent electrical model.



Source: Author.

The model replaces the mechanical mass  $M_1$  and  $M_2$  by inductors  $L_1$  and  $L_2$ . Mechanical stiffness  $K_1$  and  $K_2$  are replaced by capacitors  $C_1$  and  $C_2$  and mechanical dampers  $D_1$  and  $D_2$  by resistances  $R_1$  and  $R_2$ . The acoustical mass  $M_{a1}$ , acoustical friction  $Z_{a1}$  and acoustical compliance  $N_{a1}$  are substituted by inductor  $L_a$ , resistance  $R_a$  and capacitor  $C_a$ , respectively.

The conversion between multiphysical and electrical models is performed by equating:  $M_{1,2} = L_{1,2}$ ,  $K_{1,2} = 1/C_{1,2}$ ,  $D_{1,2} = R_{1,2}$ ,  $M_{a1} = L_a$ ,  $N_{a1} = C_a$  and  $Z_{a1} = R_a$ . In the same way the multiphysical model was represented by a state-space model, the electrical model is represented by the following:

$$\mathbf{x}(t) = [\mathbf{i}_{L_1}, \mathbf{i}_{L_2}, \mathbf{v}_{C_1}, \mathbf{v}_{C_2}, \mathbf{v}_{C_a}, \mathbf{v}_{C_o}]^T, \quad (3.108)$$

$$u(t) = V_{in} \sin(\omega t), \quad (3.109)$$

$$\mathbf{A} = \begin{bmatrix} -\frac{R_1 + \gamma_1^2 R_a}{(L_1 + \gamma_1^2 L_a)} & 0 & -\frac{1}{(L_1 + \gamma_1^2 L_a)} & 0 & -\frac{\gamma_1}{(L_1 + \gamma_1^2 L_a)} & 0 \\ 0 & -\frac{R_2}{L_2} & 0 & -\frac{1}{L_2} & -\frac{1}{\gamma_2 L_2} & -\frac{\alpha_2}{L_2} \\ \frac{1}{C_1} & 0 & 0 & 0 & 0 & 0 \\ 0 & \frac{1}{C_2} & 0 & 0 & 0 & 0 \\ \frac{\gamma_1}{C_a} & -\frac{1}{\gamma_2 C_a} & 0 & 0 & 0 & 0 \\ 0 & \frac{\alpha_2}{C_o} & 0 & 0 & 0 & -\frac{1}{R_{eq} C_o} \end{bmatrix}, \quad (3.110)$$

$$\mathbf{B} = \begin{bmatrix} \frac{1}{\alpha_1(L_1 + \gamma_1^2 L_a)} \\ 0 \\ 0 \\ 0 \\ 0 \\ 0 \end{bmatrix}, \quad (3.111)$$

$$\mathbf{y}(t) = [\mathbf{i}_{L_1}, \mathbf{i}_{L_2}, \mathbf{v}_{C_1}, \mathbf{v}_{C_2}, \mathbf{v}_{C_a}, \mathbf{v}_{C_o}]^T, \quad (3.112)$$

$$\mathbf{C} = \begin{bmatrix} 1 & 0 & 0 & 0 & 0 & 0 \\ 0 & 1 & 0 & 0 & 0 & 0 \\ 0 & 0 & 1 & 0 & 0 & 0 \\ 0 & 0 & 0 & 1 & 0 & 0 \\ 0 & 0 & 0 & 0 & 1 & 0 \\ 0 & 0 & 0 & 0 & 0 & 1 \end{bmatrix} \quad (3.113)$$

and

$$\mathbf{D} = [0]_{6 \times 1}, \quad (3.114)$$

in which,  $i_{L_1}$  and  $i_{L_2}$  are the inductor currents, and  $v_{C_1}$ ,  $v_{C_2}$ ,  $v_{C_a}$  and  $v_{C_o}$  are the capacitor voltages.

### 3.6 PIEZOELECTRIC TRANSFORMER MODEL

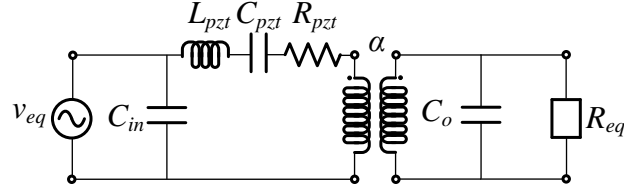
Another proposed model for the system is the piezoelectric transformer model (PZT model). It is well-known the representation for piezoelectric transformers based on a resonant circuit and an ideal transformer (ALONSO; ORDIZ; COSTA, 2008; BISOGNO, 2006).

The piezoelectric transformer has an electrical input and an electrical output, which is the same case as the electro-mechanical-acoustic CET system. The main idea is to synthesize the equivalent electrical model into the piezoelectric transformer model. For this purpose, the couplings between electrical-mechanical ( $\alpha_1$ ), mechanical-acoustical ( $\gamma_1$ ) and acoustical-mechanical ( $\gamma_2$ ) are removed while the coupling factors are added to the electrical components. The piezoelectric transformer model is shown in Figure 3.12.

The model has equivalent components denoted by  $L_{pzt}$ ,  $C_{pzt}$ ,  $R_{pzt}$  and  $\alpha$ . In addition, an equivalent input source  $v_{eq}$  replaces  $v_{in}$ . The state-space representation for the piezoelectric transformer model is given as:

$$\mathbf{x}(t) = [\mathbf{i}_{L_{pzt}}, \mathbf{v}_{C_{pzt}}, \mathbf{v}_{C_o}]^T, \quad (3.115)$$

Figure 3.12 – Piezoelectric transformer model.



Source: Author.

$$u(t) = V_{in} \sin(\omega t), \quad (3.116)$$

$$\mathbf{A} = \begin{bmatrix} -\frac{R_{pzt}}{L_{pzt}} & -\frac{1}{L_{pzt}} & -\frac{\alpha}{L_{pzt}} \\ -\frac{1}{C_{pzt}} & 0 & 0 \\ \frac{\alpha}{C_o} & 0 & -\frac{1}{R_{eq}C_o} \end{bmatrix}, \quad (3.117)$$

$$\mathbf{B} = \begin{bmatrix} \frac{1}{L_{pzt}} \\ 0 \\ 0 \end{bmatrix}, \quad (3.118)$$

$$\mathbf{y}(t) = [\mathbf{i}_{L_{pzt}}, \mathbf{v}_{C_{pzt}}, \mathbf{v}_{C_o}]^T, \quad (3.119)$$

$$\mathbf{C} = \begin{bmatrix} 1 & 0 & 0 \\ 0 & 1 & 0 \\ 0 & 0 & 1 \end{bmatrix} \quad (3.120)$$

and

$$\mathbf{D} = [0]_{3 \times 1}, \quad (3.121)$$

in which,  $i_{L_{pzt}}$  is the inductor current, and  $v_{C_{pzt}}$  and  $v_{C_o}$  are the capacitor voltages.

The parameters are obtained by the following relationships:

$$L_{pzt} = \frac{L_1}{\gamma_1^2 \gamma_2^2} + \frac{L_a}{\gamma_2^2} + L_2, \quad (3.122)$$

$$C_{pzt} = \frac{1}{\frac{1}{L_1 C_1} \left( \frac{L_1}{\gamma_1^2 \gamma_2^2} + \frac{L_a}{\gamma_2^2} + L_2 \right)}, \quad (3.123)$$

$$R_{pzt} = \frac{R_1}{\gamma_1^2 \gamma_2^2} + \frac{R_a}{\gamma_2^2} + R_2, \quad (3.124)$$

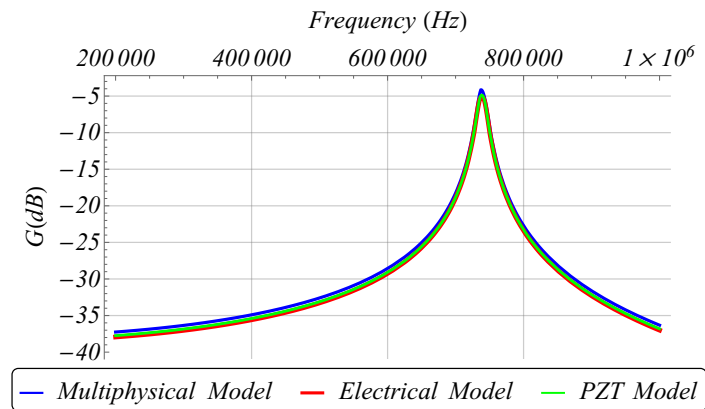
$$v_{eq} = \frac{v_{in}}{\alpha_1 \gamma_1 \gamma_2} \quad (3.125)$$

and

$$\alpha = \alpha_2. \quad (3.126)$$

In order to show that the models have good agreement to each other, the theoretical frequency responses of the models are compared as shown in Figure 3.13. The parameters for the multiphysical model are represented in Table 3.3 and Table 3.4. The parameters for the electrical and piezoelectric models are calculated based on the multiphysical model.

Figure 3.13 – Voltage gain ( $dB$ ) as function of frequency ( $Hz$ ) for different models.



Source: Author.

### 3.7 AUGMENTED-ORDER MULTIPHYSICAL MODEL BASED ON LUMPED PARAMETERS

Until this part of the Thesis, a multiphysical model based on lumped parameters, an equivalent electrical model and a piezoelectric transformer model were presented as mathematical representation for the electro-mechanical-acoustic CET system. Realizing that the electrical and piezoelectric transformer models are actually derived from the multiphysical model. In addition, a normalization procedure for multiphysics networks was applied into the multiphysical model.

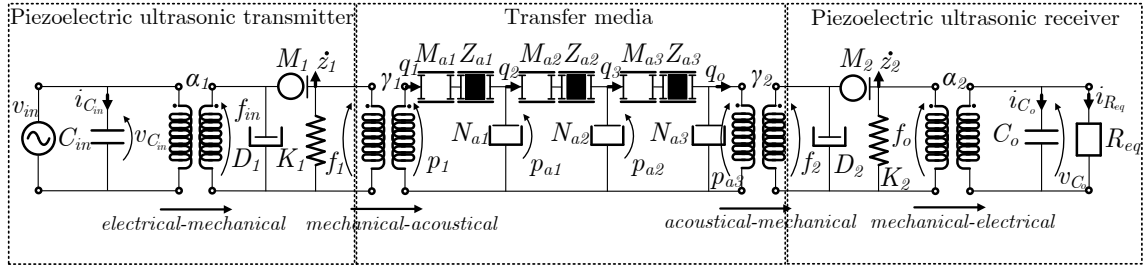
In later chapters of this work, it is going to be shown that the models have good agreement with the experimental results. However, especially for low frequencies, the models can be improved in order to increase the matching between experimental and theoretical results. In this sense, an augmented-order model is proposed in this section.

The main idea is to enhance the multiphysical model based on lumped parameters by means on an iterative process of checking the analytical model compared to the response of the real physical system. In other words, the aforementioned multiphysical model is considered as an analytical model. After the analytical model is developed, its validity is checked by evaluating the experimental response of the system. Based on this evalua-

tion, it is interesting to detect the parts of the model that should be improved. In this case, an improved model can be developed, which can be considered as a semi-analytical model.

The proposed model in this section is developed by increasing the order of the system aiming to obtain a higher degree of freedom that enables to amplify or attenuate parts of the system's frequency response. The augmented-order model is built by inserting networks on the acoustic network. The proposed model is depicted in Figure 3.14.

Figure 3.14 – Augmented-order multiphysical model based on lumped parameters.



Source: Author.

One can see that 6 new equivalent acoustical components were added to the multiphysical model: mass  $M_{a2}$ , friction  $Z_{a2}$ , compliance  $N_{a2}$ , mass  $M_{a3}$ , friction  $Z_{a3}$  and compliance  $N_{a3}$ . This leads to new system variables denoted by  $q_2$ ,  $q_3$ ,  $p_{a1}$ ,  $p_{a2}$  and  $p_{a3}$ . The order of the system is increased from 6 to 10.

The state-space representation is given by:

$$\mathbf{x}(t) = [\mathbf{x}_1, \mathbf{x}_2, \mathbf{x}_3, \mathbf{x}_4, \mathbf{x}_5, \mathbf{x}_6, \mathbf{x}_7, \mathbf{x}_8, \mathbf{x}_9, \mathbf{x}_{10}]^T, \quad (3.127)$$

$$u(t) = V_{in} \sin(\omega t), \quad (3.128)$$

$$\mathbf{A} = \begin{bmatrix} 0 & 1 & 0 & 0 & 0 & 0 & 0 & 0 & 0 & 0 \\ \frac{-K_1}{M_1 + M_{a1}\gamma_1^2} & \frac{-D_1 + Z_{a1}\gamma_1^2}{M_1 + M_{a1}\gamma_1^2} & 0 & 0 & \frac{-\gamma_1}{M_1 + M_{a1}\gamma_1^2} & 0 & 0 & 0 & 0 & 0 \\ 0 & 0 & 0 & 1 & 0 & 0 & 0 & 0 & 0 & 0 \\ 0 & 0 & \frac{-K_2}{M_2} & \frac{-D_2}{M_2} & 0 & 0 & \frac{-1}{M_2\gamma_2} & 0 & 0 & \frac{-\alpha_2}{M_2} \\ 0 & \frac{\gamma_1}{N_{a1}} & 0 & 0 & 0 & 0 & 0 & \frac{-1}{N_{a1}\gamma_2} & 0 & 0 \\ 0 & 0 & 0 & 0 & 0 & 0 & 0 & \frac{1}{N_{a2}} & \frac{-1}{N_{a2}} & 0 \\ 0 & 0 & 0 & \frac{-1}{\gamma_2 N_{a3}} & 0 & 0 & 0 & 0 & \frac{1}{N_{a3}} & 0 \\ 0 & 0 & 0 & 0 & \frac{1}{M_{a2}} & \frac{-1}{M_{a2}} & 0 & \frac{-Z_{a2}}{M_{a2}} & 0 & 0 \\ 0 & 0 & 0 & 0 & 0 & \frac{1}{M_{a3}} & \frac{-1}{M_{a3}} & 0 & \frac{-Z_{a3}}{M_{a3}} & 0 \\ 0 & 0 & 0 & \frac{\alpha_2}{C_o} & 0 & 0 & 0 & 0 & 0 & \frac{-1}{R_{eq}C_o} \end{bmatrix}, \quad (3.129)$$

$$\mathbf{B} = \begin{bmatrix} 0 \\ -\frac{1}{\alpha_1(M_1 + M_a\gamma_1^2)} \\ 0 \\ 0 \\ 0 \\ 0 \\ 0 \\ 0 \\ 0 \\ 0 \end{bmatrix}, \quad (3.130)$$

$$\mathbf{y}(t) = [\mathbf{x}_1, \mathbf{x}_2, \mathbf{x}_3, \mathbf{x}_4, \mathbf{x}_5, \mathbf{x}_6, \mathbf{x}_7, \mathbf{x}_8, \mathbf{x}_9, \mathbf{x}_{10}]^T, \quad (3.131)$$

$$\mathbf{C} = \begin{bmatrix} 1 & 0 & 0 & 0 & 0 & 0 & 0 & 0 & 0 & 0 \\ 0 & 1 & 0 & 0 & 0 & 0 & 0 & 0 & 0 & 0 \\ 0 & 0 & 1 & 0 & 0 & 0 & 0 & 0 & 0 & 0 \\ 0 & 0 & 0 & 1 & 0 & 0 & 0 & 0 & 0 & 0 \\ 0 & 0 & 0 & 0 & 1 & 0 & 0 & 0 & 0 & 0 \\ 0 & 0 & 0 & 0 & 0 & 1 & 0 & 0 & 0 & 0 \\ 0 & 0 & 0 & 0 & 0 & 0 & 1 & 0 & 0 & 0 \\ 0 & 0 & 0 & 0 & 0 & 0 & 0 & 1 & 0 & 0 \\ 0 & 0 & 0 & 0 & 0 & 0 & 0 & 0 & 1 & 0 \\ 0 & 0 & 0 & 0 & 0 & 0 & 0 & 0 & 0 & 1 \end{bmatrix} \quad (3.132)$$

and

$$\mathbf{D} = [0]_{10 \times 1}. \quad (3.133)$$

In order to equate the new components, angular resonant frequencies  $\omega_{a2}$  and  $\omega_{a3}$  are described as

$$\omega_{a2} = \frac{1}{\sqrt{M_{a2}N_{a2}}} \quad (3.134)$$

and

$$\omega_{a3} = \frac{1}{\sqrt{M_{a3}N_{a3}}}. \quad (3.135)$$

$\omega_{a2}$  and  $\omega_{a3}$  are related to the angular acoustical resonant frequency of the multiphysical model  $\omega_{a1}$ , which is defined as

$$\omega_{a1} = \frac{1}{\sqrt{M_{a1}N_{a1}}}. \quad (3.136)$$

The relation between  $\omega_{a1}$  and  $\omega_{a2}$ , and between  $\omega_{a1}$  and  $\omega_{a3}$ , are performed based

on constants  $w_1$  and  $w_2$ :

$$\omega_{a2} = w_1 \omega_{a1} \quad (3.137)$$

and

$$\omega_{a3} = w_2 \omega_{a1}. \quad (3.138)$$

By allocating  $w_1$  and  $w_2$  in a desirable way to enhance the model based on a previous comparison between the multiphysical model and the experimental response of the system,  $N_{a2}$  and  $N_{a3}$  can be calculated as

$$N_{a2} = \frac{1}{\omega_{a2}^2 M_{a2}} \quad (3.139)$$

and

$$N_{a3} = \frac{1}{\omega_{a3}^2 M_{a3}}, \quad (3.140)$$

in which  $M_{a1} = M_{a2} = M_{a3}$ . In addition,  $Z_{a1} = Z_{a2} = Z_{a3}$ .

### 3.8 DENORMALIZATION PROCEDURE

The normalized results are interesting because they show a general behavior of the system. However, it is necessary to retrieve the real system parameters in order to link the normalized results with the physical system. This process is called denormalization.

For this purpose, this section presents the relationships among unit-less, electro-mechanical, acoustical, transfer media and piezoelectric parameters.

Equations (3.84)-(3.100), are mathematically re-arranged to retrieve the system parameters. The piezoelectric parameters are described by: piezoelectric stiffness  $c_{33}^E$ , piezoelectric coupling constant  $e_{33}^E$ , permittivity of the piezoelectric layer  $\epsilon_{33}^E$ , piezoelectric component area  $A_r$  and piezoelectric component thickness  $t_p$ .

The transfer media parameters are composed of the material density  $\rho$ , wave velocity  $C_L$ , material friction coefficient  $\mu_L$ , length  $l$  and radius  $R$ .

The relationships among unit-less, electromechanical, piezoelectric, equivalent acoustical and transfer media parameters are described in Table 3.7.



Table 3.7 – Relationships among unit-less, electromechanical, piezoelectric, acoustical and transfer media parameters.

Electromechanical	Piezoelectric	Acoustical	Transfer media	Unit-less
$M_1$	$M_1$	-	-	$\frac{\Omega_2 U_2^2 R_{eq}}{\Lambda_1^2 U_1^2 Q_{el} \omega}$
$M_2$	$M_2$	-	-	$\frac{\Omega_2 R_{el}}{\Lambda_1^2 Q_{el} \omega}$
$K_1$	$\frac{c_{33}^E A r}{t_p}$	-	-	$\frac{\Omega_1^2 \Omega_2 U_2^2 R_{el} \omega}{\Lambda_1^2 U_1^2 Q_{el}}$
$K_2$	$\frac{c_{33}^E A r}{t_p}$	-	-	$\frac{\Omega_2^3 R_{el} \omega}{\Lambda_1^2 Q_{el}}$
$D_1$	$D_1$	-	-	$2\zeta_1 \frac{\Omega_1 \Omega_2 U_2^2 R_{el}}{\Lambda_1^2 U_1^2 Q_{el}}$
$D_2$	$D_2$	-	-	$2\zeta_2 \frac{\Omega_2^2 R_{el}}{\Lambda_1^2 Q_{el}}$
$C_o$	$\frac{e_{33}^E A_r}{t_p}$	-	-	$\frac{Q_{el}}{\Omega_2 R_{eq} \omega}$
$\frac{A}{\sqrt{K_1 C_{in}}}$	$\frac{e_{33}^E}{\sqrt{c_{33}^E c_{33}^E}}$	-	-	$\alpha_1$
$\frac{A}{\sqrt{K_2 C_o}}$	$\frac{e_{33}^E}{\sqrt{c_{33}^E c_{33}^E}}$	-	-	$\alpha_2$
-	-	$M_{a1}$	$\frac{\pi R^2}{\rho l}$	$\frac{\Omega_2 U_2^2 R_{el}}{\Lambda_1^2 O_1^2 Q_{el} \omega}$
-	-	$N_{a1}$	$\frac{Vol}{C_L^2 \rho}$	$\frac{\Lambda_1^2 Q_{el}}{\Omega_2 U_2^2 R_{el} \omega}$
-	-	$Z_{a1}$	$\frac{\pi R^4}{8\mu_L l}$	$\frac{\Omega_2 U_2^2 R_{el}}{\Lambda_1^2 O_1 Q_a Q_{el}}$
-	-	-	$\frac{\pi r^2}{\pi R^2}$	$\gamma_1$
-	-	-	$\frac{\pi r^2}{\pi R^2}$	$\gamma_2$

An important question related to the normalized model is: how the normalized gain curves can be used to design an electro-mechanical-acoustic CET system? The idea is that, by considering an application that requires some specifications, it is possible to use the normalized curves to determine which are the possible system's configurations that result on the project requirements.

For example, let us consider an application in which it is desirable to transfer energy through a cylindrical aluminium media and it is aimed to find the length and the diameter of the media and, the mass, the stiffness, the dampers and the capacitances of the piezoelectric transducers. The specifications for the example are described in Table 3.8.

Table 3.8 – Design specifications for the example of denormalization procedure.

Parameter	Value
Input voltage, $V_{in}$	13 V (peak-to-peak)
Output voltage, $V_o$	8 V (peak-to-peak)
Output power, $P_o$	500 mW
Operating frequency, $f$	800 kHz
Piezoelectric component radius, $r$	0.01 m
Aluminium density, $\rho$	2710 kg · m <sup>-3</sup>
Wave velocity, $C_L$	6300 m · s <sup>-1</sup>
Friction coefficient, $\mu_L$	1.2 m · Pa s

Source: (ROSE, 2014; CHENG et al., 2014).

The targets are:

- Find a suitable normalized gain curve for the required voltage transfer;
- Find the required transfer media geometry, length  $l$  and radius  $R$ ;
- Find the piezoelectric mass  $M_1$  and  $M_2$ ;
- Find the piezoelectric stiffness  $K_1$  and  $K_2$ ;
- Find the piezoelectric dampers  $D_1$  and  $D_2$ ;
- Find the piezoelectric capacitances  $C_{in}$  and  $C_o$ .

For this example, the normalized gain curve depicted in Figure 3.15 is going to be used. The gain curve relates the voltage gain to the normalized operating frequency. The operating frequency is the AC input source frequency that drives the piezoelectric transmitter.

**Step 1:** Calculate the required gain.

First, it is necessary to calculate the required gain based on the specifications as

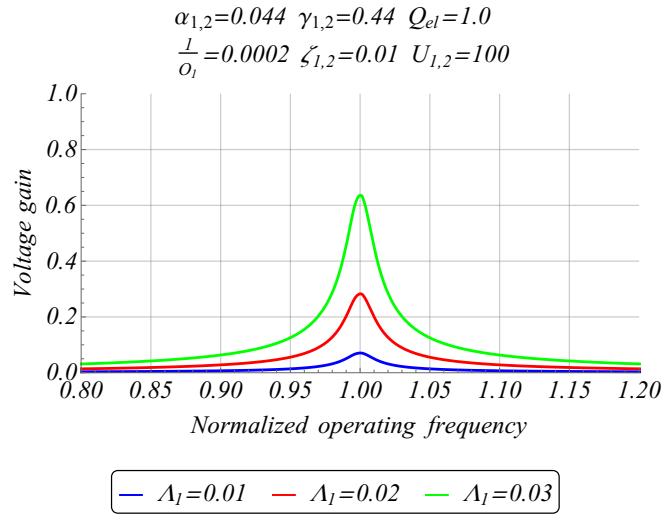
$$Gain = \frac{V_o}{V_{in}} = 0.615. \quad (3.141)$$

**Step 2:** Calculate output load.

The output load  $R_{eq}$  can be calculate based on the output voltage and power:

$$R_{eq} = \frac{V_{rms}^2}{P_o} = 16 \Omega. \quad (3.142)$$

Figure 3.15 – Voltage gain as function of normalized operating frequency.



Source: Author.

**Step 3:** Find the unit-less parameters on the normalized gain curve.

Based on the gain, it is necessary to look at the normalized gain curve, in this case, shown in Figure 3.15, and choose the set of unit-less parameters that ensures the required gain.

In Figure 3.15, it is shown the voltage gain as function of the normalized operating frequency for different values of  $\Lambda_1$  and fixed values of  $\alpha_{1,2}$ ,  $\gamma_{1,2}$ ,  $Q_{el}$ ,  $1/O_1$ ,  $\zeta_{1,2}$  and  $U_{1,2}$ . The only curve that can achieve the required gain is the curve related to  $\Lambda_1 = 0.03$  (green). In addition, it is necessary to select the frequency for the desired gain, in this case, it is close to 1.00. This means that  $\Omega_{1,2} = 1.0$  because the system's predominant frequency can be set as the piezoelectric transducers frequency ( $\Omega_{1,2}$ ).

**Step 4:** Calculate the radius of the transfer media.

By knowing the mechanical-acoustic and acoustic-mechanical coupling factors,  $\gamma_1$  and  $\gamma_2$ , it is possible to calculate the radius of the cylindrical aluminium media based on the relation between transfer media and unit-less in the last two equations in Table 3.7:

$$R = \sqrt{\frac{\pi r^2}{\pi \gamma_{1,2}}} = 0.015 \text{ m.} \quad (3.143)$$

**Step 5:** Calculate the length of the transfer media.

The length  $l$  of the transfer media can be calculated based on relation between

transfer media and unit-less related to the equivalent acoustical mass  $M_{a1}$  in Table 3.7:

$$l = \frac{\pi R^2 \Lambda_1^2 O_1^2 Q_{el} \omega}{\rho \Omega_2 U_2^2 R_{eq}} = 0.18 \text{ m}, \quad (3.144)$$

in which,  $\omega = 2\pi f$ .

**Step 6:** Calculate mechanical mass  $M_1$  and  $M_2$ .

The piezoelectric components mass can be calculated based on the two first equations in Table 3.7:

$$M_1 = \frac{\Omega_2 U_2^2 R_{eq}}{\Lambda_1^2 U_1^2 Q_{el} \omega} = 0.00353 \text{ kg} \quad (3.145)$$

and

$$M_2 = \frac{\Omega_2 R_{eq}}{\Lambda_1^2 Q_{el} \omega} = 0.00353 \text{ kg}. \quad (3.146)$$

**Step 7:** Calculate the mechanical stiffness  $K_1$  and  $K_2$ .

$$K_1 = \frac{\Omega_1^2 \Omega_2 U_2^2 R_{el} \omega}{\Lambda_1^2 U_1^2 Q_{el}} = 8.93 \times 10^{10} \text{ N} \cdot \text{m}^{-1} \quad (3.147)$$

and

$$K_2 = \frac{\Omega_2^3 R_{el} \omega}{\Lambda_1^2 Q_{el}} = 8.93 \times 10^{10} \text{ N} \cdot \text{m}^{-1}. \quad (3.148)$$

**Step 8:** Calculate the mechanical dampers  $D_1$  and  $D_2$ .

$$D_1 = 2\zeta_1 \frac{\Omega_1 \Omega_2 U_2^2 R_{el}}{\Lambda_1^2 U_1^2 Q_{el}} = 355.556 \text{ N} \cdot \text{s} \cdot \text{m}^{-1} \quad (3.149)$$

and

$$D_2 = 2\zeta_2 \frac{\Omega_2^2 R_{el}}{\Lambda_1^2 Q_{el}} = 355.556 \text{ N} \cdot \text{s} \cdot \text{m}^{-1}. \quad (3.150)$$

**Step 9:** Calculate the capacitances  $C_{in}$  and  $C_o$ . Finally, the piezoelectric capacitances are calculated as:

$$C_{in,o} = \frac{Q_{el}}{\Omega_2 R_{eq} \omega} = 12 \text{ nF}. \quad (3.151)$$

The designed system in the proposed example is summarized in Table 3.9:

Table 3.9 – Designed system based on the normalized model.

Parameter	Value
Input voltage, $V_{in}$	13 V (peak-to-peak)
Output voltage, $V_o$	8 V (peak-to-peak)
Output power, $P_o$	500 mW
Load, $R_{eq}$	16 $\Omega$
Operating frequency, $f$	800 kHz
Transfer media length, $l$	0.18 m
Transfer media radius, $R$	0.015 m
Piezoelectric component radius, $r$	0.01 m
Piezoelectric mass, $M_{1,2}$	0.00353 kg
Piezoelectric stiffness, $K_{1,2}$	$8.93 \times 10^{10} \text{ N} \cdot \text{m}^{-1}$
Piezoelectric dampers, $D_{1,2}$	$355.556 \text{ N} \cdot \text{s} \cdot \text{m}^{-1}$
Piezoelectric capacitances, $C_{in,o}$	12 nF

The system can also be designed considering additional normalized gain curves. In addition, it is possible to find other parameters rather than the ones mentioned in the example. For instance, the piezoelectric parameters can be used as input while the material (density and wave velocity), length and radius of the transfer media can be set as target to be found based on the unit-less parameters in the normalized gain curves.

The normalized model allows the normalized gain curves as design charts, which leads to a high flexibility regarding the system's design flow. In other words, it is a useful tool when the general behavior of the system is known but it is difficult to know in advance, all the real parameters of the system.

### 3.9 CONCLUSION

In this chapter, the modeling of the electro-mechanical-acoustic CET system was presented. The proposed model is based on multiphysics networks. In a first moment, the main building blocks were presented, which are lumped components that represent the elements of acoustical, electrical and mechanical systems.

The proposed analytical model was analyzed by means of a state-space representation based on the Kirchhoff's Circuit Laws and the Newton's Laws of Motion. The model includes the properties of the piezoelectric transducers and the geometry and properties of the material of the transfer media.

A decomposition into unit-less parameters for multiphysics networks was proposed in this chapter. Axioms were described in order to define the rules to extract the unit-less parameters based on the multiphysical representation of the system. The normalized model based on unit-less parameters is able to show the behavior of the system independently of specifications, such as input voltage, power, output voltage and operating frequency, and independently of the real system parameters. In this sense, several normalized gain curves were presented in this chapter.

An equivalent electrical model was introduced, which is suitable for SPICE simulation. In addition, a model based on a piezoelectric transformer was presented and compared to the other models.

In this chapter, an augmented-order multiphysical model based on lumped parameters was provided. The idea is to increase the order of the system aiming to obtain a higher degree of freedom that enables to amplify or attenuate parts of the system's frequency response. Finally, relationships among unit-less, electromechanical, piezoelectric, acoustical and transfer media parameters were developed.

## 4 ANALYSIS AND DESIGN OF THE MULTIPHYSICAL SYSTEM BASED ON RESONANT TOPOLOGIES

In this Chapter, the analysis and design of the multiphysical system based on resonant topologies are going to be presented. The idea is that the electro-mechanical-acoustic CET system is an electrical two-port system in which an AC signal supplies the ultrasound transmitter and an AC signal is generated from the ultrasound receiver. In this sense, an inverter can be used to generate the AC signal for the transmitter and a rectifier can be used to adequate the AC signal from the receiver in order to obtain a DC signal to supply a load. As long as the inverter's input is a DC source, the overall system is a DC-DC converter in which an AC-AC conversion is also performed. In other words, the system can be understood as a DC-AC-AC-DC converter (indirect DC-DC converter).

As shown in the previous chapter, the system can be represented by lumped components. This means that they can be also converted into equivalent electrical components that can be connected to the inverter and the rectifier. The matching among the multiphysical, electrical and piezoelectric transformer models allows to represent the system by any of these models.

The piezoelectric transformer model has the disadvantage of omitting the real system parameters for the mechanical and acoustical domains. However, it is suitable to be connected to other electrical systems due to its low amount of components when compared to the multiphysical model.

Resonant converters are interesting in such applications because the piezoelectric transformer model derived from the multiphysics network can be used as part of the resonant tank. Furthermore, the resonant topologies can achieve high efficiency by means of soft-switching operation conditions.

This Chapter proposes an approach to represent the electro-mechanical-acoustic CET system based on resonant topologies. After achieving the equivalent electrical representation based on the DC-DC topology, the Class-E<sup>2</sup> converter is analyzed by means of the normalized state-space models based on unit-less parameters. In addition to the resonant topologies, voltage multipliers are also considered. Notably, the Cockcroft-Walton AC-DC multiplier is an interesting solution to be used as rectifier.

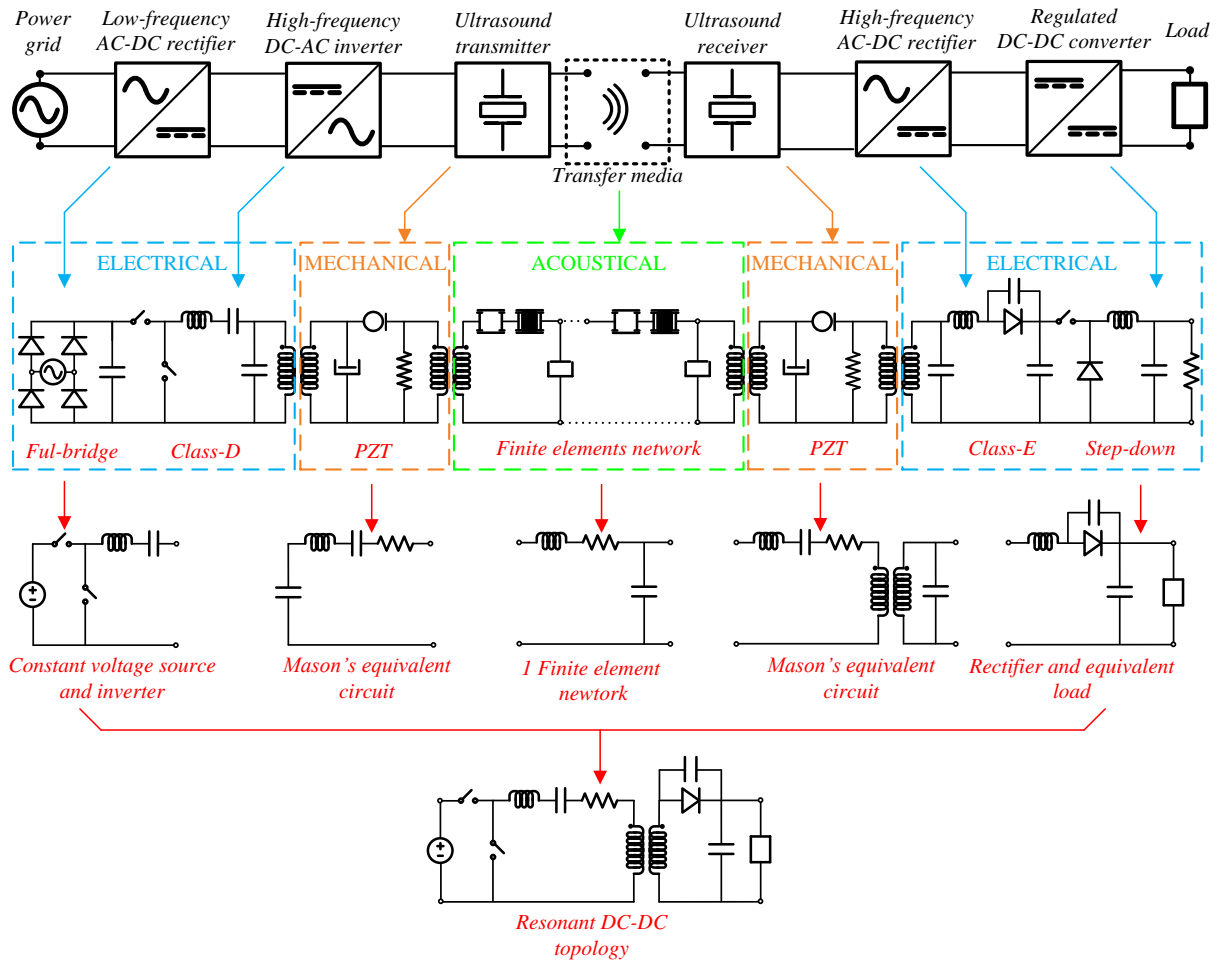
### 4.1 ELECTRO-MECHANICAL-ACOUSTIC CET BASED ON RESONANT TOPOLOGIES

Through-wall contactless power transfer systems are composed of a piezoelectric-based transmitter that sends an acoustic wave through a solid material. A piezoelectric-

based receiver catches the signal, which must be converted into a DC signal by means of an AC-DC rectifier. A DC-AC inverter is used to supply the transmitter.

Considering a grid connected application, a low-frequency AC-DC rectifier can be used to supply a high-frequency DC-AC inverter. A regulated DC-DC converter can be used cascaded with the AC-DC rectifier. The electro-mechanical-acoustic contactless energy transfer system based on resonant topology is depicted in Figure 4.1.

Figure 4.1 – Multiphysics network connected to resonant power conversion systems.



Source: Author.

The general block diagram is converted into a circuit topology representation. For instance, the low-frequency AC-DC rectifier is replaced by a full-bridge rectifier. There are many possibilities for the DC-AC inverter, like as Class-D, Class-E and full-bridge topologies, which can include the resonant tanks: LLC, LCL, LCLC, and so on. Also, resonant topologies can be used for the AC-DC rectifier. Notwithstanding, voltage multipliers are interesting for some applications. For example, the Cockcroft-Walton multiplier can provide DC output voltage based on small AC input voltage. The resonant topologies have the advantage of operation in soft-switching conditions, like as zero-voltage/current



(ZVS/ZCS) and zero-derivative (ZDS) switching (KAZIMIERCZUK; JOZWIK, 1989; KAZIMIERCZUK; CZARKOWSKI, 1995)

In Figure 4.1, the full-bridge rectifier, the Class-D resonant inverter and the Class-E ZVS resonant rectifier are shown as example of topologies that can be used as power conversion circuits for the system. Furthermore, the ultrasound transmitter and receiver have piezoelectric components as part of their structures. The piezoelectric component is an electro-mechanical device that can be represented by lumped components, as well as the acoustical domain represented by the finite elements network.

As mentioned before, the three domains are used to represent the system: electrical, mechanical and acoustical. This work resorts to a model based on lumped components. As long as the system has an electrical DC input and an electrical DC output (by disregarding the grid connection), and considering that the interface between electrical and mechanical domains is based on AC waveforms, resonant converters are suitable as topological representation for the system. However, it is necessary to include the mechanical and acoustical domains combined with the resonant DC-AC and the resonant AC-DC parts. In this sense, the mechanical and acoustical lumped components are converted into electrical components.

The mechanical part of the piezoelectric component can be converted into a Mason's equivalent circuit. The acoustical components have analogies with the electrical components, which allows to represent the acoustical part as an equivalent electrical circuit. The regulated DC-DC converter can be represented as an equivalent load for the system. These assumptions are shown in Figure 4.1.

The goal is to analytically analyze the system in order to design the power conversion circuitry that is compatible with the electro-mechanical-acoustic CET system. The parameters of the multiphysical system are calculated based on the piezoelectric transformer model shown in the previous Chapter.

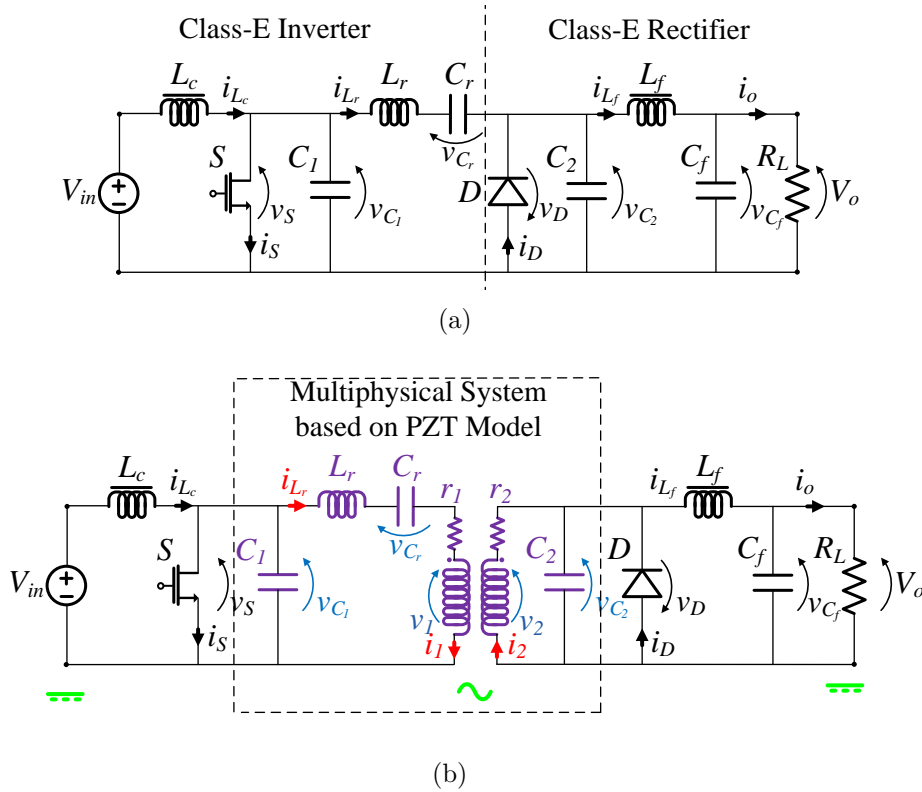
It is interesting to analyze the system independently of the real system parameters. It is because, by changing the system properties, like as transfer media, transducers type and frequency, the equivalent parameters change. Therefore, this work analyzes the system by developing its normalized state-space model, which is independent of specifications and real system parameters. Subsequently, the power conversion circuitry can be designed by setting design specifications.

## 4.2 CLASS-E<sup>2</sup> RESONANT CONVERTER

The topology under study in this section is the Class-E<sup>2</sup> resonant converter. By cascading a Class-E resonant DC-AC inverter to a Class-E resonant AC-DC rectifier, the Class-E<sup>2</sup> is obtained, which is shown in Figure 4.2(a) (KAZIMIERCZUK; JOZWIK, 1989;

JOZWIK; KAZIMIERCZUK, 1990). By including the multiphysical system based on the piezoelectric transformer model (PZT model), the electro-mechanical-acoustic contactless energy transfer system driven by a resonant power conversion circuit is achieved, which is shown in Figure 4.2(b). The symbol for the switch  $S$  represents a general switch. However, in practical implementation, the switch must include the anti-parallel diode.

Figure 4.2 – Class- $E^2$  resonant power conversion system. (a) Class- $E^2$  resonant converter. (b) Electro-mechanical-acoustic CET system based on Class- $E^2$  topology.



Source: Author.

The interesting aspect of such representation is that, it is possible to design a suitable rectifier circuit that considers the behavior of the electro-mechanical-acoustic CET system. The converter in Figure 4.2 is composed of: input voltage source  $V_{in}$ , choke inductor  $L_c$ , switch  $S$ , inverter capacitor  $C_1$ , resonant inductor  $L_r$ , resonant capacitor  $C_r$ , rectifier capacitor  $C_2$ , output filter inductor  $L_f$ , output filter capacitor  $C_f$  and load  $R_L$ . The circuit variables are described as:  $i_{L_c}$ , inductor  $L_c$  current;  $i_S$ , switch  $S$  current;  $i_{L_r}$ , inductor  $L_r$  current;  $i_D$ , diode  $D$  current;  $i_{L_f}$ , inductor  $L_f$  current;  $i_o$ , output current;  $v_S$ , switch  $S$  voltage;  $v_{C_1}$ , capacitor  $C_1$  voltage;  $v_{C_r}$ , capacitor  $C_r$  voltage;  $v_D$ , diode  $D$  voltage;  $v_{C_2}$ , capacitor  $C_2$  voltage;  $v_{C_f}$ , capacitor  $C_f$  voltage and  $V_o$ , output voltage. The equivalent model of the multiphysical system includes three capacitors and one inductor that topologically match with  $C_1$ ,  $L_r$ ,  $C_r$  and  $C_2$ . As long as there is a transformation ratio, it can be represented by a transformer model which includes a resistor  $r_1$  that

matches with the resistor in the Mason's equivalent circuit. The transformer relationships are given by:

$$\alpha = \frac{v_1}{v_2} = \frac{i_2}{i_1} = \frac{n_1}{n_2} = \frac{\sqrt{L_1}}{\sqrt{L_2}}, \quad (4.1)$$

in which,  $\alpha$  is the transformation ratio related to  $n_1/n_2$  turns,  $v_1$  is the primary side voltage,  $i_1$  is the primary side current,  $v_2$  is the secondary side voltage,  $i_2$  is the secondary side current and  $L_1$  and  $L_2$  are the associated inductors.

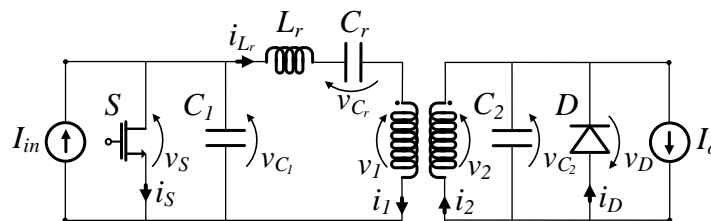
The main features of the Class-E<sup>2</sup> resonant converter are the switch  $S$  zero-voltage switching and the diode  $D$  zero-derivative voltage switching. In this sense, the modeling approach is going to be conducted by considering the following assumptions:

1. The input voltage source  $V_{in}$  and the input choke inductor  $L_c$  are replaced by a constant current source  $I_{in}$ ;
2. The output filter  $L_f - C_f$  and the load  $R_L$  are replaced by a constant current source  $I_o$ ;
3. The switch  $S$  and diode  $D$  off states are modeled as a open-circuit;
4. The switch  $S$  and diode  $D$  on states are modeled as a short-circuit;
5. The transformer is considered as an ideal component.

Assumptions 1 and 2 are useful in order to reduce the number of reactive components, which reduces the order of the system. This leads to a system that is easier to be analytically solved. Subsequently,  $V_{in}$ ,  $L_c$ ,  $L_f$ ,  $C_f$  and  $R_L$  can be retrieved from the analysis.

The model for the converter is portrayed in Figure 4.3:

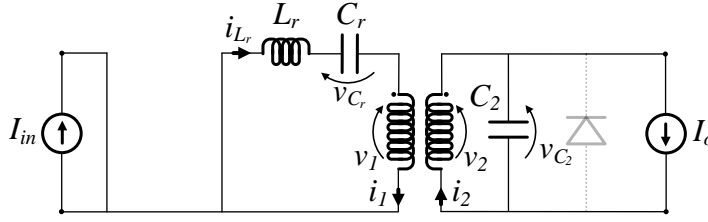
Figure 4.3 – Class-E<sup>2</sup> resonant DC-DC converter model.



Source: Author

The converter has four operating modes. Mode  $I$  occurs from 0 to  $T_1$ , being  $T_1$  the angle that the mode ends. At this mode,  $S$  is on and  $D$  is off. The circuit for mode  $I$  is shown in Figure 4.4.

Figure 4.4 – Class-E<sup>2</sup> resonant converter - Operating mode *I*: *S* on and *D* off.



Source: Author.

The converter is ruled by the following differential equations:

$$\frac{di_{L_r}(t)}{dt} = -\frac{v_{C_r}(t)}{L_r} - \alpha \frac{v_{C_2}(t)}{L_r}, \quad (4.2)$$

$$\frac{dv_{C_r}(t)}{dt} = \frac{i_{L_r}(t)}{C_r}, \quad (4.3)$$

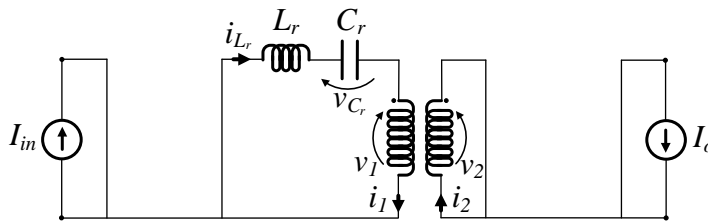
$$\frac{dv_{C_1}(t)}{dt} = 0 \quad (4.4)$$

and

$$\frac{dv_{C_2}(t)}{dt} = \alpha \frac{i_{L_r}(t)}{C_2} - \frac{I_o}{C_2}. \quad (4.5)$$

At mode *II*, *S* is on and *D* is on. The mode occurs from  $T_1$  to  $D_c 2\pi$ , being  $D_c$  the switch *S* duty cycle. The circuit is shown in Figure 4.5.

Figure 4.5 – Class-E<sup>2</sup> resonant converter - Operating mode *II*: *S* on and *D* on.



Source: Author.

The following equations are considered:

$$\frac{di_{L_r}(t)}{dt} = -\frac{v_{C_r}(t)}{L_r}, \quad (4.6)$$

$$\frac{dv_{C_r}(t)}{dt} = \frac{i_{L_r}(t)}{C_r}, \quad (4.7)$$

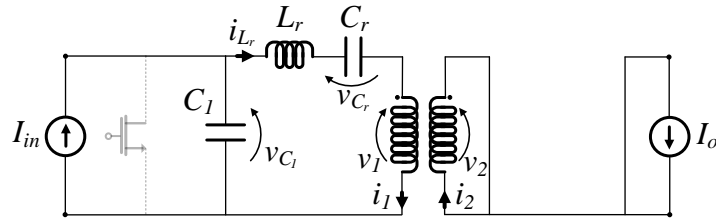
$$\frac{dv_{C_1}(t)}{dt} = 0 \quad (4.8)$$

and

$$\frac{dv_{C_2}(t)}{dt} = 0. \quad (4.9)$$

At mode *III*, *S* is off and *D* is on. The mode occurs from  $D_c 2\pi$  to  $T_2$ , being  $T_2$  the angle in which the mode ends. The circuit is shown in Figure 4.6.

Figure 4.6 – Class-E<sup>2</sup> resonant converter - Operating mode *III*: *S* off and *D* on.



Source: Author.

The converter is governed by:

$$\frac{di_{L_r}(t)}{dt} = \frac{v_{C_1}(t)}{L_r} - \frac{v_{C_r}(t)}{L_r}, \quad (4.10)$$

$$\frac{dv_{C_r}(t)}{dt} = \frac{i_{L_r}(t)}{C_r}, \quad (4.11)$$

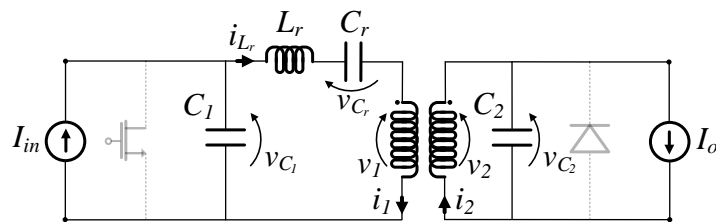
$$\frac{dv_{C_1}(t)}{dt} = \frac{I_{in}}{C_1} - \frac{i_{L_r}(t)}{C_1} \quad (4.12)$$

and

$$\frac{dv_{C_2}(t)}{dt} = 0. \quad (4.13)$$

At mode *IV*, *S* is off and *D* is off. The mode ends at  $2\pi$ . The circuit is shown in Figure 4.7.

Figure 4.7 – Class-E<sup>2</sup> resonant converter - Operating mode *IV*: *S* off and *D* off.



Source: Author.

The differential equations are:

$$\frac{di_{L_r}(t)}{dt} = \frac{v_{C_1}(t)}{L_r} - \frac{v_{C_r}(t)}{L_r} - \alpha \frac{v_{C_2}(t)}{L_r}, \quad (4.14)$$

$$\frac{dv_{C_r}(t)}{dt} = \frac{i_{L_r}(t)}{C_r}, \quad (4.15)$$

$$\frac{dv_{C_1}(t)}{dt} = \frac{I_{in}}{C_1} - \frac{i_{L_r}(t)}{C_1} \quad (4.16)$$

and

$$\frac{dv_{C_2}(t)}{dt} = \alpha \frac{i_{L_r}(t)}{C_2} - \frac{I_o}{C_2}. \quad (4.17)$$

#### 4.2.1 State-space model based on real system parameters

The system is represented as a state-space model described as:

$$\begin{aligned} \dot{\mathbf{x}}(t) &= \mathbf{A}_I \mathbf{x}(t) + \mathbf{B}_I \mathbf{u}(t), \\ \dot{\mathbf{x}}(t) &= \mathbf{A}_{II} \mathbf{x}(t) + \mathbf{B}_{II} \mathbf{u}(t), \\ \dot{\mathbf{x}}(t) &= \mathbf{A}_{III} \mathbf{x}(t) + \mathbf{B}_{III} \mathbf{u}(t), \\ \dot{\mathbf{x}}(t) &= \mathbf{A}_{IV} \mathbf{x}(t) + \mathbf{B}_{IV} \mathbf{u}(t) \end{aligned} \quad (4.18)$$

and

$$\begin{aligned} \mathbf{y}(t) &= \mathbf{C}_I \mathbf{x}(t) + \mathbf{D}_I \mathbf{u}(t), \\ \mathbf{y}(t) &= \mathbf{C}_{II} \mathbf{x}(t) + \mathbf{D}_{II} \mathbf{u}(t), \\ \mathbf{y}(t) &= \mathbf{C}_{III} \mathbf{x}(t) + \mathbf{D}_{III} \mathbf{u}(t), \\ \mathbf{y}(t) &= \mathbf{C}_{IV} \mathbf{x}(t) + \mathbf{D}_{IV} \mathbf{u}(t). \end{aligned} \quad (4.19)$$

The state vector  $\mathbf{x}(t)$  is composed of the following circuit variables

$$\mathbf{x}(t) = [\mathbf{i}_{L_r}, \mathbf{v}_{C_r}, \mathbf{v}_{C_1}, \mathbf{v}_{C_2}]^T. \quad (4.20)$$

The output vector  $\mathbf{y}(t)$  is composed of any desirable circuit variables

$$\mathbf{y}(t) = \left[ \frac{\mathbf{i}_{L_r}}{\mathbf{I}_{in}}, \frac{\mathbf{v}_{C_r}}{\mathbf{V}_{in}}, \frac{\mathbf{v}_{C_1}}{\mathbf{V}_{in}}, \frac{\mathbf{v}_{C_2}}{\mathbf{V}_{in}}, \frac{\mathbf{i}_s}{\mathbf{I}_{in}}, \frac{\mathbf{i}_D}{\mathbf{I}_{in}} \right]^T \quad (4.21)$$

and the input vector is

$$\mathbf{u}(t) = [\mathbf{I}_{in}, \mathbf{I}_o]^T. \quad (4.22)$$

Based on (4.20), (4.21) and (4.22), the state-space matrices are described by

$$\mathbf{A}_I = \begin{bmatrix} 0 & -\frac{1}{L_r} & 0 & -\frac{\alpha}{L_r} \\ \frac{1}{C_r} & 0 & 0 & 0 \\ 0 & 0 & 0 & 0 \\ \frac{\alpha}{C_2} & 0 & 0 & 0 \end{bmatrix}, \mathbf{B}_I = \begin{bmatrix} 0 & 0 \\ 0 & 0 \\ 0 & 0 \\ 0 & -\frac{1}{C_2} \end{bmatrix}, \quad (4.23)$$

$$\mathbf{A}_{II} = \begin{bmatrix} 0 & -\frac{1}{L_r} & 0 & 0 \\ \frac{1}{C_r} & 0 & 0 & 0 \\ 0 & 0 & 0 & 0 \\ 0 & 0 & 0 & 0 \end{bmatrix}, \mathbf{B}_{II} = \begin{bmatrix} 0 & 0 \\ 0 & 0 \\ 0 & 0 \\ 0 & 0 \end{bmatrix}, \quad (4.24)$$

$$\mathbf{A}_{III} = \begin{bmatrix} 0 & -\frac{1}{L_r} & \frac{1}{L_r} & 0 \\ \frac{1}{C_r} & 0 & 0 & 0 \\ -\frac{1}{C_1} & 0 & 0 & 0 \\ 0 & 0 & 0 & 0 \end{bmatrix}, \mathbf{B}_{III} = \begin{bmatrix} 0 & 0 \\ 0 & 0 \\ \frac{1}{C_1} & 0 \\ 0 & 0 \end{bmatrix}, \quad (4.25)$$

$$\mathbf{A}_{IV} = \begin{bmatrix} 0 & -\frac{1}{L_r} & \frac{1}{L_r} & -\frac{\alpha}{L_r} \\ \frac{1}{C_r} & 0 & 0 & 0 \\ -\frac{1}{C_1} & 0 & 0 & 0 \\ \frac{\alpha}{C_2} & 0 & 0 & 0 \end{bmatrix}, \mathbf{B}_{IV} = \begin{bmatrix} 0 & 0 \\ 0 & 0 \\ \frac{1}{C_1} & 0 \\ 0 & 0 \end{bmatrix}, \quad (4.26)$$

$$\mathbf{C}_I = \begin{bmatrix} \frac{1}{I_{in}} & 0 & 0 & 0 \\ 0 & \frac{1}{V_{in}} & 0 & 0 \\ 0 & 0 & \frac{1}{V_{in}} & 0 \\ 0 & 0 & 0 & \frac{1}{V_{in}} \\ -\frac{1}{I_{in}} & 0 & 0 & 0 \\ 0 & 0 & 0 & 0 \end{bmatrix}, \mathbf{D}_I = \begin{bmatrix} 0 & 0 \\ 0 & 0 \\ 0 & 0 \\ 0 & 0 \\ 0 & \frac{1}{I_{in}} \\ 0 & 0 \end{bmatrix}, \quad (4.27)$$

$$\mathbf{C}_{II} = \begin{bmatrix} \frac{1}{I_{in}} & 0 & 0 & 0 \\ 0 & \frac{1}{V_{in}} & 0 & 0 \\ 0 & 0 & \frac{1}{V_{in}} & 0 \\ 0 & 0 & 0 & \frac{1}{V_{in}} \\ -\frac{1}{I_{in}} & 0 & 0 & 0 \\ -\frac{\alpha}{I_{in}} & 0 & 0 & 0 \end{bmatrix}, \mathbf{D}_{II} = \begin{bmatrix} 0 & 0 \\ 0 & 0 \\ 0 & 0 \\ 0 & 0 \\ 0 & \frac{1}{I_{in}} \\ \frac{1}{I_{in}} & 0 \end{bmatrix}, \quad (4.28)$$

$$\mathbf{C}_{III} = \begin{bmatrix} \frac{1}{I_{in}} & 0 & 0 & 0 \\ 0 & \frac{1}{V_{in}} & 0 & 0 \\ 0 & 0 & \frac{1}{V_{in}} & 0 \\ 0 & 0 & 0 & \frac{1}{V_{in}} \\ 0 & 0 & 0 & 0 \\ -\frac{\alpha}{I_{in}} & 0 & 0 & 0 \end{bmatrix}, \mathbf{D}_{III} = \begin{bmatrix} 0 & 0 \\ 0 & 0 \\ 0 & 0 \\ 0 & 0 \\ 0 & 0 \\ \frac{1}{I_{in}} & 0 \end{bmatrix} \quad (4.29)$$

and

$$\mathbf{C}_{IV} = \begin{bmatrix} \frac{1}{I_{in}} & 0 & 0 & 0 \\ 0 & \frac{1}{V_{in}} & 0 & 0 \\ 0 & 0 & \frac{1}{V_{in}} & 0 \\ 0 & 0 & 0 & \frac{1}{V_{in}} \\ 0 & 0 & 0 & 0 \\ 0 & 0 & 0 & 0 \end{bmatrix}, \mathbf{D}_{IV} = \begin{bmatrix} 0 & 0 \\ 0 & 0 \\ 0 & 0 \\ 0 & 0 \\ 0 & 0 \\ 0 & 0 \end{bmatrix}. \quad (4.30)$$

#### 4.2.2 Normalized state-space model based on real system parameters

A new vector space  $\mathbf{e}(t)$  is defined based on the square roots of the storage energy in the reactive components

$$\mathbf{e}(t) = \begin{bmatrix} i_{L_r} \frac{\sqrt{L_r}}{\sqrt{2}} & 0 & 0 & 0 \\ 0 & v_{C_r} \frac{\sqrt{C_r}}{\sqrt{2}} & 0 & 0 \\ 0 & 0 & v_{C_1} \frac{\sqrt{C_1}}{\sqrt{2}} & 0 \\ 0 & 0 & 0 & v_{C_2} \frac{\sqrt{C_2}}{\sqrt{2}} \end{bmatrix}, \quad (4.31)$$

which leads to

$$\mathbf{P} = \mathbf{e}(t) \cdot \mathbf{x}(t) = \begin{bmatrix} \frac{\sqrt{L_r}}{\sqrt{2}} & 0 & 0 & 0 \\ 0 & \frac{\sqrt{C_r}}{\sqrt{2}} & 0 & 0 \\ 0 & 0 & \frac{\sqrt{C_1}}{\sqrt{2}} & 0 \\ 0 & 0 & 0 & \frac{\sqrt{C_2}}{\sqrt{2}} \end{bmatrix}. \quad (4.32)$$

A new input matrix is calculated as

$$\overline{\mathbf{B}}_I = \frac{1}{\omega} \mathbf{P} \mathbf{B}_I, \quad (4.33)$$

which gives

$$\overline{\mathbf{B}}_I = \begin{bmatrix} 0 & 0 \\ 0 & 0 \\ 0 & 0 \\ 0 & -\frac{1}{\sqrt{2}C_2\omega} \end{bmatrix}. \quad (4.34)$$

A correction factor  $\Gamma$  must be equated as following:

$$\Gamma = \frac{\sqrt{2}C_2\omega}{I_{in}}. \quad (4.35)$$

Matrix  $\mathbf{P}$  is equated again by means of (3.66). By using (3.70), (3.71), (3.72) and



(3.73), the new state-space model is found by:

$$\overline{\mathbf{A}}_I = \begin{bmatrix} 0 & -\frac{1}{\sqrt{L_r C_r \omega}} & 0 & -\frac{\alpha}{\sqrt{L_r C_2 \omega}} \\ \frac{1}{\sqrt{L_r C_r \omega}} & 0 & 0 & 0 \\ 0 & 0 & 0 & 0 \\ \frac{\alpha}{\sqrt{L_r C_2}} & 0 & 0 & 0 \end{bmatrix}, \overline{\mathbf{B}}_I = \begin{bmatrix} 0 & 0 \\ 0 & 0 \\ 0 & 0 \\ 0 & -\frac{1}{I_{in}} \end{bmatrix}, \quad (4.36)$$

$$\overline{\mathbf{A}}_{II} = \begin{bmatrix} 0 & -\frac{1}{\sqrt{L_r C_r}} & 0 & 0 \\ \frac{1}{\sqrt{L_r C_r}} & 0 & 0 & 0 \\ 0 & 0 & 0 & 0 \\ 0 & 0 & 0 & 0 \end{bmatrix}, \overline{\mathbf{B}}_{II} = \begin{bmatrix} 0 & 0 \\ 0 & 0 \\ 0 & 0 \\ 0 & 0 \end{bmatrix}, \quad (4.37)$$

$$\overline{\mathbf{A}}_{III} = \begin{bmatrix} 0 & -\frac{1}{\sqrt{L_r C_r}} & \frac{1}{\sqrt{L_r C_1}} & 0 \\ \frac{1}{\sqrt{L_r C_r}} & 0 & 0 & 0 \\ -\frac{1}{\sqrt{L_r C_1 \omega}} & 0 & 0 & 0 \\ 0 & 0 & 0 & 0 \end{bmatrix}, \overline{\mathbf{B}}_{III} = \begin{bmatrix} 0 & 0 \\ 0 & 0 \\ \frac{\sqrt{C_2}}{\sqrt{C_1} I_{in}} & 0 \\ 0 & 0 \end{bmatrix}, \quad (4.38)$$

$$\overline{\mathbf{A}}_{IV} = \begin{bmatrix} 0 & -\frac{1}{\sqrt{L_r C_r \omega}} & \frac{1}{\sqrt{L_r C_1 \omega}} & -\frac{\alpha}{\sqrt{L_r C_2}} \\ \frac{1}{\sqrt{L_r C_r}} & 0 & 0 & 0 \\ -\frac{1}{\sqrt{L_r C_1}} & 0 & 0 & 0 \\ \frac{\alpha}{\sqrt{L_r C_2}} & 0 & 0 & 0 \end{bmatrix}, \overline{\mathbf{B}}_{IV} = \begin{bmatrix} 0 & 0 \\ 0 & 0 \\ \frac{\sqrt{C_2}}{\sqrt{C_1} I_{in}} & 0 \\ 0 & -\frac{1}{I_{in}} \end{bmatrix}, \quad (4.39)$$

$$\overline{\mathbf{C}}_I = \begin{bmatrix} \frac{1}{\sqrt{L_r C_2 \omega}} & 0 & 0 & 0 \\ 0 & \frac{I_{in}}{V_{in} \sqrt{C_r C_2 \omega}} & 0 & 0 \\ 0 & 0 & \frac{I_{in}}{V_{in} \sqrt{C_1 C_2}} & 0 \\ 0 & 0 & 0 & \frac{I_{in}}{V_{in} C_2 \omega} \\ -\frac{1}{\sqrt{L_r C_2}} & 0 & 0 & 0 \\ 0 & 0 & 0 & 0 \end{bmatrix}, \overline{\mathbf{D}}_I = \begin{bmatrix} 0 & 0 \\ 0 & 0 \\ 0 & 0 \\ 0 & 0 \\ 0 & \frac{1}{I_{in}} \\ 0 & 0 \end{bmatrix}, \quad (4.40)$$

$$\overline{\mathbf{C}}_{II} = \begin{bmatrix} \frac{1}{\sqrt{L_r C_2 \omega}} & 0 & 0 & 0 \\ 0 & \frac{I_{in}}{V_{in} \sqrt{C_r C_2 \omega}} & 0 & 0 \\ 0 & 0 & \frac{I_{in}}{V_{in} \sqrt{C_1 C_2 \omega}} & 0 \\ 0 & 0 & 0 & \frac{I_{in}}{V_{in} C_2 \omega} \\ -\frac{1}{\sqrt{L_r C_2 \omega}} & 0 & 0 & 0 \\ -\frac{\alpha}{\sqrt{L_r C_2}} & 0 & 0 & 0 \end{bmatrix}, \overline{\mathbf{D}}_{II} = \begin{bmatrix} 0 & 0 \\ 0 & 0 \\ 0 & 0 \\ 0 & 0 \\ 0 & \frac{1}{I_{in}} \\ \frac{1}{I_{in}} & 0 \end{bmatrix}, \quad (4.41)$$

$$\overline{\mathbf{C}}_{III} = \begin{bmatrix} \frac{1}{\sqrt{L_r C_2 \omega}} & 0 & 0 & 0 \\ 0 & \frac{I_{in}}{V_{in} \sqrt{C_r C_2 \omega}} & 0 & 0 \\ 0 & 0 & \frac{I_{in}}{V_{in} \sqrt{C_1 C_2 \omega}} & 0 \\ 0 & 0 & 0 & \frac{I_{in}}{V_{in} C_2 \omega} \\ 0 & 0 & 0 & 0 \\ -\frac{\alpha}{\sqrt{L_r C_2}} & 0 & 0 & 0 \end{bmatrix}, \overline{\mathbf{D}}_{III} = \begin{bmatrix} 0 & 0 \\ 0 & 0 \\ 0 & 0 \\ 0 & 0 \\ 0 & 0 \\ \frac{1}{I_{in}} & 0 \end{bmatrix} \quad (4.42)$$

and

$$\overline{\mathbf{C}}_{IV} = \begin{bmatrix} \frac{1}{\sqrt{L_r C_2 \omega}} & 0 & 0 & 0 \\ 0 & \frac{I_{in}}{V_{in} \sqrt{C_r C_2 \omega}} & 0 & 0 \\ 0 & 0 & \frac{I_{in}}{V_{in} \sqrt{C_1 C_2 \omega}} & 0 \\ 0 & 0 & 0 & \frac{I_{in}}{V_{in} C_2 \omega} \\ 0 & 0 & 0 & 0 \\ 0 & 0 & 0 & 0 \end{bmatrix}, \overline{\mathbf{D}}_{IV} = \begin{bmatrix} 0 & 0 \\ 0 & 0 \\ 0 & 0 \\ 0 & 0 \\ 0 & 0 \\ 0 & 0 \end{bmatrix}. \quad (4.43)$$

The system is normalized in relation to the input source  $I_{in}$  and angular operating frequency  $\omega$ . As long as matrices  $\overline{\mathbf{B}}_I$ ,  $\overline{\mathbf{B}}_{II}$ ,  $\overline{\mathbf{B}}_{III}$ ,  $\overline{\mathbf{B}}_{IV}$ ,  $\overline{\mathbf{D}}_I$ ,  $\overline{\mathbf{D}}_{II}$ ,  $\overline{\mathbf{D}}_{III}$  and  $\overline{\mathbf{D}}_{IV}$  multiply the input vector  $\mathbf{u}(\omega t)$ , the term  $1/I_{in}$  can be repositioned into  $\mathbf{u}(\omega t)$

$$\mathbf{u}(\omega t) = [\mathbf{I}_{in}, \mathbf{I}_o]^T = \begin{bmatrix} \mathbf{I}_{in} & \mathbf{I}_o \\ \mathbf{I}_{in} & \mathbf{I}_{in} \end{bmatrix}^T = [\mathbf{1}, \mathbf{S}]^T. \quad (4.44)$$

It can be seen that the system has two inputs, one is the normalized input current source and the other one is the current transfer function  $S$

$$S = \frac{I_o}{I_{in}}, \quad (4.45)$$

which is related to the transfer power ratio  $T_{POT}$  and its inverse  $a$  by

$$S = \sqrt{T_{POT}} = \frac{1}{\sqrt{a}}, \quad (4.46)$$

finally

$$\mathbf{u}(\omega t) = \left[ \mathbf{1}, \frac{\mathbf{1}}{\sqrt{a}} \right]^T. \quad (4.47)$$

### 4.2.3 Normalized state-space model based on unit-less parameters

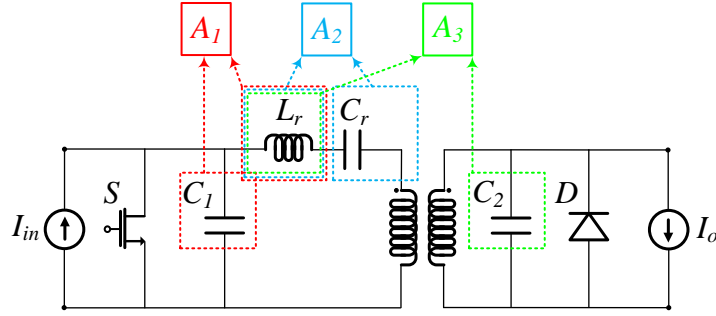
The system in the previous subsection is still dependent on the real system parameters. In order to convert the inductances, capacitances and resistances into unit-less parameters, a decomposition into unit-less parameters scheme is performed as depicted in Figure 4.8.

The resonant frequencies  $\omega_1$ ,  $\omega_2$  and  $\omega_3$  are equated as function of the reactive components as

$$\omega_1 = \frac{1}{\sqrt{L_r C_1}}, \quad (4.48)$$

$$\omega_2 = \frac{1}{\sqrt{L_r C_r}} \quad (4.49)$$

Figure 4.8 – Decomposition into unit-less parameters scheme for the Class-E<sup>2</sup> resonant converter.



Source: Author.

and

$$\omega_3 = \frac{1}{\sqrt{L_r C_2}}. \quad (4.50)$$

The normalized resonant frequencies  $A_1$ ,  $A_2$  and  $A_3$  can be obtained by dividing the resonant frequencies by the angular operating frequency  $\omega$  as

$$A_1 = \frac{\omega_1}{\omega}, \quad (4.51)$$

$$A_2 = \frac{\omega_2}{\omega} \quad (4.52)$$

and

$$A_3 = \frac{\omega_3}{\omega}. \quad (4.53)$$

Based on (4.51), (4.52) and (4.53), the terms in the state and input matrices can be converted into unit-less parameters as described as follows:

- $\frac{1}{\sqrt{L_r C_r \omega}} \xleftrightarrow{(4.49)} \frac{\omega_2}{\omega} \xleftrightarrow{(4.52)} A_2$ ;
- $\frac{\alpha}{\sqrt{L_r C_2 \omega}} \xleftrightarrow{(4.50)} \frac{\omega_3}{\omega} \xleftrightarrow{(4.53)} \alpha A_3$ ;
- $\frac{1}{\sqrt{L_r C_1 \omega}} \xleftrightarrow{(4.48)} \frac{\omega_1}{\omega} \xleftrightarrow{(4.51)} A_1$ ;
- $\frac{\sqrt{C_2}}{\sqrt{C_1}} \times \frac{\sqrt{L_r \omega}}{\sqrt{L_r \omega}} \xleftrightarrow{(4.48), (4.50)} \frac{\sqrt{L_r C_2 \omega}}{\sqrt{L_r C_1 \omega}} \xleftrightarrow{(4.48), (4.50)} \frac{\omega_1}{\omega_3} \xleftrightarrow{(4.51), (4.53)} \frac{A_1}{A_3}$ .

In order to convert the terms of the transmission and output matrices, the input to output relationship is used as

$$a = \frac{V_{in}}{I_{in} R_L}. \quad (4.54)$$

Furthermore, the circuit quality factor can be equated as function of the reactive components by

$$Q_L = \frac{R_L}{\omega_3 L_r} = \omega_3 C_2 R_L. \quad (4.55)$$

The terms are converted into unit-less parameters as follows:

- $\frac{I_{in}}{\sqrt{C_r C_2} V_{in} \omega} \xleftrightarrow{\times \frac{L_r}{L_r}} \frac{L_r I_{in}}{\sqrt{L_r C_r} \sqrt{L_2 C_r} V_{in} \omega} \stackrel{(4.49), (4.50), (4.54)}{\iff} \frac{L_r \omega_3 \omega_2}{a R_L \omega} \stackrel{(4.55), (4.52)}{\iff} \frac{A_2}{a Q_L};$
- $\frac{I_{in}}{\sqrt{C_1 C_2} V_{in} \omega} \xleftrightarrow{\times \frac{L_r}{L_r}} \frac{L_r I_{in}}{\sqrt{L_r C_1} \sqrt{L_2 C_r} V_{in} \omega} \stackrel{(4.48), (4.50), (4.54)}{\iff} \frac{L_r \omega_3 \omega_2}{a R_L \omega} \stackrel{(4.55), (4.51)}{\iff} \frac{A_1}{a Q_L};$
- $\frac{I_{in}}{C_2 V_{in} \omega} \stackrel{(4.54)}{\iff} \frac{1}{C_2 a R_L \omega} \xleftrightarrow{\times \frac{\omega_3}{\omega_3}} \frac{\omega_3}{C_2 a R_L \omega_3} \stackrel{(4.55), (4.53)}{\iff} \frac{A_3}{a Q_L}.$

The system can be represented by a normalized state-space model based on unit-less parameters described as:

$$\begin{aligned} \dot{\mathbf{e}}(\omega t) &= \overline{\mathbf{E}}_I \mathbf{e}(\omega t) + \overline{\mathbf{F}}_I \mathbf{u}(\omega t), \\ \dot{\mathbf{e}}(\omega t) &= \overline{\mathbf{E}}_{II} \mathbf{e}(\omega t) + \overline{\mathbf{F}}_{II} \mathbf{u}(\omega t), \\ \dot{\mathbf{e}}(\omega t) &= \overline{\mathbf{E}}_{III} \mathbf{e}(\omega t) + \overline{\mathbf{F}}_{III} \mathbf{u}(\omega t), \\ \dot{\mathbf{e}}(\omega t) &= \overline{\mathbf{E}}_{IV} \mathbf{e}(\omega t) + \overline{\mathbf{F}}_{IV} \mathbf{u}(\omega t) \end{aligned} \quad (4.56)$$

and

$$\begin{aligned} \mathbf{y}(\omega t) &= \overline{\mathbf{G}}_I \mathbf{e}(\omega t) + \overline{\mathbf{H}}_I \mathbf{u}(\omega t), \\ \mathbf{y}(\omega t) &= \overline{\mathbf{G}}_{II} \mathbf{e}(\omega t) + \overline{\mathbf{H}}_{II} \mathbf{u}(\omega t), \\ \mathbf{y}(\omega t) &= \overline{\mathbf{G}}_{III} \mathbf{e}(\omega t) + \overline{\mathbf{H}}_{III} \mathbf{u}(\omega t), \\ \mathbf{y}(\omega t) &= \overline{\mathbf{G}}_{IV} \mathbf{e}(\omega t) + \overline{\mathbf{H}}_{IV} \mathbf{u}(\omega t), \end{aligned} \quad (4.57)$$

in which,

$$\overline{\mathbf{E}}_I = \begin{bmatrix} 0 & -A_2 & 0 & -\alpha A_3 \\ A_2 & 0 & 0 & 0 \\ 0 & 0 & 0 & 0 \\ \alpha A_3 & 0 & 0 & 0 \end{bmatrix}, \overline{\mathbf{F}}_I = \begin{bmatrix} 0 & 0 \\ 0 & 0 \\ 0 & 0 \\ 0 & -1 \end{bmatrix}, \quad (4.58)$$

$$\overline{\mathbf{E}}_{II} = \begin{bmatrix} 0 & -A_2 & 0 & 0 \\ A_2 & 0 & 0 & 0 \\ 0 & 0 & 0 & 0 \\ 0 & 0 & 0 & 0 \end{bmatrix}, \overline{\mathbf{F}}_{II} = \begin{bmatrix} 0 & 0 \\ 0 & 0 \\ 0 & 0 \\ 0 & 0 \end{bmatrix}, \quad (4.59)$$

$$\overline{\mathbf{E}}_{III} = \begin{bmatrix} 0 & -A_2 & A_1 & 0 \\ A_2 & 0 & 0 & 0 \\ -A_1 & 0 & 0 & 0 \\ 0 & 0 & 0 & 0 \end{bmatrix}, \overline{\mathbf{F}}_{III} = \begin{bmatrix} 0 & 0 \\ 0 & 0 \\ \frac{A_1}{A_3} & 0 \\ 0 & 0 \end{bmatrix}, \quad (4.60)$$

$$\overline{\mathbf{E}}_{IV} = \begin{bmatrix} 0 & -A_2 & A_1 & -\alpha A_3 \\ A_2 & 0 & 0 & 0 \\ -A_1 & 0 & 0 & 0 \\ \alpha A_3 & 0 & 0 & 0 \end{bmatrix}, \overline{\mathbf{F}}_{IV} = \begin{bmatrix} 0 & 0 \\ 0 & 0 \\ \frac{A_1}{A_3} & 0 \\ 0 & -1 \end{bmatrix}, \quad (4.61)$$

$$\overline{\mathbf{G}}_I = \begin{bmatrix} A_3 & 0 & 0 & 0 \\ 0 & \frac{A_2}{aQ_L} & 0 & 0 \\ 0 & 0 & \frac{A_1}{aQ_L} & 0 \\ 0 & 0 & 0 & \frac{A_3}{aQ_L} \\ -A_3 & 0 & 0 & 0 \\ 0 & 0 & 0 & 0 \end{bmatrix}, \overline{\mathbf{H}}_I = \begin{bmatrix} 0 & 0 \\ 0 & 0 \\ 0 & 0 \\ 0 & 0 \\ 0 & 1 \\ 0 & 0 \end{bmatrix}, \quad (4.62)$$

$$\overline{\mathbf{G}}_{II} = \begin{bmatrix} A_3 & 0 & 0 & 0 \\ 0 & \frac{A_2}{aQ_L} & 0 & 0 \\ 0 & 0 & \frac{A_1}{aQ_L} & 0 \\ 0 & 0 & 0 & \frac{A_3}{aQ_L} \\ -A_3 & 0 & 0 & 0 \\ -\alpha A_3 & 0 & 0 & 0 \end{bmatrix}, \overline{\mathbf{H}}_{II} = \begin{bmatrix} 0 & 0 \\ 0 & 0 \\ 0 & 0 \\ 0 & 0 \\ 0 & 1 \\ 1 & 0 \end{bmatrix}, \quad (4.63)$$

$$\overline{\mathbf{G}}_{III} = \begin{bmatrix} A_3 & 0 & 0 & 0 \\ 0 & \frac{A_2}{aQ_L} & 0 & 0 \\ 0 & 0 & \frac{A_1}{aQ_L} & 0 \\ 0 & 0 & 0 & \frac{A_3}{aQ_L} \\ 0 & 0 & 0 & 0 \\ -A_3 & 0 & 0 & 0 \end{bmatrix}, \overline{\mathbf{H}}_{III} = \begin{bmatrix} 0 & 0 \\ 0 & 0 \\ 0 & 0 \\ 0 & 0 \\ 0 & 0 \\ 1 & 0 \end{bmatrix} \quad (4.64)$$

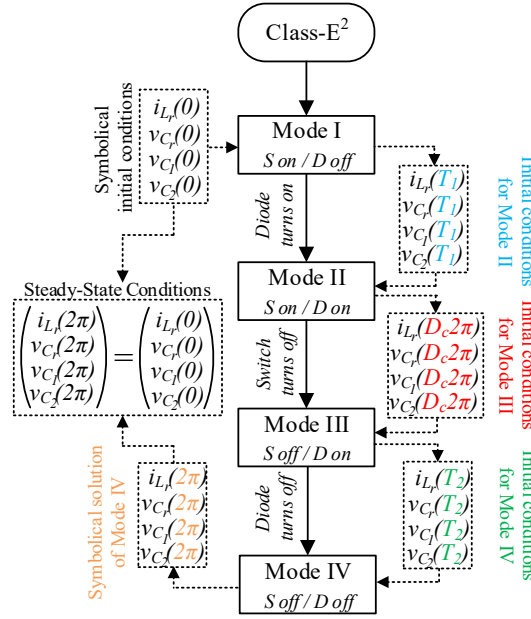
and

$$\overline{\mathbf{G}}_{IV} = \begin{bmatrix} A_3 & 0 & 0 & 0 \\ 0 & \frac{A_2}{aQ_L} & 0 & 0 \\ 0 & 0 & \frac{A_1}{aQ_L} & 0 \\ 0 & 0 & 0 & \frac{A_3}{aQ_L} \\ 0 & 0 & 0 & 0 \\ 0 & 0 & 0 & 0 \end{bmatrix}, \overline{\mathbf{H}}_{IV} = \begin{bmatrix} 0 & 0 \\ 0 & 0 \\ 0 & 0 \\ 0 & 0 \\ 0 & 0 \\ 0 & 0 \end{bmatrix}. \quad (4.65)$$

By symbolically solving the state-space representation for each operating mode ( $i = I, II, III, IV$ ), steady-state solutions can be achieved. An algorithm is proposed to solve the system, which is depicted as a flowchart in Figure 4.9.

In order to solve mode  $I$ , symbolical initial conditions are used as: initial resonant inductor current  $i_{L_r}(0)$ , initial resonant capacitor voltage  $v_{C_r}(0)$ , initial capacitor  $C_1$  voltage  $v_{C_1}(0)$  and initial rectifier capacitor  $C_2$  voltage  $v_{C_2}(0)$ . By solving mode  $I$ , one equation for each state variable is found, which are dependent of the unit-less parameters

Figure 4.9 – Flowchart to solve the Class-E<sup>2</sup> resonant DC-DC converter model.



Source: Author.

and as function of  $\omega t$ . By replacing  $\omega t$  by  $T_1$ , which represents the end of mode *I*, the initial conditions to solve mode *II* are achieved and can be described by  $i_{L_r}(T_1)$ ,  $v_{C_r}(T_1)$ ,  $v_{C_1}(T_1)$  and  $v_{C_2}(T_2)$ . By solving mode *II* and replacing  $\omega t$  by  $D_c 2\pi$ , which characterizes the end of mode *II*, the initial conditions for mode *III* are set as  $i_{L_r}(D_c 2\pi)$ ,  $v_{C_r}(D_c 2\pi)$ ,  $v_{C_1}(D_c 2\pi)$  and  $v_{C_2}(D_c 2\pi)$ . The same concept is used for mode *III*, which ends at  $T_2$ , being  $i_{L_r}(T_2)$ ,  $v_{C_r}(T_2)$ ,  $v_{C_1}(T_2)$  and  $v_{C_2}(T_2)$  the initial conditions to solve mode *IV*. The last operating mode ends at  $2\pi$ , which leads to the final conditions described as  $i_{L_r}(2\pi)$ ,  $v_{C_r}(2\pi)$ ,  $v_{C_1}(2\pi)$  and  $v_{C_2}(2\pi)$ . The aforementioned symbolical solutions are dependent of nine parameters  $A_1$ ,  $A_2$ ,  $A_3$ ,  $a$ ,  $D_c$ ,  $i_{L_r}(0)$ ,  $v_{C_r}(0)$ ,  $v_{C_1}(0)$  and  $v_{C_2}(0)$ . By equating the final conditions as equal to the initial conditions (steady-state condition), a linear system composed of four equations can be evaluated. In order to ensure the soft-switching operation of both switch *S* and diode *D*, the zero-voltage switching conditions must be addressed to the linear system. When the switch *S* turns on at  $2\pi$ , the capacitor  $C_1$  voltage is 0 and the input current  $I_{in}$  is equal to the resonant current  $i_{L_r}$ . When the diode turns off at  $T_2$ , the capacitor  $C_2$  voltage and its derivative are 0. The following steady-state and soft-switching conditions are considered:  $i_{L_r}(2\pi) = i_{L_r}(0)$  (steady-state condition),  $v_{C_r}(2\pi) = v_{C_r}(0)$  (steady-state condition),  $v_{C_1}(2\pi) = 0$  (switch *S* ZVS condition),  $v_{C_2}(2\pi) = v_{C_2}(0)$  (steady-state condition),  $i_{L_r}(2\pi) = I_{in}$  (switch *S* ZVS condition),  $v_{C_2}(T_2) = 0$  (diode *D* ZDVS condition) and  $i_{L_r}(T_2) = 1/\alpha I_o$  (diode *D* ZDVS condition).

The inherent system condition for capacitor  $C_1$  voltage simplifies the linear system

by equating  $v_{C_1}(0) = 0$ . Based on that, the following linear system is equated:

$$\begin{pmatrix} i_{L_r}(2\pi)_{[A_1, A_2, A_3, i_{L_r}(0), v_{C_r}(0), v_{C_2}(0), D_c, T_1, T_2, a]} \\ v_{C_r}(2\pi)_{[A_1, A_2, A_3, i_{L_r}(0), v_{C_r}(0), v_{C_2}(0), D_c, T_1, T_2, a]} \\ v_{C_1}(2\pi)_{[A_1, A_2, A_3, i_{L_r}(0), v_{C_r}(0), v_{C_2}(0), D_c, T_1, T_2, a]} \\ v_{C_2}(2\pi)_{[A_1, A_2, A_3, i_{L_r}(0), v_{C_r}(0), v_{C_2}(0), D_c, T_1, T_2, a]} \\ i_{L_r}(2\pi)_{[A_1, A_2, A_3, i_{L_r}(0), v_{C_r}(0), v_{C_2}(0), D_c, T_1, T_2, a]} \\ v_{C_2}(T_2)_{[A_1, A_2, A_3, i_{L_r}(0), v_{C_r}(0), v_{C_2}(0), D_c, T_1, T_2, a]} \\ i_{L_r}(T_2)_{[A_1, A_2, A_3, i_{L_r}(0), v_{C_r}(0), v_{C_2}(0), D_c, T_1, T_2, a]} \end{pmatrix} = \begin{pmatrix} i_{L_r}(0) \\ v_{C_r}(0) \\ 0 \\ v_{C_2}(0) \\ \frac{1}{A_3} \\ 0 \\ \frac{1}{\alpha A_3 \sqrt{a}} \end{pmatrix} \quad (4.66)$$

The system has 7 equations and 10 variables. In this case, a parameter sweep can be performed in duty cycle  $D_c$ , and by defining two variables, like as  $A_2$  and  $A_3$ , the system can be solved. By varying  $D_c$ , the system can be solved and the soft-switching conditions can be ensured for any operating point.

In order to calculate  $Q_L$ , the output voltage must be considered. The DC output voltage is equal to the average value of the capacitor  $C_2$  voltage. In this case, the fourth term on (4.21) should be evaluated as:

$$\frac{V_o}{V_{in}} = \frac{1}{2\pi} \int_0^{2\pi} \mathbf{y}_4(\omega t) d\omega t. \quad (4.67)$$

The solution of (4.67) is dependent of  $Q_L$  and a constant  $C$ . This allows the following relationships by considering  $S = 1/\sqrt{a}$ :

$$\begin{aligned} \frac{V_o}{V_{in}} = \frac{1}{2\pi} \int_0^{2\pi} \mathbf{y}_4(\omega t) d\omega t &\iff \frac{V_o}{V_{in}} = CQ_L \iff \frac{V_o I_o I_{in}}{V_{in} I_o I_{in}} = CQ_L \\ &\iff \frac{R_L}{R_{in}} S = CQ_L \iff \frac{1}{a\sqrt{a}} = CQ_L, \end{aligned} \quad (4.68)$$

which leads to

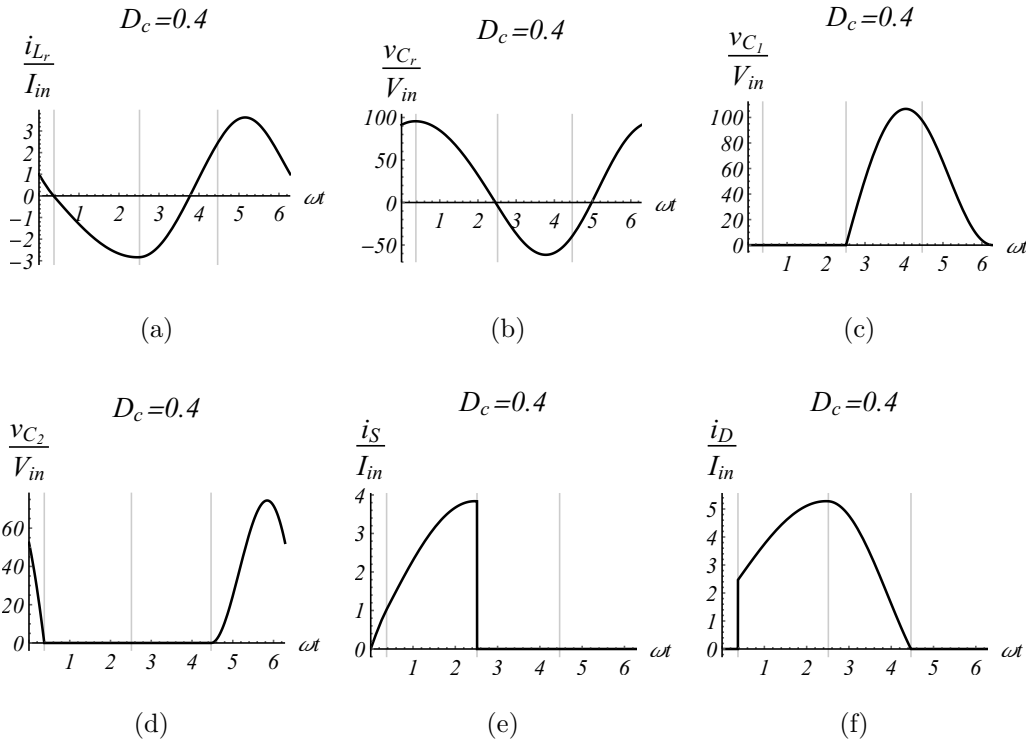
$$Q_L = \frac{1}{a\sqrt{a}C}. \quad (4.69)$$

In order to show the theoretical results for the Class E<sup>2</sup> resonant converter, an algorithm was implemented in a mathematical software aiming to find the state-space model solutions for any operating point. In addition, maximum values on the switches can be calculated and normalized gain and component stress curves can be obtained. Furthermore, by solving the output equation, the normalized steady-state waveforms are obtained as shown in Figure 4.10 for  $D_c = 0.4$ , Figure 4.11 for  $D_c = 0.5$  and Figure 4.12 for  $D_c = 0.6$ .

For all operating points, the optimal steady-state operation condition can be achieved. In other words, the switch  $S$  zero-voltage soft-switching occurs in the end of one

cycle, as shown in Figures 4.10(c), 4.11(c) and 4.12(c). The switch  $S$  voltage is the same as the capacitor  $C_1$  voltage due to their parallel connection. Furthermore, the diode  $D$  turns off with zero-derivative voltage soft-switching, which means that the diode  $D$  current smoothly becomes 0, as depicted in Figures 4.10(f), 4.11(f) and 4.12(f). It is important to note that the waveforms are normalized in relation to the input in frequency. The current waveforms are normalized by the input current  $I_{in}$ . This means that, by multiplying the normalized current waveforms by a specific value for  $I_{in}$ , the non-normalized waveforms are achieved.

Figure 4.10 – Normalized waveforms for the Class-E<sup>2</sup> resonant DC-DC converter for  $D_c = 0.4$ . (a) Resonant current. (b) Resonant voltage. (c) Inverter’s capacitor voltage. (d) Rectifier’s capacitor voltage. (e) Switch  $S$  current. (f) Diode  $D$  current.



Source: Author.

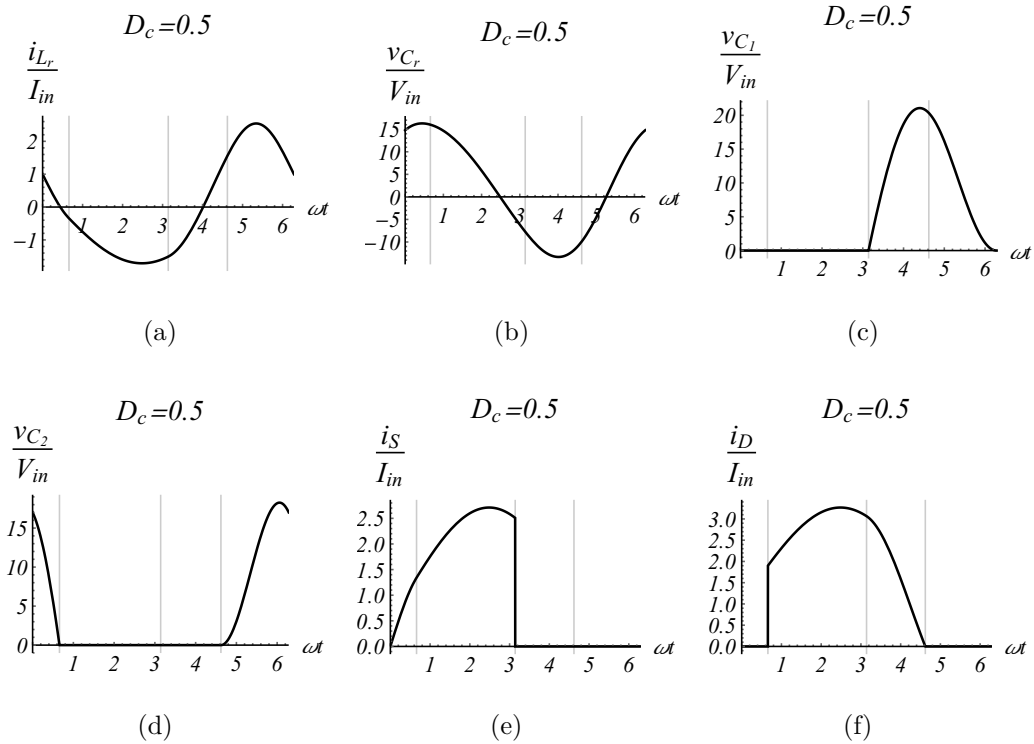
The voltage waveforms are normalized by the input voltage  $V_{in}$ . In this case, the system was analyzed by considering a input current source, which means that it is necessary to adequate the normalization by considering

$$V_{in} = \frac{V_o I_{in}}{a}. \quad (4.70)$$

By performing a parameter sweep on  $D_c$ , other important parameters can be evaluated, like as the transfer power ratio, current transfer function, quality factor and so on. Based on that, gain curves can be drawn. In addition, the normalized maximum



Figure 4.11 – Normalized waveforms for the Class-E<sup>2</sup> resonant DC-DC converter for  $D_c = 0.5$ . (a) Resonant current. (b) Resonant voltage. (c) Inverter’s capacitor voltage. (d) Rectifier’s capacitor voltage. (e) Switch  $S$  current. (f) Diode  $D$  current.



Source: Author.

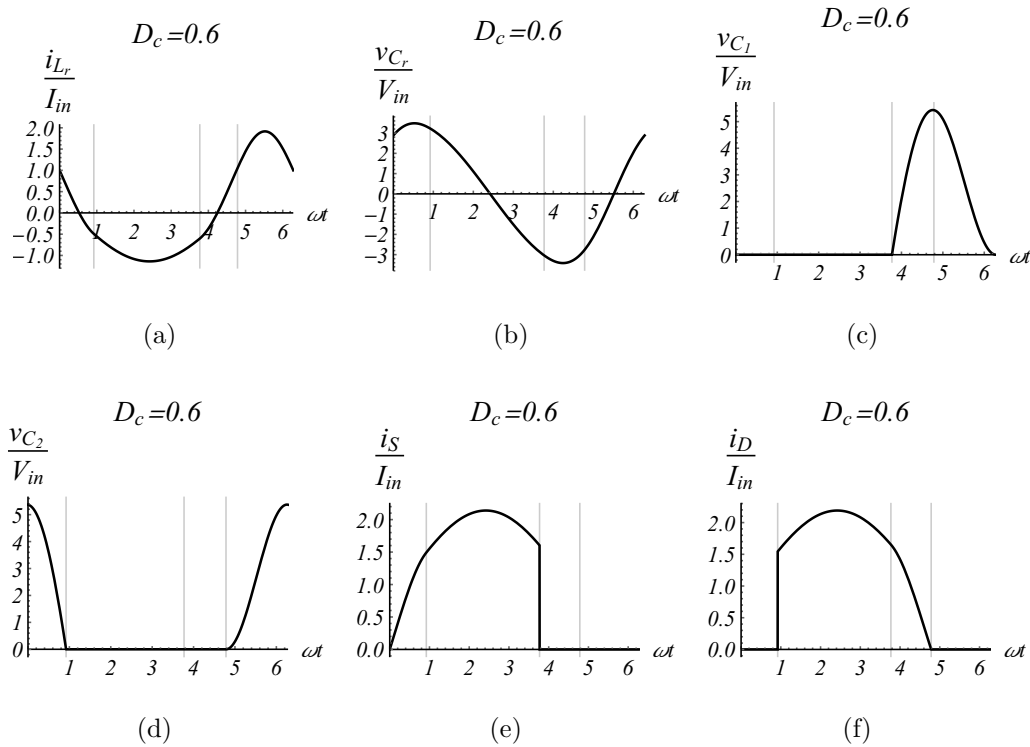
voltage and current on the diode and the switch can be calculated for any  $D_c$ , then component stress curves are obtained. Such curves represent the behavior of the system in a generalized way and can be used to design or select the components.

The normalized gain and component stress curves for the Class-E<sup>2</sup> resonant DC-DC converter are shown in Figure 4.13. The system was analyzed for different values of  $A_2$  and fixed  $A_3 = 1.25$ . In addition, the transformation ratio was selected as  $\alpha = 1$  for Figures 4.13(a)-(h). Notwithstanding, the current transfer function  $S$  as function of transformation ratio  $\alpha$  is depicted in Figure 4.13.

It can be seen in Figure 4.13(a) that  $S$  decreases when  $D_c$  increases. However, the component stress is greater for low values of duty cycle  $D_c$ , as shown in Figures 4.13(e), 4.13(f), 4.13(g) and 4.13(h). For  $A_2 = 0.95$ , the operational range is smaller than  $A_2 = 0.55$  and  $A_2 = 0.75$ . This is because convergence errors occur more often closer to the resonant frequency  $A_2 = 1.0$ .

By relating the output variables to each other, it is possible to plot the phase diagram. The phase diagram for  $D_c = 0.5$  considering  $i_{L_r}/I_{in}$  and  $v_{C_1}/V_{in}$  is shown in Figure 4.14, in which Figure 4.14(a) depicts the ZVS operation and Figure 4.14(b) the

Figure 4.12 – Normalized waveforms for the Class-E<sup>2</sup> resonant DC-DC converter for  $D_c = 0.6$ . (a) Resonant current. (b) Resonant voltage. (c) Inverter’s capacitor voltage. (d) Rectifier’s capacitor voltage. (e) Switch  $S$  current. (f) Diode  $D$  current.

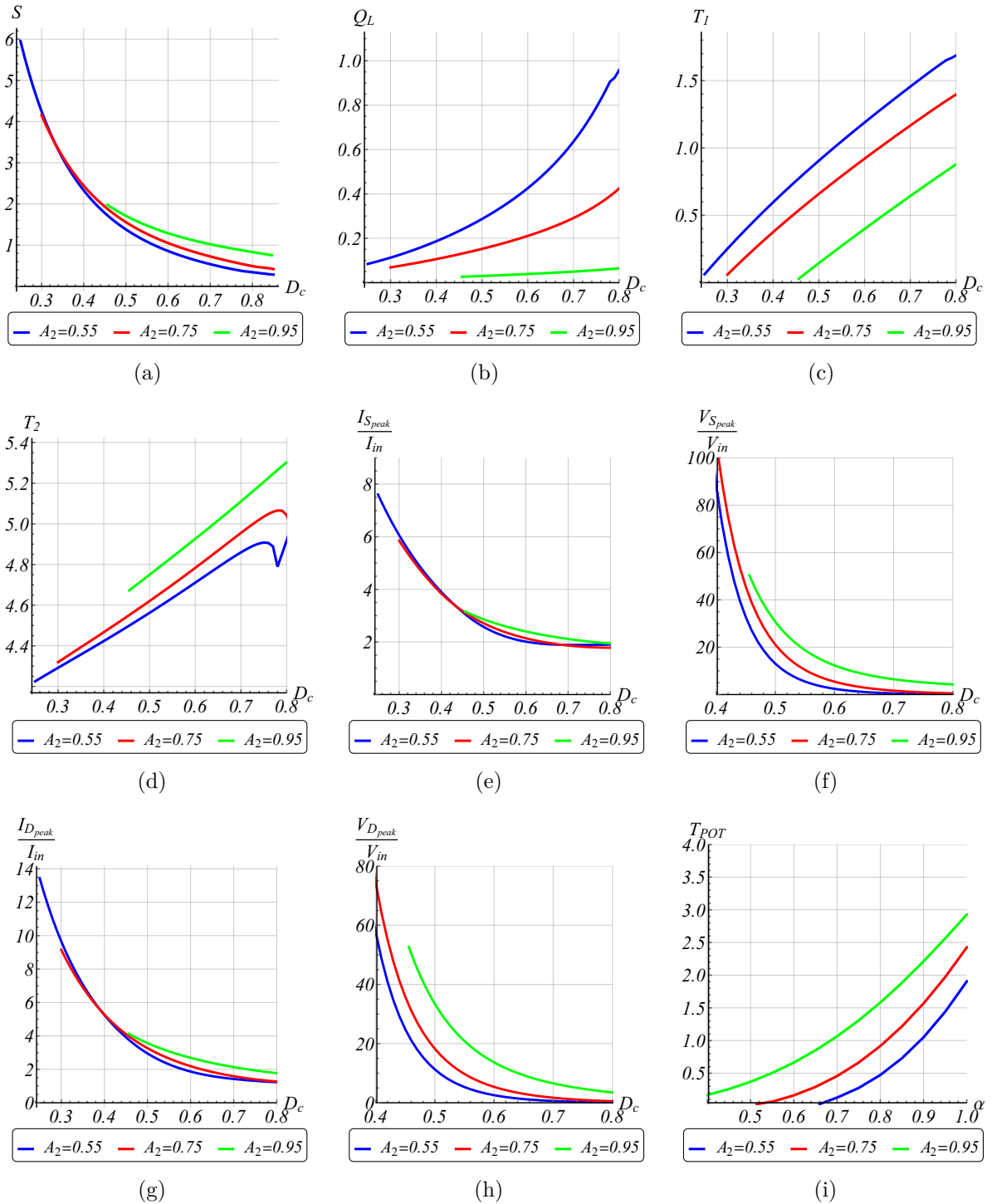


Source: Author.

non-ZVS operation. It can be seen in the first quadrant of Figure 4.14(b) that the graph has a discontinuity that characterizes the non-ZVS operation.

The diode  $D$  ZDVS operation can be also analyzed by means of the phase diagram considering  $i_{L_r}/I_{in}$  and  $v_{C_2}/V_{in}$  as shown in Figure 4.15. The ZDVS condition is portrayed Figure 4.15(a) and the non-ZDVS in Figure 4.15(b). The plot in Figure 4.15(b) characterizes that the diode  $D$  turns off but its derivative is different from 0.

Figure 4.13 – Normalized gain and component stress curves for the Class-E<sup>2</sup> converter:  
 (a) Current transfer function  $S$  as function of  $D_c$ . (b) Quality factor  $Q_L$  as  
 function of  $D_c$ . (c) Time  $T_1$  as function of  $D_c$ . (d) Time  $T_2$  as function of  $D_c$ .  
 (e) Peak switch current  $I_{S_{peak}}/I_{in}$  as function of  $D_c$ . (f) Peak switch voltage  
 $V_{S_{peak}}/V_{in}$  as function of  $D_c$ . (g) Peak diode current  $I_{D_{peak}}/I_{in}$  as function of  
 $D_c$ . (h) Peak diode voltage  $V_{D_{peak}}/V_{in}$  as function of  $D_c$ . (i) Transfer power  
 ratio  $T_{POR}$  as function of transformation ratio  $\alpha$ .



Source: Author.

Figure 4.14 – Phase diagram of the Class-E<sup>2</sup> converter for  $D_c = 0.5$  considering  $i_{L_r}/I_{in}$  and  $v_{C_1}/V_{in}$ : (a) ZVS. (b) Non-ZVS.

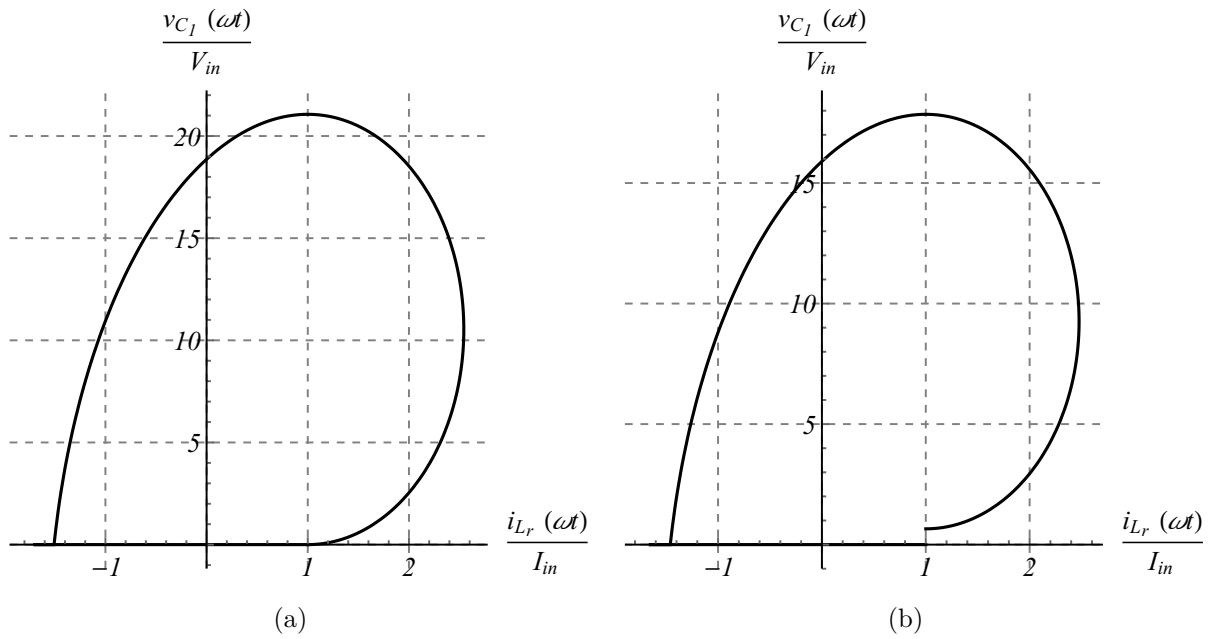
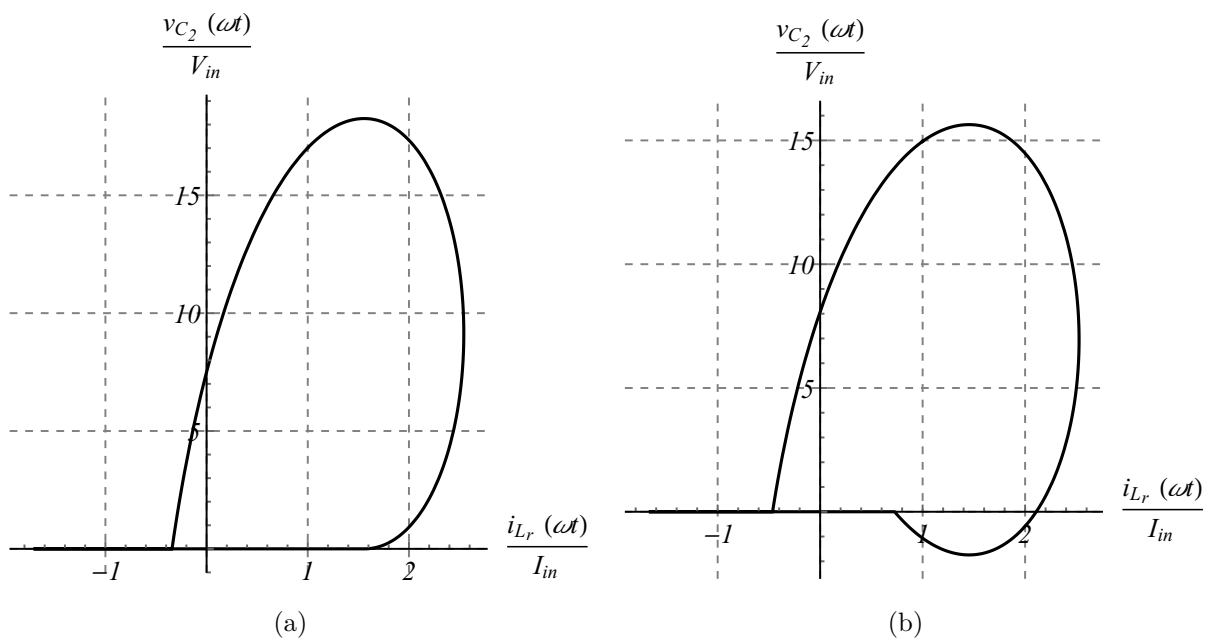


Figure 4.15 – Phase diagram of the Class-E<sup>2</sup> converter for  $D_c = 0.5$  considering  $i_{L_r}/I_{in}$  and  $v_{C_2}/V_{in}$ : (a) ZDVS. (b) Non-ZDVS.



## 4.3 DESIGN METHODOLOGY

The next step is to define a design procedure that allows to find the real values for the components based on the normalized gain curves. An operating point should be selected, and based on that, it is necessary to extract the unit-less parameters in the gain curves. In this sense, it is better to represent the normalized curves in a table format as shown in Table 4.1 and in Table 4.2, as examples.

Table 4.1 – Unit-less parameters for the Class-E<sup>2</sup> resonant converter considering  $\alpha = 1.0$ ,  $A_2 = 0.55$  and  $A_3 = 1.25$ .

$D_c$	$S$	$A_1$	$Q_L$	$T_1$	$T_2$	$a$
0.25	5.949	0.86	0.084	0.062	4.225	0.028
0.30	4.245	0.89	0.106	0.251	4.291	0.055
0.35	3.107	0.92	0.139	0.429	4.357	0.103
0.40	2.328	0.96	0.178	0.596	4.423	0.184
0.45	1.778	1.02	0.223	0.755	4.491	0.316
0.50	1.380	1.10	0.275	0.905	4.562	0.524
0.55	1.083	1.20	0.336	1.050	4.635	0.851
0.60	0.857	1.34	0.409	1.189	4.710	1.360
0.65	0.679	1.58	0.498	1.323	4.786	2.164
0.70	0.537	1.88	0.609	1.455	4.859	3.461
0.75	0.422	2.34	0.755	1.582	4.908	5.609

Table 4.2 – Unit-less parameters for the Class-E<sup>2</sup> resonant converter considering  $\alpha = 1.0$ ,  $A_2 = 0.75$  and  $A_3 = 1.25$ .

$D_c$	$S$	$A_1$	$Q_L$	$T_1$	$T_2$	$a$
0.30	4.154	0.724	0.069	0.059	4.319	0.057
0.35	3.147	0.758	0.086	0.222	4.393	0.100
0.40	2.441	0.804	0.106	0.375	4.467	0.167
0.45	1.933	0.865	0.128	0.520	4.542	0.267
0.50	1.557	0.946	0.152	0.659	4.620	0.412
0.55	1.272	1.055	0.179	0.791	4.700	0.617
0.60	1.050	1.203	0.210	0.920	4.783	0.906
0.65	0.872	1.406	0.247	1.045	4.868	1.314
0.70	0.724	1.698	0.291	1.166	4.955	1.903
0.75	0.599	2.135	0.347	1.284	5.035	2.784
0.80	0.490	2.854	0.424	1.397	5.042	4.153

By selecting a value for duty cycle  $D_c$ , the corresponding unit-less parameters must be used. The unit-less parameters are used to obtain the real system parameters. It is necessary to describe the components based on the unit-less parameters. For this

purpose, relationships (4.48)-(4.53) and (4.55) are re-arranged and the design equations are obtained as:

$$L_r = \frac{R_L}{A_3 Q_L \omega}, \quad (4.71)$$

$$C_r = \frac{A_3 Q_L}{A_2^2 R_L \omega}, \quad (4.72)$$

$$C_1 = \frac{A_3 Q_L}{A_1^2 R_L \omega} \quad (4.73)$$

and

$$C_2 = \frac{Q_L}{A_3 R_L \omega}. \quad (4.74)$$

The choke inductor  $L_c$  can be designed by defining a normalized resonant frequency  $A_c$  between  $L_c$  and  $C_1$  as follows:

$$A_c = \frac{\omega_c}{\omega}, \quad (4.75)$$

in which, the angular frequency is  $\omega_c = 1/\sqrt{L_c C_1}$ . The lower  $A_c$ , the lower the ripple in the choke inductor  $L_c$ , which is calculated by

$$L_c = \frac{A_1^2 R_L}{A_c Q_L \omega}. \quad (4.76)$$

The output filter inductor can be designed in the same way as  $L_c$ , by considering a normalized frequency  $A_f$  between  $L_f$  and  $C_f$ :

$$A_f = \frac{\omega_f}{\omega}, \quad (4.77)$$

being  $\omega_f = 1/\sqrt{L_f C_f}$ . The equation for  $L_f$  is dependent of  $T_1$  and  $T_2$ :

$$L_f = \frac{(1 - T_2 + T_1) R_L}{10 A_f \omega}. \quad (4.78)$$

The output filter capacitor  $C_f$  is designed as (KAZIMIERCZUK; CZARKOWSKI, 1995)

$$C_f = \frac{25}{\omega^2 L_f}. \quad (4.79)$$

The design equations are also dependent on specifications. A design methodology is going to be proposed. The following step-by-step procedure is a generic example and can be modified according to the designer's needs.

1. *Define specifications:* output voltage  $V_o$ , output power  $P_o$  and operating frequency  $f_s$ ;
2. *Auxiliary calculation:* load  $R_L$ , output current  $I_o$ , input voltage  $V_{in}$  and angular

operating frequency  $\omega$ :

$$R_L = \frac{V_o}{I_o}, \quad (4.80)$$

$$I_o = \frac{P_o}{V_o}, \quad (4.81)$$

$$V_{in} = \frac{P_o}{\eta I_{in}} \times 100 \quad (4.82)$$

and

$$\omega = 2\pi f_s; \quad (4.83)$$

3. Calculate required gain  $S$ :

$$S = \frac{I_o}{I_{in}}; \quad (4.84)$$

4. *Select operating point  $D_c$* : based on the required gain, the operating point must be selected to achieve the required power transfer.
5. *Design of the resonant circuit  $L_r$ - $C_r$ - $C_1$ - $C_2$* : by means of the unit-less parameters, the resonant circuit is designed based on (4.71), (4.72), (4.73) and (4.74);
6. *Design of the choke inductor  $L_c$  and output filter  $L_f$ - $C_f$* : by defining the normalized resonant frequencies  $A_c$  and  $A_f$ , which are related to the ripple in the input current and the output ripple, respectively, the choke inductor and the output filter are designed by (4.76), (4.78) and (4.79).

The aforementioned design procedure is a standard step-by-step procedure that can be used to design the Class-E<sup>2</sup> resonant converter. When considering the resonant circuit  $L_r$ ,  $C_r$ ,  $C_1$  and  $C_2$  as model for the multiphysics network, it is necessary to consider these components as specifications for the system. They can be analytically calculated based on the multiphysical, equivalent electrical or piezoelectric transformer models.

Efficiency  $\eta$  is used in (4.82) in order to highlight the possibility of including a parameter that indicates a lossy system. As an example of the formulas application, let's consider the design of a Class-E<sup>2</sup> resonant converter based on the given specifications shown in Table 4.3.

Table 4.3 – Design specifications for the electro-mechanical-acoustic CET system based on Class-E<sup>2</sup> topology.

Specification / Input	Value
Output voltage, $V_o$	4 V
Load, $R_L$	20 $\Omega$
Operating frequency, $f_s$	800 kHz
Normalized resonant frequency, $A_1$	0.94
Normalized resonant frequency, $A_2$	0.75
Normalized resonant frequency, $A_3$	1.25

Based on  $A_1$ ,  $A_2$  and  $A_3$ , the proposed algorithm shown in Figure 4.9 should be solved. The results are a set of unit-less parameters that are used to design the system's components. By selecting  $D_c = 0.5$ , the unit-less parameters are extracted from Table 4.2. The unit-less parameters are shown in Table 4.4.

Table 4.4 – Unit-less parameters for the electro-mechanical-acoustic CET system based on Class-E<sup>2</sup> topology.

Parameter	Value	Method
Normalized resonant frequency, $A_1$	0.94	Calculated based on the PZT model
Normalized resonant frequency, $A_2$	0.75	Calculated based on the PZT
Normalized resonant frequency, $A_3$	1.25	Calculated based on the PZT model
Duty cycle, $D_c$	0.5	Selected as input
Diode turn-on time, $T_1$	0.659	Found based on the normalized model
Diode turn-off time, $T_2$	4.620	Found based on the normalized model
Quality factor, $Q_L$	0.152	Found based on the normalized model
Current transfer function, $S$	1.557	Found based on the normalized model
Choke inductor ripple, $A_c$	0.09	Defined as input
Output ripple, $A_f$	0.1	Defined as input

Based on Tables 4.3 and 4.4, the components are calculated by (4.71)-(4.79). The designed Class-E<sup>2</sup> converter for the CET system is shown in Table 4.5.



Table 4.5 – Components for the electro-mechanical-acoustic CET system based on Class-E<sup>2</sup> topology.

Component	Value
Resonant inductor, $L_r$	$22 \mu H$
Resonant capacitor, $C_r$	$3.3 nF$
Inverter capacitor, $C_1$	$2.2 nF$
Choke inductor, $L_c$	$260 \mu H$
Rectifier capacitor, $C_2$	$1.2 nF$
Output filter inductor, $L_f$	$175 \mu H$
Output filter capacitor, $C_f$	$25 nF$
Load, $R_L$	$20 \Omega$

In addition, auxiliary calculation leads to:  $V_{in} = 6.25 V$  and  $P_o = 800 mW$ .

#### 4.4 DESIGN OF THE POWER CIRCUITRY FOR THE ELECTRO-MECHANICAL-ACOUSTIC CET SYSTEM BASED ON CLASS-E<sup>2</sup> RESONANT CONVERTER

In this Section, a design procedure for the power conversion circuitry of the electro-mechanical-acoustic CET system is proposed. The idea is to design the circuits that perform the electrical energy management. For instance, the Class-E inverter can be designed to supply the ultrasound transmitter. Also, the Class-E rectifier can be designed to perform the AC-DC conversion based on the output of the ultrasound receiver. Besides that, the Class-E<sup>2</sup> DC-DC converter can be designed based on its resonant tank as topological representation of the multiphysical network.

The design flow is described by the following steps:

1. *Define the inputs:* the first step is to define the inputs for the design flowchart. The inputs are related to the real physical system and are listed as:
  - Length of the transfer media,  $l(m)$ ;
  - Radius of the transfer media,  $R(m)$ ;
  - Density of the transfer media material,  $\rho(kg/m^3)$ ;
  - Wave velocity in the transfer media material,  $C_L(m/s)$ ;
  - Transfer media friction coefficient,  $\mu_L(m \cdot Pa \cdot s)$ ;
  - Piezoelectric component mass,  $M_{1,2}(kg)$ ;
  - Piezoelectric component damper,  $D_{1,2}(N \cdot s \cdot m^{-1})$ ;

- Piezoelectric component stiffness,  $K_{1,2}(N \cdot m^{-1})$
- Piezoelectric component capacitance,  $C_{in,o}(F)$ ;
- Piezoelectric anti-resonant frequency,  $f_a(Hz)$ ;
- Piezoelectric component radius,  $r(m)$ ;
- Electro-mechanical coupling,  $\alpha_{1,2}$ ;
- Output DC voltage,  $V_o(V)$ ;
- Output load,  $R_L(\Omega)$ ;
- Input voltage,  $V_{in}(V)$
- Operating frequency,  $f_s(Hz)$ ;
- Choke inductor ripple,  $A_c$ ;
- Output filter ripple,  $A_f$ ;

2. *Auxiliary calculation:* based on the inputs, it is useful to calculate the following auxiliary parameters:

- Output power,  $P_o(W)$ ;
- Output current,  $I_o(A)$ ;
- Input current,  $I_{in}(A)$ ;
- Angular operating frequency,  $\omega_s$ ;
- Required current gain,  $S$ ;

which are equated as

$$P_o = \frac{V_o^2}{R_L}; I_o = \frac{P_o}{V_o}; I_{in} = \frac{P_o}{\eta V_{in}} \times 100; \omega_s = 2\pi f_s; S = \frac{I_o}{I_{in}}; \quad (4.85)$$

3. *Calculate the elements of the acoustic network:* based on the inputs, the acoustical equivalent mass  $M_{a1}$ , equivalent friction  $Z_{a1}$  and equivalent compliance  $N_{a1}$  can be found as

$$M_{a1} = \frac{1}{M_a}; M_a = \frac{\rho l}{\pi R^2}; Z_{a1} = \frac{1}{Z_a}; Z_a = \frac{8\mu_L l}{\pi R^4}; N_{a1} = \frac{Vol}{C_L^2 \rho}. \quad (4.86)$$

The mechanical-acoustic coupling is calculated by

$$\gamma_{1,2} = \frac{\pi r^2}{\pi R^2}. \quad (4.87)$$

4. *Equating for the piezoelectric transformer model:* the equivalent acoustical components are converted into the equivalent electrical model by  $M_{1,2} = L_{1,2}$ ,  $K_{1,2} =$

$1/C_{1,2}$ ,  $D_{1,2} = R_{1,2}$ ,  $M_{a1} = L_a$ ,  $N_{a1} = C_a$  and  $Z_{a1} = R_a$ . Then, the piezoelectric transformer model components are equated by (3.122), (3.123), (3.124) and (3.125);

5. *Calculate the normalized electrical resonant frequencies for the Class- $E^2$  resonant tank:* the normalized resonant frequencies are calculated as

$$A_1 = \frac{\omega_1}{\omega}; A_2 = \frac{\omega_2}{\omega}; A_3 = \frac{\omega_3}{\omega}, \quad (4.88)$$

being,

$$\omega_1 = \frac{1}{\sqrt{L_{pzt}C_{in}}}; \omega_2 = \frac{1}{\sqrt{L_{pzt}C_{pzt}}}; \omega_3 = \frac{1}{\sqrt{L_{pzt}C_o}}; \quad (4.89)$$

6. *Solve the normalized model of the Class- $E^2$  resonant converter:* at this point, it is necessary to solve the normalized state-space model of the converter. The normalized resonant frequencies  $A_1$ ,  $A_2$ , and  $A_3$  should be used as input. A parameter sweep should be performed in the duty cycle  $D_c$ . Based on the required current gain  $S$ , the duty cycle  $D_c$  should be selected and from its result, the quality factor  $Q_L$ , diode switching times  $T_1$  and  $T_2$ , and inverse transfer power ratio  $a$  are consequences of the choice of the duty cycle. For this purpose, the normalized gain curves should be used;

7. *Design of the Class- $E$  inverter stage:* the inverter stage is composed of the choke inductor  $L_c$  and the parallel capacitor  $C_1$ . The piezoelectric capacitance  $C_{in}$  is used to represent  $C_1$ . The choke inductor is designed by:

$$L_c = \frac{A_1^2 R_L}{A_c Q_L \omega}; \quad (4.90)$$

8. *Design of the Class- $E$  rectifier stage:* The rectifier stage is composed of the rectifier capacitor  $C_2$ , the output filter inductor  $L_f$  and the output filter capacitor  $C_f$ . The piezoelectric capacitance  $C_o$  is used to represent  $C_2$ . The output filter components are designed by

$$L_f = \frac{(1 - T_2 + T_1)R_L}{10A_f\omega}; C_f = \frac{25}{\omega^2 L_f}. \quad (4.91)$$

## 4.5 OTHER TOPOLOGIES

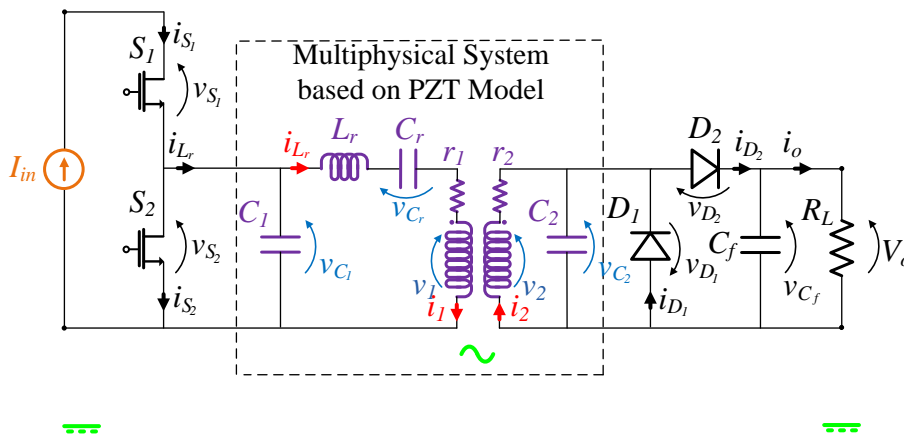
The electro-mechanical-acoustic CET system based on resonant topology was analyzed considering the Class-E<sup>2</sup> resonant converter. However, it is possible to develop the same concepts for other topologies. Although the topologies in this section are not going to be deeply analyzed, they are going to be highlighted to characterize other possibilities to drive the system.

### 4.5.1 Class-D<sup>2</sup> resonant converter

The Class-D<sup>2</sup> resonant converter is other topology that can be used to analyze the electro-mechanical-acoustic CET system. It is composed of a Class-D inverter and a Class-D rectifier, which are connected in the equivalent model of the multiphysical system.

The CET system based on Class-D<sup>2</sup> topology is show in Figure 4.16.

Figure 4.16 – Electro-mechanical-acoustic CET system based on Class-D<sup>2</sup> topology.



Source: Author.

The converter is composed of: input voltage source  $V_{in}$ , switch  $S_1$ , switch  $S_2$ , resonant inductor  $L_r$ , resonant capacitor  $C_r$ , diode  $D_1$ , diode  $D_2$ , output capacitor  $C_f$  and load  $R_L$ . The circuit variables are:  $i_{L_r}$ , inductor  $L_r$  current;  $v_{C_r}$ , capacitor  $C_r$  voltage;  $v_{C_f}$ , capacitor  $C_f$  voltage;  $i_{S_1}$ , switch  $S_1$  current;  $i_{S_2}$ , switch  $S_2$  current;  $v_{S_1}$ , switch  $S_1$  voltage;  $v_{S_2}$ , switch  $S_2$  voltage;  $i_{D_1}$ , diode  $D_1$  current;  $i_{D_2}$ , diode  $D_2$  current;  $v_{D_1}$ , diode  $D_1$  voltage;  $v_{D_2}$ , diode  $D_2$  voltage;  $i_o$ , output current; and  $V_o$ , output voltage.

When  $D_1$  is on and  $D_2$  is off, capacitor  $C_2$  is short-circuited. When  $D_1$  is off and  $D_2$  is on, capacitor  $C_2$  has parallel connection to  $C_f$ . In this sense, they can be combined

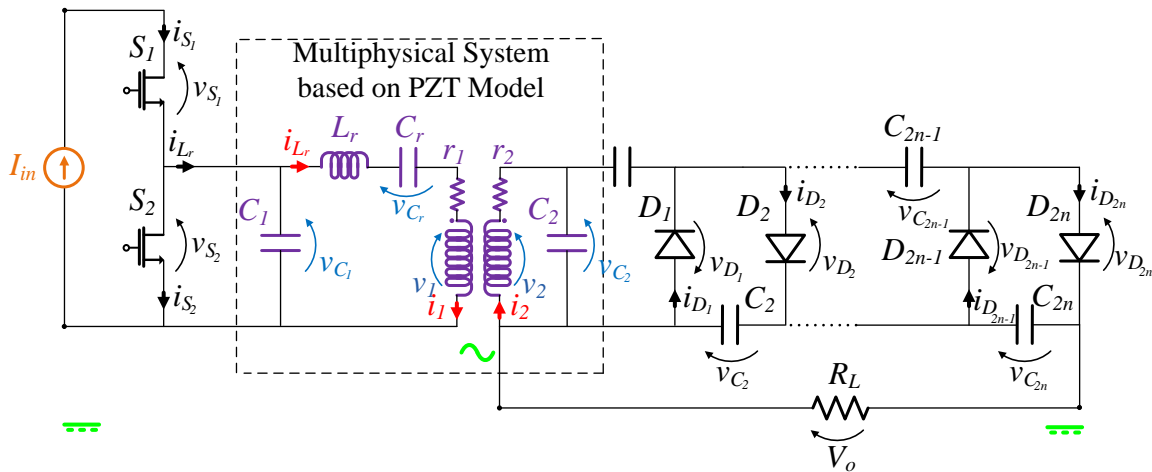
into a single capacitor, which determines one resonant frequency with  $L_r$ .

This topology is easier to be designed than the Class-E<sup>2</sup> converter. It is because it is not necessary to find the soft-switching conditions of diodes  $D_1$  and  $D_2$ . However, the Class-D<sup>2</sup> has lower efficiency than the Class-E<sup>2</sup> because the diodes operate in hard-switching mode. The complete analysis for the Class-D<sup>2</sup> resonant converter is shown in Appendix C.

#### 4.5.2 Cockcroft-Walton-based converters

As previously discussed, besides the resonant AC-DC rectifiers, the voltage multipliers can also be used for the rectification stage. A DC-DC converter based on Cockcroft-Walton (CW) AC-DC multiplier is a system composed of any DC-AC inverter cascaded with the voltage multiplier. For instance, a Class-DCW is obtained by connecting a Class-D inverter to a Cockcroft-Walton rectifier. Figure 4.17 shows the electro-mechanical-acoustic CET system based on Class-DCW.

Figure 4.17 – Electro-mechanical-acoustic CET system based on Class-DCW topology.

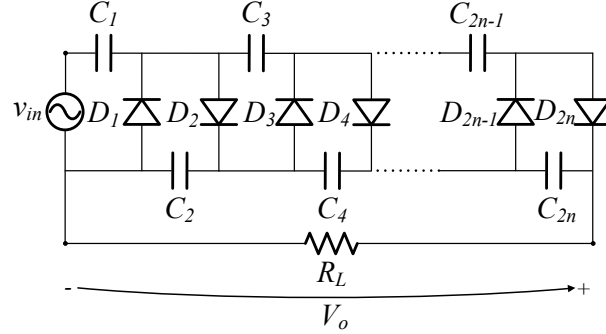


Source: Author.

The Cockcroft-Walton circuit operates different than the resonant converters regarding its connection to other systems. The resonant rectifiers are dependent of the resonant inverters because their frequencies are interdependent to each other. On the other hand, Cockcroft-Walton multipliers can be designed independently of the dynamic behavior of the inverter. For this reason, it can be analyzed separated from the multiphysical system. In other words, the Cockcroft-Walton recognizes the multiphysical system as a sinusoidal input source, and steps-up the voltage while performing the rectification. Although there are several variations for this converter, this work focus on a topology

based on diodes and capacitors. The topology under study is shown in Figure 4.18.

Figure 4.18 – Cockcroft-Walton AC-DC rectifier.



Source: Author.

The converter can be designed with  $n$ -stages, which is an important feature for this rectifier. The input source is represented by

$$v_{in} = V_{in} \sin(\omega t), \quad (4.92)$$

being  $V_{in}$  the peak value of the input voltage.

The converter is composed of capacitors  $C_1, C_2, \dots, C_{2n-1}$  and  $C_{2n}$ , diodes  $D_1, D_2, \dots, D_{2n-1}$  and  $D_{2n}$ . The output load is represented by  $R_L$ .

When the circuit has no load, the output voltage  $V_o$  is

$$V_o = 2nV_{in}. \quad (4.93)$$

When load is connected, the output voltage is affected by a voltage drop  $\Delta V_o$  and a voltage ripple  $\delta V_o$  is perceived. The analytical expressions for the Cockcroft-Walton multiplier are given as (WEINER, 1969; KHALIFA, 1990; KOBOUGIAS; TATAKIS, 2010):

$$\Delta V_o = \frac{S}{f} \left( \sum_{i=1}^n \frac{(n+1+i)^2}{C_{2i-1}} + \sum_{i=1}^{n-1} \frac{(n+1-i)(n-i)}{C_{2i}} \right) V_{in}, \quad (4.94)$$

$$\delta V_o = \frac{S}{f} \left( \sum_{i=1}^n \frac{(n+1-i)}{C_{2i}} \right) V_{in} \quad (4.95)$$

and

$$V_o = \left( 2n - \frac{1}{V_{in}} \left( \Delta V_o + \frac{1}{2} \delta V_o \right) \right) V_{in} - 2nV_D, \quad (4.96)$$

which include the input source frequency  $f$ , diode voltage drop  $V_D$  and AC-to-DC transfer function  $S$ :

$$S = \frac{I_o}{V_{in}}, \quad (4.97)$$

being  $I_o$  the output current.

In the Cockcroft-Walton multiplier, it is necessary to evaluate a trade-off between number of diodes and voltage transfer. By increasing the number of stages, higher is the output voltage. However, the higher the number of diodes, the higher is the overall diode voltage drop. On the other hand, the Cockcroft-Walton multiplier is an interesting topology because it can be designed apart from the rest of the system.

A discussion about the practical implementation of the driving circuits is conducted in Appendix E.

#### 4.6 CONCLUSION

In this Chapter, an analysis and design methodology for the electro-mechanical-acoustic CET system based on resonant topologies was proposed. The piezoelectric transformer model, which represents the multiphysical system, is connected to power conversion circuits by considering it as part of the resonant tank.

The Class-E<sup>2</sup> resonant converter was studied in this Chapter. A normalized state-space model based on unit-less parameters was presented and normalized gain and component stress curves were portrayed to show the general behavior of the system.

A design methodology was proposed in which, based on unit-less parameters derived from the piezoelectric transformer model, and based on design specifications, suitable rectifiers and inverters can be designed to drive the electro-mechanical-acoustic CET system. Furthermore, other topologies, like as the Class-D<sup>2</sup> and the Class-DCW converters were pointed out as options to be used as power conversion circuits.





## 5 GENERALIZED AVERAGED DYNAMIC MODEL

In the previous chapter, the Class-E<sup>2</sup> resonant DC-DC converter was used as topological representation for the electro-mechanical-acoustic CET system. The  $C_1 - L_r - C_r - C_2$  resonant circuit and the transformer were considered as an equivalent electrical representation for the multiphysical system. It was shown that the component design equations for the inverter and the rectifier stages can be derived from the normalized model of the converter. The performed analysis in Chapter 4 is considered as the *steady-state modeling* of the system, and it is useful to design the circuit and verify component stress.

In this Chapter, the *dynamic modeling* is going to be performed for the Class-E<sup>2</sup> converter. The dynamic model (AC model) is used to verify how the disturbances on circuit variables, input sources, frequency, duty cycle or components, affect the system. Furthermore, it is used to develop closed-loop control systems (ERICKSON, 2000).

Usually, power converters are modeled based on the averaged state-space model or the switched model. However, these techniques are only valid for waveforms with small ripple. In other words, they are restricted to DC variables. In this sense, the classical AC modeling techniques are not suitable for resonant converters because they have large amplitudes on the waveforms and AC variables.

In order to model the Class-E<sup>2</sup> converter, the *generalized averaged model* (GAM) is going to be used. This model is able to reconstruct the waveforms even though they have large amplitudes and high harmonic content (SANDERS et al., 1991), (SANDERS et al., 1990), (BACHA; MUNTEANU; BRATCU, 2013).

The generalized averaged model captures different harmonic components and the reconstruction of the waveforms is based on expressing the electrical signal in terms of its Fourier series. Several works deal with the generalized averaged model for power converters. Sanders et al. (1991) has shown the basis for the GAM method applied to resonant converters. Javaid & Dujic (2015) has applied the GAM for the Buck, Boost and Buck-Boost converters by means of their state-space representation.

Even though many works have dealt with the GAM, it still is a complex task to systematize the method application. It is because the method requires the development of non-linear differential equations and then, a convolution operator is applied into switching functions and state variables.

In this Thesis, the GAM is applied in the Class-E<sup>2</sup> converter. The development of this chapter is based on the works of Sanders et al. (1991), Bacha, Munteanu & Bratcu (2013), Javaid & Dujic (2015) and Engleitner (2011). The basis for the GAM are well defined in the aforementioned works. However, so far, there is no application of the GAM for the Class-E<sup>2</sup> converter in the literature.

It is important to note that the development of a control system for the electro-mechanical-acoustic CET system based on resonant converters is out of the scope of

this Thesis. However, this Thesis provides the dynamic model of the Class-E<sup>2</sup> converter because this topology is the focus of study in this work and the results shown in this Chapter can be used to understand the system's behavior and to provide basis for future works.

## 5.1 SWITCHING FUNCTION

Switched power converters operate based on modes. It means that the configuration of the converter changes dependent on the condition of its switches. Each configuration leads to a state-space model.

In order to obtain a unique state-space model that represents the converter, switching functions can be defined. The Class-E<sup>2</sup> converter has four operating modes ruled by the switch  $S$  and the diode  $D$  operation. In this sense, two switching functions should be defined.

The switching functions should be able to recreate the state-space models for each mode. The switching function that represents the effect of the switch  $S$  is defined as a Fourier series (SANDERS et al., 1991):

$$f_1(t) = \langle s_1 \rangle_0 + \sum_{k=1}^{k_{max}} \left( \langle s_1 \rangle_k e^{jkt} + \langle s_1 \rangle_{-k} e^{-jkt} \right), \quad (5.1)$$

in which,  $f_1(t)$  is the switching function, notation  $\langle \rangle_k$  represents the function evaluated considering harmonic  $k$ ,  $k_{max}$  is the maximum number of considered harmonics and  $\langle s_1 \rangle_k$  represents the Fourier coefficient for harmonic  $k$ .

The Fourier coefficients are calculated by

$$\langle s_1 \rangle_k = \frac{1}{2\pi} \left( \int_{D_c 2\pi}^{2\pi} e^{-jk\tau} d\tau \right). \quad (5.2)$$

The switching function that represents the effect of the diode  $D$  is defined as a Fourier series by:

$$f_2(t) = \langle s_2 \rangle_0 + \sum_{k=1}^{k_{max}} \left( \langle s_2 \rangle_k e^{jkt} + \langle s_2 \rangle_{-k} e^{-jkt} \right), \quad (5.3)$$

in which,  $f_2(t)$  is the switching function and  $\langle s_2 \rangle_k$  represents the Fourier coefficient for harmonic  $k$ .

The Fourier coefficients are given by:

$$\langle s_2 \rangle_k = \frac{1}{2\pi} \left( \int_0^{T_1} e^{-jk\tau} d\tau + \int_{T_2}^{2\pi} e^{-jk\tau} d\tau \right). \quad (5.4)$$

Note that the intervals of integration are related to the switch and diode operations.

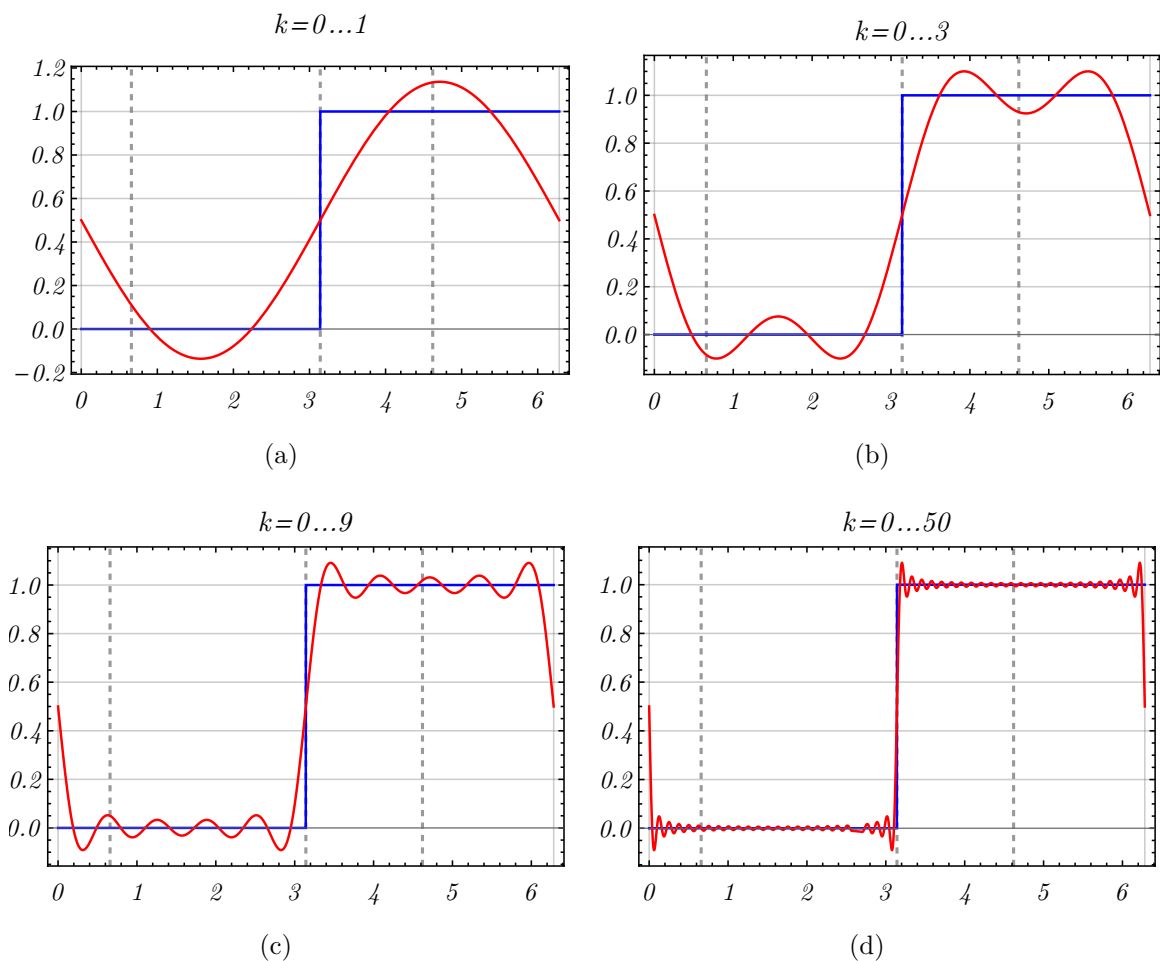
For instance, switching function  $f_1(t)$  is able to represent the transitions on-off and off-on for the switch  $S$ . In the same way, switching function  $f_2(t)$  represents the transitions off-on and on-off for the diode  $D$ .

The number of harmonics defines the coverage of the model. The accuracy of the waveform reconstruction depends on the considered number of harmonics. If the waveform has high harmonic content, it is necessary to use a relatively high number of harmonics.

Mathematically, the transition from a mode to another is represented by a square waveform. It is because the terms of the state-space matrices suddenly change when the circuit configuration changes.

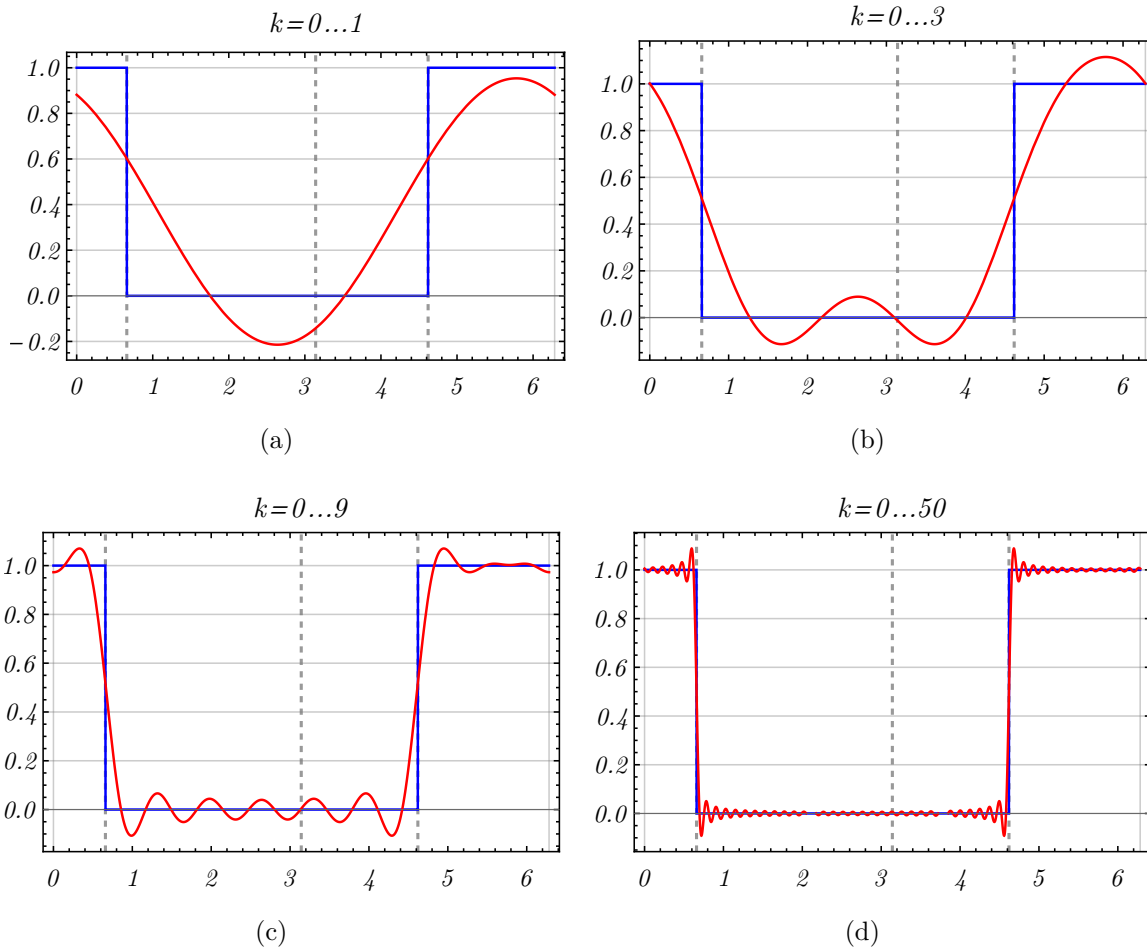
A square waveform has high harmonic content, which means that it is necessary to include several harmonics in the waveform reconstruction to achieve a suitable representation. The switching function described by the Fourier series for different number of harmonics  $k$  is depicted in Figure 5.1 for the switch  $S$  behavior and in Figure 5.2 for the diode  $D$  behavior.

Figure 5.1 – Switching function described by Fourier series for the switch  $S$  behavior. (a)  $k = 0\dots1$ . (b)  $k = 0\dots3$ . (c)  $k = 0\dots9$ . (d)  $k = 0\dots50$ .



Source: Author.

Figure 5.2 – Switching function described by Fourier series for the diode  $D$  behavior. (a)  $k = 0 \dots 1$ . (b)  $k = 0 \dots 3$ . (c)  $k = 0 \dots 9$ . (d)  $k = 0 \dots 50$ .



Source: Author.

It is possible to conclude that the higher the number of harmonics, the better is the approximation of the function. However, it is important to highlight that the computational effort is higher when the number of harmonics is increased.

## 5.2 NON-LINEAR DIFFERENTIAL EQUATIONS

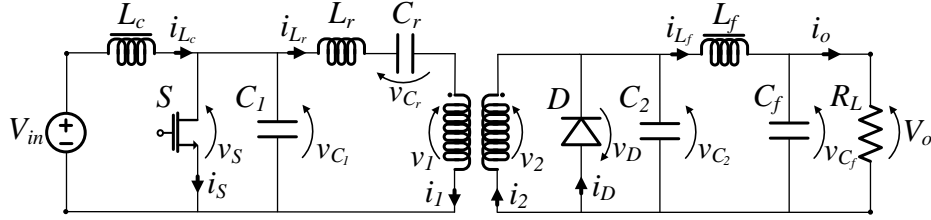
The switching functions are going to be used to construct a non-linear model for the Class-E<sup>2</sup> converter. As described in Chapter 4, the converter has four operating modes:

1. Mode I ( $0 < \omega t \leq T_1$ ):  $S$  on and  $D$  off;
2. Mode II ( $T_1 < \omega t \leq D_c 2\pi$ ):  $S$  on and  $D$  on;
3. Mode III ( $D_c 2\pi < \omega t \leq T_2$ ):  $S$  off and  $D$  on;

4. Mode IV ( $T_2 < \omega t \leq 2\pi$ ):  $S$  off and  $D$  off.

The topology to be considered is shown in Figure 5.3.

Figure 5.3 – Class-E<sup>2</sup> resonant DC-DC converter.



Source: Author

For the dynamic model, the choke inductor  $L_c$  and the output filter  $L_f - C_f$  are considered. It is interesting to consider the most comprehensive topology as possible. For instance, by including the output filter, it is possible to derive the transfer function from the DC input source to the DC output source, which means that a control system can be developed to regulate the DC output voltage. The transformer relationships are  $\alpha = v_1/v_2 = i_2/i_1$ .

The topologies for each mode, circuit variables and components were detailed in Chapter 4. For this reason, they are omitted in this Chapter.

The state vector  $\mathbf{x}(t)$  is composed of the following circuit variables

$$\mathbf{x}(t) = [\mathbf{i}_{L_c}, \mathbf{v}_{C_1}, \mathbf{i}_{L_r}, \mathbf{v}_{C_r}, \mathbf{v}_{C_2}, \mathbf{i}_{L_f}, \mathbf{v}_{C_f}]^T. \quad (5.5)$$

Each circuit variable has a differential governing equation for each operating mode. The governing equations for mode I are described by

$$\frac{di_{L_c}(t)}{dt} = \frac{V_{in}}{L_c}, \quad (5.6)$$

$$\frac{dv_{C_1}(t)}{dt} = 0, \quad (5.7)$$

$$\frac{di_{L_r}(t)}{dt} = -\frac{v_{C_r}(t)}{L_r} - \alpha \frac{v_{C_2}(t)}{L_r}, \quad (5.8)$$

$$\frac{dv_{C_r}(t)}{dt} = \frac{i_{L_r}(t)}{C_r}, \quad (5.9)$$

$$\frac{dv_{C_2}(t)}{dt} = \alpha \frac{i_{L_r}(t)}{C_2} - \frac{i_{L_f}(t)}{C_2}, \quad (5.10)$$

$$\frac{di_{L_f}(t)}{dt} = \frac{v_{C_2}(t)}{L_f} - \frac{v_{C_f}(t)}{L_f} \quad (5.11)$$

and

$$\frac{dv_{C_f}(t)}{dt} = \frac{i_{L_f}(t)}{C_f} - \frac{v_{C_f}(t)}{R_L C_f}. \quad (5.12)$$

Mode *II* is equated by

$$\frac{di_{L_c}(t)}{dt} = \frac{V_{in}}{L_c}, \quad (5.13)$$

$$\frac{dv_{C_1}(t)}{dt} = 0, \quad (5.14)$$

$$\frac{di_{L_r}(t)}{dt} = -\frac{v_{C_r}(t)}{L_r}, \quad (5.15)$$

$$\frac{dv_{C_r}(t)}{dt} = \frac{i_{L_r}(t)}{C_r}, \quad (5.16)$$

$$\frac{dv_{C_2}(t)}{dt} = 0, \quad (5.17)$$

$$\frac{di_{L_f}(t)}{dt} = -\frac{v_{C_f}(t)}{L_f} \quad (5.18)$$

and

$$\frac{dv_{C_f}(t)}{dt} = \frac{i_{L_f}(t)}{C_f} - \frac{v_{C_f}(t)}{R_L C_f}. \quad (5.19)$$

The differential governing equations for mode *III* are

$$\frac{di_{L_c}(t)}{dt} = \frac{V_{in}}{L_c} - \frac{v_{C_1}(t)}{L_c}, \quad (5.20)$$

$$\frac{dv_{C_1}(t)}{dt} = \frac{i_{L_c}(t)}{C_1} - \frac{i_{L_r}(t)}{C_1}, \quad (5.21)$$

$$\frac{di_{L_r}(t)}{dt} = \frac{v_{C_1}(t)}{L_r} - \frac{v_{C_r}(t)}{L_r}, \quad (5.22)$$

$$\frac{dv_{C_r}(t)}{dt} = \frac{i_{L_r}(t)}{C_r}, \quad (5.23)$$

$$\frac{dv_{C_2}(t)}{dt} = 0, \quad (5.24)$$

$$\frac{di_{L_f}(t)}{dt} = -\frac{v_{C_f}(t)}{L_f} \quad (5.25)$$

and

$$\frac{dv_{C_f}(t)}{dt} = \frac{i_{L_f}(t)}{C_f} - \frac{v_{C_f}(t)}{R_L C_f}. \quad (5.26)$$

Finally, mode *IV* is mathematically described by

$$\frac{di_{L_c}(t)}{dt} = \frac{V_{in}}{L_c} - \frac{v_{C_1}(t)}{L_c}, \quad (5.27)$$

$$\frac{dv_{C_1}(t)}{dt} = \frac{i_{L_c}(t)}{C_1} - \frac{i_{L_r}(t)}{C_1}, \quad (5.28)$$

$$\frac{di_{L_r}(t)}{dt} = \frac{v_{C_1}(t)}{L_r} - \frac{v_{C_r}(t)}{L_r} - \alpha \frac{v_{C_2}(t)}{L_r}, \quad (5.29)$$

$$\frac{dv_{C_r}(t)}{dt} = \frac{i_{L_r}(t)}{C_r}, \quad (5.30)$$

$$\frac{dv_{C_2}(t)}{dt} = \alpha \frac{i_{L_r}(t)}{C_2} - \frac{i_{L_f}(t)}{C_2}, \quad (5.31)$$

$$\frac{di_{L_f}(t)}{dt} = \frac{v_{C_2}(t)}{L_f} - \frac{v_{C_f}(t)}{L_f} \quad (5.32)$$

and

$$\frac{dv_{C_f}(t)}{dt} = \frac{i_{L_f}(t)}{C_f} - \frac{v_{C_f}(t)}{R_L C_f}. \quad (5.33)$$

The non-linear differential equations are equated based on the linear differential equations and the switching functions  $f_1(t)$  and  $f_2(t)$ . In (5.2), the coefficients of  $f_1(t)$  are defined at the interval  $D_c 2\pi - 2\pi$ . This means that, by multiplying the terms in the differential equations by  $f_1(t)$ , the terms are turned into zero at modes *I* and *II*. This is because modes *I* and *II* are defined from  $0-T_1$  and from  $T_1-D_c 2\pi$ , respectively. In other words, mode *I* and *II* are not included into the defined interval in (5.2).

In the same way, by multiplying the terms in the differential equations by  $f_2(t)$ , the terms are turned into zero at modes *II* and *III* due to the limits in the integral calculation in (5.4). Based on that, the non-linear equations are described as

$$\frac{di_{L_c}(t)}{dt} = \frac{V_{in}}{L_c} - \frac{v_{C_1}(t)}{L_c} f_1(t), \quad (5.34)$$

$$\frac{dv_{C_1}(t)}{dt} = \frac{i_{L_c}(t)}{C_1} f_1(t) - \frac{i_{L_r}(t)}{C_1} f_1(t), \quad (5.35)$$

$$\frac{di_{L_r}(t)}{dt} = \frac{v_{C_1}(t)}{L_r} f_1(t) - \frac{v_{C_r}(t)}{L_r} - \alpha \frac{v_{C_2}(t)}{L_r} f_2(t), \quad (5.36)$$

$$\frac{dv_{C_r}(t)}{dt} = \frac{i_{L_r}(t)}{C_r}, \quad (5.37)$$

$$\frac{dv_{C_2}(t)}{dt} = \alpha \frac{i_{L_r}(t)}{C_2} f_2(t) - \frac{i_{L_f}(t)}{C_2} f_2(t), \quad (5.38)$$

$$\frac{di_{L_f}(t)}{dt} = \frac{v_{C_2}(t)}{L_f} f_2(t) - \frac{v_{C_f}(t)}{L_f} \quad (5.39)$$

and

$$\frac{dv_{C_f}(t)}{dt} = \frac{i_{L_f}(t)}{C_f} - \frac{v_{C_f}(t)}{R_L C_f}. \quad (5.40)$$

### 5.3 CONVOLUTION BETWEEN SWITCHING FUNCTIONS AND STATE VARIABLES

The switching functions are composed of the Fourier coefficients, which are described based on the harmonic  $k$ . In this sense, in order to achieve a linear model, the switching functions in the non-linear differential equations are replaced by the Fourier coefficients regarding the harmonic of interest.

The non-linearity comes from the multiplication of a state variable by a switching function. The non-linearities are going to be replaced by terms generated from a convolution operation in the form (SANDERS et al., 1991):

$$\langle x(t) s_{1,2} \rangle_k = \sum_{i=-i_c}^{i_c} \langle x(t) \rangle_{k-i} \langle s_{1,2} \rangle_i, \quad (5.41)$$

in which,  $x(t)$  is a state variable,  $s_{1,2}$  represents a Fourier coefficient and  $i_c$  is the convolution index. In practical terms, the convolution operation allows the non-linearities avoidance by generating a sum of products of a state variable by a Fourier switching function coefficient.

The notation  $\langle \rangle_k$  should be used to denote the considered harmonic  $k$ , wherefore it is necessary to use the derivative property of Fourier (SANDERS et al., 1991):

$$\frac{d\langle x(t) \rangle_k}{dt} = \langle g(x(t), s_{1,2}) \rangle_k - jk\omega_s \langle x(t) \rangle_k, \quad (5.42)$$

being  $g(x(t), s_{1,2})$  a function that is dependent on a state variable and a Fourier coefficient.

Therefore, the differential equations become (time notation  $t$  is omitted for simplicity)

$$\frac{d\langle i_{L_c} \rangle_k}{dt} = \frac{V_{in}}{L_c} - \sum_{i=-i_c}^{i_c} \frac{\langle s_1 \rangle_i \langle v_{C_1} \rangle_{k-i}}{L_c} - jk\omega_s \langle i_{L_c} \rangle_k, \quad (5.43)$$



$$\frac{d\langle v_{C_1} \rangle_k}{dt} = \sum_{i=-i_c}^{i_c} \frac{\langle s_1 \rangle_i \langle i_{L_c} \rangle_{k-i}}{C_1} - \sum_{i=-i_c}^{i_c} \frac{\langle s_1 \rangle_i \langle i_{L_r} \rangle_{k-i}}{C_1} - jk\omega_s \langle v_{C_1} \rangle_k, \quad (5.44)$$

$$\frac{d\langle i_{L_r} \rangle_k}{dt} = \sum_{i=-i_c}^{i_c} \frac{\langle s_1 \rangle_i \langle v_{C_1} \rangle_{k-i}}{L_r} - \frac{\langle v_{C_r} \rangle_k}{L_r} - \alpha \sum_{i=-i_c}^{i_c} \frac{\langle s_2 \rangle_i \langle v_{C_2} \rangle_{k-i}}{L_r} - jk\omega_s \langle i_{L_r} \rangle_k, \quad (5.45)$$

$$\frac{d\langle v_{C_r} \rangle_k}{dt} = \frac{\langle i_{L_r} \rangle_k}{C_r} - jk\omega_s \langle v_{C_r} \rangle_k, \quad (5.46)$$

$$\frac{d\langle v_{C_2} \rangle_k}{dt} = \alpha \sum_{i=-i_c}^{i_c} \frac{\langle s_2 \rangle_i \langle i_{L_r} \rangle_{k-i}}{C_2} - \sum_{i=-i_c}^{i_c} \frac{\langle s_2 \rangle_i \langle i_{L_f} \rangle_{k-i}}{C_2} - jk\omega_s \langle v_{C_2} \rangle_k, \quad (5.47)$$

$$\frac{d\langle i_{L_f} \rangle_k}{dt} = \sum_{i=-i_c}^{i_c} \frac{\langle s_2 \rangle_i \langle v_{C_2} \rangle_{k-i}}{L_f} - \frac{\langle v_{C_f} \rangle_k}{L_f} - jk\omega_s \langle i_{L_f} \rangle_k, \quad (5.48)$$

and

$$\frac{d\langle v_{C_f} \rangle_k}{dt} = \frac{\langle i_{L_f} \rangle_k}{C_f} - \frac{\langle v_{C_f} \rangle_k}{R_L C_f} - jk\omega_s \langle v_{C_f} \rangle_k. \quad (5.49)$$

The set of differential equations should be applied for each value of harmonic  $k$ . In addition, the convolution index should be defined in order to solve the summation.

#### 5.4 LARGE-SIGNAL MODEL

By applying the summations, negative index terms appear. Also, the sets of differential equations become interdependent.

In order to obtain the large-signal model, it is important to note that each state variable with coefficient different from zero has a conjugate that must be considered. Furthermore, the maximum number of considered harmonics determines the order of the system. The selection of the harmonics is based on the harmonic content of the waveforms. A detailed study about that was performed by Engleitner (2011).

For the Class-E<sup>2</sup> resonant converter, it is going to be considered  $k_{max} = 5$ . Due to the high number of variables, auxiliary variables  $y_i$  are going to be defined in order to represent the real and imaginary parts. The definitions are performed considering the index  $a$  varying from 1 to  $k_{max}$  with steps of 1 and the index  $b$  varying from 1 to  $k_{max}$  with steps of 2. Also,  $k$  must be considered from 0 to  $k_{max}$  with steps of 1. The definitions are shown as follows:

$$\langle i_{L_c} \rangle_0 \triangleq y_1, \quad (5.50)$$

$$\langle i_{L_c} \rangle_k \triangleq y_{2a} + jy_{2a+1}, \quad (5.51)$$

$$\langle i_{L_c} \rangle_{-k} \triangleq y_{2a} - jy_{2a+1}, \quad (5.52)$$

$$\langle v_{C_1} \rangle_0 \triangleq y_{2k_{max}+2}, \quad (5.53)$$

$$\langle v_{C_1} \rangle_k \triangleq y_{2k_{max}+2+b} + jy_{2k_{max}+3+b}, \quad (5.54)$$

$$\langle v_{C_1} \rangle_{-k} \triangleq y_{2k_{max}+2+b} - jy_{2k_{max}+3+b}, \quad (5.55)$$

$$\langle i_{L_r} \rangle_0 \triangleq y_{4k_{max}+3}, \quad (5.56)$$

$$\langle i_{L_r} \rangle_k \triangleq y_{4k_{max}+3+b} + jy_{4k_{max}+4+b}, \quad (5.57)$$

$$\langle i_{L_r} \rangle_{-k} \triangleq y_{4k_{max}+3+b} - jy_{4k_{max}+4+b}, \quad (5.58)$$

$$\langle v_{C_r} \rangle_0 \triangleq y_{6k_{max}+4}, \quad (5.59)$$

$$\langle v_{C_r} \rangle_k \triangleq y_{6k_{max}+4+b} + jy_{4k_{max}+5+b}, \quad (5.60)$$

$$\langle v_{C_r} \rangle_{-k} \triangleq y_{6k_{max}+4+b} - jy_{6k_{max}+5+b}, \quad (5.61)$$

$$\langle v_{C_2} \rangle_0 \triangleq y_{8k_{max}+5}, \quad (5.62)$$

$$\langle v_{C_2} \rangle_k \triangleq y_{8k_{max}+5+b} + jy_{8k_{max}+6+b}, \quad (5.63)$$

$$\langle v_{C_2} \rangle_{-k} \triangleq y_{8k_{max}+5+b} - jy_{8k_{max}+6+b}, \quad (5.64)$$

$$\langle i_{L_f} \rangle_0 \triangleq y_{10k_{max}+6}, \quad (5.65)$$

$$\langle i_{L_f} \rangle_k \triangleq y_{10k_{max}+6+b} + jy_{10k_{max}+7+b}, \quad (5.66)$$

$$\langle i_{L_f} \rangle_{-k} \triangleq y_{10k_{max}+6+b} - jy_{10k_{max}+7+b}, \quad (5.67)$$

$$\langle v_{C_f} \rangle_0 \triangleq y_{12k_{max}+7}, \quad (5.68)$$

$$\langle v_{C_f} \rangle_k \triangleq y_{12k_{max}+7+b} + jy_{12k_{max}+8+b} \quad (5.69)$$

and

$$\langle v_{C_f} \rangle_{-k} \triangleq y_{12k_{max}+7+b} - jy_{12k_{max}+8+b}. \quad (5.70)$$

The definitions should be applied into the set of differential equations shown in the previous section. The convolution index determines the amount of terms generated by the summations, which implies in the number of terms from the definitions that should be replaced into the differential equations.

As a thumb-rule, the convolution index can be defined as 2 for converters with 2, 3 or 4 reactive components, and 3 for converters with 5, 6 or 7 reactive components. In the Class-E<sup>2</sup> converter, the convolution index was defined as 3.

Based on the order of the system  $n_o$  and the number maximum of selected harmonics  $k_{max}$ , the number of state variables  $nv$  can be found as

$$nv = n_o + 2k_{max}n_o. \quad (5.71)$$

In order to clarify how the definitions are applied into the differential equations, lets consider the equation for the choke inductor in (5.43). By considering  $i_c = 3$  and equating for  $k = 0$ , the following is obtained:

$$\begin{aligned} \frac{d\langle i_{L_c} \rangle_0}{dt} = & \frac{V_{in}}{L_c} - \frac{\langle s_1 \rangle_{-3} \langle v_{C_1} \rangle_3}{L_c} - \frac{\langle s_1 \rangle_{-2} \langle v_{C_1} \rangle_2}{L_c} - \frac{\langle s_1 \rangle_{-1} \langle v_{C_1} \rangle_1}{L_c} - \frac{\langle s_1 \rangle_0 \langle v_{C_1} \rangle_0}{L_c} \\ & - \frac{\langle s_1 \rangle_1 \langle v_{C_1} \rangle_{-1}}{L_c} - \frac{\langle s_1 \rangle_2 \langle v_{C_1} \rangle_{-2}}{L_c} - \frac{\langle s_1 \rangle_3 \langle v_{C_1} \rangle_{-3}}{L_c} - j\omega_s \langle i_{L_c} \rangle_0. \end{aligned} \quad (5.72)$$

The definitions should be applied into (5.72):

$$\begin{aligned} \frac{d\langle i_{L_c} \rangle_0}{dt} = & \frac{V_{in}}{L_c} - \frac{\langle s_1 \rangle_{-3} (y_{17} + jy_{18})}{L_c} - \frac{\langle s_1 \rangle_{-2} (y_{15} + jy_{16})}{L_c} - \frac{\langle s_1 \rangle_{-1} (y_{13} + jy_{14})}{L_c} - \frac{\langle s_1 \rangle_0 y_{12}}{L_c} \\ & - \frac{\langle s_1 \rangle_1 (y_{13} - jy_{14})}{L_c} - \frac{\langle s_1 \rangle_2 (y_{15} - jy_{16})}{L_c} - \frac{\langle s_1 \rangle_3 (y_{17} - jy_{18})}{L_c}. \end{aligned} \quad (5.73)$$

The coefficients for the switching function are evaluated based on (5.2), which leads

to:

$$\langle s_1 \rangle_0 = \frac{1}{2\pi} \left( \int_{D_c 2\pi}^{2\pi} e^{-j0\tau} d\tau \right) = 1 - D_c, \quad (5.74)$$

$$\langle s_1 \rangle_1 = \frac{j(1 - \cos(D_c 2\pi) + j \sin(D_c 2\pi))}{2\pi}, \quad (5.75)$$

$$\langle s_1 \rangle_2 = \frac{j(1 - \cos(D_c 4\pi) + j \sin(D_c 4\pi))}{4\pi}, \quad (5.76)$$

$$\langle s_1 \rangle_3 = \frac{j(1 - \cos(D_c 6\pi) + j \sin(D_c 6\pi))}{6\pi}, \quad (5.77)$$

$$\langle s_1 \rangle_{-1} = \frac{j(-1 + \cos(D_c 2\pi) + j \sin(D_c 2\pi))}{2\pi}, \quad (5.78)$$

$$\langle s_1 \rangle_{-2} = \frac{j(-1 + \cos(D_c 4\pi) + j \sin(D_c 4\pi))}{4\pi}, \quad (5.79)$$

$$\langle s_1 \rangle_{-3} = \frac{j(-1 + \cos(D_c 6\pi) + j \sin(D_c 6\pi))}{6\pi}. \quad (5.80)$$

By replacing the coefficients into (5.73) and re-arranging it, the following is obtained:

$$\begin{aligned} \frac{d\langle i_{L_c} \rangle_0}{dt} &= \frac{V_{in}}{L_c} + \frac{(-1 + D_c)}{L_c} y_{12} \\ &+ \left[ \frac{j(1 - \cos(D_c 2\pi) - j \sin(D_c 2\pi))}{2\pi L_c} - \frac{j(1 - \cos(D_c 2\pi) + j \sin(D_c 2\pi))}{2\pi L_c} \right] y_{13} \\ &+ \left[ -\frac{1 - \cos(D_c 2\pi) - j \sin(D_c 2\pi)}{2\pi L_c} - \frac{1 - \cos(D_c 2\pi) + j \sin(D_c 2\pi)}{2\pi L_c} \right] y_{14} \\ &+ \left[ \frac{j(1 - \cos(D_c 4\pi) - j \sin(D_c 4\pi))}{4\pi L_c} - \frac{j(1 - \cos(D_c 4\pi) + j \sin(D_c 4\pi))}{4\pi L_c} \right] y_{15} \\ &+ \left[ -\frac{1 - \cos(D_c 4\pi) - j \sin(D_c 4\pi)}{4\pi L_c} - \frac{1 - \cos(D_c 4\pi) + j \sin(D_c 4\pi)}{4\pi L_c} \right] y_{16} \\ &+ \left[ \frac{j(1 - \cos(D_c 6\pi) - j \sin(D_c 6\pi))}{6\pi L_c} - \frac{j(1 - \cos(D_c 6\pi) + j \sin(D_c 6\pi))}{6\pi L_c} \right] y_{17} \\ &+ \left[ -\frac{1 - \cos(D_c 6\pi) - j \sin(D_c 6\pi)}{6\pi L_c} - \frac{1 - \cos(D_c 6\pi) + j \sin(D_c 6\pi)}{6\pi L_c} \right] y_{18}. \end{aligned} \quad (5.81)$$

The next step is to separate the real and imaginary parts. If the considered harmonic of the state variable is 0, only the real part should be considered. If the considered harmonic is different from 0, then the state variable is split into two state variables. For

example,  $\text{Re}[d\langle i_{L_c} \rangle_1/dt] = y_2$  and  $\text{Im}[d\langle i_{L_c} \rangle_1/dt] = y_3$ . Thus,  $y_2$  is composed of the real terms and  $y_3$  of imaginary terms.

Equation (5.81) considers  $k = 0$ , which means that only the real part is considered. The resulting equation is

$$\begin{aligned} \frac{dy_1}{dt} = & \frac{V_{in}}{L_c} + \frac{(-1 + D_c)}{L_c} y_{12} + \left( \frac{\sin(D_c 2\pi)}{\pi L_c} \right) y_{13} + \left( \frac{-1 + \cos(D_c 2\pi)}{\pi L_c} \right) y_{14} + \left( \frac{\sin(D_c 4\pi)}{2\pi L_c} \right) y_{15} \\ & + \left( \frac{-1 + \cos(D_c 4\pi)}{2\pi L_c} \right) y_{16} + \left( \frac{\sin(D_c 6\pi)}{3\pi L_c} \right) y_{17} + \left( \frac{-1 + \cos(D_c 6\pi)}{3\pi L_c} \right) y_{18}. \end{aligned} \quad (5.82)$$

The state variables are now described by the definitions, named by  $y_i$ . One can see that  $d\langle i_{L_c} \rangle_0/dt$  was replaced by  $dy_1/dt$ .

Based on (5.71), the system has 77 state variables. This means that, manually derive all the equations, is a cumbersome task. In this sense, the development of the equations was performed based on an implementation of an algorithm. The algorithm performs all the aforementioned steps for any harmonic  $k$  and returns the state-space matrices. The algorithm code in high level of abstraction is described in Appendix F.

Some important notes about the construction of the large-signal model for the Class-E<sup>2</sup> converter are highlighted:

1. The input source  $V_{in}$  term must only appear in the differential equation related to  $k = 0$ ;
2. The summations can generate state-variables with index higher than  $k_{max}$ . In such cases, those terms must be neglected.

The large-signal model of the system is represented by a state-space model. The state-vector for the large-signal model is

$$\mathbf{x}(t) = [\mathbf{y}_1, \mathbf{y}_2, \mathbf{y}_3, \dots, \mathbf{y}_{77}]^T. \quad (5.83)$$

The large-signal state-space model can be described as

$$\dot{\mathbf{x}}(t) = \mathbf{A}_{\mathbf{L}77 \times 77} \mathbf{x}(t) + \mathbf{B}_{\mathbf{L}77 \times 1} V_{in}. \quad (5.84)$$

Due to the size of the matrices, their terms are detailed in Appendix G.

The solution of the large-signal model is given by

$$\mathbf{X} = -\mathbf{A}^{-1} \cdot \mathbf{B} V_{in}, \quad (5.85)$$

in which  $\mathbf{X}$  is the solution of the system in equilibrium (ERICKSON, 2000).

The solution of the large-signal model shows how the state variables behave in

steady-state condition. In order to reconstruct the waveforms, the Fourier series should be invoked as

$$x(t) = \langle X \rangle_0 + \sum_{k=1}^{k_{max}} 2(\langle X \rangle_k \cos(k\omega_s t) - \langle X \rangle_{-k} \sin(k\omega_s t)), \quad (5.86)$$

being  $\langle X \rangle_0$  the solution of the system in equilibrium considering  $k = 0$ . In addition  $\langle X \rangle_k$  and  $\langle X \rangle_{-k}$  represent the solutions for the other harmonics.

It is important to note that the large-signal was built based on the definitions  $y_i$ . This means, one should take care when applying (5.86) in a mathematical software. It is because, the positions of the terms in the state vector, are not necessarily the same provided by the summation in (5.86). In other words, subscript  $-k$  formally indicates the harmonic. However, computationally it can indicate a vector position.

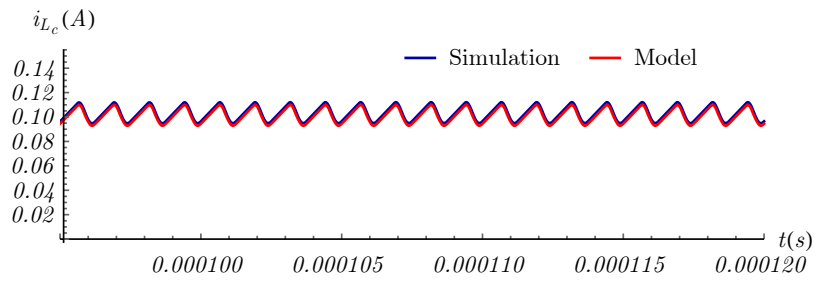
The large-signal model is going to be validate by a comparison between theoretical and simulation results. The used parameters to numerically solve the large-signal model are shown Table 5.1.

Table 5.1 – Parameters to numerically solve the large-signal model.

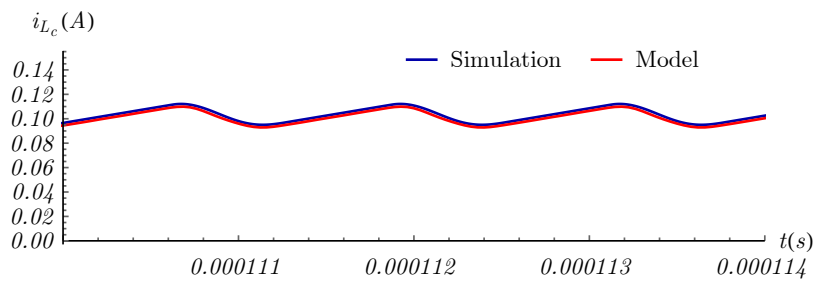
Parameter	Value
Input voltage, $V_{in}$	6.25
Resonant inductor, $L_r$	22 $\mu H$
Resonant capacitor, $C_r$	3.3 nF
Inverter capacitor, $C_1$	2.2 nF
Choke inductor, $L_c$	260 $\mu H$
Rectifier capacitor, $C_2$	1.2 nF
Output filter inductor, $L_f$	175 $\mu H$
Output filter capacitor, $C_f$	25 nF
Turns ratio, $\alpha$	1.0
Load, $R_L$	20 $\Omega$
Duty cycle, $D_c$	0.5
Diode turn-on time, $T_1$	0.659
Diode turn-off time, $T_2$	4.620

The comparisons for the choke inductor current  $i_{L_c}$ , inverter capacitor voltage  $v_{C_1}$ , resonant current  $i_{L_r}$ , resonant voltage  $v_{C_r}$ , rectifier capacitor voltage  $v_{C_2}$ , output filter inductor current  $i_{L_f}$  and output filter capacitor voltage  $v_{C_f}$  are shown in Figures 5.4-5.10. Different time windows are considered in order to make easier the graphical validation of the model.

Figure 5.4 – Choke inductor current,  $i_{L_c}(t)$ . (a) Time window:  $9.5 - 12 \mu s$ . (b) Time window:  $11 - 11.4 \mu s$ .



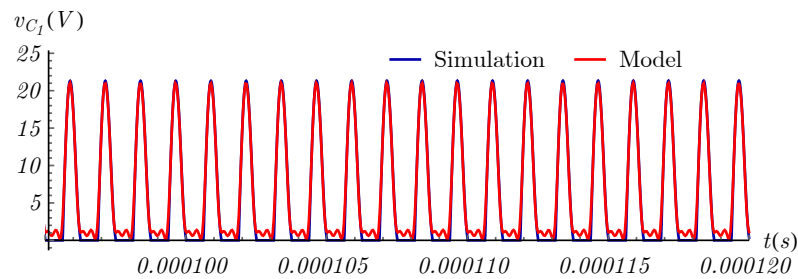
(a)



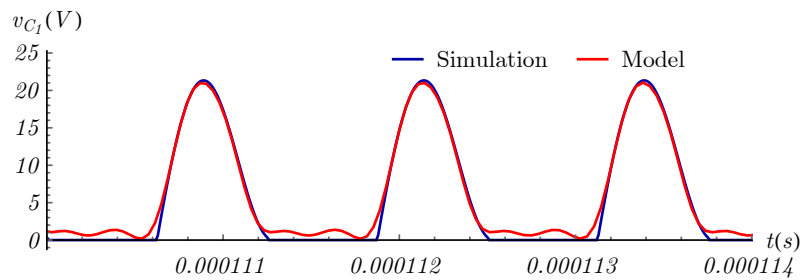
(b)

Source: Author.

Figure 5.5 – Inverter capacitor voltage,  $v_{C_1}(t)$ . (a) Time window:  $9.5 - 12 \mu s$ . (b) Time window:  $11 - 11.4 \mu s$ .



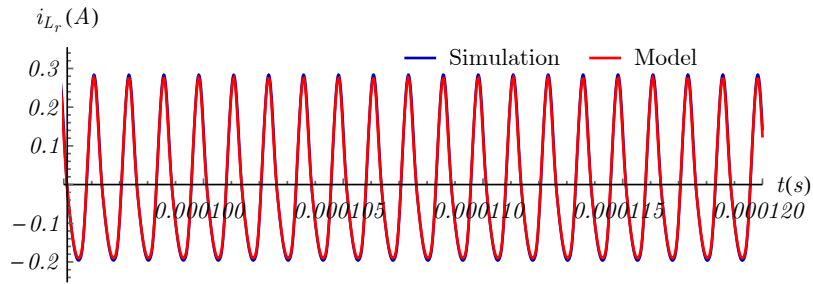
(a)



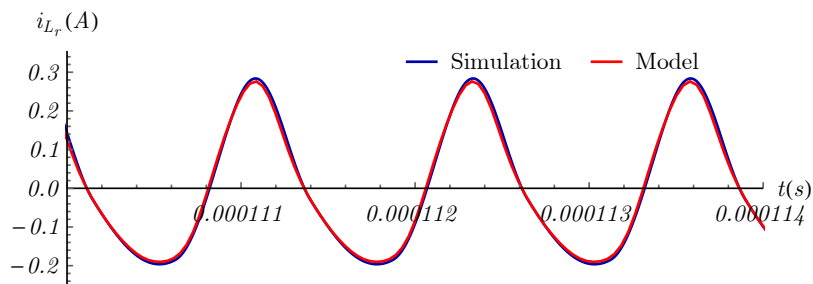
(b)

Source: Author.

Figure 5.6 – Resonant current,  $i_{L_r}(t)$ . (a) Time window:  $9.5 - 12 \mu s$ . (b) Time window:  $11 - 11.4 \mu s$ .



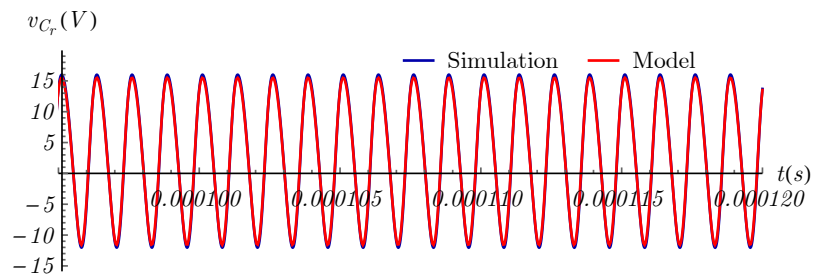
(a)



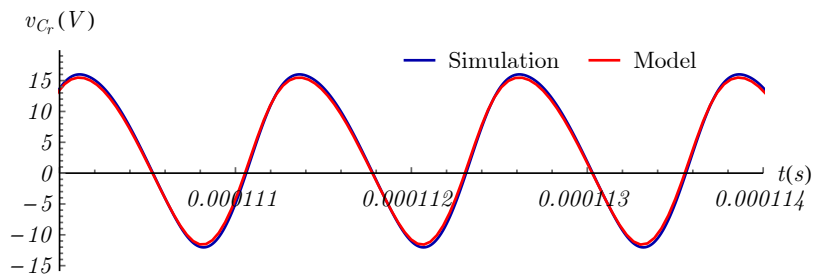
(b)

Source: Author.

Figure 5.7 – Resonant voltage,  $v_{C_r}(t)$ . (a) Time window:  $9.5 - 12 \mu s$ . (b) Time window:  $11 - 11.4 \mu s$ .



(a)

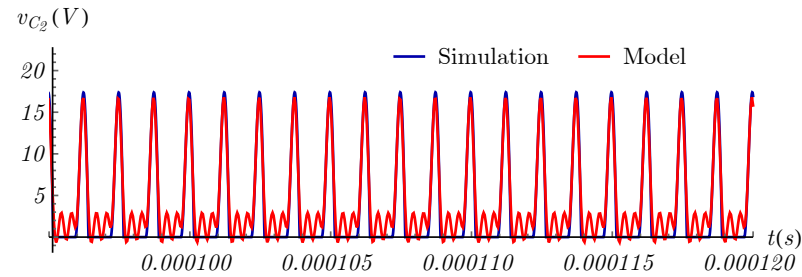


(b)

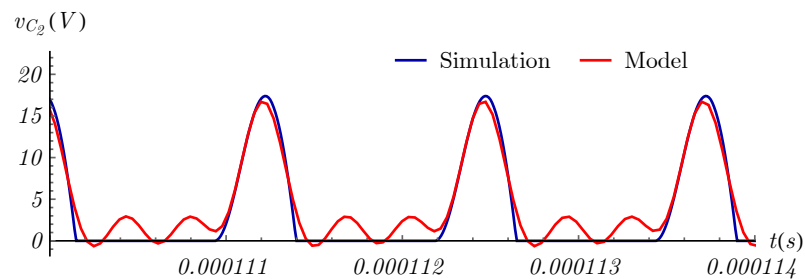
Source: Author.



Figure 5.8 – Rectifier capacitor voltage,  $v_{C_2}(t)$ . (a) Time window:  $9.5 - 12 \mu s$ . (b) Time window:  $11 - 11.4 \mu s$ .



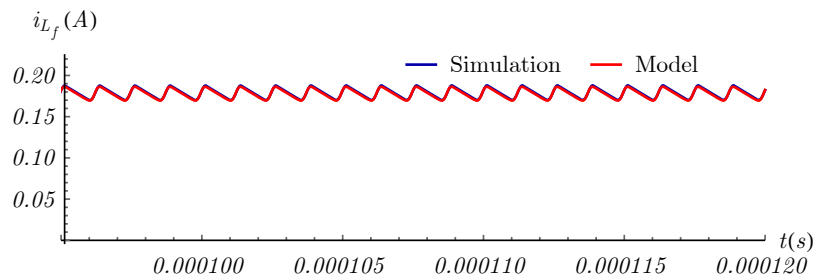
(a)



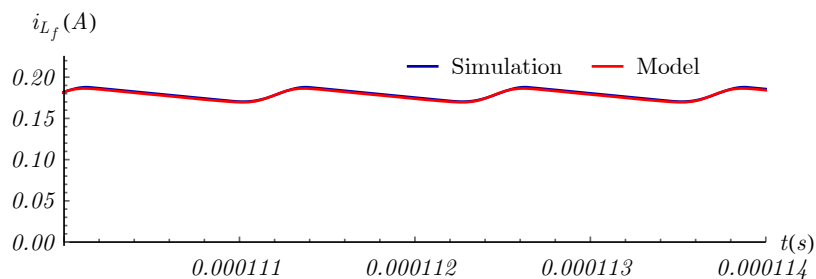
(b)

Source: Author.

Figure 5.9 – Output filter inductor current,  $i_{L_f}(t)$ . (a) Time window:  $9.5 - 12 \mu s$ . (b) Time window:  $11 - 11.4 \mu s$ .



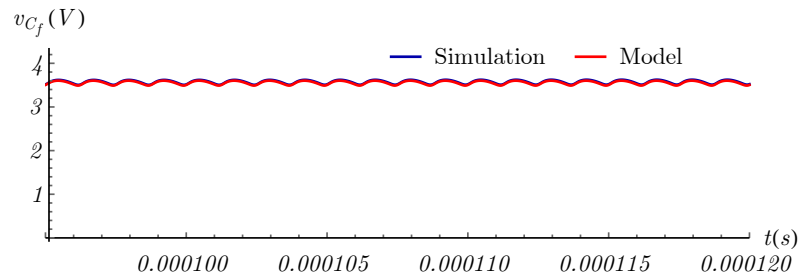
(a)



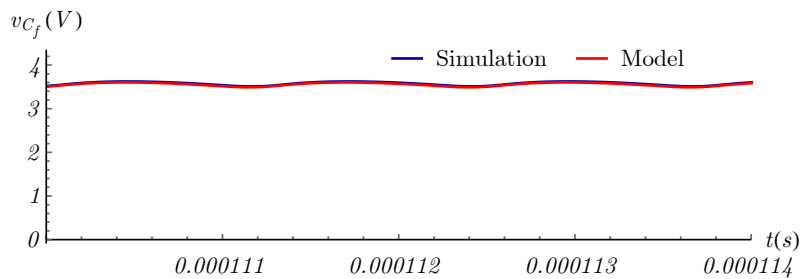
(b)

Source: Author.

Figure 5.10 – Output filter capacitor voltage,  $v_{C_f}(t)$ . (a) Time window:  $9.5 - 12 \mu s$ . (b) Time window:  $11 - 11.4 \mu s$ .



(a)



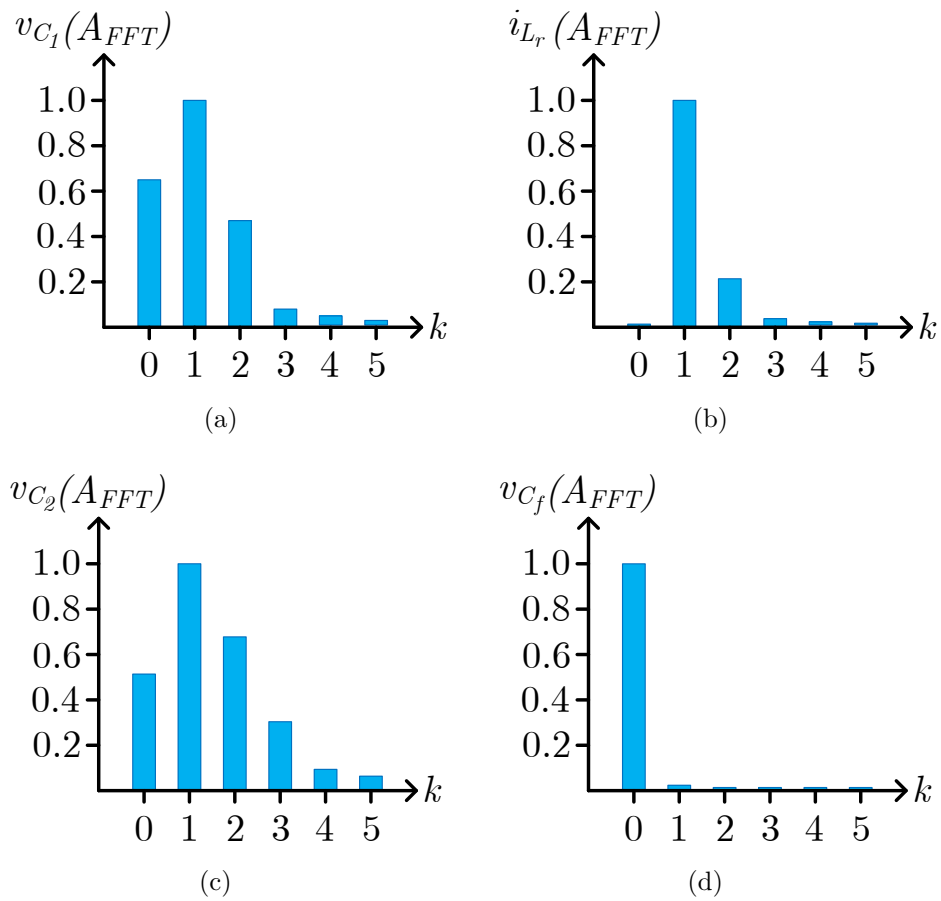
(b)

Source: Author.

In order to clarify the harmonic content influence on the waveforms, the *Fast Fourier Transform (FFT)* was applied into the Class-E<sup>2</sup> converter waveforms. Figure 5.11 shows the amplitude of the normalized harmonic content  $A_{FFT}$  for each harmonic  $k$ .

It can be seen in Figure 5.11(a) and Figure 5.11(c) that the capacitors  $C_1$  and  $C_2$  are influenced by the high-order harmonics. On the other hand, the resonant current is mostly affected by  $k = 1$ . Finally, the high-order harmonics has almost no influence on the output DC voltage, as depicted in Figure 5.11(d).

Figure 5.11 – Harmonic content of the Class-E<sup>2</sup> resonant converter. (a) Inverter capacitor  $C_1$  voltage,  $v_{C_1}$ . (b) Resonant current,  $i_{L_r}$ . (c) Rectifier capacitor  $C_2$  voltage,  $v_{C_2}$ . (d) Output voltage,  $v_{C_f}$ .



Source: Author.

## 5.5 SMALL-SIGNAL MODEL

The small-signal model is derived from the large-signal model. For this purpose, perturbations are inserted into the system's variables and the non-linear second order terms are neglected. The perturbation and linearization are performed based on Engleitner (2011) and Erickson (2000). The perturbation in the input source, frequency and state variables are given by

$$\langle u(t) \rangle_{T_s} = V_{in} + \hat{v}_{in}, \quad (5.87)$$

$$\langle \omega_s \rangle_{T_s} = \Omega_s + \hat{\omega}_s, \quad (5.88)$$

and

$$\langle y(t) \rangle_{T_s} = Y + \hat{y}, \quad (5.89)$$

in which:  $\hat{v}_{in}$ ,  $\hat{\omega}_s$  and  $\hat{y}$  are small variations in the input source, frequency and state variables, respectively.  $\Omega_s$  is the operating frequency and  $Y$  is the equilibrium solution of the large-signal model, which means  $Y = X$ . For clarification,  $Y$  is represented as

$$\mathbf{Y} = [\langle \mathbf{I}_{L_c} \rangle_{\mathbf{k}}, \langle \mathbf{V}_{C_1} \rangle_{\mathbf{k}}, \langle \mathbf{I}_{L_r} \rangle_{\mathbf{k}}, \langle \mathbf{V}_{C_r} \rangle_{\mathbf{k}}, \langle \mathbf{V}_{C_2} \rangle_{\mathbf{k}}, \langle \mathbf{I}_{L_f} \rangle_{\mathbf{k}}, \langle \mathbf{V}_{C_f} \rangle_{\mathbf{k}}]^T. \quad (5.90)$$

The capital letters in (5.90) indicates the constant value from the equilibrium solution of the large-signal model.

The small-signal model is represented by its state-space representation

$$\dot{\hat{\mathbf{x}}}(t) = \mathbf{A}_{S_{77 \times 77}} \hat{\mathbf{x}}(t) + \mathbf{B}_{S_{77 \times 2}} \hat{\mathbf{u}}_{\mathbf{d}}(t)_{2 \times 1}. \quad (5.91)$$

The state-vector of the small-signal model is given as

$$\hat{\mathbf{x}}(t) = [\hat{y}_1, \hat{y}_2, \hat{y}_3, \dots, \hat{y}_{77}]^T. \quad (5.92)$$

$\hat{\mathbf{u}}_{\mathbf{d}}(t)_{2 \times 1}$  represents the disturbances that can be added to evaluate the model. In this case, frequency and input source are considered, thus

$$\hat{\mathbf{u}}_{\mathbf{d}}(t)_{2 \times 1} = \begin{bmatrix} \hat{\omega}_s \\ \hat{v}_{in} \end{bmatrix}. \quad (5.93)$$

The state-space matrices are based on the differential equations after the perturbation and linearization. The small-signal differential equations for the Class-E<sup>2</sup> resonant

converter are given by

$$\frac{d\langle \hat{i}_{L_c} \rangle_k}{dt} = \frac{\hat{v}_{in}}{L_c} - \sum_{i=-i_c}^{i_c} \frac{\langle s_1 \rangle_i \langle \hat{v}_{C_1} \rangle_{k-i}}{L_c} - jk\Omega_s \langle \hat{i}_{L_c} \rangle_k - jk\hat{\omega}_s \langle I_{L_c} \rangle_k, \quad (5.94)$$

$$\frac{d\langle \hat{v}_{C_1} \rangle_k}{dt} = \sum_{i=-i_c}^{i_c} \frac{\langle s_1 \rangle_i \langle \hat{i}_{L_c} \rangle_{k-i}}{C_1} - \sum_{i=-i_c}^{i_c} \frac{\langle s_1 \rangle_i \langle \hat{i}_{L_r} \rangle_{k-i}}{C_1} - jk\Omega_s \langle \hat{v}_{C_1} \rangle_k - jk\hat{\omega}_s \langle V_{C_1} \rangle_k, \quad (5.95)$$

$$\frac{d\langle \hat{i}_{L_r} \rangle_k}{dt} = \sum_{i=-i_c}^{i_c} \frac{\langle s_1 \rangle_i \langle \hat{v}_{C_1} \rangle_{k-i}}{L_r} - \frac{\langle \hat{v}_{C_r} \rangle_k}{L_r} - \alpha \sum_{i=-i_c}^{i_c} \frac{\langle s_2 \rangle_i \langle \hat{v}_{C_2} \rangle_{k-i}}{L_r} - jk\Omega_s \langle \hat{i}_{L_r} \rangle_k - jk\hat{\omega}_s \langle I_{L_r} \rangle_k, \quad (5.96)$$

$$\frac{d\langle \hat{v}_{C_r} \rangle_k}{dt} = \frac{\langle \hat{i}_{L_r} \rangle_k}{C_r} - jk\Omega_s \langle \hat{v}_{C_r} \rangle_k - jk\hat{\omega}_s \langle V_{C_r} \rangle_k, \quad (5.97)$$

$$\frac{d\langle \hat{v}_{C_2} \rangle_k}{dt} = \alpha \sum_{i=-i_c}^{i_c} \frac{\langle s_2 \rangle_i \langle \hat{i}_{L_r} \rangle_{k-i}}{C_2} - \sum_{i=-i_c}^{i_c} \frac{\langle s_2 \rangle_i \langle \hat{i}_{L_f} \rangle_{k-i}}{C_2} - jk\Omega_s \langle \hat{v}_{C_2} \rangle_k - jk\hat{\omega}_s \langle V_{C_2} \rangle_k, \quad (5.98)$$

$$\frac{d\langle \hat{i}_{L_f} \rangle_k}{dt} = \sum_{i=-i_c}^{i_c} \frac{\langle s_2 \rangle_i \langle \hat{v}_{C_2} \rangle_{k-i}}{L_f} - \frac{\langle \hat{v}_{C_f} \rangle_k}{L_f} - jk\Omega_s \langle \hat{i}_{L_f} \rangle_k - jk\hat{\omega}_s \langle I_{L_f} \rangle_k, \quad (5.99)$$

and

$$\frac{d\langle \hat{v}_{C_f} \rangle_k}{dt} = \frac{\langle \hat{i}_{L_f} \rangle_k}{C_f} - \frac{\langle \hat{v}_{C_f} \rangle_k}{R_L C_f} - jk\Omega_s \langle \hat{v}_{C_f} \rangle_k - jk\hat{\omega}_s \langle V_{C_f} \rangle_k. \quad (5.100)$$

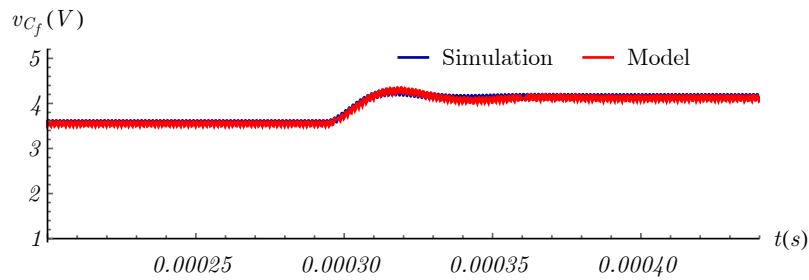
In the same way of the large-signal model, (5.94)-(5.100) should be evaluated considering  $\mathbf{k} = [\mathbf{0} \dots \mathbf{k}_{\max}]$ . The dynamic matrix is similar to the one developed for the large-signal model. The difference is related to the term  $\Omega_s$ , which replaces  $\omega_s$ . In this sense, one can resort the terms shown in Appendix G. The small-signal model input matrix  $\mathbf{B}_s$  is detailed in Appendix H.

In order to validate the model, Fig. 5.12 shows a disturbance in the input source applied into the output filter capacitor voltage. The considered disturbance is 1 V.

Fig. 5.13 shows the same disturbance into the resonant current. Model is compared to the simulation result.

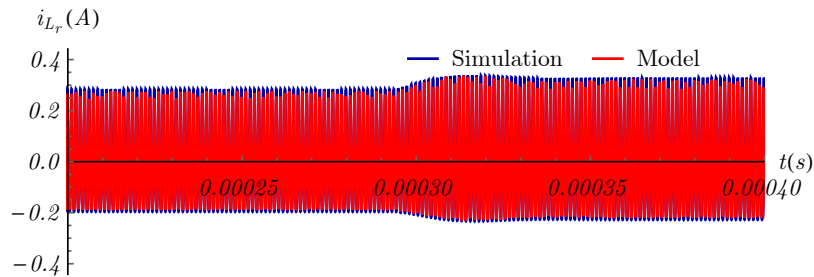
Finally, a disturbance in the frequency is applied into the output filter capacitor voltage, as shown in Fig. 5.14. The frequency disturbance is 20 kHz.

Figure 5.12 – Output filter capacitor voltage,  $v_{C_f}(t)$  with disturbance in the input voltage,  $\hat{v}_{in} = 1V$  (Time window: 200 – 440  $\mu s$ ).



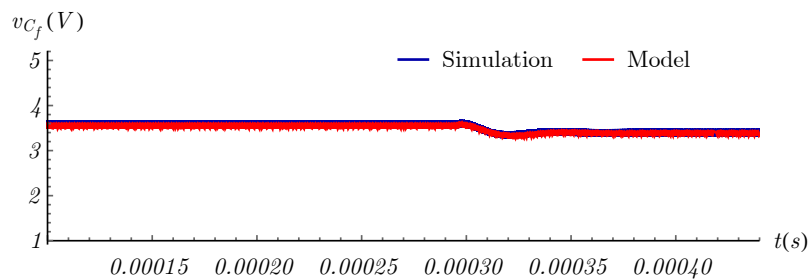
Source: Author

Figure 5.13 – Resonant current,  $i_{L_r}(t)$  with disturbance in the input voltage,  $\hat{v}_{in} = 1V$  (Time window: 200 – 400  $\mu s$ ).



Source: Author

Figure 5.14 – Output filter capacitor voltage,  $v_{C_f}(t)$  with disturbance in the frequency (Time window: 100 – 440  $\mu s$ ).



Source: Author

## 5.6 CONCLUSION

The dynamic model (AC model) was developed for the Class-E<sup>2</sup> resonant DC-DC converter in this Chapter. Due to the AC variables and waveforms with large ripple, the standard averaged and switched models are not suitable for resonant converters. In this sense, the generalized averaged model was used as methodology for the dynamic modeling.

First, switching functions were considered to describe the system based on non-linear differential equations. Subsequently, the convolution operator was applied between the switching functions and state-variables, which led to a linear state-space model that can be numerically solved. Additional steps were detailed in order to develop the large-signal and small-signal models, like as: definitions of variables, separation of real and imaginary parts, perturbation and linearization (small-signal model).

The reconstruction of the waveforms is based on the Fourier series. The large-signal model was evaluated by a comparison of the theoretical and simulation results. Furthermore, by applying disturbances in the frequency and the input voltage source, the small-signal model was validated.

Even though the development of a closed-loop control system for the electro-mechanical-acoustic CET system is out of scope of this Thesis, the developed dynamic model can be used to understand how the disturbances affect the system's variables. In this case, considering the Class-E<sup>2</sup> resonant converter as a topological representation of the CET system.





## 6 RESULTS

The main achieved results are shown in this Chapter. The main results are related to an evaluation of the developed models by comparing them to the experimental response of the physical system. The models are validated in different scenarios regarding transfer media and piezoelectric transducers.

This chapter also discusses the results related to the power conversion circuits designed for the electro-mechanical-acoustic CET system. In this sense, printed circuit boards (PCB) were developed to evaluate the designed converters.

### 6.1 COMPARISON BETWEEN MODELS AND EXPERIMENTAL RESPONSE

In this section, the results regarding the developed models are going to be compared to the experimental response of the physical system. The experimental response is the gain (dB) as function of the operating frequency (Hz).

The experimental response is obtained by means of the frequency analyzer FRA5087. The physical system is the piezoelectric transmitter connected to the solid transfer media, which is connected to the piezoelectric receiver. The frequency analyzer is connected, by means of a BNC cable, in the input of the system (transmitter), and the output of the system (receiver) is connected to the frequency analyzer.

First, the procedure to perform the comparison between the models and the experimental response is going to be shown in details considering one example by using a cylindrical aluminium with length  $l = 100\text{ mm}$  and radius  $R = 15\text{ mm}$ . The coupling factors are  $\alpha_{1,2} = 0.044$  and  $\gamma_{1,2} = 0.44$ . The piezoelectric transducers frequency is  $f = 738\text{ kHz}$ . Subsequently, other comparisons are going to be shown for different scenarios of transfer media and transducers. The properties of the materials that are going to be used are described in Table 6.1 and Table 6.2 for aluminium and steel, respectively.

Table 6.1 – Properties of the aluminium.

Parameter	Value
Density, $\rho$	$2710\text{ kg/m}^3$
Friction coefficient, $\mu_L$	$1.2\text{ m} \cdot \text{Pa} \cdot \text{s}$
Wave velocity, $C_L$	$6300\text{ m/s}$

Source: (ROSE, 2014; CHENG et al., 2014).

Table 6.2 – Properties of the steel.

Parameter	Value
Density, $\rho$	7832 kg/m <sup>3</sup>
Friction coefficient, $\mu_L$	4.5 m · Pa · s
Wave velocity, $C_L$	5800 m/s

Source: (ROSE, 2014; CHENG et al., 2014).

### 6.1.1 Results for aluminium - 100 mm length and 15 mm radius considering 738 kHz piezoelectric transducers

As a first comparison, the following theoretical and simulation results are going to be used: multiphysical model based on lumped parameters (mathematical software), equivalent electrical model (SPICE simulation) and PZT model (mathematical software).

The following experimental data are used: experimental raw data, experimental data with a Gaussian filter and experimental data with a moving average filter (MAF).

The system has reflections due to the characteristics of the materials, especially when considering metals. The experimental response of the system shows fluctuations in the gain when the frequency is varied. For this reason, a Gaussian and a moving average filters are used to smooth the data (SMITH, 2003).

The parameters for the 738 kHz piezoelectric transducers are described in Table 6.3. The piezoelectric transducers were designed for the selected frequencies and some parameters were given by the manufacturer and confirmed by measurement. The radius and thickness of the piezoelectric component are  $r = 0.01\text{ m}$  and  $t_p = 0.003\text{ m}$ .

Table 6.3 – Parameters for the  $f = 738\text{ kHz}$  piezoelectric transducers.

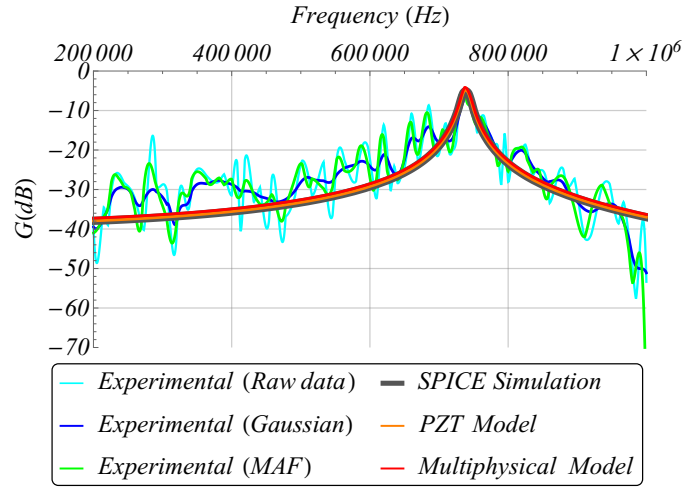
Parameter	Description	Value
$M_{1,2}$	Piezoelectric mass	0.0075 kg
$D_{1,2}$	Piezoelectric damper	696.373 N · s · m <sup>-1</sup>
$K_{1,2}$	Piezoelectric stiffness	16.1 × 10 <sup>10</sup> N · m <sup>-1</sup>
$C_{in,o}$	Piezoelectric capacitance	22 nF

The models are compared to the frequency response of the system that is obtained by sweeping the operating frequency from 200 kHz to 1 MHz. The comparison among experimental raw data, experimental data with Gaussian and moving average filter, SPICE simulation, PZT model and multiphysical model is shown in Figure 6.1.

The SPICE simulation, PZT model and multiphysical model are in agreement to each other. In addition, the models follow the behavior of the physical system when close to the frequency of  $f = 738\text{ Hz}$ .

It can be seen in Figure 6.1 that the experimental response has higher gain than

Figure 6.1 – Experimental x Theoretical: Gain (dB) as function of frequency (Hz) for  $f = 738 \text{ Hz}$  considering aluminium ( $l = 100 \text{ mm}$ ;  $R = 15 \text{ mm}$ ) as transfer media.



Source: Author.

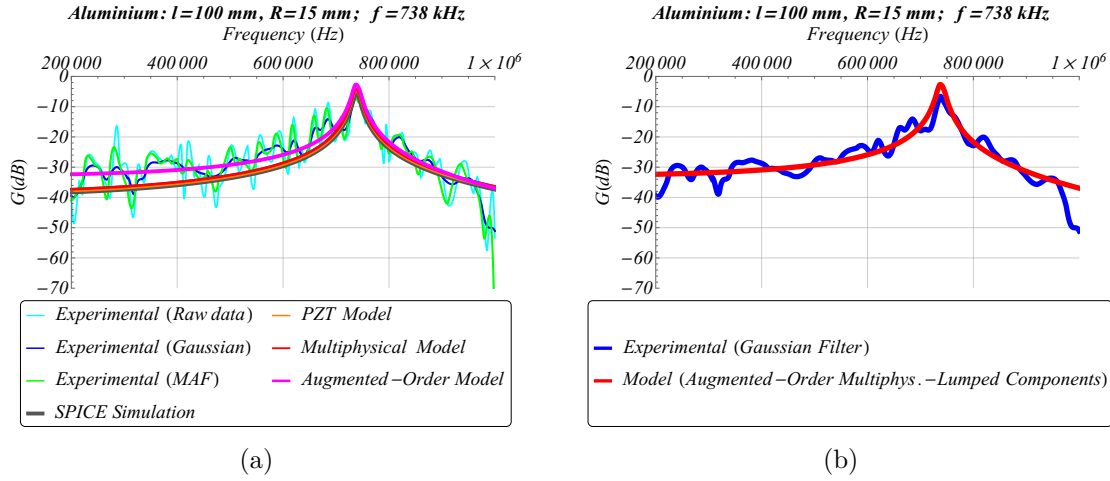
the models for frequencies below  $600 \text{ kHz}$  and especially in low frequencies ( $< 450 \text{ kHz}$ ). In this case, the model can be enhanced by introducing the features of the developed augmented-order model. Until now, the models shown in Figure 6.1 are analytical. The augmented-order model can be considered as a semi-analytical model because it is developed based on the analytical state-space model. However, it is based on a comparison of theoretical and experimental results in order to enhance desirable regions of the frequency response.

The augmented-order model is going to be used to amplify the gain of the multiphysical model for frequencies below  $600 \text{ kHz}$  while keeping the same gain of the multiphysical model for high frequencies. By allocating the constants as  $w_1 = 0.1$  and  $w_2 = 0.02$ , which are related to the relation of the angular resonant frequencies of the added elements in the augmented-order model to the acoustical resonant frequency of the multiphysical model, it is possible to enhance the model. The comparison of theoretical and experimental results including the augmented-order model is shown in Figure 6.2. In Figure 6.2(b), a comparison of the experimental data with Gaussian filter and the model based on the augmented-order model is depicted. The used parameters of the models are described in Table 6.5.

The parameters for the models are shown in the end of this section. Note that there are a sequence of Tables with the parameters for each of the comparisons that are performed in this section.

Regarding the choice of  $w_1$  and  $w_2$ , there are many techniques to allocate them. They can be chosen based on the designer's understanding of the system. In addition, search and optimization algorithms can be used to find the values. However, such tech-

Figure 6.2 – Experimental x Theoretical: Gain ( $dB$ ) as function of frequency ( $Hz$ ) for  $f = 738 Hz$  considering aluminium ( $l = 100 mm$ ;  $R = 15 mm$ ) as transfer media.



Source: Author.

niques are out of the scope of this Thesis and are suggested as future works. In the next subsections, the results for other transfer medias and transducers are going to be shown. Later, an error analysis between the experimental data and the models is going to be performed.

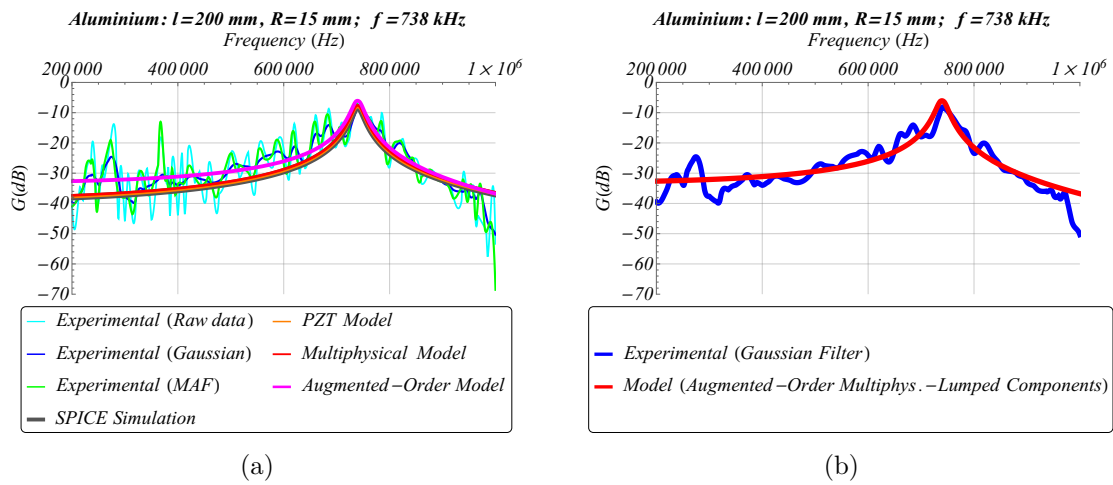
### 6.1.2 Results for aluminium - 200 mm length and 15 mm radius considering 738 kHz piezoelectric transducers

The same comparison in the previous subsection is going to be shown considering the transfer media as a cylindrical aluminium element with  $l = 200 mm$  and  $R = 15 mm$ . The comparison is shown in Figure 6.3, in which the experimental raw data, Gaussian filter and moving average filter are compared to the models in Figure 6.3(a), and the comparison between the augmented-order model and the filtered experimental data by Gaussian filter is portrayed in Figure 6.3(b). The constants for the augmented-order model are  $w_1 = 0.1$  and  $w_2 = 0.03$ . The parameters for the models are described in Table 6.6, in the end of this section.

### 6.1.3 Results for steel - 100 mm length and 15 mm radius considering 738 kHz piezoelectric transducers

The analysis is now performed considering steel as transfer media. In this case, the properties of the material lead to changes in the equivalent acoustical components.

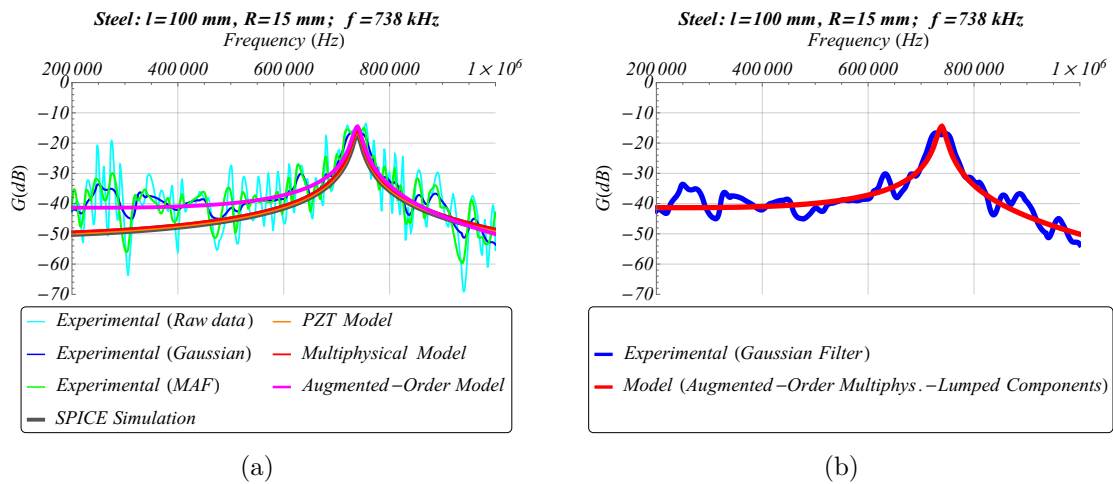
Figure 6.3 – Experimental x Theoretical: Gain ( $dB$ ) as function of frequency ( $Hz$ ) for  $f = 738 Hz$  considering aluminium ( $l = 200 mm$ ;  $R = 15 mm$ ) as transfer media.



Source: Author.

The comparison between experimental and theoretical results are shown in Figure 6.4.

Figure 6.4 – Experimental x Theoretical: Gain ( $dB$ ) as function of frequency ( $Hz$ ) for  $f = 738 Hz$  considering steel ( $l = 100 mm$ ;  $R = 15 mm$ ) as transfer media.



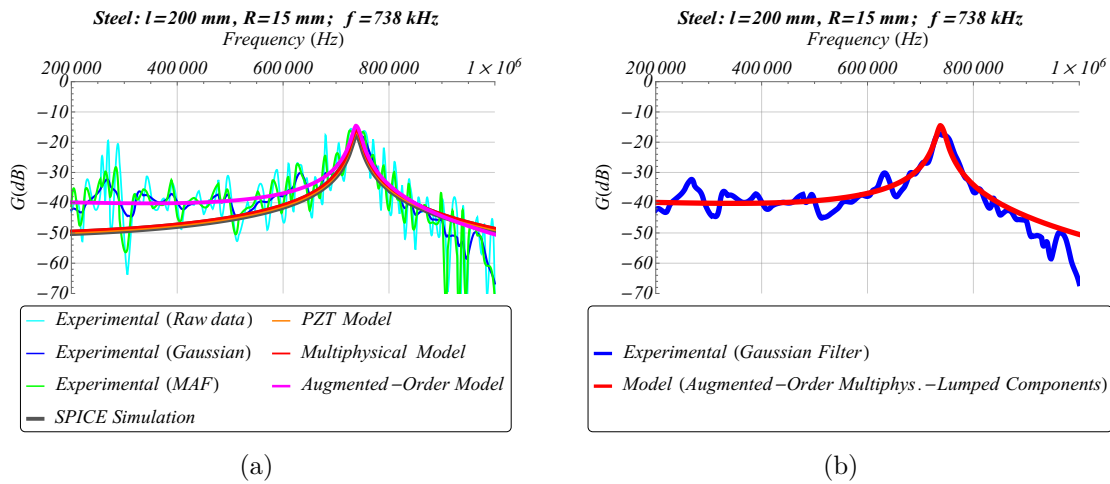
Source: Author.

The constants for the augmented-order model are  $w_1 = 0.01$  and  $w_2 = 0.05$ . The parameters for the models are described in Table 6.7.

### 6.1.4 Results for steel - 200 mm length and 15 mm radius considering 738 kHz piezoelectric transducers

The length of the transfer media is going to be considered as  $l = 200\text{ m}$ . The comparison is shown in Figure 6.5.

Figure 6.5 – Experimental x Theoretical: Gain (dB) as function of frequency (Hz) for  $f = 738\text{ Hz}$  considering steel ( $l = 200\text{ mm}$ ;  $R = 15\text{ mm}$ ) as transfer media.



Source: Author.

The constants for the augmented-order model are  $w_1 = 0.3$  and  $w_2 = 0.013$ . The parameters for the models are described in Table 6.8.

### 6.1.5 Results for aluminium - 100 mm length and 15 mm radius considering 1040 kHz piezoelectric transducers

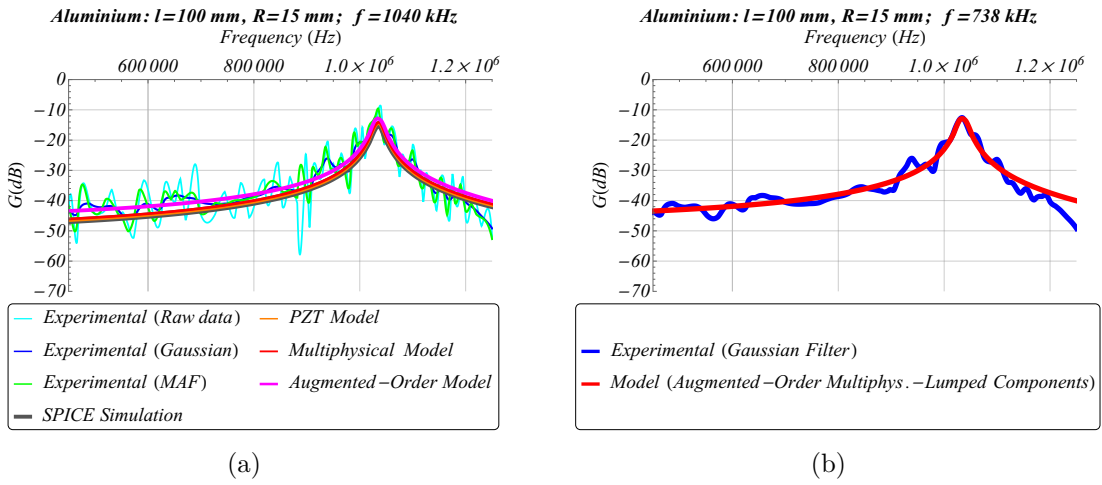
In order to evaluate different transducers, the models are going to be compared to the experimental results considering piezoelectric transducers with main frequency of  $1040\text{ kHz}$ . The parameters for the  $1040\text{ kHz}$  piezoelectric transducers are described in Table 6.4. It is considered  $r = 0.01\text{ m}$  and  $t_p = 0.003\text{ m}$ .

The comparison between experimental and theoretical for this scenario is shown in Figure 6.6. The comparison is also performed considering the experimental data (raw, Gaussian and moving average filter) and the SPICE simulation, PZT, multiphysical and augmented-order models. In addition, the comparison between the augmented-order model and the experimental data with Gaussian filter is highlighted.

The constants are  $w_1 = 0.05$  and  $w_2 = 0.09$ . The parameters for the models are described in Table 6.9. For the  $1040\text{ kHz}$  piezoelectric transducer, the frequency sweeping was performed from  $450\text{ kHz}$  to  $1250\text{ kHz}$ .

Table 6.4 – Parameters for the  $f = 1040 \text{ kHz}$  piezoelectric transducers.

Parameter	Description	Value
$M_{1,2}$	Piezoelectric mass	$0.0075 \text{ kg}$
$D_{1,2}$	Piezoelectric damper	$975.465 \text{ N} \cdot \text{s} \cdot \text{m}^{-1}$
$K_{1,2}$	Piezoelectric stiffness	$3.171 \times 10^{11} \text{ N} \times \text{m}^{-1}$
$C_{in,o}$	Piezoelectric capacitance	$0.16 \text{ nF}$

Figure 6.6 – Experimental x Theoretical: Gain ( $\text{dB}$ ) as function of frequency ( $\text{Hz}$ ) for  $f = 1040 \text{ Hz}$  considering aluminium ( $l = 100 \text{ mm}$ ;  $R = 15 \text{ mm}$ ) as transfer media.

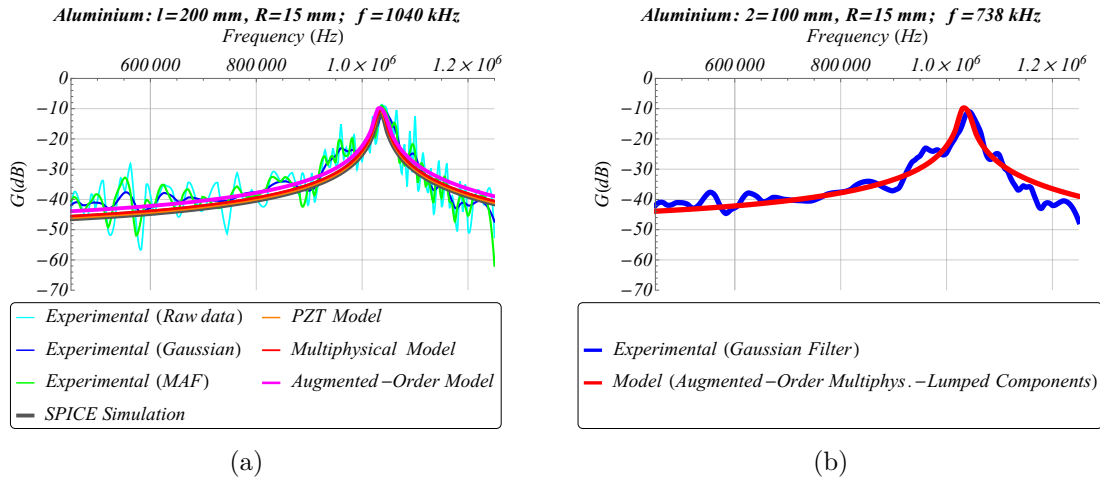
It can be seen that the predominant frequency is at  $1040 \text{ kHz}$ , which is the piezoelectric transducers frequency. These results show that the model is able to consider the system's predominant frequency. In other words, the main frequency of the multiphysical system.

### 6.1.6 Results for aluminium - 200 mm length and 15 mm radius considering 1040 kHz piezoelectric transducers

The same scenario of the previous subsection is considered for  $l = 200 \text{ mm}$ . The results are shown in Figure 6.7.

The constants for the augmented-order model are  $w_1 = 1.0$  and  $w_2 = 0.7$ . The parameters for the models are described in Table 6.10 in the end of this section.

Figure 6.7 – Experimental x Theoretical: Gain (dB) as function of frequency (Hz) for  $f = 1040 \text{ Hz}$  considering aluminium ( $l = 200 \text{ mm}$ ;  $R = 15 \text{ mm}$ ) as transfer media.

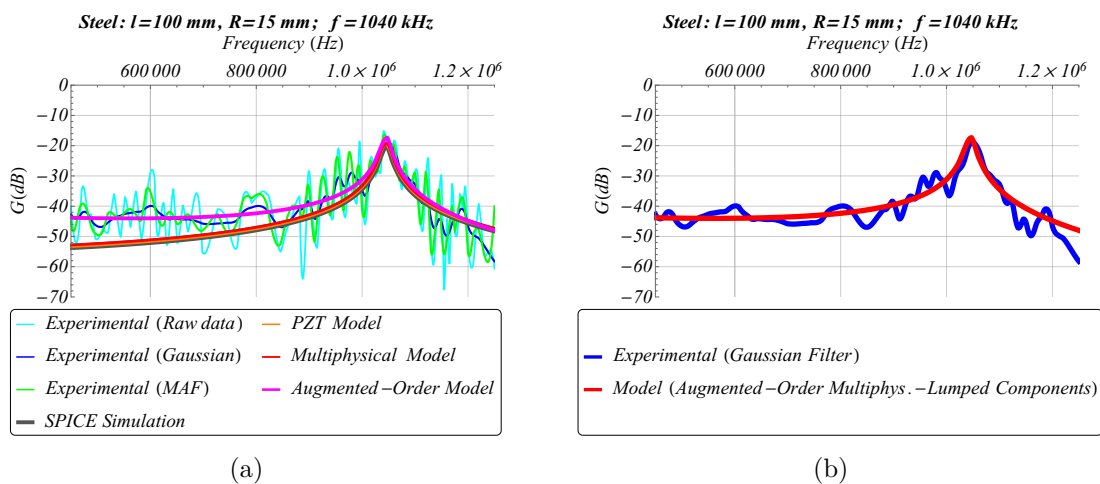


Source: Author.

### 6.1.7 Results for steel - 100 mm length and 15 mm radius considering 1040 kHz piezoelectric transducers

The comparison between theoretical and experimental results for the  $1040 \text{ kHz}$  piezoelectric transducers considering steel as transfer media is portrayed in Figure 6.8.

Figure 6.8 – Experimental x Theoretical: Gain (dB) as function of frequency (Hz) for  $f = 1040 \text{ Hz}$  considering steel ( $l = 100 \text{ mm}$ ;  $R = 15 \text{ mm}$ ) as transfer media.



Source: Author.

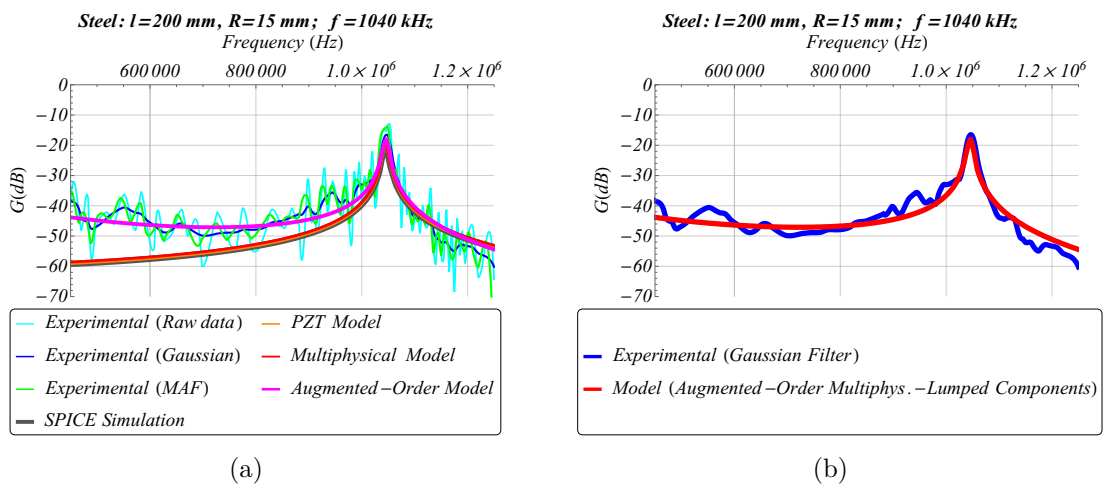
The constants for the augmented-order model are  $w_1 = 0.1$  and  $w_2 = 0.2$ . The parameters for the models are described in Table 6.11.



### 6.1.8 Results for steel - 200 mm length and 15 mm radius considering 1040 kHz piezoelectric transducers

The results considering the length of the steel as 200 mm for the 1040 kHz piezoelectric transducers are shown in Figure 6.9.

Figure 6.9 – Experimental x Theoretical: Gain (dB) as function of frequency (Hz) for  $f = 1040$  Hz considering steel ( $l = 200$  mm;  $R = 15$  mm) as transfer media.



Source: Author.

The constants for the augmented-order model are  $w_1 = 0.1$  and  $w_2 = 0.0152$ . The parameters for the models are described in Table 6.12.

Table 6.5 – Parameters for the models:  $f = 738 \text{ kHz}$  piezoelectric transducers considering aluminium ( $l = 100 \text{ mm}$ ;  $R = 15 \text{ mm}$ ) as transfer media.

Parameter	Description	Value	Model
$M_{a1}$	Equiv. acoustical mass	$2.60 \times 10^{-6} \text{ m}^4/\text{kg}$	Multiphysical
$N_{a1}$	Equiv. acoustical compliance	$6.57 \times 10^{-16} \text{ m}^3/\text{Pa}$	Multiphysical
$Z_{a1}$	Equiv. acoustical friction	$1.65 \times 10^{-7} \text{ m} \cdot \text{Pa} \cdot \text{s}$	Multiphysical
$L_{1,2}$	Inductor	$7.5 \text{ mH}$	SPICE
$C_{1,2}$	Capacitor	$6.2 \text{ pF}$	SPICE
$R_{1,2}$	Resistor	$680 \Omega$	SPICE
$L_a$	Inductor	$2.6 \mu\text{H}$	SPICE
$C_a$	Capacitor	$0.00062 \text{ pF}$	SPICE
$R_a$	Resistor	$0.16 \mu\Omega$	SPICE
$L_{pzt}$	Inductor	$199 \text{ mH}$	PZT
$C_{pzt}$	Capacitor	$0.22 \text{ pF}$	PZT
$R_{pzt}$	Resistor	$18 \text{ k}\Omega$	PZT
$w_1$	Design constant	0.1	Augmented
$w_2$	Design constant	0.02	Augmented
$M_{a2,a3}$	Equiv. acoustical mass	$2.60 \times 10^{-6} \text{ m}^4/\text{kg}$	Augmented
$Z_{a2,a3}$	Equiv. acoustical friction	$1.65 \times 10^{-7} \text{ m} \cdot \text{Pa} \cdot \text{s}$	Augmented
$N_{a2}$	Equiv. acoustical compliance	$1.31 \times 10^{-13} \text{ m}^3/\text{Pa}$	Augmented
$N_{a3}$	Equiv. acoustical compliance	$1.46 \times 10^{-12} \text{ m}^3/\text{Pa}$	Augmented

Table 6.6 – Parameters for the models:  $f = 738 \text{ kHz}$  piezoelectric transducers considering aluminium ( $l = 200 \text{ mm}$ ;  $R = 15 \text{ mm}$ ) as transfer media.

Parameter	Description	Value	Model
$M_{a1}$	Equiv. acoustical mass	$1.30 \times 10^{-6} \text{ m}^4/\text{kg}$	Multiphysical
$N_{a1}$	Equiv. acoustical compliance	$1.31 \times 10^{-15} \text{ m}^3/\text{Pa}$	Multiphysical
$Z_{a1}$	Equiv. acoustical friction	$8.28 \times 10^{-8} \text{ m} \cdot \text{Pa} \cdot \text{s}$	Multiphysical
$L_{1,2}$	Inductor	$7.5 \text{ mH}$	SPICE
$C_{1,2}$	Capacitor	$6.2 \text{ pF}$	SPICE
$R_{1,2}$	Resistor	$680 \Omega$	SPICE
$L_a$	Inductor	$1.30 \mu\text{H}$	SPICE
$C_a$	Capacitor	$0.0013 \text{ pF}$	SPICE
$R_a$	Resistor	$0.082 \mu\Omega$	SPICE
$L_{pzt}$	Inductor	$199 \text{ mH}$	PZT
$C_{pzt}$	Capacitor	$0.22 \text{ pF}$	PZT
$R_{pzt}$	Resistor	$27 \text{ k}\Omega$	PZT
$w_1$	Design constant	0.1	Augmented
$w_2$	Design constant	0.03	Augmented
$M_{a2,a3}$	Equiv. acoustical mass	$1.30 \times 10^{-6} \text{ m}^4/\text{kg}$	Augmented
$Z_{a2,a3}$	Equiv. acoustical friction	$8.28 \times 10^{-8} \text{ m} \cdot \text{Pa} \cdot \text{s}$	Augmented
$N_{a2}$	Equiv. acoustical compliance	$1.31 \times 10^{-13} \text{ m}^3/\text{Pa}$	Augmented
$N_{a3}$	Equiv. acoustical compliance	$1.46 \times 10^{-12} \text{ m}^3/\text{Pa}$	Augmented

Table 6.7 – Parameters for the models:  $f = 738 \text{ kHz}$  piezoelectric transducers considering steel ( $l = 100 \text{ mm}$ ;  $R = 15 \text{ mm}$ ) as transfer media.

Parameter	Description	Value	Model
$M_{a1}$	Equiv. acoustical mass	$0.902 \times 10^{-6} \text{ m}^4/\text{kg}$	Multiphysical
$N_{a1}$	Equiv. acoustical compliance	$0.26 \times 10^{-15} \text{ m}^3/\text{Pa}$	Multiphysical
$Z_{a1}$	Equiv. acoustical friction	$4.41 \times 10^{-8} \text{ m} \cdot \text{Pa} \cdot \text{s}$	Multiphysical
$L_{1,2}$	Inductor	$7.5 \text{ mH}$	SPICE
$C_{1,2}$	Capacitor	$6.2 \text{ pF}$	SPICE
$R_{1,2}$	Resistor	$680 \Omega$	SPICE
$L_a$	Inductor	$0.90 \mu\text{H}$	SPICE
$C_a$	Capacitor	$0.00024 \text{ pF}$	SPICE
$R_a$	Resistor	$0.043 \mu\Omega$	SPICE
$L_{pzt}$	Inductor	$199 \text{ mH}$	PZT
$C_{pzt}$	Capacitor	$0.22 \text{ pF}$	PZT
$R_{pzt}$	Resistor	$18 \text{ k}\Omega$	PZT
$w_1$	Design constant	0.01	Augmented
$w_2$	Design constant	0.05	Augmented
$M_{a2,a3}$	Equiv. acoustical mass	$0.902 \times 10^{-6} \text{ m}^4/\text{kg}$	Augmented
$Z_{a2,a3}$	Equiv. acoustical friction	$4.41 \times 10^{-8} \text{ m} \cdot \text{Pa} \cdot \text{s}$	Augmented
$N_{a2}$	Equiv. acoustical compliance	$26.8 \times 10^{-13} \text{ m}^3/\text{Pa}$	Augmented
$N_{a3}$	Equiv. acoustical compliance	$1.07 \times 10^{-13} \text{ m}^3/\text{Pa}$	Augmented

Table 6.8 – Parameters for the models:  $f = 738 \text{ kHz}$  piezoelectric transducers considering steel ( $l = 200 \text{ mm}$ ;  $R = 15 \text{ mm}$ ) as transfer media.

Parameter	Description	Value	Model
$M_{a1}$	Equiv. acoustical mass	$0.45 \times 10^{-6} \text{ m}^4/\text{kg}$	Multiphysical
$N_{a1}$	Equiv. acoustical compliance	$0.53 \times 10^{-15} \text{ m}^3/\text{Pa}$	Multiphysical
$Z_{a1}$	Equiv. acoustical friction	$2.20 \times 10^{-8} \text{ m} \cdot \text{Pa} \cdot \text{s}$	Multiphysical
$L_{1,2}$	Inductor	$7.5 \text{ mH}$	SPICE
$C_{1,2}$	Capacitor	$6.2 \text{ pF}$	SPICE
$R_{1,2}$	Resistor	$680 \Omega$	SPICE
$L_a$	Inductor	$0.45 \mu\text{H}$	SPICE
$C_a$	Capacitor	$0.00051 \text{ pF}$	SPICE
$R_a$	Resistor	$0.022 \mu\Omega$	SPICE
$L_{pzt}$	Inductor	$199 \text{ mH}$	PZT
$C_{pzt}$	Capacitor	$0.24 \text{ pF}$	PZT
$R_{pzt}$	Resistor	$18 \text{ k}\Omega$	PZT
$w_1$	Design constant	0.3	Augmented
$w_2$	Design constant	0.013	Augmented
$M_{a2,a3}$	Equiv. acoustical mass	$0.45 \times 10^{-6} \text{ m}^4/\text{kg}$	Augmented
$Z_{a2,a3}$	Equiv. acoustical friction	$2.20 \times 10^{-8} \text{ m} \cdot \text{Pa} \cdot \text{s}$	Augmented
$N_{a2}$	Equiv. acoustical compliance	$5.96 \times 10^{-15} \text{ m}^3/\text{Pa}$	Augmented
$N_{a3}$	Equiv. acoustical compliance	$3.17 \times 10^{-12} \text{ m}^3/\text{Pa}$	Augmented

Table 6.9 – Parameters for the models:  $f = 1040 \text{ kHz}$  piezoelectric transducers considering aluminium ( $l = 100 \text{ mm}$ ;  $R = 15 \text{ mm}$ ) as transfer media.

Parameter	Description	Value	Model
$M_{a1}$	Equiv. acoustical mass	$2.60 \times 10^{-6} \text{ m}^4/\text{kg}$	Multiphysical
$N_{a1}$	Equiv. acoustical compliance	$6.57 \times 10^{-16} \text{ m}^3/\text{Pa}$	Multiphysical
$Z_{a1}$	Equiv. acoustical friction	$16.5 \times 10^{-8} \text{ m} \cdot \text{Pa} \cdot \text{s}$	Multiphysical
$L_{1,2}$	Inductor	$7.5 \text{ mH}$	SPICE
$C_{1,2}$	Capacitor	$3 \text{ pF}$	SPICE
$R_{1,2}$	Resistor	$910 \Omega$	SPICE
$L_a$	Inductor	$0.45 \mu\text{H}$	SPICE
$C_a$	Capacitor	$0.00051 \text{ pF}$	SPICE
$R_a$	Resistor	$0.022 \mu\Omega$	SPICE
$L_{pzt}$	Inductor	$199 \text{ mH}$	PZT
$C_{pzt}$	Capacitor	$0.24 \text{ pF}$	PZT
$R_{pzt}$	Resistor	$18 \text{ k}\Omega$	PZT
$w_1$	Design constant	0.05	Augmented
$w_2$	Design constant	0.09	Augmented
$M_{a2,a3}$	Equiv. acoustical mass	$2.60 \times 10^{-6} \text{ m}^4/\text{kg}$	Augmented
$Z_{a2,a3}$	Equiv. acoustical friction	$16.5 \times 10^{-8} \text{ m} \cdot \text{Pa} \cdot \text{s}$	Augmented
$N_{a2}$	Equiv. acoustical compliance	$2.62 \times 10^{-13} \text{ m}^3/\text{Pa}$	Augmented
$N_{a3}$	Equiv. acoustical compliance	$8.11 \times 10^{-14} \text{ m}^3/\text{Pa}$	Augmented

Table 6.10 – Parameters for the models:  $f = 1040 \text{ kHz}$  piezoelectric transducers considering aluminium ( $l = 200 \text{ mm}$ ;  $R = 15 \text{ mm}$ ) as transfer media.

Parameter	Description	Value	Model
$M_{a1}$	Equiv. acoustical mass	$1.30 \times 10^{-6} \text{ m}^4/\text{kg}$	Multiphysical
$N_{a1}$	Equiv. acoustical compliance	$1.31 \times 10^{-15} \text{ m}^3/\text{Pa}$	Multiphysical
$Z_{a1}$	Equiv. acoustical friction	$8.28 \times 10^{-8} \text{ m} \cdot \text{Pa} \cdot \text{s}$	Multiphysical
$L_{1,2}$	Inductor	$7.5 \text{ mH}$	SPICE
$C_{1,2}$	Capacitor	$3 \text{ pF}$	SPICE
$R_{1,2}$	Resistor	$910 \Omega$	SPICE
$L_a$	Inductor	$1.30 \mu\text{H}$	SPICE
$C_a$	Capacitor	$0.0013 \text{ pF}$	SPICE
$R_a$	Resistor	$0.082 \mu\Omega$	SPICE
$L_{pzt}$	Inductor	$199 \text{ mH}$	PZT
$C_{pzt}$	Capacitor	$0.11 \text{ pF}$	PZT
$R_{pzt}$	Resistor	$16 \text{ k}\Omega$	PZT
$w_1$	Design constant	1.0	Augmented
$w_2$	Design constant	0.7	Augmented
$M_{a2,a3}$	Equiv. acoustical mass	$1.30 \times 10^{-6} \text{ m}^4/\text{kg}$	Augmented
$Z_{a2,a3}$	Equiv. acoustical friction	$8.28 \times 10^{-8} \text{ m} \cdot \text{Pa} \cdot \text{s}$	Augmented
$N_{a2}$	Equiv. acoustical compliance	$1.31 \times 10^{-15} \text{ m}^3/\text{Pa}$	Augmented
$N_{a3}$	Equiv. acoustical compliance	$2.68 \times 10^{-15} \text{ m}^3/\text{Pa}$	Augmented

Table 6.11 – Parameters for the models:  $f = 1040 \text{ kHz}$  piezoelectric transducers considering steel ( $l = 100 \text{ mm}$ ;  $R = 15 \text{ mm}$ ) as transfer media.

Parameter	Description	Value	Model
$M_{a1}$	Equiv. acoustical mass	$9.02 \times 10^{-7} \text{ m}^4/\text{kg}$	Multiphysical
$N_{a1}$	Equiv. acoustical compliance	$2.68 \times 10^{-16} \text{ m}^3/\text{Pa}$	Multiphysical
$Z_{a1}$	Equiv. acoustical friction	$4.41 \times 10^{-8} \text{ m} \cdot \text{Pa} \cdot \text{s}$	Multiphysical
$L_{1,2}$	Inductor	$7.5 \text{ mH}$	SPICE
$C_{1,2}$	Capacitor	$3 \text{ pF}$	SPICE
$R_{1,2}$	Resistor	$910 \Omega$	SPICE
$L_a$	Inductor	$0.90 \mu\text{H}$	SPICE
$C_a$	Capacitor	$0.00027 \text{ pF}$	SPICE
$R_a$	Resistor	$0.043 \mu\Omega$	SPICE
$L_{pzt}$	Inductor	$199 \text{ mH}$	PZT
$C_{pzt}$	Capacitor	$0.11 \text{ pF}$	PZT
$R_{pzt}$	Resistor	$24 \text{ k}\Omega$	PZT
$w_1$	Design constant	1.0	Augmented
$w_2$	Design constant	0.7	Augmented
$M_{a2,a3}$	Equiv. acoustical mass	$9.02 \times 10^{-7} \text{ m}^4/\text{kg}$	Augmented
$Z_{a2,a3}$	Equiv. acoustical friction	$4.41 \times 10^{-8} \text{ m} \cdot \text{Pa} \cdot \text{s}$	Augmented
$N_{a2}$	Equiv. acoustical compliance	$2.68 \times 10^{-14} \text{ m}^3/\text{Pa}$	Augmented
$N_{a3}$	Equiv. acoustical compliance	$6.70 \times 10^{-15} \text{ m}^3/\text{Pa}$	Augmented

Table 6.12 – Parameters for the models:  $f = 1040 \text{ kHz}$  piezoelectric transducers considering steel ( $l = 200 \text{ mm}$ ;  $R = 15 \text{ mm}$ ) as transfer media.

Parameter	Description	Value	Model
$M_{a1}$	Equiv. acoustical mass	$4.51 \times 10^{-7} \text{ m}^4/\text{kg}$	Multiphysical
$N_{a1}$	Equiv. acoustical compliance	$5.36 \times 10^{-16} \text{ m}^3/\text{Pa}$	Multiphysical
$Z_{a1}$	Equiv. acoustical friction	$2.20 \times 10^{-8} \text{ m} \cdot \text{Pa} \cdot \text{s}$	Multiphysical
$L_{1,2}$	Inductor	$7.5 \text{ mH}$	SPICE
$C_{1,2}$	Capacitor	$3 \text{ pF}$	SPICE
$R_{1,2}$	Resistor	$910 \Omega$	SPICE
$L_a$	Inductor	$0.45 \mu\text{H}$	SPICE
$C_a$	Capacitor	$0.00051 \text{ pF}$	SPICE
$R_a$	Resistor	$0.022 \mu\Omega$	SPICE
$L_{pzt}$	Inductor	$199 \text{ mH}$	PZT
$C_{pzt}$	Capacitor	$0.11 \text{ pF}$	PZT
$R_{pzt}$	Resistor	$12 \text{ k}\Omega$	PZT
$w_1$	Design constant	0.1	Augmented
$w_2$	Design constant	0.0152	Augmented
$M_{a2,a3}$	Equiv. acoustical mass	$4.51 \times 10^{-7} \text{ m}^4/\text{kg}$	Augmented
$Z_{a2,a3}$	Equiv. acoustical friction	$2.20 \times 10^{-8} \text{ m} \cdot \text{Pa} \cdot \text{s}$	Augmented
$N_{a2}$	Equiv. acoustical compliance	$5.36 \times 10^{-14} \text{ m}^3/\text{Pa}$	Augmented
$N_{a3}$	Equiv. acoustical compliance	$2.32 \times 10^{-12} \text{ m}^3/\text{Pa}$	Augmented

## 6.2 ERROR ANALYSIS

In order to quantitatively evaluate the models, an error analysis is performed in this section. The following error analysis techniques are used:

- Mean relative error ( $MRE$ );
- Standard deviation ( $\sigma$ );
- Quadratic error ( $\bar{q}$ ).

The mean relative error is calculated by

$$MRE(\%) = \left| \frac{Exp(f) - Theo(f)}{Exp(f)} \right| \times 100, \quad (6.1)$$

in which  $Exp(f)$  is a function dependent of frequency  $f$  related to the gain curve of the experimental response of the system and  $Theo(f)$  is a function dependent of frequency  $f$  related to the gain curve of the theoretical results.

The standard deviation is used to measure the dispersion of a set of values. When the values tend to be close to the mean, the standard deviation is low.

The standard deviation  $\sigma$  can be evaluated as

$$\sigma = \sqrt{\frac{1}{N} \sum_{i=1}^N (x_i - \mu)^2}, \quad (6.2)$$

being:  $N$  the number of elements,  $x_i$  the element related to index  $i$  and  $\mu$  is the mean of the values. The standard deviation is expressed in the same units of the data. In this case, it is going to be used to measure the dispersion of the error values.

The quadratic error is a technique to measure the error of a model. It can be calculated as:

$$\bar{q} = \sqrt{\frac{1}{N} \sum_{i=1}^N (\hat{x}_i - x_i)^2}, \quad (6.3)$$

in which  $\hat{x}_i$  represents the theoretical values,  $x_i$  the experimental values and  $N$  is the number of elements.

The quadratic error represents the average squared difference between the theoretical and experimental values. The error analysis was performed by evaluating the comparison between the experimental data with Gaussian filter and the theoretical results from the augmented-order multiphysical model based on lumped components.

The error analysis is conducted for all the results shown in the previous section. The idea is to qualitatively validate the models by calculating the errors between experimental and theoretical in percentage, which gives a readable indicator for the proposed method.

The error analysis is summarized in Table 6.13.

Table 6.13 – Error analysis for the comparison experimental x theoretical.

Setup	$MRE$	$\sigma$	$\bar{q}$
Aluminium: $l = 100\text{ mm}$ ; $R = 15\text{ mm}$ @738 kHz	10.61 %	10.73%	03.74 %
Aluminium: $l = 200\text{ mm}$ ; $R = 15\text{ mm}$ @738 kHz	10.27 %	08.76%	03.48 %
Steel: $l = 100\text{ mm}$ ; $R = 15\text{ mm}$ @738 kHz	06.95 %	05.74%	03.11 %
Steel: $l = 200\text{ mm}$ ; $R = 15\text{ mm}$ @738 kHz	06.19 %	05.25%	03.53 %
Aluminium: $l = 100\text{ mm}$ ; $R = 15\text{ mm}$ @1040 kHz	05.00 %	03.86%	02.23 %
Aluminium: $l = 200\text{ mm}$ ; $R = 15\text{ mm}$ @1040 kHz	07.64 %	06.49%	02.99 %
Steel: $l = 100\text{ mm}$ ; $R = 15\text{ mm}$ @1040 kHz	10.69 %	09.42%	05.69 %
Steel: $l = 200\text{ mm}$ ; $R = 15\text{ mm}$ @1040 kHz	05.65 %	04.24%	02.89 %

The mean relative error indicator is less than 10.7% for all the setups. The quadratic error is less than 5.7% for all the setups. The maximum mean relative error occurs for the steel with  $l = 100\text{ mm}$  and  $R = 15\text{ mm}$  at 1040 kHz while the maximum quadratic error occurs also for steel with  $l = 100\text{ mm}$  and  $R = 15\text{ mm}$  at 1040 kHz. The standard deviation indicates the volatility of the values. This means that the lower the value, the lower is the deviation of the values in comparison to their mean. The lower standard deviation occurs for aluminium with  $l = 100\text{ mm}$  and  $R = 15\text{ mm}$  at 1040 kHz.

### 6.3 POWER CONVERSION CIRCUITRY

Based on the developed methodology in Chapter 4, two power conversion circuits were designed and implemented in order to manage the power that is transferred through the electro-mechanical-acoustic CET system.

One board includes the Class-E resonant rectifier designed as subsystem of the Class-E<sup>2</sup> topology in Chapter 4. The other board includes a Cockcroft-Walton multiplier. The way to implement the standard formulas of the Cockcroft-Walton multiplier was to put them into a genetic algorithm especially developed for this purpose. The genetic algorithm is not considered as main part of this work. For this reason, it is detailed in Appendix D. The choice of the converters is based on the idea of showing one example for step-up applications (Cockcroft-Walton multiplier) and one for step-down applications (Class-E resonant rectifier.)

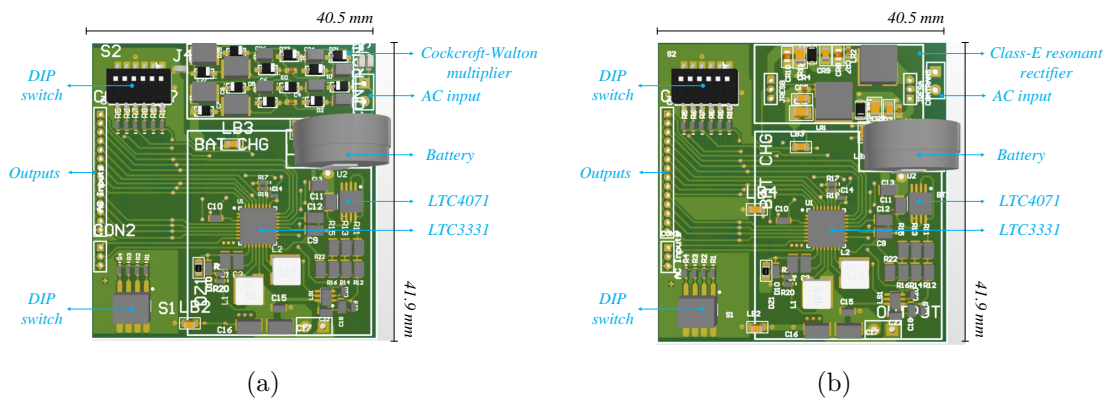
A maximum power point tracking and a battery charger were included in both boards. In order to match the impedances from the load and the electro-mechanical-acoustic system, the AC-DC converter must regulate its input voltage to provide a range that gets maximum power from the input. Due to the complexity of the system, it

is expected that uncertainties or changing in the parameters occur. For example, the transformation ratio can slightly vary due to the physical coupling between the transducers and the media. This leads to a different voltage transfer function from the ultrasound transmitter to the ultrasound receiver. In this sense, in order to develop a demonstrator with practical functionalities, the MPPT and the battery charger circuits were included in the boards.

The proposed solution for the MPPT circuit is a regulated buck-boost switched regulator from Linear Technology, the LTC3331. The battery charger circuit is the integrated circuit LTC4071.

The PCB layout of the developed system is depicted in Figure 6.10.

Figure 6.10 – Developed power conversion circuit. (a) AC-DC converter based on Cockcroft-Walton multiplier. (b) AC-DC converter based on Class-E resonant rectifier.



Source: Author.

The experimental setup is portrayed in Figure 6.11. The complete system is shown in Figure 6.11(a) and the developed printed circuit boards in Figure 6.11(b).

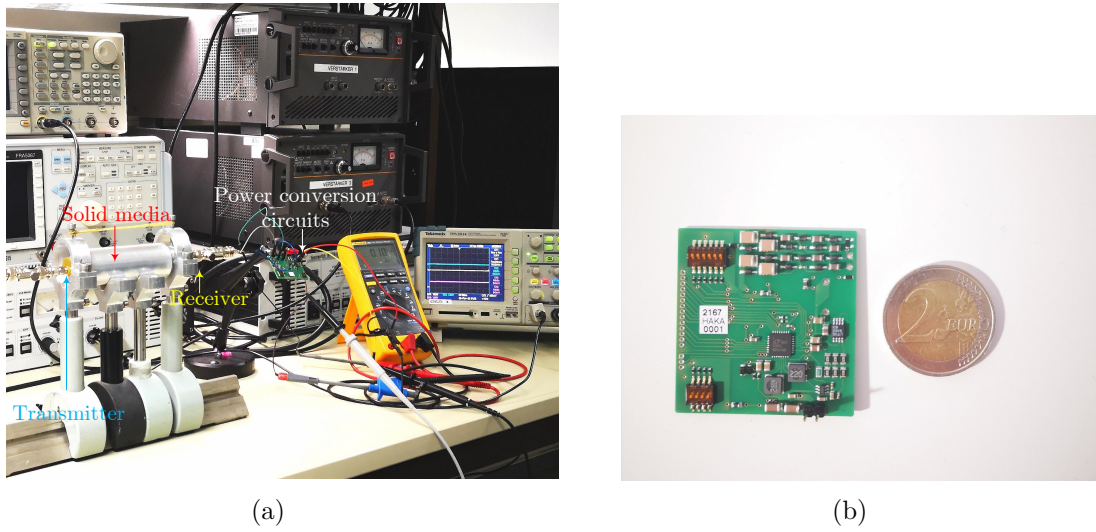
### 6.3.1 Evaluation of the electro-mechanical-acoustic CET system with Class-E resonant rectifier

The circuit was connected to the electro-mechanical-acoustic CET system. It was considered a cylindrical aluminium media with length  $l = 100 \text{ mm}$  and radius  $R = 15 \text{ mm}$ . The piezoelectric transmitter was driven by a power amplifier at  $738 \text{ kHz}$ . The rectifier was designed based on the approach shown in Chapter 4. The design, considering a nominal operating point, is described in Table 6.14.

In order to evaluate the contactless power transfer for different loads, the MPPT and battery charger circuits were disconnected. The system was tested by measuring the input voltage and current in the piezoelectric transmitter,  $v_{in}$  and  $i_{in}$ , the voltage and



Figure 6.11 – Experimental setup. (a) Electro-mechanical-acoustic CET system connected to power conversion circuits. (b) Developed printed circuit board.



Source: Author.

Table 6.14 – Specification and components for the designed Class-E resonant rectifier.

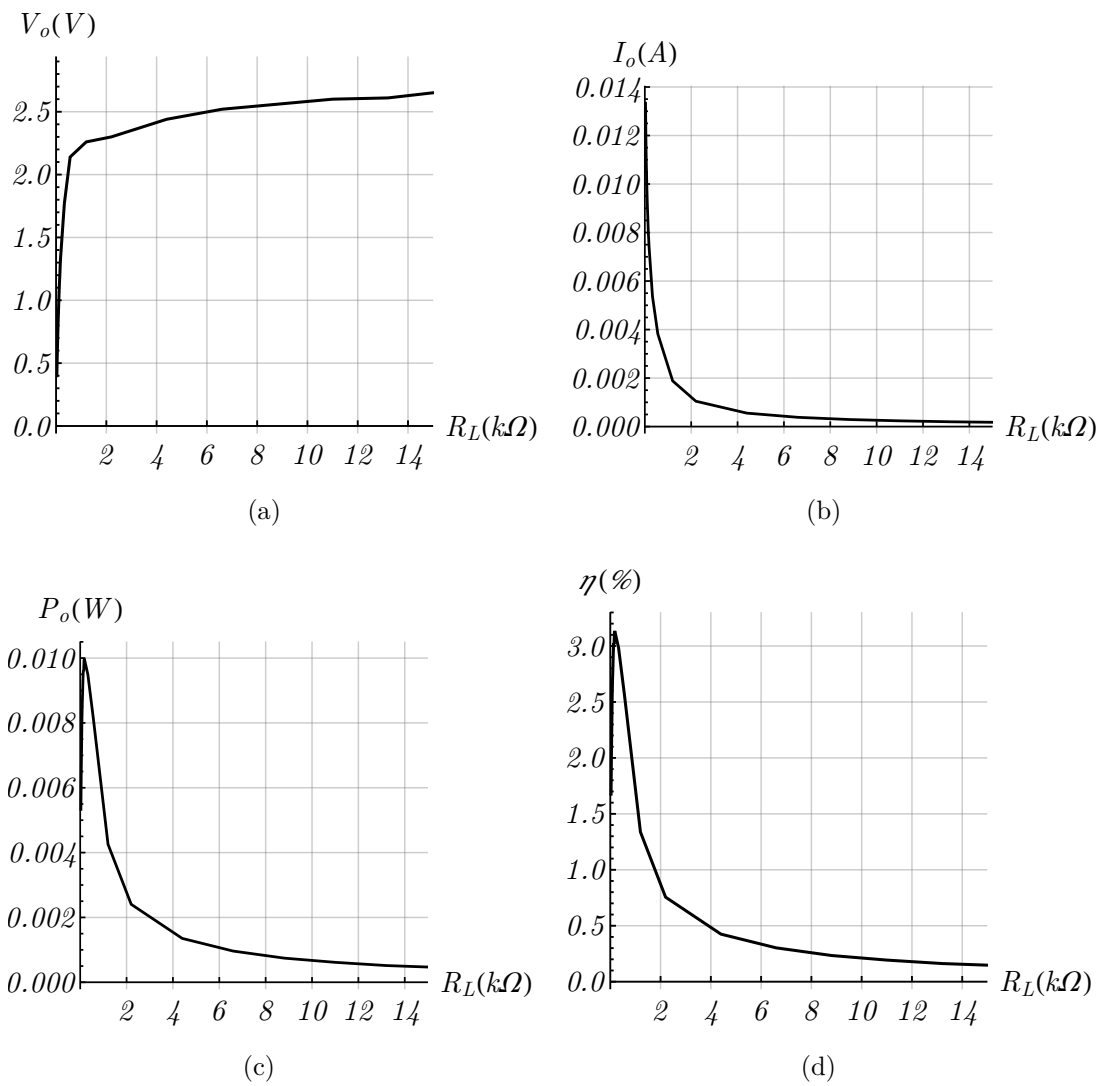
Specification / Component	Value
Output voltage, $V_o$	2.5 V
Load, $R_L$	6000 $\Omega$
Rectifier capacitor, $C_2$	22 nF
Output filter inductor, $L_f$	346 $\mu$ H
Output filter capacitor, $C_f$	13 nF

current in the piezoelectric receiver,  $v_{rc}$  and  $i_{rc}$ , and the load output voltage and load output current,  $V_o$  and  $I_o$ . Additionally, for the Class-E resonant rectifier, the voltage in the capacitor  $C_2$ , which is the diode voltage, was measured in order to validate the design regarding the soft-switching operation. The output voltage  $V_o$ , output current  $I_o$ , output power  $P_o$  and efficiency  $\eta$  as function of the load  $R_L$  are shown in Figures 6.12(a)-6.12(d). The input voltage was considered as  $V_{in_{rms}} = 12$  V and the input power  $P_{in} = 0.318$  W.

It can be seen that the overall efficiency ( $\eta$ ) is 3.2%. The maximum power achieved is 10 mW. The Class-E was designed to operate with soft-switching condition. In this sense, a comparison among theoretical (normalized model), SPICE simulation and experimental is shown in Figure 6.13 regarding the voltage on the capacitor  $C_2$ ,  $v_{C_2}$ . Note that the theoretical chart was de-normalized in relation to the input voltage in order to facilitate the comparison.

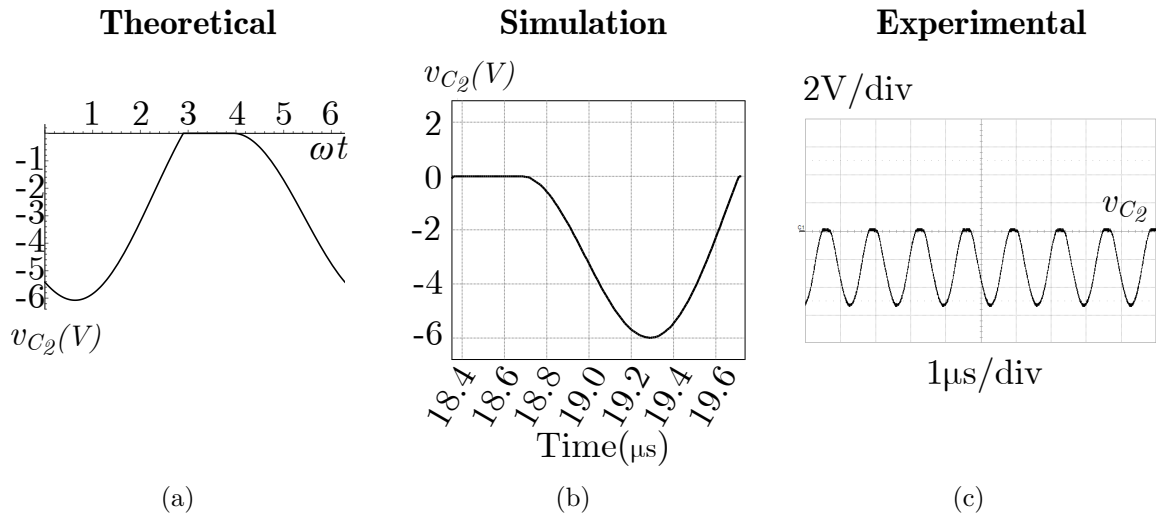
The same comparison is performed for the output voltage  $V_o$ , which is shown in Figure 6.14.

Figure 6.12 – Experimental results for the electro-mechanical-acoustic CET system with resonant Class-E rectifier considering load variation ( $P_{in} = 0.318 W$ ). (a) Output voltage  $V_o$ . (b) Output current  $I_o$ . (c) Output power  $P_o$ . (d) Efficiency  $\eta$ .



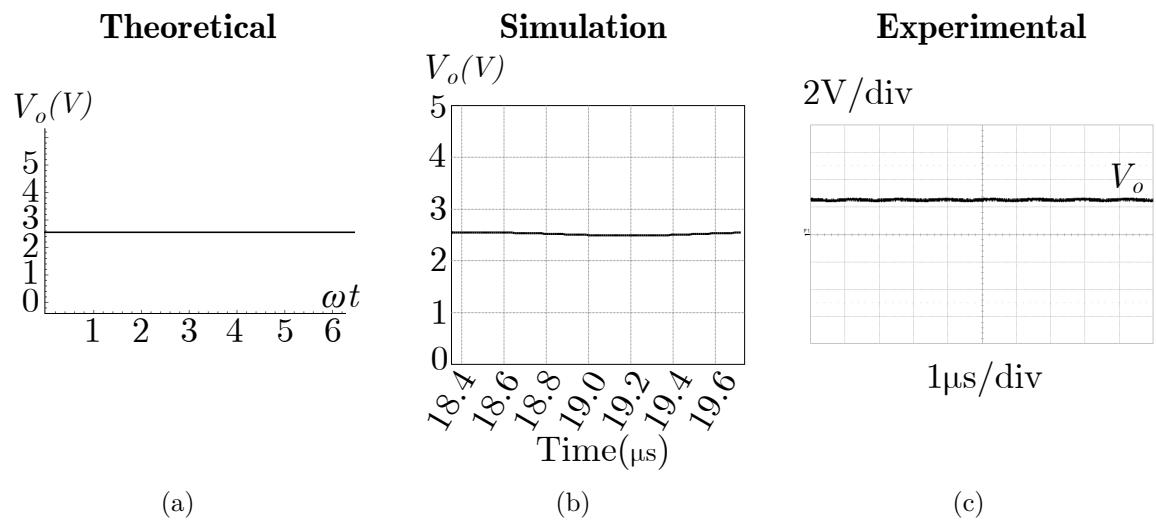
Source: Author.

Figure 6.13 – Waveforms for the Class-E resonant rectifier -  $v_{C_2}$ . (a) Theoretical. (b) Simulation. (c) Experimental.



Source: Author.

Figure 6.14 – Waveforms for the Class-E resonant rectifier -  $V_o$ . (a) Theoretical. (b) Simulation. (c) Experimental.



Source: Author.

### 6.3.2 Evaluation of the electro-mechanical-acoustic CET system with Cockcroft-Walton multiplier

Considering the Cockcroft-Walton multiplier as rectifier, the results are going to be shown. The parameters for the converter are shown in Table 6.15. The reference output voltage is  $V_o = 2.8 V$  and the load is  $R_L = 1.2 k\Omega$ .

The Cockcroft-Walton multiplier was designed based on the genetic algorithm detailed in Appendix D. The design procedure includes the definition of the maximum allowed output voltage ripple  $\delta V_{o_{max}}$ , which was selected as  $179 \mu V$  and the definition of the diode voltage drop  $V_D$ , which was set as  $0.3 V$ .

Table 6.15 – Designed Cockcroft-Walton multiplier.

Components	Value
Capacitors, $C_{1,2,4}$	$5.6 \mu F$
Capacitor, $C_3$	$22 nF$
Capacitor, $C_{5,6}$	$6.8 \mu F$

The output voltage  $V_o$ , output current  $I_o$ , output power  $P_o$  and efficiency  $\eta$  as function of the load  $R_L$  are shown in Figures 6.15(a)-6.15(d). The input voltage was considered as  $V_{in_{rms}} = 12 V$  and the input power  $P_{in} = 0.24 W$ .

Figure 6.15(a) shows the output voltage  $V_o$  when load is varied from 0 to  $140 k\Omega$ . It can be seen the raising behavior of the voltage when load is increased.

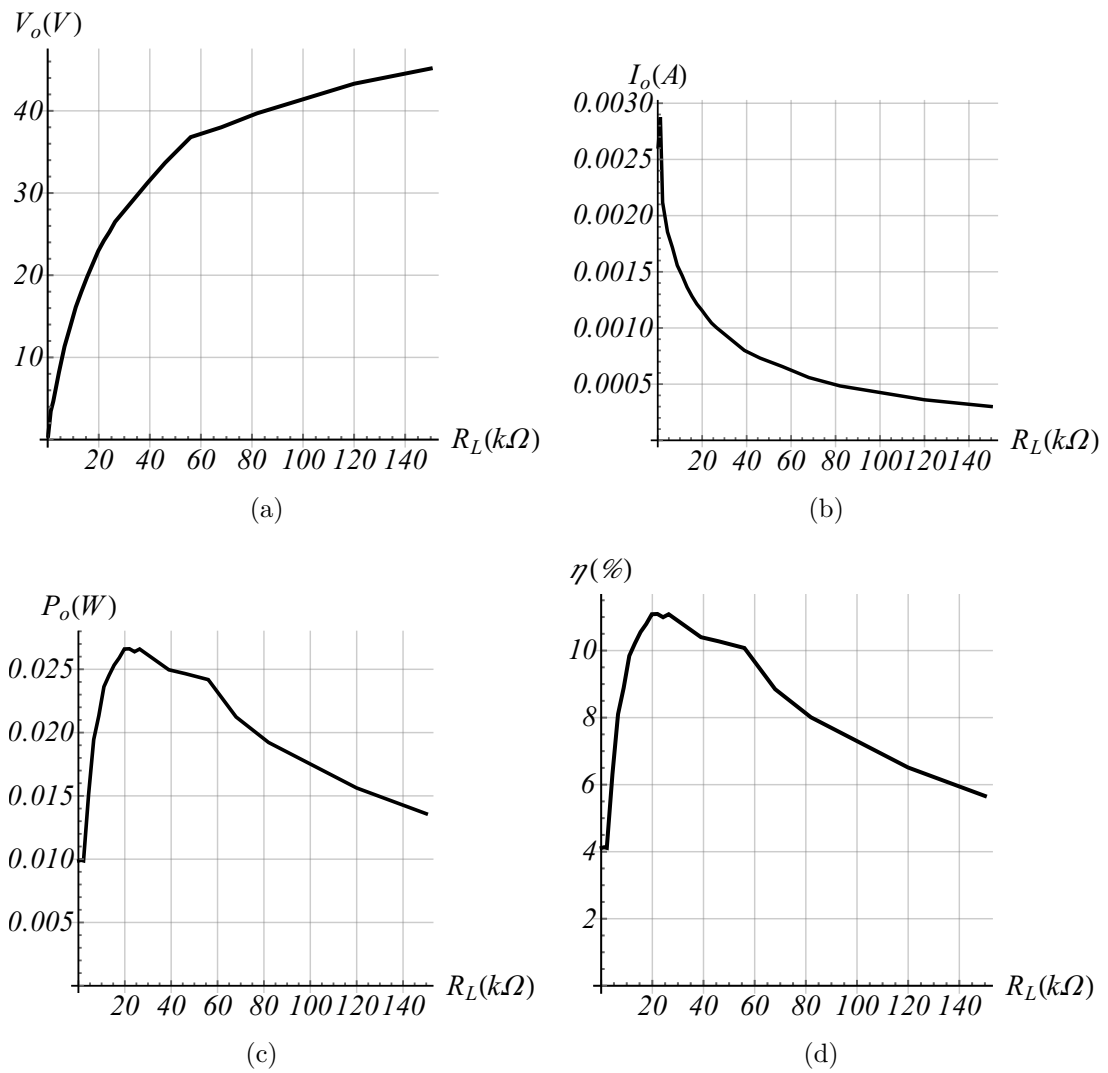
Figure 6.15(c) depicts the output power  $P_o$  as function of load  $R_L$ . The maximum achieved power is around  $27 mW$ .

Efficiency  $\eta$  as function of load  $R_L$  is shown in Figure 6.15(d). Maximum efficiency is achieved considering load near to  $20 k\Omega$ . In this case, efficiency is around 12 %.

The experimental waveforms are shown for different loads in Figure 6.16. The represented waveforms are: output voltage  $V_o$ , piezoelectric receiver current  $i_{rc}$ , piezoelectric receiver voltage  $v_{rc}$  and piezoelectric transmitter input voltage  $v_{in}$ .

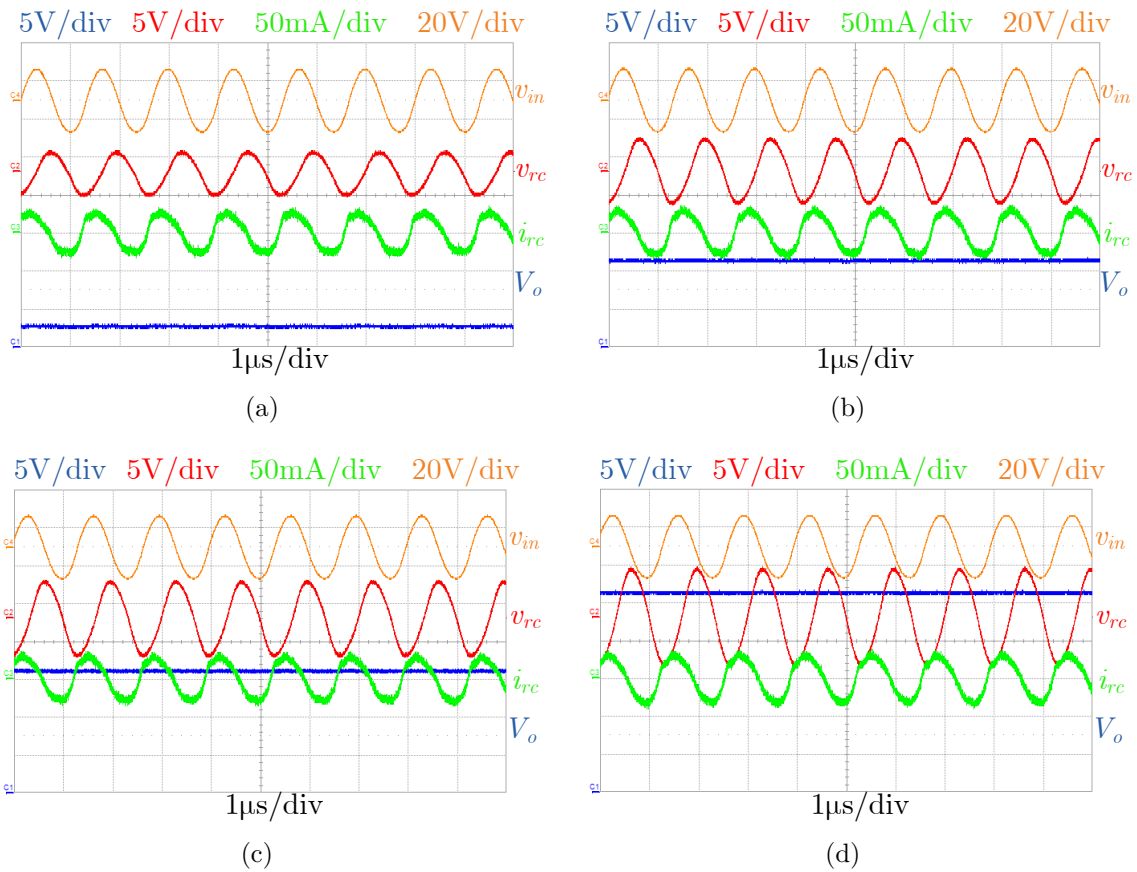
Figure 6.16(a)-Figure 6.16(d) are related to loads:  $1.2 k\Omega$ ,  $6.6 k\Omega$ ,  $11 k\Omega$  and  $26 k\Omega$ , respectively. It is possible to achieve relatively high voltages with the Cockcroft-Walton multiplier as shown in Figure 6.16(d).

Figure 6.15 – Experimental results for the electro-mechanical-acoustic CET system with Cockcroft-Walton multiplier considering load variation ( $P_{in} = 0.24 W$ ). (a) Output voltage  $V_o$ . (b) Output current  $I_o$ . (c) Output power  $P_o$ . (d) Efficiency  $\eta$ .



Source: Author.

Figure 6.16 – Experimental results for the electro-mechanical-acoustic CET system with Cockcroft-Walton multiplier. (a)  $R_L = 1.2\text{ k}\Omega$ . (b)  $R_L = 6.6\text{ k}\Omega$ . (c)  $R_L = 11\text{ k}\Omega$ . (d)  $R_L = 26\text{ k}\Omega$ .



Source: Author.

#### 6.4 COMPARISON WITH RELATED WORKS

The proposed model was compared to related works. In this regard, modeling methodologies for acoustic CET systems are considered.

The comparison factors are: transfer media materials that were analyzed, transmission distance, frequency range, methodology, included domains and error. The quadratic error was calculated based on the comparison of the model with the measured results. The comparison is described in Table 6.16. For the error comparison, the augmented-order multiphysical model was considered.

The present work is alongside works from Yang et al. (2018a) and Wilt et al. (2015) regarding model error ( $< 5\%$ ). Longest distance transmission is  $300\text{ mm}$  reported by Yang et al. (2018b). Present work shows the second longest distance between transducers.

Works based on Leach's model, impedance matrix and transfer matrix include only the electrical domain. It is because they do not include the physical components of the mechanical and acoustical domains into the modeling development (YANG et al., 2018a; YANG et al., 2018b; BAO et al., 2007; WILT et al., 2015).

Finite element method reported by Lawry et al. (2009) includes all the domains. However, its error is higher than the present work.

Present work and the impedance matrix methodology presented by Bao et al. (2007) consider aluminium and steel as transfer media. The other reported works only deal with steel for the acoustic media.

The highest reported frequency was  $7\text{ Mhz}$  in Wilt et al. (2015). This frequency is the upper limit of the considered range. The present work overall frequency range is  $200 - 1250\text{ kHz}$ . However, this range is dependent of the operating frequency of the transducers. Considering the  $738\text{ kHz}$  transducers, the frequency range of the present work is  $200 - 1000\text{ kHz}$ . On the other hand, for the  $1040\text{ kHz}$  transducers, the frequency range is  $450 - 1250\text{ kHz}$ .

Table 6.16 is an interesting resource to evaluate the present work based on the literature. It is because, qualitative and quantitative factors are considered to highlight the differences among methodologies.

Table 6.16 – Comparison with related works.

<b>Work</b>	<b>Medium</b>	<b>Distance</b>	<b>Frequency range</b>	<b>Methodology</b>	<b>Domains</b>	<b>Error</b>
Yang et al. (2018a)	Steel	22 mm	1 – 3 MHz	Leach’s Model	Electrical	< 5%
Lawry et al. (2009)	Steel	57 mm	0.9 – 1.3 MHz	FEM	All	≈ 8%
Yang et al. (2018b)	Steel	300 mm	942 – 945 kHz	Impedance matrix	Electrical	-
Bao et al. (2007)	Aluminium, steel	2 mm, 4 mm	300 – 900 kHz	Impedance matrix	Electrical	-
Wilt et al. (2015)	Steel	74.8 mm	2 – 7 MHz	Transfer matrix	Electrical	< 5%
Moss et al. (2008)	Aluminium	1.6 mm	600 – 1300 kHz	SPICE	Electrical, acoustical	≈ 6%
Present work	Aluminium, steel	100 mm, 200 mm	200 – 1250 kHz	Multiphysics networks	All	< 5%



## 6.5 CONCLUSION

In this section, the results were presented in order to compare the developed models with the experimental response of the system. Furthermore, an experimental investigation of the power conversion circuits was conducted in order to evaluate the functionality of the power management circuits developed for the electro-mechanical-acoustic CET system.

By means of an error analysis, it was shown that the models have less than 10.7% mean error and less than 5.7% considering quadratic error. When connected to the power conversion circuits, the overall system can achieve 12% efficiency for step-up applications by means of a Cockcroft-Walton multiplier and 3.2% efficiency for step-down applications using a Class-E resonant rectifier.

The augmented-order multiphysical model has shown good agreement with the physical system. The model can be considered as semi-analytical because it is developed based on a previous comparison of the analytical model to the experimental response. It is important to highlight that semi-analytical models have good acceptance for systems with high complexity. Lenk et al. (2011) defined a flowchart for models development that includes one stage of comparison between theoretical and experimental responses in order to enhance the system. In this sense, even though the augmented-order multiphysical model was not fully analytically developed, it still is a feasible resource to analyze multiphysical systems.



## 7 CONCLUSION

This Doctoral Thesis has presented the development of a modeling methodology for an electro-mechanical-acoustic contactless energy transfer system, especially when solids are considered as transfer media. By using ultrasound waves, power can be wirelessly transferred through air, living tissues and solids. This system can be used in low power applications, like as sensor nodes in metal enclosures and bio-implantable medical devices.

In order to model the electro-mechanical-acoustic contactless energy transfer system, it was proposed a multiphysical model based on lumped parameters. The model includes three domains: electrical, mechanical and acoustical. The electrical domain is analyzed by the Kirchhoff's Laws of Circuits, the mechanical domain by the Newton's Laws of Motion and the acoustical domain by means of electro-acoustic and mechanical-acoustic analogies.

The decomposition into unit-less parameters scheme was extended for multiphysics networks and applied into the multiphysical model based on lumped parameters. This allows to convert the real system parameters into unit-less parameters. Furthermore, by means of an equivalent transformation, it is possible to normalize the system in relation to the amplitude of the input source and the operating frequency in a systematical way. These concepts lead to a normalized state-space model based on unit-less parameters, which has the advantage of allowing the achievement of normalized gain curves that can be used to understand the system without knowing the real system parameters.

An equivalent electrical model was presented and a piezoelectric transformer model was derived from it. It was shown that the multiphysical, electrical and piezoelectric transformer model have agreement to each other. In this sense, the piezoelectric transformer model was used as part of the resonant tank in resonant topologies. These topologies can be used to represent the system. The Class-E<sup>2</sup> resonant converter was analyzed and designed including the piezoelectric transformer representation of the multiphysical system.

The AC model of the Class-E<sup>2</sup> resonant converter as developed in this work. The standard averaged and switched models are not suitable when the system has AC variables and DC variables with large ripple. In this sense, the generalized averaged dynamic model was used as methodology to develop the large-signal and small-signal models of the Class-E<sup>2</sup> resonant converter.

It was shown that the multiphysical model can be enhanced by comparing its response to the experimental response of the system. This idea has resulted in the development of an augmented-order multiphysical model based on lumped parameters.

The models were compared to the experimental response of the system. An error analysis has shown that for the proposed setups, the maximum mean relative error between theoretical and experimental was 10.69% and the maximum quadratic error was

5.69 %.

Qualitatively, it can be concluded that the multiphysical model based on lumped parameters is able to include all the required power conversions: electrical-to-mechanical, mechanical-to-acoustic, acoustic-to-mechanical and mechanical-to-electrical into a single state-space representation. In addition, the model is analytically developed and included the real system parameters. The electrical equivalent model is suitable for SPICE simulations. However, the understanding of the real system components is diminished. The piezoelectric transformer model is the simplest among the studied models. On the other hand, it is useful to be included as part of resonant power converters. The augmented-order multiphysical model has shown better accuracy than the other models. However, it requires a previous comparison between theoretical and experimental responses to be fully addressed.

A practical demonstrator was assembled, which included: ultrasound transmitter, transfer media, ultrasound receiver and the power conversion circuitry. An experimental investigation has demonstrated the feasibility of the proposed system by means of two experimental setups: one including a resonant rectifier for step-down applications and one including a Cockcroft-Walton multiplier for step-up applications.

The concepts used to develop the multiphysical models can be applied to analyze systems that include electrical, mechanical and acoustical parts. For instance, miniaturized force sensors, loudspeakers, ultrasonic distance sensors, piezoelectric valves, machine tool sensors and wireless power transfer are highlighted as applications that can be surveyed.

## 7.1 PUBLISHED WORKS

The published works in *journal / magazines* are mentioned as follows:

1. Mendonça, L. S; Martins, L. T.; Radecker, M.; Bisogno, F. E.; Killat, D., "Normalized Modeling of Piezoelectric Energy Harvester Based on Equivalence Transformation and Unit-Less Parameters", *IEEE Journal of Microelectromechanical Systems*, Vol: 28, Issue: 4, June 2019.
2. Mendonça, L. S; Naidon, T. C.; De Freitas, G. G.; Martins, M. L. S; Bisogno, F. E, "Energy-Based Normalization for Resonant Power Converters", *IEEE Transactions on Power Electronics*, Vol: 33, Issue: 8, August 2018.
3. Mendonça, L. S; Cipriani, J. S.; Naidon, T. C; Bisogno, F. E., "Steady-State Analysis and Design Methodology for Class-E<sup>2</sup> Resonant DC/DC Converters based on a Normalized State-Space Model", *Revista Eletrônica de Potência (SOBRAEP)*, June 2020.

4. Mendonça, L. S.; Bisogno, F. E., "Resonance-Based Normalization Theory for Analysis and Design of Resonant Power Converters", *Revista Eletrônica de Potência (SO-BRAEP)*, July 2019.

The works related to conferences are described as follows:

1. Mendonça L. S.; Naidon T. C.; Raposo R. F.; Bisogno, F. E., "An Unit-less Mathematical Model for Analysis and Design of Class-E Resonant Converters", *2019 IEEE 15th Brazilian Power Electronics Conference and 5th IEEE Southern Power Electronics Conference (COBEP/SPEC)*, December 2019.
2. Mendonça L. S.; Radecker, M.; Killat, D.; Bisogno, F. E., "Normalized State-Space Models of Resonant Rectifiers", *2019 Kleinheubach Conference*, September 2019.
3. Mendonça L. S.; Radecker, M.; Killat, D.; Bisogno, F. E., "Ultrasound Piezo-Harvester Energy Transfer Systems for Machine Tool Sensor-Charger Applications", *PCIM Europe 2019; International Exhibition and Conference for Power Electronics, Intelligent Motion, Renewable Energy and Energy Management*, July 2019.

## 7.2 FUTURE WORKS

Some ideas for the future works are pointed out as follows:

- Considering the augmented-order multiphysical model, a search and optimization or genetic algorithms can be implemented to find the constants  $w_1$  and  $w_2$  of the added acoustic networks;
- Development of a communication circuit to transfer information from sensors supplied by the rectifier back to the transmitter side of the system. One idea is to use a backscattering system to transmit information;
- Development of a control loop system in order to regulate the output voltage when disturbances in the frequency occur;
- Evaluate the proposed models for cases in which the transfer media is a living tissue in order to analyze the bio-implantable medical device applications;
- Include the model of the battery into the analysis of the rectifier circuits;
- Evaluation of the battery charging time by using the electro-mechanical-acoustic CET system;
- Different testing conditions, like as misalignment between transducers and transfer media.



## REFERENCES

- ABDULLAHI, M.; OYADIJI, S. O. Acoustic wave propagation in air-filled pipes using finite element analysis. **Applied Sciences**, v. 8, p. 1–20, Aug 2018.
- ABRAMOV, E.; ZELTSER, I.; PERETZ, M. M. A network-based approach for modeling resonant capacitive wireless power transfer systems. **CPSS Transactions on Power Electronics and Applications**, v. 4, n. 1, p. 19–29, March 2019. ISSN 2475-742X.
- AGHAKHANI, A.; BASDOGAN, I. Equivalent impedance electroelastic modeling of multiple piezo-patch energy harvesters on a thin plate with ac-dc conversion. **IEEE/ASME Transactions on Mechatronics**, v. 22, n. 4, p. 1575–1584, Aug 2017.
- ALDHAHER, S.; YATES, D. C.; MITCHESON, P. D. Modeling and analysis of class ef and class e/f inverters with series-tuned resonant networks. **IEEE Transactions on Power Electronics**, v. 31, n. 5, p. 3415–3430, May 2016. ISSN 1941-0107.
- ALMEIDA, P. S. et al. Offline soft-switched led driver based on an integrated bridgeless boost asymmetrical half-bridge converter. **IEEE Transactions on Industry Applications**, v. 51, n. 1, p. 761–769, 2015.
- ALONSO, J. M.; ORDIZ, C.; COSTA, M. A. D. A novel control method for piezoelectric-transformer based power supplies assuring zero-voltage-switching operation. **IEEE Transactions on Industrial Electronics**, v. 55, n. 3, p. 1085–1089, 2008.
- AMAR, A. B.; KOUKI, A. B.; CAO, H. Power Approaches for Implantable Medical Devices. **Sensors**, v. 15, p. 28890–28914, 2015. ISSN 1424-8220.
- ANDRADE, A. S. et al. Synthesis and comparative analysis of very high step up dc dc converters adopting coupled inductor and voltage multiplier cells. **IEEE Transactions on Power Electronics**, v. 33, n. 7, p. 5880–5897, July 2018. ISSN 0885-8993.
- ARTEAGA, J. M. et al. Dynamic capabilities of multi-mhz inductive power transfer systems demonstrated with batteryless drones. **IEEE Transactions on Power Electronics**, v. 34, n. 6, p. 5093–5104, June 2019. ISSN 0885-8993.
- AYACHIT, A. et al. Zero-voltage switching operation of transformer class-e inverter at any coupling coefficient. **IEEE Transactions on Industrial Electronics**, v. 66, n. 3, p. 1809–1819, March 2019. ISSN 1557-9948.
- AZAD, A. N. et al. Analysis, optimization, and demonstration of a vehicular detection system intended for dynamic wireless charging applications. **IEEE Transactions on Transportation Electrification**, v. 5, n. 1, p. 147–161, March 2019. ISSN 2332-7782.
- BABAEI, E.; ASL, E. S.; BABAYI, M. H. Steady-state and small-signal analysis of high-voltage gain half-bridge switched boost inverter. **IEEE Transactions on Industrial Electronics**, v. 63, n. 6, p. 3546–3553, June 2016. ISSN 1557-9948.

- BACHA, S.; MUNTEANU, I.; BRATCU, A. I. **Power Electronic Converters Modeling and Control**. 2013.
- BAO, X. et al. Wireless piezoelectric acoustic-electric power feedthru. In: **Proceedings of SPIE**. [S.l.: s.n.], 2007.
- BAR-COHEN, Y. et al. High-power piezoelectric acoustic-electric power feed thru for metal walls. In: **Proc. SPIE**. [S.l.: s.n.], 2008. v. 6930, p. 69300Z1–69300Z9.
- BISOGNO, F. E. **Energy-Related System Normalization and Decomposition Targeting Sensitivity Consideration, PhD Dissertation**. 2006.
- CALDER, R. J.; LEE, S.; LORENZ, R. D. Efficient, mhz frequency, resonant converter for sub-meter (30 cm) distance wireless power transfer. In: **2013 IEEE Energy Conversion Congress and Exposition**. [S.l.: s.n.], 2013. p. 1917–1924. ISSN 2329-3721.
- CHEN, C.-T. **Linear System Theory and Design**. 1999.
- CHEN, Y. **Piezoelectric Power Transducers and its Interfacing Circuitry on Energy Harvesting and Structural Damping Applications, Doctorate Thesis**. 2013.
- CHENG, J. et al. Measurement and calculation of the viscosity of metals - a review of the current status and developing trends. **Measurement Science and Technology**, v. 25, n. 6, p. 062001, Apr 2014.
- COCHRAN, G. V. B. et al. Piezoelectric Internal Fixation Devices: A New Approach to Electrical Augmentation of Osteogenesis. **Journal of Orthopaedic Research**, v. 3, 1985.
- COCKCROFT, J. D.; WALTON, E. T. S. Experiments with high velocity positive ions. In: **Proc. Roy. Soc. A**. [S.l.: s.n.], 1932. v. 136, n. 830, p. 619–630.
- DAI, J.; LUDOIS, D. C. Capacitive power transfer through a conformal bumper for electric vehicle charging. **IEEE Journal of Emerging and Selected Topics in Power Electronics**, v. 4, n. 3, p. 1015–1025, Sep. 2016. ISSN 2168-6777.
- DEHGHANI, S.; JOHNSON, T. A 2.4-ghz cmos class-e synchronous rectifier. **IEEE Transactions on Microwave Theory and Techniques**, v. 64, n. 5, p. 1655–1666, May 2016. ISSN 0018-9480.
- DENISOV, A.; YEATMAN, E. Ultrasonic vs. inductive power delivery for miniature biomedical implants. In: **2010 International Conference on Body Sensor Networks**. [S.l.: s.n.], 2010. p. 84–89. ISSN 2376-8886.
- DUDHAL, S.; UPADHYE, V.; AGASHE, S. D. Step approach for finite element modeling of ultrasound transducer. In: **2016 International Conference on Automatic Control and Dynamic Optimization Techniques (ICACDOT)**. [S.l.: s.n.], 2016. p. 1052–1055.



DUTOIT, N.; WARDLE, B.; KIM, S. Design considerations for mems-scale piezoelectric mechanical vibration energy harvesters. **Integrated Ferroelectrics**, v. 71, p. 121–160, Feb 2005. ISSN 1607-8489.

EDWARDS, B. C. Design and Deployment of a Space Elevator. **Acta Astronautica**, v. 47, n. 10, p. 735–744, 2000.

ENGLEITNER, R. **Análise Estática Normalizada e Modelagem de Pequenos Sinais do Conversor Classe-E utilizando Transformadores Piezoelétricos**, Master's Dissertation. 2011.

EPC. **What is GaN?** [S.l.], 2017. Disponível em: <<http://epc-co.com/epc/GalliumNitride/WhatisGaN.aspx>>.

ERFANI, R. et al. Modeling and experimental validation of a capacitive link for wireless power transfer to biomedical implants. **IEEE Transactions on Circuits and Systems II: Express Briefs**, v. 65, n. 7, p. 923–927, July 2018. ISSN 1549-7747.

ERICKSON, R. W. **Fundamentals of Power Electronics**. 2000.

FAKIDIS, J. **Optical Wireless Energy Transfer for Self-Sufficient Small Cells**. 07 2017. Tese (Doutorado), 07 2017.

FOROUZESH, M. et al. Step up dc dc converters: A comprehensive review of voltage-boosting techniques, topologies, and applications. **IEEE Transactions on Power Electronics**, v. 32, n. 12, p. 9143–9178, Dec 2017. ISSN 0885-8993.

FRAUNHOFER-IBMT-THERANOSTISCHE-PROJEKT. **Theranostische implantate. VDE-Positionpapier**, 2011.

GASSMANN, J. **Modellierung un Simulation von Federschwingsystemen in Mechanischen Uhren**, PhD Dissertation. 2007.

HEYWANG, W.; LUBITZ, K.; WERSING, W. **Piezoelectricity**. 2008.

HOANG, N. K.; LEE, J.; LEE, S. Maximum power transfer considering limited available input power in ultrasonic wireless power transfer for implanted medical devices. In: **2014 IEEE Fourth International Conference on Consumer Electronics - Berlin**. [S.l.: s.n.], 2014.

ISHIYAMA, T. et al. Impact of a wireless power transmission system using an ultrasonic air transducer for low-power mobile applications. In: **IEEE Symposium on Ultrasonics, 2003**. [S.l.: s.n.], 2003. v. 2, p. 1368–1371 Vol.2.

JAVAID, U.; DUJÍĆ, D. Arbitrary order generalized state space average modeling of switching converters. In: **2015 IEEE Energy Conversion Congress and Exposition (ECCE)**. [S.l.: s.n.], 2015.

- JEDI, H.; KAZIMIERCZUK, M. K. High-frequency single-switch zvs inverter for driving capacitive loads. In: **IECON 2018 - 44th Annual Conference of the IEEE Industrial Electronics Society**. [S.l.: s.n.], 2018. p. 1255–1260. ISSN 1553-572X.
- JEDI, H. et al. High-frequency single-switch zvs gate driver based on a class phi2 resonant inverter. **IEEE Transactions on Industrial Electronics**, v. 67, n. 6, p. 4527–4535, 2020.
- JIANG, W.; WRIGHT, W. M. D. Wireless communication using ultrasound air with parallel ook channels. In: **International System Safety Conference**. [S.l.: s.n.], 2013.
- JOZWIK, J. J.; KAZIMIERCZUK, M. K. Analysis and design of class-e2 dc/dc converter. **IEEE Transactions on Industrial Electronics**, v. 37, n. 2, p. 173–183, 1990.
- KAZIMIERCZUK, M. K.; CZARKOWSKI, D. **Resonant Power Converters**. 1995.
- KAZIMIERCZUK, M. K.; JOZWIK, J. Class e2 narrow-band resonant dc/dc converters. **IEEE Transactions on Instrumentation and Measurement**, v. 38, n. 6, p. 1064–1068, 1989.
- KAZIMIERCZUK, M. K.; TOMESCU, B.; IVASCU, A. Class e resonant rectifier with a series capacitor. **IEEE Transactions on Circuits and Systems I: Fundamental Theory and Applications**, v. 41, n. 12, p. 885–890, 1994.
- KAZMIERKOWSKI, M. P.; MORADEWICZ, A. J. Unplugged But Connected: Review of Contactless Energy Transfer Systems. **IEEE Industrial Electronics Magazine**, v. 6, p. 47–55, 2012. ISSN 13169804.
- KEE, S. D. et al. The class-e/f family of zvs switching amplifiers. **IEEE Transactions on Microwave Theory and Techniques**, v. 51, n. 6, p. 1677–1690, June 2003. ISSN 1557-9670.
- KHALIFA, M. **High-Voltage Engineering, Theory and Practice, Electrical Engineering and Electronics, A Series of Reference Books and Textbooks, vol. 63**. 1990.
- KIM, S.; RHEE, D. Experimental demonstration of optical wireless power transfer with a dc-to-dc transfer efficiency of 12.1%. **Optical Engineering**, v. 57, n. 8, p. 1 – 5 – 5, 2018. Disponível em: <<https://doi.org/10.1117/1.OE.57.8.086108>>.
- KISHORE, P. M.; BHIMASINGU. A split source boost switched capacitor multilevel inverter for low power applications. In: **2017 National Power Electronics Conference (NPEC)**. [S.l.: s.n.], 2017. p. 112–117. ISSN null.
- KLINE, M. et al. Capacitive power transfer for contactless charging. In: **2011 Twenty-Sixth Annual IEEE Applied Power Electronics Conference and Exposition (APEC)**. [S.l.: s.n.], 2011. p. 1398–1404. ISSN 1048-2334.

- KOBOUGIAS, I. C.; TATAKIS, E. C. Optimal design of a half wave cockcroft walton voltage multiplier with minimum total capacitance. **IEEE Transactions on Power Electronics**, v. 25, n. 9, p. 2460–2468, Sep. 2010. ISSN 0885-8993.
- KRIMHOLTZ, R.; LEEDOM, D. A.; MATTACI, G. L. New equivalent circuits for elementary piezoelectric transducer. **Electronics Letters**, n. 6, p. 398–399, 1942.
- LASKOVSKI, A. N.; YUCE, M. R. Class-e oscillators as wireless power transmitters for biomedical implants. In: **2010 3rd International Symposium on Applied Sciences in Biomedical and Communication Technologies (ISABEL 2010)**. [S.l.: s.n.], 2010. p. 1–5. ISSN 2325-5315.
- LAWRY, T. et al. Finite Element Modeling and Simulation of a Two-Transducer Through-Wall Ultrasonic Communication System. **International Mechanical Engineering Congress and Exposition (IMECE)**, 2009.
- LAWRY, T. J. et al. Analytical modeling of a sandwiched plate piezoelectric transformer-based acoustic-electric transmission channel. **IEEE Transactions on Ultrasonics, Ferroelectrics, and Frequency Control**, v. 59, n. 11, p. 2476–2486, November 2012. ISSN 0885-3010.
- LENK, A. et al. **Electromechanical Systems in Microtechnology and Mechatronics**. 2011.
- LI, S. et al. A double-sided lcc compensation network and its tuning method for wireless power transfer. **IEEE Transactions on Vehicular Technology**, v. 64, n. 6, p. 2261–2273, June 2015. ISSN 0018-9545.
- LIM, J.; KHWAJA, T. S.; HA, J. Wireless optical power transfer system by spatial wavelength division and distributed laser cavity resonance. **Optics Express**, v. 27, n. 12, p. 924–935, Jun 2019.
- LIN, W. et al. The performance comparison of greinacher rectifiers for wireless power transmission. **WIT Transactions on Engineering Sciences**, v. 88, p. 237–243, 2014.
- LIN, Y.; CHIANG, M.; CHEN, J. A wireless sensor utilizing ultrasound for wireless power and data transmission. In: **2017 IEEE Wireless Power Transfer Conference (WPTC)**. [S.l.: s.n.], 2017. p. 1–3.
- LOTFI, A. et al. Steady-state analysis of class-e shunt inductor inverter outside zcs and zdcs conditions. **IEEE Transactions on Components, Packaging and Manufacturing Technology**, v. 9, n. 8, p. 1587–1594, Aug 2019. ISSN 2156-3985.
- LU, F. et al. A double-sidedlclc-compensated capacitive power transfer system for electric vehicle charging. **IEEE Transactions on Power Electronics**, v. 30, n. 11, p. 6011–6014, Nov 2015. ISSN 0885-8993.

- LU, F.; ZHANG, H.; MI, C. A review on the recent development of capacitive wireless power transfer technology. **Energy**, v. 10, p. 1–30, November 2017.
- LU, M.; NGO, K. D. T. Systematic design of coils in series series inductive power transfer for power transferability and efficiency. **IEEE Transactions on Power Electronics**, v. 33, n. 4, p. 3333–3345, April 2018. ISSN 0885-8993.
- MAHMOOD, M. F.; MOHAMMED, S. L.; GHARGHAN, S. K. Ultrasound sensor-based wireless power transfer for low-power medical devices. **Journal of Low Power Electronics and Applications**, v. 9, n. 3, 2019. ISSN 2079-9268. Disponível em: <<https://www.mdpi.com/2079-9268/9/3/20>>.
- MANO, N.; MAIO, F.; HELLER, A. Characteristics of a Miniature Compartment-Less Glucose-O<sub>2</sub> Biofuel Cell and its Operation in a Living Plant. **American Chemical Society**, v. 125, p. 6588–6594, 2003.
- MARSCHNER, U.; WERTHSCHUTZKY, R. **Aufgaben und Lösungen zur Schaltdarstellung un Simulation elektromechanischer Systeme**. 2015.
- MASON, W. P. **Electromechanical Transducers and Wave Filters**. 1942.
- MELANIE, M. **An Introduction to Genetic Algorithms**. 1999.
- MELODIE, C. et al. Piezoelectric Materials for Medical Applications. **Organic and Inorganic Mateirals Applications**, 2018.
- MENDONÇA, L. S. **Abordagem Normalizada para Conversores Ressonantes, Master's Dissertation**. 2017.
- MENDONÇA, L. S. et al. Energy-based normalization for resonant power converters. **IEEE Transactions on Power Electronics**, v. 33, n. 8, p. 6526–6536, Aug 2018. ISSN 0885-8993.
- MENG, X. et al. Fully enclosed bearing-structured self-powered rotation sensor based on electrification at rolling interfaces for multi-tasking motion measurement. **Nano Energy**, v. 12, p. 606–611, Mar 2015.
- MIAO, Z.; LIU, D.; GONG, C. Efficiency enhancement for an inductive wireless power transfer system by optimizing the impedance matching networks. **IEEE Transactions on Biomedical Circuits and Systems**, v. 11, n. 5, p. 1160–1170, 2017.
- MINNAERT, B.; STEVENS, N. Design of a capacitive wireless power transfer link with minimal receiver circuitry. In: **2018 IEEE PELS Workshop on Emerging Technologies: Wireless Power Transfer (Wow)**. [S.l.: s.n.], 2018. p. 1–5.
- MOSS, S. et al. Modelling and Experimental Validation of the Acoustic Electric Feedthrough Technique. **Air Vehicles Division**, p. 1–32, 2008.

- MUHARAM, A. et al. 13.56 mhz scalable shielded-capacitive power transfer for electric vehicle wireless charging. In: **2020 IEEE PELS Workshop on Emerging Technologies: Wireless Power Transfer (WoW)**. [S.l.: s.n.], 2020. p. 298–303.
- NAGASHIMA, T. et al. Analysis and design of loosely inductive coupled wireless power transfer system based on class-e<sup>2</sup>dc-dc converter for efficiency enhancement. **IEEE Transactions on Circuits and Systems I: Regular Papers**, v. 62, n. 11, p. 2781–2791, Nov 2015. ISSN 1549-8328.
- NAGATSUKA, Y. et al. Compact contactless power transfer system for electric vehicles. In: **The 2010 International Power Electronics Conference - ECCE ASIA -**. [S.l.: s.n.], 2010. p. 807–813.
- NAMADMALAN, A.; ALONSO, J. M.; IQBAL, A. Accurate fundamental harmonic modeling of inductive power transfer battery chargers. **IEEE Transactions on Transportation Electrification**, p. 1–1, 2021.
- NEWELL, D.; DUFFY, M. Review of power conversion and energy management for low-power, low-voltage energy harvesting powered wireless sensors. **IEEE Transactions on Power Electronics**, v. 34, n. 10, p. 9794–9805, Oct 2019. ISSN 0885-8993.
- NING, P. et al. A compact wireless charging system development. In: **2013 Twenty-Eighth Annual IEEE Applied Power Electronics Conference and Exposition (APEC)**. [S.l.: s.n.], 2013. p. 3045–3050. ISSN 1048-2334.
- OLYMPUS. **Ultrasonic Transducers Technical Notes**. 2006.
- OUTEIRO, M. T.; BUJA, G.; CZARKOWSKI, D. Resonant power converters: An overview with multiple elements in the resonant tank network. **IEEE Industrial Electronics Magazine**, v. 10, n. 2, p. 21–45, June 2016. ISSN 1941-0115.
- OZERI, S.; SHMILOVITZ, D. Ultrasonic transcutaneous energy transfer for powering implanted devices. **Ultrasonics**, v. 50, n. 6, Nov 2010. ISSN 10.1016/j.ultras.2009.11.004.
- PARESCHI, F. et al. Class-e isolated dc-dc converter with high-rate and cost-effective bidirectional data channel. **IEEE Transactions on Power Electronics**, p. 1–1, 2019. ISSN 1941-0107.
- PHADUNGTHIN, J. H. R. Application study on induction heating using half bridge llc resonant inverter. In: **2017 12th IEEE Conference on Industrial Electronics and Applications (ICIEA)**. [S.l.: s.n.], 2017. p. 1582–1585. ISSN 2158-2297.
- RADZIEMSKI, L.; S., I. R.; MAKINI, S. In Vivo Demonstration of Ultrasound Power Delivery to Charge Implanted Medical Devices via Acute and Survival Porcine Studies. **Ultrasonics**, v. 64, p. 1–9, 2017.
- ROSA, B. M. G.; YANG, G. Z. Active implantable sensor powered by ultrasounds with application in the monitoring of physiological parameters for soft tissues. In: **IEEE 13th Int. Conf. Wearable Implant. Body Sensor Netw.** [S.l.: s.n.], 2016. p. 84–89.

- ROSE, J. L. **Ultrasonic Waves in Solid Media**. 2014.
- SAHAI, A.; GRAHAM, D. Optical wireless power transmission at long wavelengths. In: **2011 International Conference on Space Optical Systems and Applications (ICSOS)**. [S.l.: s.n.], 2011. p. 164–170.
- SAKAI, N. et al. One-kilowatt capacitive power transfer via wheels of a compact electric vehicle. In: **2016 IEEE Wireless Power Transfer Conference (WPTC)**. [S.l.: s.n.], 2016. p. 1–3.
- SAMPLE, A. P.; MEYER, D. T.; SMITH, J. R. Analysis, experimental results, and range adaptation of magnetically coupled resonators for wireless power transfer. **IEEE Transactions on Industrial Electronics**, v. 58, n. 2, p. 544–554, Feb 2011. ISSN 0278-0046.
- SANDERS, S. et al. Generalized Averaging Method for Power Conversion Circuits. **IEEE Transactions on Power Electronics**, v. 6, p. 251–259, 1991.
- SANDERS, S. R. et al. Generalized averaging method for power conversion circuits. In: **21st Annual IEEE Conference on Power Electronics Specialists**. [S.l.: s.n.], 1990. p. 333–340.
- SCHMID, H.; HUBER, A. Analysis of switched-capacitor circuits using driving-point signal-flow graphs. **Analog Integr Circ Sig Process**, v. 96, Jan 2018.
- SHANG, M.; WANG, H. A voltage quadrupler rectifier based pulsewidth modulated llc converter with wide output range. **IEEE Transactions on Industry Applications**, v. 54, n. 6, p. 6159–6168, Nov 2018. ISSN 0093-9994.
- SHIH, P.-J.; SHIH, W.-P. Design, fabrication, and application of bio-implantable acoustic power transmission. **Journal of Microelectromechanical Systems**, v. 19, p. 494–502, 2010.
- SINGH, R.; CHANDRA, M.; SINGH, B. Solution of 3-dimensional wave equation by method of separation of variables. **International Journal of Current Research and Review**, v. 7, n. 14, p. 54–56, Jun 2015.
- SMITH, S. W. **Digital Signal Processing: A Practical Guide for Engineers and Scientists**. 2003.
- STONE, W. C.; HOGAN, B. P. **Optical Energy Transfer and Conversion System, U.S. Patent 9869819**. 1988.
- TAALLA, R. V. et al. A review on miniaturized ultrasonic wireless power transfer to implantable medical devices. **IEEE Access**, v. 7, p. 2092–2106, 2019. ISSN 2169-3536.
- TANZAWA, T.; TANAKA, T. A dynamic analysis of the dickson charge pump circuit. **IEEE Journal of Solid-State Circuits**, v. 32, n. 8, p. 1231–1240, Aug 1997. ISSN 0018-9200.

- TEBIANIAN J. QUAICOE, B. J. H. High frequency full-bridge class-d inverter using egan fet with dynamic dead-time control. In: **2016 IEEE PELS Workshop on Emerging Technologies: Wireless Power Transfer (WoW)**. [S.l.: s.n.], 2016. p. 95–99. ISSN null.
- THEODORIDIS, M. P. Effective capacitive power transfer. **IEEE Transactions on Power Electronics**, v. 27, n. 12, p. 4906–4913, Dec 2012. ISSN 0885-8993.
- TRAUTMANN, M. et al. Implementation of simultaneous energy and data transfer in a contactless connector. In: **2016 IEEE Topical Conference on Wireless Sensors and Sensor Networks (WiSNet)**. [S.l.: s.n.], 2016. ISSN 2332-5615.
- WANG, C. et al. Analysis and design of high performance voltage- doubler rectifier. In: **2010 5th IEEE Conference on Industrial Electronics and Applications**. [S.l.: s.n.], 2010. p. 1124–1129. ISSN 2156-2318.
- WEINER, M. M. Analysis of Cockcroft-Walton Voltage Multipliers with an Arbitrary Number of Stages. **Review of Scientific Instruments**, v. 40, p. 330–333, fev. 1969.
- WILT, K. et al. One-dimensional Pressure Transfer Models for Acoustic-Electric Transmission Channels. **Journal of Sound and Vibration**, v. 352, p. 158–173, 2015.
- W.TITOW. **PVC Plastics: Properties, Processing, and Applications**. 1990.
- WU, H. et al. Resonant converter with resonant voltage multiplier rectifier and constant frequency phase shift control for isolated buck boost power conversion. **IEEE Transactions on Industrial Electronics**, v. 62, n. 11, p. 6974–6985, Nov 2015. ISSN 0278-0046.
- WU, H. H. et al. A high efficiency 5 kw inductive charger for evs using dual side control. **IEEE Transactions on Industrial Informatics**, v. 8, n. 3, p. 585–595, Aug 2012. ISSN 1551-3203.
- YANG, D. et al. Modeling and characteristic analysis of wireless ultrasonic vibration energy transmission channels through planar and curved metal barriers. **Schock and Vibration**, v. 2018, n. 5367017, Jan 2018.
- YANG, H. et al. An ultrasonic through-metal-wall power transfer system with regulated dc output. **Applied Sciences**, v. 8, p. 692, 04 2018.
- YANG, J. **An Introduction to the Theory of Piezoelectricity**. 2018.
- YANG, Y. et al. Comparison of inductor-half-bridge and class-e resonant topologies for piezoelectric transformer applications. In: **2009 IEEE Energy Conversion Congress and Exposition**. [S.l.: s.n.], 2009. p. 776–782.
- YAO, Y. et al. Analysis and design of a simultaneous wireless power and data transfer system featuring high data rate and signal-to-noise ratio. **IEEE Transactions on Industrial Electronics**, p. 1–1, 2020.

- ZOID, T. et al. A Development of Acoustic Energy Transfer System Through Air Medium Using Push-Pull Power Converter. **WSEAS Transactions on Power Systems**, v. 11, p. 35–42, 2016. ISSN 2224-350X.
- ZHAKSYLYK, Y. et al. Analysis of fundamental differences between capacitive and inductive impedance matching for inductive wireless power transfer. **Electronics**, v. 9, n. 476, p. 1–14, Mar 2020.
- ZHANG, C. et al. A new energy harvesting and wireless power transfer system for smart grid. In: **2016 IEEE 7th International Symposium on Power Electronics for Distributed Generation Systems (PEDG)**. [S.l.: s.n.], 2016. p. 1–5. ISSN 2329-5767.
- ZHANG, J. The fem analysis of pzt5h piezoelectric square sheet thickness mode vibration. In: **2017 Far East NDT New Technology Application Forum (FENDT)**. [S.l.: s.n.], 2017. p. 154–158.
- ZHANG, S. et al. A high-power-factor integrated-stage ac-dc led driver based on flyback-class e converter. In: **2017 IEEE Industry Applications Society Annual Meeting**. [S.l.: s.n.], 2017. p. 1–5.
- ZHU, J. et al. A novel capacitive coupler array with free-positioning feature for mobile tablet applications. **IEEE Transactions on Power Electronics**, v. 34, n. 7, p. 6014–6019, July 2019. ISSN 0885-8993.
- ZIMMERMAN, W. **Multiphysics Modeling with Finite Element Methods**. 2006.
- ZUMBAHLEN, H. **Linear Circuit Design Handbook**, Newnes. 2008.



## APPENDICES

---



## Appendix A – Generic Transfer Media Decomposition into Lumped Components

### A.1 GENERIC TRANSFER MEDIA DECOMPOSITION INTO LUMPED COMPONENTS

This appendix shows the decomposition of a transfer media into lumped components considering  $n$  number of acoustic networks. In a generalized way, the transfer media with  $n$ -networks is represented by the following state-space model: the state vector is composed of the acoustic sound pressures and velocities

$$\mathbf{x}(t) = \begin{bmatrix} q_1 & 0 & 0 & 0 & 0 & 0 \\ 0 & \ddots & 0 & 0 & 0 & 0 \\ 0 & 0 & q_{\frac{n}{2}} & 0 & 0 & 0 \\ 0 & 0 & 0 & p_1 & 0 & 0 \\ 0 & 0 & 0 & 0 & \ddots & 0 \\ 0 & 0 & 0 & 0 & 0 & p_{\frac{n}{2}} \end{bmatrix}. \quad (\text{A.1})$$

The output vector is selected with all desirable variables divided by the acoustic sound pressure amplitude  $P_{in}$  or acoustic sound velocity amplitude  $Q_{in}$

$$\mathbf{y}(t) = \left[ \frac{\mathbf{q}_1}{\mathbf{Q}_{in}}, \dots, \frac{\mathbf{q}_{\frac{n}{2}}}{\mathbf{Q}_{in}}, \frac{\mathbf{p}_1}{\mathbf{P}_{in}}, \dots, \frac{\mathbf{p}_{\frac{n}{2}}}{\mathbf{P}_{in}} \right]^T. \quad (\text{A.2})$$

The state-space matrices are equated as

$$\mathbf{A} = \begin{bmatrix} -\frac{Z_{a,1}}{M_{a,1}} & 0 & 0 & 0 & -\frac{1}{M_{a,1}} & 0 & 0 & 0 \\ 0 & -\frac{Z_{a,2}}{M_{a,2}} & 0 & 0 & \frac{1}{M_{a,2}} & -\frac{1}{M_{a,2}} & 0 & 0 \\ 0 & 0 & \ddots & 0 & 0 & \ddots & \ddots & 0 \\ 0 & 0 & 0 & -\frac{Z_{a,\frac{n}{2}}}{M_{a,\frac{n}{2}}} & 0 & 0 & \frac{1}{M_{a,\frac{n}{2}}} & -\frac{1}{M_{a,\frac{n}{2}}} \\ \frac{1}{N_{a,1}} & -\frac{1}{N_{a,1}} & 0 & 0 & 0 & 0 & 0 & 0 \\ 0 & \frac{1}{N_{a,2}} & -\frac{1}{N_{a,2}} & 0 & 0 & 0 & 0 & 0 \\ 0 & 0 & \ddots & \ddots & 0 & 0 & 0 & 0 \\ 0 & 0 & 0 & 0 & \frac{1}{N_{a,n}} & 0 & 0 & -\frac{1}{Z_{o,\frac{n}{2}}} \end{bmatrix}, \quad (\text{A.3})$$

$$\mathbf{B} = \left[ \frac{1}{M_{a,1}} \quad 0 \quad \dots \quad 0 \right]^T, \quad (\text{A.4})$$

$$\mathbf{C} = \begin{bmatrix} \frac{1}{Q_{in}} & 0 & 0 & 0 & 0 & 0 \\ 0 & \ddots & 0 & 0 & 0 & 0 \\ 0 & 0 & \frac{1}{Q_{in}} & 0 & 0 & 0 \\ 0 & 0 & 0 & \frac{1}{P_{in}} & 0 & 0 \\ 0 & 0 & 0 & 0 & \ddots & 0 \\ 0 & 0 & 0 & 0 & 0 & \frac{1}{P_{in}} \end{bmatrix} \quad (\text{A.5})$$

and

$$\mathbf{D} = [0 \quad \dots \quad 0]^T. \quad (\text{A.6})$$

A new vector space is described as

$$\mathbf{e}(t) = \begin{bmatrix} q_1 \frac{\sqrt{M_{a,1}}}{\sqrt{2}} & 0 & 0 & 0 & 0 & 0 \\ 0 & \ddots & 0 & 0 & 0 & 0 \\ 0 & 0 & q_{\frac{n}{2}} \frac{\sqrt{M_{a,\frac{n}{2}}}}{\sqrt{2}} & 0 & 0 & 0 \\ 0 & 0 & 0 & p_1 \frac{\sqrt{N_{a,1}}}{\sqrt{2}} & 0 & 0 \\ 0 & 0 & 0 & 0 & \ddots & 0 \\ 0 & 0 & 0 & 0 & 0 & p_{\frac{n}{2}} \frac{\sqrt{N_{a,\frac{n}{2}}}}{\sqrt{2}} \end{bmatrix}, \quad (\text{A.7})$$

which leads to

$$\mathbf{P} = \mathbf{e}(t) \cdot \mathbf{x}(t) = \begin{bmatrix} \frac{\sqrt{M_{a,1}}}{\sqrt{2}} & 0 & 0 & 0 & 0 & 0 \\ 0 & \ddots & 0 & 0 & 0 & 0 \\ 0 & 0 & \frac{\sqrt{M_{a,\frac{n}{2}}}}{\sqrt{2}} & 0 & 0 & 0 \\ 0 & 0 & 0 & \frac{\sqrt{N_{a,1}}}{\sqrt{2}} & 0 & 0 \\ 0 & 0 & 0 & 0 & \ddots & 0 \\ 0 & 0 & 0 & 0 & 0 & \frac{\sqrt{N_{a,\frac{n}{2}}}}{\sqrt{2}} \end{bmatrix}. \quad (\text{A.8})$$

A new input matrix is equated by,

$$\bar{\mathbf{B}} = \begin{bmatrix} \frac{1}{\sqrt{2M_{a,1}\omega}} \\ \vdots \\ 0 \end{bmatrix}. \quad (\text{A.9})$$

The correction factor  $\Gamma$  is equated as

$$\Gamma = \frac{\sqrt{2M_{a,1}\omega}}{P_a}. \quad (\text{A.10})$$

By using the correction factor, matrix  $\mathbf{P}$  is equated again. The new state-space

model is described by means of (3.70), (3.71), (3.72) and (3.73),

$$\bar{\mathbf{A}} = \begin{bmatrix} -\frac{Z_{a,1}}{\omega M_{a,1}} & 0 & 0 & 0 & -\frac{\omega^{-1}}{\sqrt{M_{a,1}N_{a,1}}} & 0 & 0 & 0 \\ & -\frac{Z_{a,2}}{\omega M_{a,2}} & 0 & 0 & \frac{\omega^{-1}}{\sqrt{M_{a,2}N_{a,1}}} & -\frac{\omega^{-1}}{\sqrt{M_{a,2}N_{a,2}}} & 0 & 0 \\ 0 & 0 & \ddots & 0 & 0 & \ddots & \ddots & 0 \\ 0 & 0 & 0 & -\frac{Z_{a,n}}{\omega M_{a,n}} & 0 & 0 & \frac{\omega^{-1}}{\sqrt{M_{a,n}N_{a,n}}} & -\frac{\omega^{-1}}{\sqrt{M_{a,n}N_{a,n}}} \\ \frac{\omega^{-1}}{\sqrt{M_{a,1}N_{a,1}}} & -\frac{\omega^{-1}}{\sqrt{M_{a,2}N_{a,1}}} & 0 & 0 & 0 & 0 & 0 & 0 \\ 0 & \frac{\omega^{-1}}{\sqrt{M_{a,2}N_{a,2}}} & -\frac{\omega^{-1}}{\sqrt{M_{a,3}N_{a,2}}} & 0 & 0 & 0 & 0 & 0 \\ 0 & 0 & \ddots & \ddots & 0 & 0 & 0 & 0 \\ 0 & 0 & 0 & 0 & \frac{\omega^{-1}}{\sqrt{M_{a,n}N_{a,n}}} & 0 & 0 & -\frac{\omega^{-1}}{N_{a,5}Z_{o,\frac{n}{2}}} \end{bmatrix}, \quad (\text{A.11})$$

$$\bar{\mathbf{B}} = [1 \ 0 \ \dots \ 0]^T, \quad (\text{A.12})$$

$$\bar{\mathbf{C}} = \begin{bmatrix} \frac{P_{in}}{Q_{in}\omega M_{a,1}} & 0 & 0 & 0 & 0 & 0 & 0 \\ 0 & \frac{P_{in}}{Q_{in}\omega\sqrt{M_{a,1}M_{a,2}}} & 0 & 0 & 0 & 0 & 0 \\ 0 & 0 & \ddots & 0 & 0 & 0 & 0 \\ 0 & 0 & 0 & \frac{P_{in}}{Q_{in}\omega\sqrt{M_{a,1}M_{a,n}}} & 0 & 0 & 0 \\ 0 & 0 & 0 & 0 & \frac{1}{\omega\sqrt{M_{a,1}N_{a,1}}} & 0 & 0 \\ 0 & 0 & 0 & 0 & 0 & \ddots & 0 \\ 0 & 0 & 0 & 0 & 0 & 0 & \frac{1}{\omega\sqrt{M_{a,1}N_{a,n}}} \end{bmatrix} \quad (\text{A.13})$$

and

$$\bar{\mathbf{D}} = [0 \ \dots \ 0]^T. \quad (\text{A.14})$$

The decomposition into unit-less parameters for the transfer media representation is portrayed in Figure A.1:

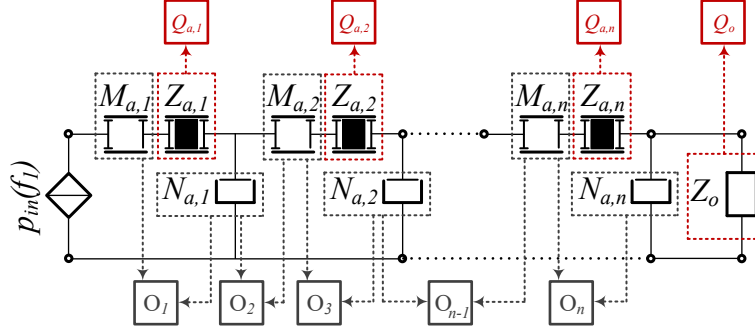
The unit-less parameters are equated as

$$O_1 = \frac{\omega_1}{\omega}, \quad (\text{A.15})$$

$$O_2 = \frac{\omega_2}{\omega}, \quad (\text{A.16})$$

$$O_{n-1} = \frac{\omega_{n-1}}{\omega}, \quad (\text{A.17})$$

Figure A.1 – Decomposition into unit-less parameters for the transfer media representation.



Source: Author.

$$O_n = \frac{\omega_n}{\omega}, \quad (\text{A.18})$$

$$Q_{a,1} = \frac{\omega_1 M_{a,1}}{Z_{a,1}} = \frac{1}{\omega_1 N_{a,1} Z_{a,1}}, \quad (\text{A.19})$$

$$Q_{a,2} = \frac{\omega_2 M_{a,2}}{Z_{a,2}} = \frac{1}{\omega_2 N_{a,2} Z_{a,2}}, \quad (\text{A.20})$$

$$Q_{a,n} = \frac{\omega_n M_{a,n}}{Z_{a,n}} = \frac{1}{\omega_n N_{a,n} Z_{a,n}}, \quad (\text{A.21})$$

$$Q_o = \frac{Z_o}{\omega_n N_{a,n}} = \omega_n N_{a,n} Z_o, \quad (\text{A.22})$$

$$T_{POT} = \frac{1}{a} = \frac{Z_o Q_{in}}{P_{in}}, \quad (\text{A.23})$$

 in which, the angular resonant frequencies  $\omega_1$ ,  $\omega_2$ ,  $\omega_{n-1}$  and  $\omega_n$  are given by

$$\omega_1 = \frac{1}{\sqrt{M_{a,1} N_{a,1}}}, \quad (\text{A.24})$$

$$\omega_2 = \frac{1}{\sqrt{M_{a,2} N_{a,2}}}, \quad (\text{A.25})$$

$$\omega_{n-1} = \frac{1}{\sqrt{M_{a,n-1} N_{a,n-1}}} \quad (\text{A.26})$$

and

$$\omega_n = \frac{1}{\sqrt{M_{a,n} N_{a,n}}}. \quad (\text{A.27})$$

The terms of the state-space matrices are converted into unit-less parameters by means of (A.15)-(A.27). The normalized state-space model for the transfer media with n-networks is represented by

$$\bar{\mathbf{E}} = \begin{bmatrix} -\frac{O_1}{Q_1} & 0 & 0 & 0 & -O_1 & 0 & 0 & 0 \\ & -\frac{O_2}{Q_2} & 0 & 0 & O_2 & -O_3 & 0 & 0 \\ 0 & 0 & \ddots & 0 & 0 & \ddots & \ddots & 0 \\ 0 & 0 & 0 & -\frac{O_n}{Q_n} & 0 & 0 & O_{n-1} & -O_n \\ O_1 & -O_2 & 0 & 0 & 0 & 0 & 0 & 0 \\ 0 & O_3 & -O_4 & 0 & 0 & 0 & 0 & 0 \\ 0 & 0 & \ddots & \ddots & 0 & 0 & 0 & 0 \\ 0 & 0 & 0 & 0 & O_n & 0 & 0 & -\frac{O_n}{Q_o} \end{bmatrix}, \quad (\text{A.28})$$

$$\bar{\mathbf{F}} = [1 \ 0 \ \dots \ 0]^T, \quad (\text{A.29})$$

$$\bar{\mathbf{G}} = \begin{bmatrix} aQ_o \frac{\prod_{i=1}^n O_{2i-1}}{\prod_{i=1}^{n-1} O_{2i}^2} & 0 & 0 & 0 & 0 & 0 & 0 \\ 0 & aQ_o \frac{\prod_{i=1}^1 O_{2i-1} \prod_{i=2}^n O_{2i-1}^2}{\prod_{i=1}^1 O_{2i} \prod_{i=2}^{n-1} O_{2i}^2} & 0 & 0 & 0 & 0 & 0 \\ 0 & 0 & \ddots & 0 & 0 & 0 & 0 \\ 0 & 0 & 0 & aQ_o \frac{\prod_{i=1}^n O_{2i-1}}{\prod_{i=1}^{n-1} O_{2i}} & 0 & 0 & 0 \\ 0 & 0 & 0 & 0 & O_1 & 0 & 0 \\ 0 & 0 & 0 & 0 & 0 & \ddots & 0 \\ 0 & 0 & 0 & 0 & 0 & 0 & \frac{\prod_{i=1}^n O_{2i-1}}{\prod_{i=1}^{n-1} O_{2i}} \end{bmatrix} \quad (\text{A.30})$$

and

$$\bar{\mathbf{H}} = [0 \ \dots \ 0]^T. \quad (\text{A.31})$$

The linear system to be solved is described as follows:

$$\begin{pmatrix} q_1(2\pi)_{[O_1, O_2, \dots, O_n, Q_1, Q_2, \dots, Q_n, q_1(0), \dots, q_n(0), p_1(0), \dots, p_n(0), Q_o]} \\ \vdots \\ q_n(2\pi)_{[O_1, O_2, \dots, O_n, Q_1, Q_2, \dots, Q_n, q_1(0), \dots, q_n(0), p_1(0), \dots, p_n(0), Q_o]} \\ p_1(2\pi)_{[O_1, O_2, \dots, O_n, Q_1, Q_2, \dots, Q_n, q_1(0), \dots, q_n(0), p_1(0), \dots, p_n(0), Q_o]} \\ \vdots \\ p_n(2\pi)_{[O_1, O_2, \dots, O_n, Q_1, Q_2, \dots, Q_n, q_1(0), \dots, q_n(0), p_1(0), \dots, p_n(0), Q_o]} \end{pmatrix} = \begin{pmatrix} q_1(0) \\ \vdots \\ q_n(0) \\ p_1(0) \\ \vdots \\ p_n(0) \end{pmatrix}. \quad (\text{A.32})$$





## Appendix B – Proofs

### B.1 PROOF OF LEMMA 1

**Lemma 1.** *The multiplication of the state and input matrices from a generic state-space model in (3.5) and (3.6) by a linear operator, proportionally modifies the independent variable of the derivative operator and the argument of the related function.*

*Proof:* Consider a generic state-space model described by:

$$\frac{d\mathbf{x}(t)}{dt} = \mathbf{A}_k \mathbf{x}(t) + \mathbf{B}_k u(t) = \frac{d}{dt} \begin{bmatrix} \mathbf{x}_1(t) \\ \vdots \\ \mathbf{x}_m(t) \end{bmatrix} = \begin{bmatrix} a_{11} & \cdots & a_{1n} \\ \vdots & \ddots & \vdots \\ a_{m1} & \cdots & a_{mn} \end{bmatrix} \begin{bmatrix} \mathbf{x}_1(t) \\ \vdots \\ \mathbf{x}_m(t) \end{bmatrix} + \begin{bmatrix} b_1 \\ \vdots \\ b_m \end{bmatrix} u(t). \quad (\text{B.1})$$

The model in (B.1) can be described by a set of differential equations:

$$\begin{aligned} \frac{d\mathbf{x}_1(t)}{dt} &= a_{11}\mathbf{x}_1(t) \dots a_{1n}\mathbf{x}_m(t) + b_1 u(t) \\ &\vdots \\ \frac{d\mathbf{x}_m(t)}{dt} &= a_{m1}\mathbf{x}_1(t) \dots a_{mn}\mathbf{x}_m(t) + b_m u(t). \end{aligned} \quad (\text{B.2})$$

By multiplying the state and input matrices by  $\frac{1}{\omega}$  gives

$$\frac{1}{\omega} \mathbf{A}_i = \begin{bmatrix} \frac{a_{11}}{\omega} & \cdots & \frac{a_{1n}}{\omega} \\ \vdots & \ddots & \vdots \\ \frac{a_{m1}}{\omega} & \cdots & \frac{a_{mn}}{\omega} \end{bmatrix} \quad (\text{B.3})$$

and

$$\frac{1}{\omega} \mathbf{B}_i = \begin{bmatrix} \frac{b_1}{\omega} \\ \vdots \\ \frac{b_m}{\omega} \end{bmatrix} u(t). \quad (\text{B.4})$$

If (B.3) and (B.4) are true for any values of the terms of the matrices, then, the term  $\frac{1}{\omega}$  is a linear operator and the following relation is true:

$$\dot{\mathbf{x}}(t) = \frac{d\mathbf{x}(t)}{dt} \Leftrightarrow \frac{1}{\omega} \dot{\mathbf{x}}(t) = \frac{d\mathbf{x}(\omega t)}{d\omega t} \quad (\text{B.5})$$

This operation modifies the independent variable time  $t$  to frequency  $\omega t$ . By means of such operation, the system is normalized by the frequency.

■

## B.2 PROOF OF THEOREM 1

**Theorem 1.** *A generic system described by a state-space model  $\mathbf{x}(t) = \mathbf{A}\mathbf{x}(t) + \mathbf{B}u$  and  $\mathbf{y}(t) = \mathbf{C}\mathbf{x}(t) + \mathbf{D}u$  can be represented as a dimensionless model normalized by the input source and the operating frequency by using the transfer power ratio and the resonance among the storage elements.*

*Proof:* Considering *Axiom 1-Axiom 15*, a system can be interpreted by means of the relationships among storage elements and the system's quality factors. Considering *Lemma 1*, a system can be normalized by the operating angular frequency. An equivalence transformation  $\mathbf{P}$  can be used to modify the vector space of a system, also, it can be used to normalize the system in relation to the input source, as shown in (3.77), which does not interfere in the state matrix. The system parameters can be converted into unit-less parameters using (3.84)-(3.100).

■

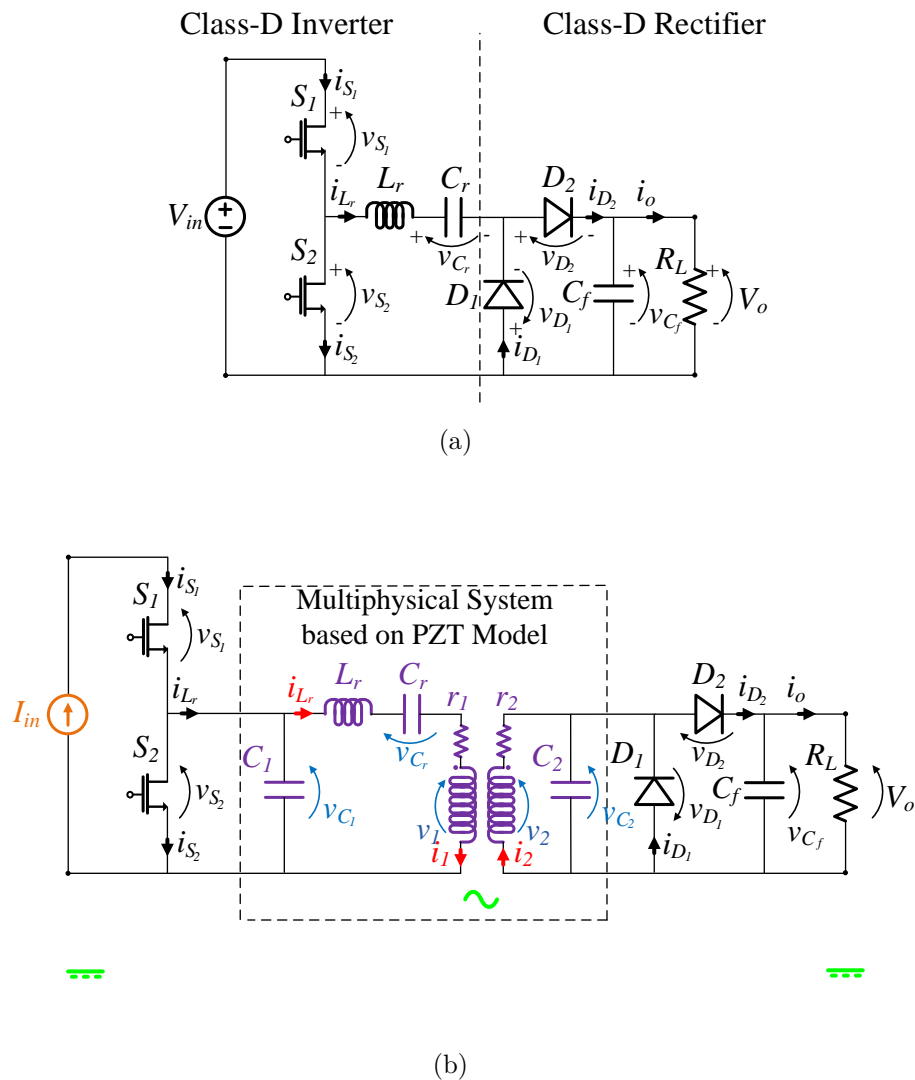
## Appendix C – Class-D<sup>2</sup> Resonant Converter

### C.1 CLASS-D<sup>2</sup> RESONANT CONVERTER

The Class-D<sup>2</sup> resonant converter is other topology that can be used to analyze the electro-mechanical-acoustic CET system. It is composed of a Class-D inverter and a Class-D rectifier, which are connected in the equivalent model of the multiphysical system.

The converter is shown in Figure C.1(a) and the CET system in Figure C.1(b).

Figure C.1 – Class-D<sup>2</sup> resonant power conversion system. (a) Class-D<sup>2</sup> resonant converter. (b) Electro-mechanical-acoustic CET system based on Class-D<sup>2</sup> topology.

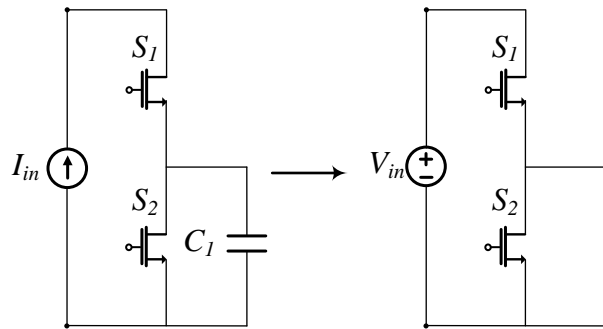


The converter is composed of: input voltage source  $V_{in}$ , switch  $S_1$ , switch  $S_2$ , resonant inductor  $L_r$ , resonant capacitor  $C_r$ , diode  $D_1$ , diode  $D_2$ , output capacitor  $C_f$  and load  $R_L$ . The circuit variables are:  $i_{L_r}$ , inductor  $L_r$  current;  $v_{C_r}$ , capacitor  $C_r$  voltage;  $v_{C_f}$ , capacitor  $C_f$  voltage;  $i_{S_1}$ , switch  $S_1$  current;  $i_{S_2}$ , switch  $S_2$  current;  $v_{S_1}$ , switch  $S_1$

voltage;  $v_{S_2}$ , switch  $S_2$  voltage;  $i_{D_1}$ , diode  $D_1$  current;  $i_{D_2}$ , diode  $D_2$  current;  $v_{D_1}$ , diode  $D_1$  voltage;  $v_{D_2}$ , diode  $D_2$  voltage;  $i_o$ , output current; and  $V_o$ , output voltage.

Due to the capacitor  $C_1$  from the equivalent electrical model of the multiphysics system, the input voltage source  $V_{in}$  is replaced by a input current source  $I_{in}$  as shown in Figure C.1(b). In order to evaluate the system considering input voltage to output voltage transfer function,  $I_{in}$  and  $C_1$  are replaced by a voltage constant source  $V_{in}$ . This assumption is shown in Figure C.2.

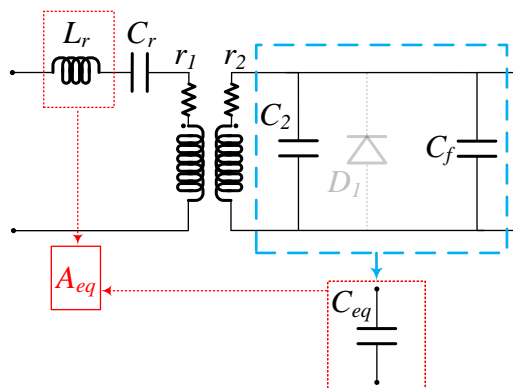
Figure C.2 – Assumption for the input source of the Class- $D^2$  resonant DC-DC converter.



Source: Author.

When  $D_1$  is on and  $D_2$  is off, capacitor  $C_2$  in Figure C.1(b) is short-circuited. When  $D_1$  is off and  $D_2$  is on, capacitor  $C_2$  has parallel connection to  $C_f$ . In this sense, they can be combined into a single capacitor, which determines one resonant frequency with  $L_f$ . This assumption is shown in Figure C.3.

Figure C.3 – Assumption for the output capacitor of the Class- $D^2$  resonant DC-DC converter.



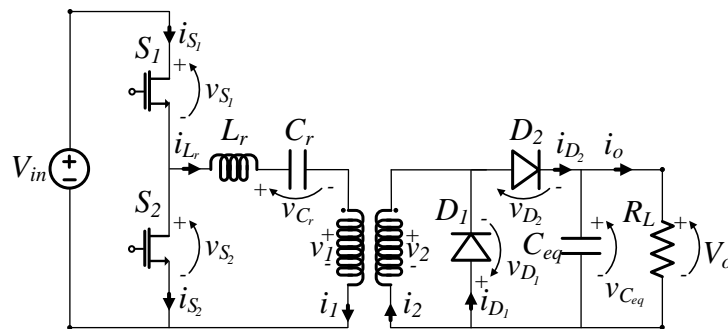
Source: Author.

Based on that, the converter is going to be analyzed considering the following assumptions:

1. The input current source  $I_{in}$  and the capacitor  $C_1$  are replaced by a constant voltage source  $V_{in}$ ;
2. The capacitors  $C_2$  and  $C_f$  are combined into a single capacitor  $C_{eq}$ ;
3. The switches  $S_1$  and  $S_2$  and diodes  $D_1$  and  $D_2$  off states are modeled as a open-circuit;
4. The switches  $S_1$  and  $S_2$  and diodes  $D_1$  and  $D_2$  on states are modeled as a short-circuit;
5. The transformer is considered as an ideal component.

The model for the converter is depicted in Figure C.4.

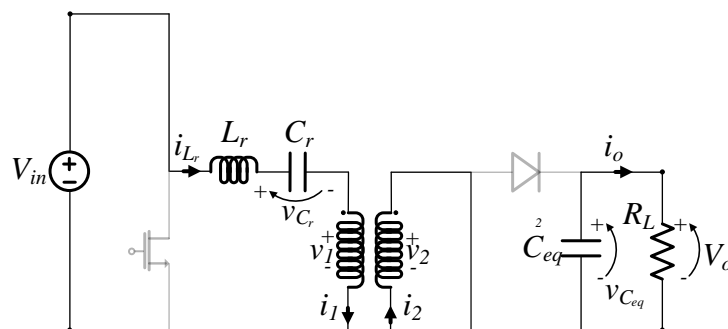
Figure C.4 – Class- $D^2$  resonant DC-DC converter model.



Source: Author.

The converter has four operating modes. At mode  $I$ ,  $S_1$  and  $D_1$  are on and  $S_2$  and  $D_2$  are off. The mode occurs from 0 to  $T_1$ , being  $T_1$  the time that the mode ends. The circuit for mode  $I$  is shown in Figure C.5.

Figure C.5 – Class- $D^2$  resonant DC-DC converter - Operating mode  $I$ :  $S_1$  and  $D_1$  on;  $S_2$  and  $D_2$  off.



Source: Author.

The converter is governed by the following differential equations:

$$\frac{di_{L_r}(t)}{dt} = \frac{V_{in}}{L_r} - \frac{v_{C_1}(t)}{L_r}, \quad (C.1)$$

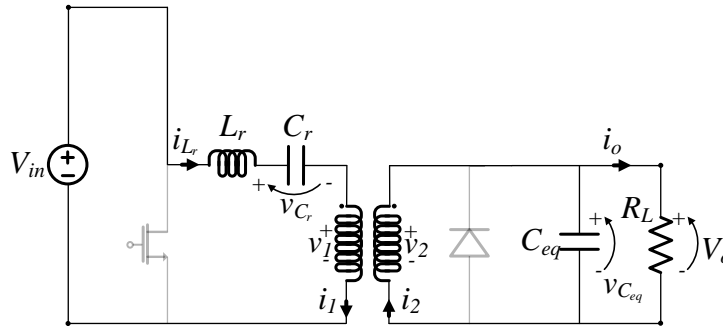
$$\frac{dv_{C_r}(t)}{dt} = \frac{i_{L_r}(t)}{C_r}, \quad (C.2)$$

and

$$\frac{dv_{C_{eq}}(t)}{dt} = -\frac{v_{C_{eq}}(t)}{R_L C_{eq}}. \quad (C.3)$$

At mode *II*,  $S_1$  and  $D_2$  are on and  $S_2$  and  $D_1$  are off. The mode ends at  $D_c 2\pi$ . The circuit is depicted in Figure C.6.

Figure C.6 – Class-D<sup>2</sup> resonant DC-DC converter - Operating mode *II*:  $S_1$  and  $D_2$  on;  $S_2$  and  $D_1$  off.



Source: Author.

The following equations are considered:

$$\frac{di_{L_r}(t)}{dt} = \frac{V_{in}}{L_r} - \frac{v_{C_1}(t)}{L_r} - \alpha \frac{v_{C_{eq}}(t)}{L_r}, \quad (C.4)$$

$$\frac{dv_{C_r}(t)}{dt} = \frac{i_{L_r}(t)}{C_r}, \quad (C.5)$$

and

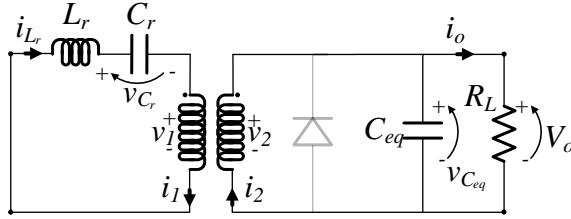
$$\frac{dv_{C_{eq}}(t)}{dt} = \alpha \frac{i_{L_r}(t)}{C_{eq}} - \frac{v_{C_{eq}}(t)}{R_L C_{eq}}. \quad (C.6)$$

At mode *III*,  $S_2$  and  $D_2$  are on and  $S_1$  and  $D_1$  are off. The mode occurs from  $D_c 2\pi$  to  $T_2$ , being  $T_2$  the time in which the mode ends. The circuit is shown in Figure C.7.

The converter is governed by:

$$\frac{di_{L_r}(t)}{dt} = -\frac{v_{C_1}(t)}{L_r} - \alpha \frac{v_{C_{eq}}(t)}{L_r}, \quad (C.7)$$

Figure C.7 – Class- $D^2$  resonant DC-DC converter - Operating mode  $III$ :  $S_2$  and  $D_2$  on;  $S_1$  and  $D_1$  off.



Source: Author.

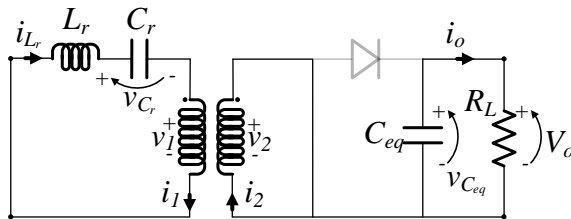
$$\frac{dv_{C_r}(t)}{dt} = \frac{i_{L_r}(t)}{C_r}, \quad (\text{C.8})$$

and

$$\frac{dv_{C_{eq}}(t)}{dt} = \alpha \frac{i_{L_r}(t)}{C_{eq}} - \frac{v_{C_{eq}}(t)}{R_L C_{eq}}. \quad (\text{C.9})$$

At mode  $IV$ ,  $S_2$  and  $D_1$  are on and  $S_1$  and  $D_2$  are off. The mode ends at  $2\pi$ . The circuit is shown in Figure C.8.

Figure C.8 – Class- $D^2$  resonant DC-DC converter - Operating mode  $IV$ :  $S_2$  and  $D_1$  on;  $S_1$  and  $D_2$  off.



Source: Author.

The differential equations are:

$$\frac{di_{L_r}(t)}{dt} = -\frac{v_{C_1}(t)}{L_r}, \quad (\text{C.10})$$

$$\frac{dv_{C_r}(t)}{dt} = \frac{i_{L_r}(t)}{C_r}, \quad (\text{C.11})$$

and

$$\frac{dv_{C_{eq}}(t)}{dt} = -\frac{v_{C_{eq}}(t)}{R_L C_{eq}}. \quad (\text{C.12})$$

The state vector  $\mathbf{x}(t)$  and output vector  $\mathbf{y}(t)$  are written as

$$\mathbf{x}(t) = [\mathbf{i}_{L_r}, \mathbf{v}_{C_r}, \mathbf{v}_{C_{eq}}]^T \quad (\text{C.13})$$

and

$$\mathbf{y}(t) = \left[ \frac{\mathbf{i}_{L_r}}{\mathbf{I}_{in}}, \frac{\mathbf{v}_{C_r}}{\mathbf{V}_{in}}, \frac{\mathbf{v}_{C_{eq}}}{\mathbf{V}_{in}}, \frac{\mathbf{i}_{S_1}}{\mathbf{I}_{in}}, \frac{\mathbf{i}_{S_2}}{\mathbf{I}_{in}}, \frac{\mathbf{i}_{D_1}}{\mathbf{I}_{in}}, \frac{\mathbf{i}_{D_2}}{\mathbf{I}_{in}}, \frac{\mathbf{v}_{S_1}}{\mathbf{V}_{in}}, \frac{\mathbf{v}_{S_2}}{\mathbf{V}_{in}}, \frac{\mathbf{v}_{D_1}}{\mathbf{V}_{in}}, \frac{\mathbf{v}_{D_2}}{\mathbf{V}_{in}}, \frac{\mathbf{i}_{in}}{\mathbf{I}_{in}} \right]^T. \quad (\text{C.14})$$

The input is  $u(t) = V_{in}$ . The system representation based on (4.18) and (4.19) is given by the following matrices:

$$\mathbf{A}_I = \begin{bmatrix} 0 & -\frac{1}{L_r} & 0 \\ \frac{1}{C_r} & 0 & 0 \\ 0 & 0 & -\frac{R_L}{C_2} \end{bmatrix}, \quad (\text{C.15})$$

$$\mathbf{B}_I = \begin{bmatrix} \frac{1}{L_r} \\ 0 \\ 0 \end{bmatrix}, \quad (\text{C.16})$$

$$\mathbf{A}_{II} = \begin{bmatrix} 0 & -\frac{1}{L_r} & -\frac{\alpha}{L_r} \\ \frac{1}{C_r} & 0 & 0 \\ \frac{\alpha}{C_2} & 0 & -\frac{1}{R_L C_2} \end{bmatrix}, \quad (\text{C.17})$$

$$\mathbf{B}_{II} = \begin{bmatrix} \frac{1}{L_r} \\ 0 \\ 0 \end{bmatrix}, \quad (\text{C.18})$$

$$\mathbf{A}_{III} = \begin{bmatrix} 0 & -\frac{1}{L_r} & -\frac{\alpha}{L_r} \\ \frac{1}{C_r} & 0 & 0 \\ \frac{\alpha}{C_2} & 0 & -\frac{1}{R_L C_2} \end{bmatrix}, \quad (\text{C.19})$$

$$\mathbf{B}_{III} = \begin{bmatrix} 0 \\ 0 \\ 0 \end{bmatrix}, \quad (\text{C.20})$$

$$\mathbf{A}_{IV} = \begin{bmatrix} 0 & -\frac{1}{L_r} & 0 \\ \frac{1}{C_r} & 0 & 0 \\ 0 & 0 & -\frac{R_L}{C_2} \end{bmatrix}, \quad (\text{C.21})$$



$$\mathbf{B}_{IV} = \begin{bmatrix} 0 \\ 0 \\ 0 \end{bmatrix}, \quad (\text{C.22})$$

$$\mathbf{C}_I = \begin{bmatrix} \frac{1}{I_{in}} & 0 & 0 & 0 & 0 & \frac{1}{I_{in}} & 0 & 0 & -\frac{1}{I_{in}} & 0 & 0 & \frac{1}{I_{in}} \\ 0 & \frac{1}{V_{in}} & 0 & 0 & 0 & 0 & 0 & 0 & 0 & 0 & 0 & 0 \\ 0 & 0 & \frac{1}{V_{in}} & 0 & 0 & 0 & 0 & 0 & 0 & \frac{1}{V_{in}} & 0 & 0 \end{bmatrix}^T, \quad (\text{C.23})$$

$$\mathbf{C}_{II} = \begin{bmatrix} \frac{1}{I_{in}} & 0 & 0 & 0 & 0 & \frac{1}{I_{in}} & 0 & \frac{1}{I_{in}} & 0 & 0 & 0 & \frac{1}{I_{in}} \\ 0 & \frac{1}{V_{in}} & 0 & 0 & 0 & 0 & 0 & 0 & 0 & 0 & 0 & 0 \\ 0 & 0 & \frac{1}{V_{in}} & 0 & 0 & 0 & 0 & 0 & 0 & 0 & -\frac{1}{V_{in}} & 0 \end{bmatrix}^T, \quad (\text{C.24})$$

$$\mathbf{C}_{III} = \begin{bmatrix} \frac{1}{I_{in}} & 0 & 0 & 0 & 0 & 0 & -\frac{1}{I_{in}} & \frac{1}{I_{in}} & 0 & 0 & 0 & \frac{1}{I_{in}} \\ 0 & \frac{1}{V_{in}} & 0 & 0 & 0 & 0 & 0 & 0 & 0 & 0 & 0 & 0 \\ 0 & 0 & \frac{1}{V_{in}} & 0 & 0 & 0 & 0 & 0 & 0 & 0 & -\frac{1}{V_{in}} & 0 \end{bmatrix}^T, \quad (\text{C.25})$$

$$\mathbf{C}_{IV} = \begin{bmatrix} \frac{1}{I_{in}} & 0 & 0 & 0 & 0 & 0 & -\frac{1}{I_{in}} & 0 & -\frac{1}{I_{in}} & 0 & 0 & \frac{1}{I_{in}} \\ 0 & \frac{1}{V_{in}} & 0 & 0 & 0 & 0 & 0 & 0 & 0 & 0 & 0 & 0 \\ 0 & 0 & \frac{1}{V_{in}} & 0 & 0 & 0 & 0 & 0 & 0 & -\frac{1}{V_{in}} & 0 & 0 \end{bmatrix}^T, \quad (\text{C.26})$$

$$\mathbf{D}_I = \left[ 0 \ 0 \ 0 \ 0 \ 0 \ 0 \ 0 \ 0 \ 0 \ \frac{1}{V_{in}} \ 0 \ 0 \ 0 \right]^T, \quad (\text{C.27})$$

$$\mathbf{D}_{II} = \left[ 0 \ 0 \ 0 \ 0 \ 0 \ 0 \ 0 \ 0 \ 0 \ \frac{1}{V_{in}} \ 0 \ 0 \ 0 \right]^T, \quad (\text{C.28})$$

$$\mathbf{D}_{III} = \left[ 0 \ 0 \ 0 \ 0 \ 0 \ 0 \ 0 \ 0 \ \frac{1}{V_{in}} \ 0 \ 0 \ 0 \ 0 \right]^T \quad (\text{C.29})$$

and

$$\mathbf{D}_{IV} = \left[ 0 \ 0 \ 0 \ 0 \ 0 \ 0 \ 0 \ 0 \ \frac{1}{V_{in}} \ 0 \ 0 \ 0 \ 0 \right]^T. \quad (\text{C.30})$$

The new vector space  $\mathbf{e}(t)$  is defined based on the square roots of the storage energy in the reactive components

$$\mathbf{e}(t) = \begin{bmatrix} i_{L_r} \frac{\sqrt{L_r}}{\sqrt{2}} & 0 & 0 \\ 0 & v_{C_r} \frac{\sqrt{C_r}}{\sqrt{2}} & 0 \\ 0 & 0 & v_{C_{eq}} \frac{\sqrt{C_{eq}}}{\sqrt{2}} \end{bmatrix}, \quad (\text{C.31})$$

which leads to

$$\mathbf{P} = \mathbf{e}(t) \cdot \mathbf{x}(t) = \begin{bmatrix} \frac{\sqrt{L_r}}{\sqrt{2}} & 0 & 0 \\ 0 & \frac{\sqrt{C_r}}{\sqrt{2}} & 0 \\ 0 & 0 & \frac{\sqrt{C_{eq}}}{\sqrt{2}} \end{bmatrix}. \quad (\text{C.32})$$

The new input matrix is calculated as

$$\overline{\mathbf{B}}_I = \frac{1}{\omega} \mathbf{P} \mathbf{B}_I, \quad (\text{C.33})$$

which gives

$$\overline{\mathbf{B}}_I = \left[ \frac{1}{\sqrt{2L_r\omega}} \quad 0 \quad 0 \right]^T. \quad (\text{C.34})$$

The correction factor  $\Gamma$  is:

$$\Gamma = \frac{\sqrt{2L_r\omega}}{V_{in}}. \quad (\text{C.35})$$

The new state-space model is equated by means of (3.70), (3.71), (3.72) and (3.73), which leads to

$$\overline{\mathbf{A}}_I = \begin{bmatrix} 0 & -\frac{1}{\sqrt{L_r C_r \omega}} & 0 \\ \frac{1}{\sqrt{L_r C_r \omega}} & 0 & 0 \\ 0 & 0 & -\frac{1}{C_2 R_L \omega} \end{bmatrix}, \quad (\text{C.36})$$

$$\overline{\mathbf{B}}_I = \left[ \frac{1}{V_{in}} \quad 0 \quad 0 \right]^T, \quad (\text{C.37})$$

$$\overline{\mathbf{A}}_{II} = \begin{bmatrix} 0 & -\frac{1}{\sqrt{L_r C_r \omega}} & -\frac{\alpha}{\sqrt{L_r C_{eq}}} \\ \frac{1}{\sqrt{L_r C_r}} & 0 & 0 \\ \frac{\alpha}{L_r C_{eq}} & 0 & -\frac{1}{C_{eq} R_L \omega} \end{bmatrix}, \quad (\text{C.38})$$

$$\overline{\mathbf{B}}_{II} = \left[ \frac{1}{V_{in}} \quad 0 \quad 0 \right]^T, \quad (\text{C.39})$$

$$\overline{\mathbf{A}}_{III} = \begin{bmatrix} 0 & -\frac{1}{\sqrt{L_r C_r \omega}} & -\frac{\alpha}{\sqrt{L_r C_{eq} \omega}} \\ \frac{1}{\sqrt{L_r C_r \omega}} & 0 & 0 \\ \frac{\alpha}{L_r C_{eq}} & 0 & -\frac{1}{C_{eq} R_L \omega} \end{bmatrix}, \quad (\text{C.40})$$

$$\overline{\mathbf{B}}_{III} = \left[ 0 \quad 0 \quad 0 \right]^T, \quad (\text{C.41})$$

$$\overline{\mathbf{A}}_{IV} = \begin{bmatrix} 0 & -\frac{1}{\sqrt{L_r C_r \omega}} & 0 \\ \frac{1}{\sqrt{L_r C_r}} & 0 & 0 \\ 0 & 0 & -\frac{1}{C_{eq} R_L \omega} \end{bmatrix}, \quad (\text{C.42})$$

$$\overline{\mathbf{B}}_{IV} = \left[ 0 \quad 0 \quad 0 \right]^T, \quad (\text{C.43})$$

$$\overline{\mathbf{C}}_I = \begin{bmatrix} \frac{V_{in}}{I_{in}L_r\omega} & 0 & 0 & 0 & 0 & \frac{V_{in}}{I_{in}L_r\omega} & 0 & 0 & \frac{V_{in}}{I_{in}L_r\omega} & 0 & 0 & \frac{V_{in}}{I_{in}L_r\omega} \\ 0 & \frac{1}{\sqrt{L_rC_r}\omega} & 0 & 0 & 0 & 0 & 0 & 0 & 0 & 0 & 0 & 0 \\ 0 & 0 & \frac{1}{\sqrt{L_rC_{eq}}\omega} & 0 & 0 & 0 & 0 & 0 & 0 & \frac{1}{\sqrt{L_rC_{eq}}} & 0 & 0 \end{bmatrix}^T, \quad (\text{C.44})$$

$$\overline{\mathbf{C}}_{II} = \begin{bmatrix} \frac{V_{in}}{I_{in}L_r\omega} & 0 & 0 & 0 & 0 & \frac{V_{in}}{I_{in}L_r\omega} & 0 & \frac{V_{in}}{I_{in}L_r\omega} & 0 & 0 & 0 & \frac{V_{in}}{I_{in}L_r\omega} \\ 0 & \frac{1}{\sqrt{L_rC_r}} & 0 & 0 & 0 & 0 & 0 & 0 & 0 & 0 & 0 & 0 \\ 0 & 0 & \frac{1}{\sqrt{L_rC_{eq}}} & 0 & 0 & 0 & 0 & 0 & 0 & 0 & -\frac{1}{\sqrt{L_rC_{eq}}} & 0 \end{bmatrix}^T, \quad (\text{C.45})$$

$$\overline{\mathbf{C}}_{III} = \begin{bmatrix} \frac{V_{in}}{I_{in}L_r\omega} & 0 & 0 & 0 & 0 & 0 & -\frac{V_{in}}{I_{in}L_r\omega} & \frac{V_{in}}{I_{in}L_r\omega} & 0 & 0 & 0 & \frac{V_{in}}{I_{in}L_r\omega} \\ 0 & \frac{1}{L_rC_r} & 0 & 0 & 0 & 0 & 0 & 0 & 0 & 0 & 0 & 0 \\ 0 & 0 & \frac{1}{L_rC_{eq}} & 0 & 0 & 0 & 0 & 0 & 0 & 0 & -\frac{1}{L_rC_{eq}} & 0 \end{bmatrix}^T, \quad (\text{C.46})$$

$$\overline{\mathbf{C}}_{IV} = \begin{bmatrix} \frac{V_{in}}{I_{in}L_r\omega} & 0 & 0 & 0 & 0 & 0 & -\frac{V_{in}}{I_{in}L_r\omega} & 0 & -\frac{V_{in}}{I_{in}L_r\omega} & 0 & 0 & \frac{V_{in}}{I_{in}L_r\omega} \\ 0 & \frac{1}{L_rC_r} & 0 & 0 & 0 & 0 & 0 & 0 & 0 & 0 & 0 & 0 \\ 0 & 0 & \frac{1}{L_rC_{eq}} & 0 & 0 & 0 & 0 & 0 & 0 & -\frac{1}{L_rC_{eq}} & 0 & 0 \end{bmatrix}^T, \quad (\text{C.47})$$

$$\overline{\mathbf{D}}_I = \left[ 0 \ 0 \ 0 \ 0 \ 0 \ 0 \ 0 \ 0 \ 0 \ \frac{1}{V_{in}} \ 0 \ 0 \ 0 \right]^T, \quad (\text{C.48})$$

$$\overline{\mathbf{D}}_{II} = \left[ 0 \ 0 \ 0 \ 0 \ 0 \ 0 \ 0 \ 0 \ 0 \ \frac{1}{V_{in}} \ 0 \ 0 \ 0 \right]^T, \quad (\text{C.49})$$

$$\overline{\mathbf{D}}_{III} = \left[ 0 \ 0 \ 0 \ 0 \ 0 \ 0 \ 0 \ 0 \ 0 \ \frac{1}{V_{in}} \ 0 \ 0 \ 0 \ 0 \right]^T \quad (\text{C.50})$$

and

$$\overline{\mathbf{D}}_{IV} = \left[ 0 \ 0 \ 0 \ 0 \ 0 \ 0 \ 0 \ 0 \ 0 \ \frac{1}{V_{in}} \ 0 \ 0 \ 0 \ 0 \right]^T. \quad (\text{C.51})$$

In order to represent the system independently of real system parameters, the unitless parameters should be extracted. The normalized resonant frequencies  $A_1$  and  $A_2$  are equated as function of the reactive components as

$$A_1 = \frac{\omega_1}{\omega}, \quad (\text{C.52})$$

$$A_2 = \frac{\omega_2}{\omega}, \quad (\text{C.53})$$

$$\omega_1 = \frac{1}{\sqrt{L_r C_r}} \quad (\text{C.54})$$

and

$$\omega_2 = \frac{1}{\sqrt{L_r C_{eq}}}. \quad (\text{C.55})$$

The quality factor  $Q_L$  is equated by:

$$Q_L = \frac{R_L}{\omega_2 L_r} = \omega_2 C_{eq} R_L. \quad (\text{C.56})$$

The transfer power ratio  $T_{POT}$  and its inverse  $a$  are given as

$$T_{POT} = \frac{1}{a} = \frac{R_L I_{in}}{V_{in}}. \quad (\text{C.57})$$

Based on the aforementioned relationships, the system can be described as a normalized-state space model (4.56) and (4.57):

$$\overline{\mathbf{E}}_I = \begin{bmatrix} 0 & -A_1 & 0 \\ A_1 & 0 & 0 \\ 0 & 0 & -\frac{A_2}{Q_L} \end{bmatrix}, \quad (\text{C.58})$$

$$\overline{\mathbf{F}}_I = [1 \ 0 \ 0]^T, \quad (\text{C.59})$$

$$\overline{\mathbf{E}}_{II} = \begin{bmatrix} 0 & -A_1 & -\alpha A_2 \\ A_1 & 0 & 0 \\ \alpha A_2 & 0 & -\frac{A_2}{Q_L} \end{bmatrix}, \quad (\text{C.60})$$

$$\overline{\mathbf{F}}_{II} = [1 \ 0 \ 0]^T, \quad (\text{C.61})$$

$$\overline{\mathbf{E}}_{III} = \begin{bmatrix} 0 & -A_1 & -\alpha A_2 \\ A_1 & 0 & 0 \\ \alpha A_2 & 0 & -\frac{A_2}{Q_L} \end{bmatrix}, \quad (\text{C.62})$$

$$\overline{\mathbf{F}}_{III} = [0 \ 0 \ 0]^T, \quad (\text{C.63})$$

$$\overline{\mathbf{E}}_{IV} = \begin{bmatrix} 0 & -A_1 & 0 \\ A_1 & 0 & 0 \\ 0 & 0 & -\frac{A_2}{Q_L} \end{bmatrix}, \quad (\text{C.64})$$

$$\overline{\mathbf{F}}_{IV} = [0 \ 0 \ 0]^T, \quad (\text{C.65})$$

$$\overline{\mathbf{G}}_I = \begin{bmatrix} aQ_L A_2 & 0 & 0 & 0 & 0 & aQ_L A_2 & 0 & 0 & aQ_L A_2 & 0 & 0 & aQ_L A_2 \\ 0 & A_1 & 0 & 0 & 0 & 0 & 0 & 0 & 0 & 0 & 0 & 0 \\ 0 & 0 & A_2 & 0 & 0 & 0 & 0 & 0 & 0 & A_2 & 0 & 0 \end{bmatrix}^T, \quad (\text{C.66})$$

$$\overline{\mathbf{G}}_{II} = \begin{bmatrix} aQ_L A_2 & 0 & 0 & 0 & 0 & aQ_L A_2 & 0 & aQ_L A_2 & 0 & 0 & 0 & aQ_L A_2 \\ 0 & A_1 & 0 & 0 & 0 & 0 & 0 & 0 & 0 & 0 & 0 & 0 \\ 0 & 0 & A_2 & 0 & 0 & 0 & 0 & 0 & 0 & 0 & -A_2 & 0 \end{bmatrix}^T, \quad (\text{C.67})$$

$$\overline{\mathbf{G}}_{III} = \begin{bmatrix} aQ_L A_2 & 0 & 0 & 0 & 0 & 0 & -aQ_L A_2 & aQ_L A_2 & 0 & 0 & 0 & aQ_L A_2 \\ 0 & A_1 & 0 & 0 & 0 & 0 & 0 & 0 & 0 & 0 & 0 & 0 \\ 0 & 0 & A_2 & 0 & 0 & 0 & 0 & 0 & 0 & 0 & -A_2 & 0 \end{bmatrix}^T, \quad (\text{C.68})$$

$$\overline{\mathbf{G}}_{IV} = \begin{bmatrix} aQ_L A_2 & 0 & 0 & 0 & 0 & 0 & -aQ_L A_2 & 0 & -aQ_L A_2 & 0 & 0 & aQ_L A_2 \\ 0 & A_1 & 0 & 0 & 0 & 0 & 0 & 0 & 0 & 0 & 0 & 0 \\ 0 & 0 & A_2 & 0 & 0 & 0 & 0 & 0 & 0 & -A_2 & 0 & 0 \end{bmatrix}^T, \quad (\text{C.69})$$

$$\overline{\mathbf{D}}_I = [0 \ 0 \ 0 \ 0 \ 0 \ 0 \ 0 \ 0 \ 0 \ 1 \ 0 \ 0 \ 0]^T, \quad (\text{C.70})$$

$$\overline{\mathbf{D}}_{II} = [0 \ 0 \ 0 \ 0 \ 0 \ 0 \ 0 \ 0 \ 0 \ 1 \ 0 \ 0 \ 0]^T, \quad (\text{C.71})$$

$$\overline{\mathbf{D}}_{III} = [0 \ 0 \ 0 \ 0 \ 0 \ 0 \ 0 \ 0 \ 1 \ 0 \ 0 \ 0 \ 0]^T \quad (\text{C.72})$$

and

$$\overline{\mathbf{D}}_{IV} = [0 \ 0 \ 0 \ 0 \ 0 \ 0 \ 0 \ 0 \ 1 \ 0 \ 0 \ 0 \ 0]^T. \quad (\text{C.73})$$

The same procedure used to solve the Class-E<sup>2</sup> converter is applied for the Class-D<sup>2</sup>. However, the linear system is composed by different relations. The following steady-state conditions are considered:

- $i_{L_r}(2\pi) = i_{L_r}(0)$  (steady-state condition);
- $v_{C_r}(2\pi) = v_{C_r}(0)$  (steady-state condition);
- $v_{C_{eq}}(2\pi) = v_{C_{eq}}(0)$  (steady-state condition);
- $\alpha i_{L_r}(T_1) = 0$  (steady-state condition);
- $\alpha i_{L_r}(T_2) = 0$  (steady-state condition).

The linear system is equated as:

$$\begin{pmatrix} i_{L_r}(2\pi)_{[A_1, A_2, Q_L, i_{L_r}(0), v_{C_r}(0), v_{C_{eq}}(0), D_c, T_1, T_2]} \\ v_{C_r}(2\pi)_{[A_1, A_2, Q_L, i_{L_r}(0), v_{C_r}(0), v_{C_{eq}}(0), D_c, T_1, T_2]} \\ v_{C_{eq}}(2\pi)_{[A_1, A_2, Q_L, i_{L_r}(0), v_{C_r}(0), v_{C_{eq}}(0), D_c, T_1, T_2]} \\ \alpha i_{L_r}(T_1)_{[A_1, A_2, Q_L, i_{L_r}(0), v_{C_r}(0), v_{C_{eq}}(0), D_c, T_1, T_2]} \\ \alpha i_{L_r}(T_2)_{[A_1, A_2, Q_L, i_{L_r}(0), v_{C_r}(0), v_{C_{eq}}(0), D_c, T_1, T_2]} \end{pmatrix} = \begin{pmatrix} i_{L_r}(0) \\ v_{C_r}(0) \\ v_{C_{eq}}(0) \\ 0 \\ 0 \end{pmatrix} \quad (\text{C.74})$$

The system has 5 equations and 9 variables. By performing a parameter sweep on  $D_c$  and defining  $A_1$ ,  $A_2$  and  $Q_L$ , it is possible to find initial conditions  $i_{L_r}(0)$ ,  $v_{C_r}(0)$  and  $v_{C_{eq}}(0)$ . Also,  $T_1$  and  $T_2$  can be found.

The inverse transfer power ratio  $a$  appears only in the transmission matrices. For this reason, it is not included in the linear system. However, to solve the output equations, it is necessary a numerical value for  $a$ , which can be calculated by

$$\frac{1}{a} = T_{POT} = \frac{1}{2\pi} \int_0^{2\pi} v_{C_{eq}}(\omega t) d\omega t, \quad (\text{C.75})$$

in which,  $v_{C_{eq}}$  is used as output voltage.

Based on the presented approach, the normalized waveforms for the Class-D<sup>2</sup> resonant DC-DC converter are shown in Figures C.9 and C.10, considering  $D_c = 0.25$  and  $D_c = 0.5$ , respectively. It was considered  $A_1 = 1.1$ ,  $A_2 = 0.2$  and  $Q_L = 3.5$ .

The phase diagrams for different values of  $D_c$  are depicted in Figure C.11. For all phase diagrams,  $i_{L_r}/I_{in}$  and  $v_{C_r}/I_{in}$  were considered as variables.

The normalized and component stress curves are shown in Figure C.12. The curves in Figures C.12(a)-(g) are evaluated as function of duty cycle  $D_c$  and in Figures C.12(h),(i) as function of quality factor  $Q_L$ . In addition, the curves are represented for different values of  $\alpha$ . It can be seen in Figure C.12(a) that  $T_{POT}$  is higher for values close to  $D_c = 0.5$  for any value of  $\alpha$ . However, for  $D_c = 0.5$ , the diodes  $D_1$  and  $D_2$  peak voltages are greater than other values for  $D_c$ . In Figure C.12(h) and Figure C.12(i), it can be seen that the greater the quality factor  $Q_L$ , greater  $T_{POT}$  and  $V_{or_{ms}}/V_{in}$ .

Figure C.9 – Normalized waveforms for the Class-D<sup>2</sup> resonant DC-DC converter for  $D_c = 0.25$ . (a)-(f) Circuit variables.

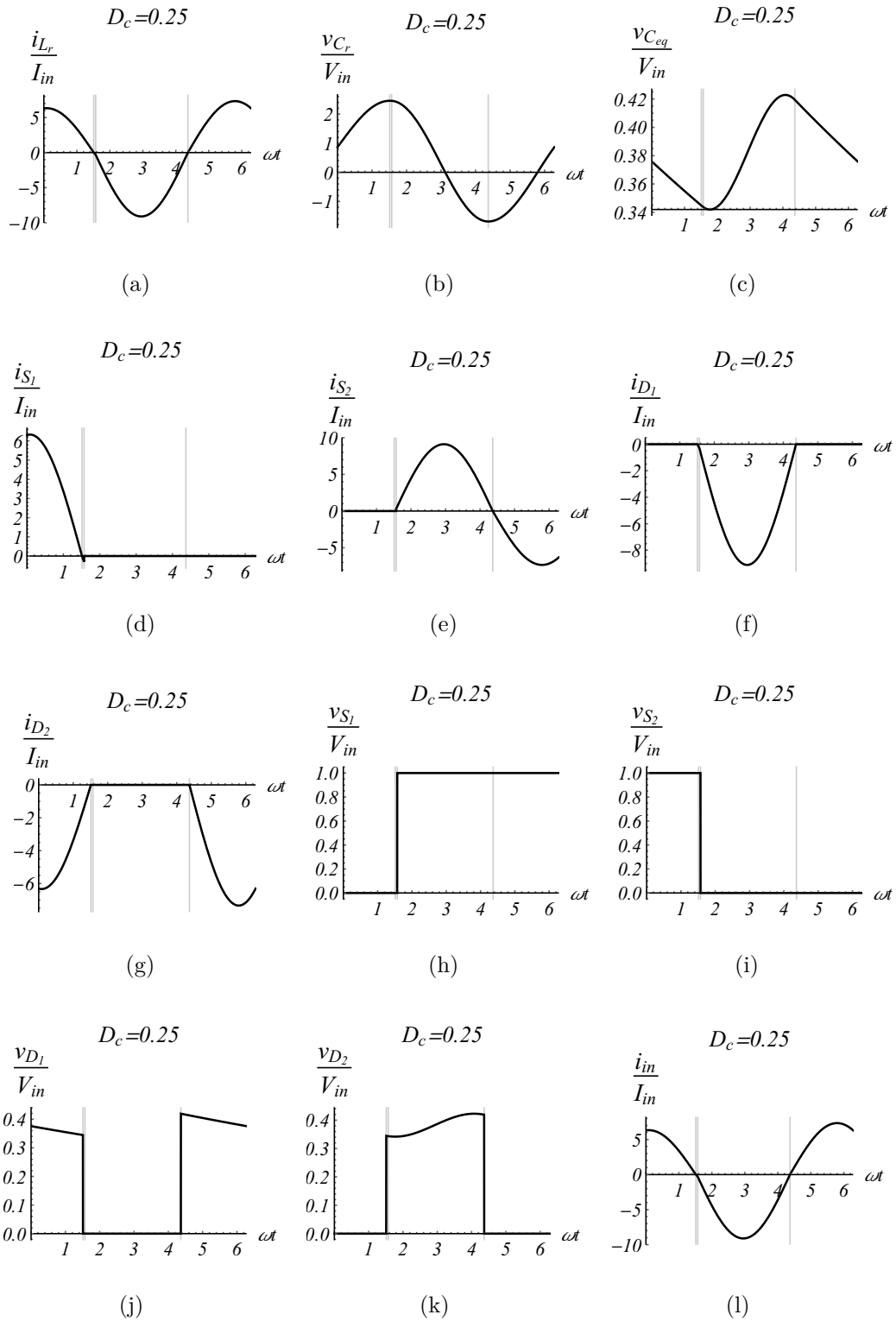


Figure C.10 – Normalized waveforms for the Class- $D^2$  resonant DC-DC converter for  $D_c = 0.5$ . (a)-(f) Circuit variables.

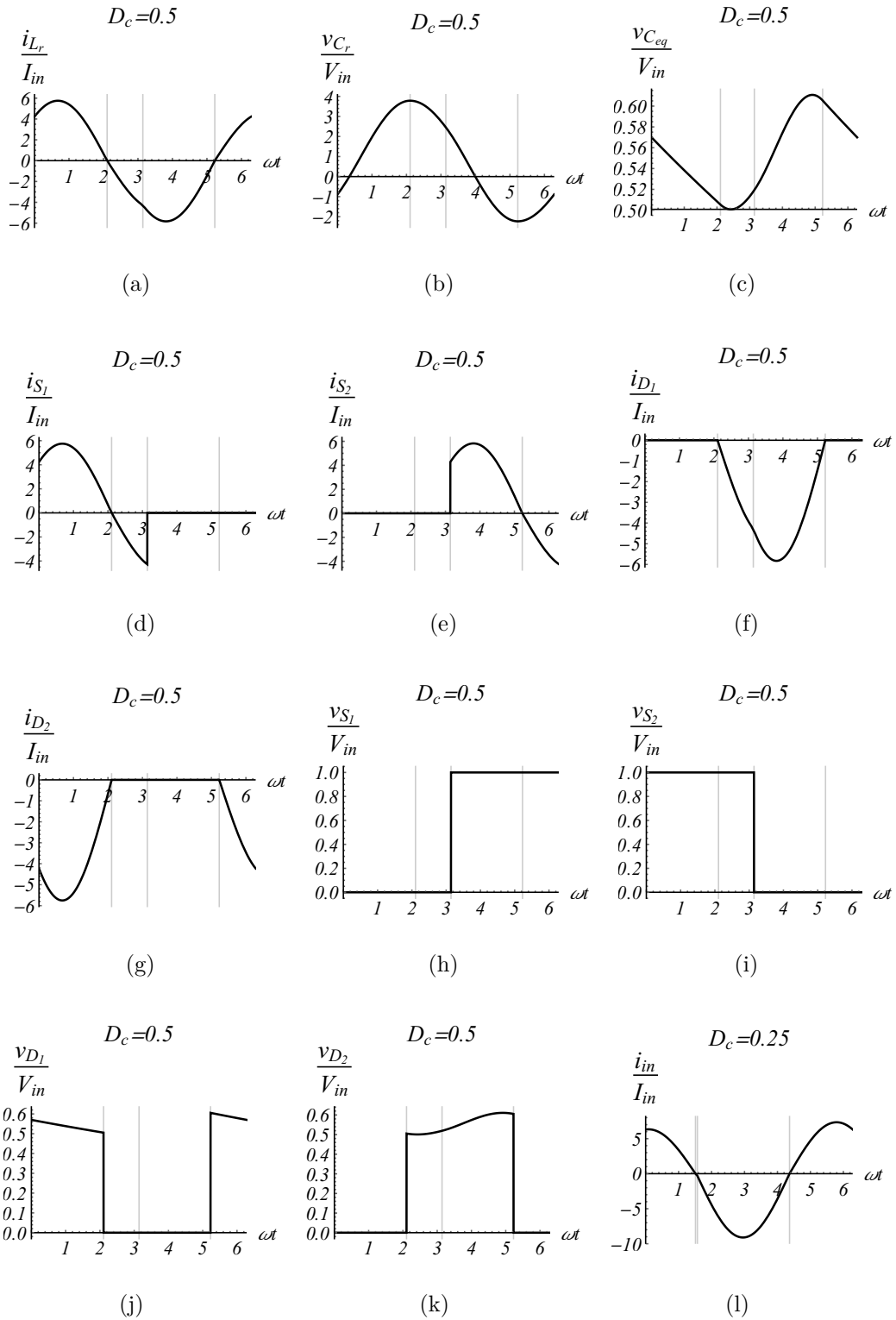




Figure C.11 – Phase diagrams for the Class- $D^2$  resonant DC-DC converter. (a)  $D_c = 0.3$ . (b)  $D_c = 0.35$ . (c)  $D_c = 0.4$ . (d)  $D_c = 0.45$ . (e)  $D_c = 0.5$ . (f)  $D_c = 0.55$ . (g)  $D_c = 0.6$ . (h)  $D_c = 0.65$ . (i)  $D_c = 0.7$ .

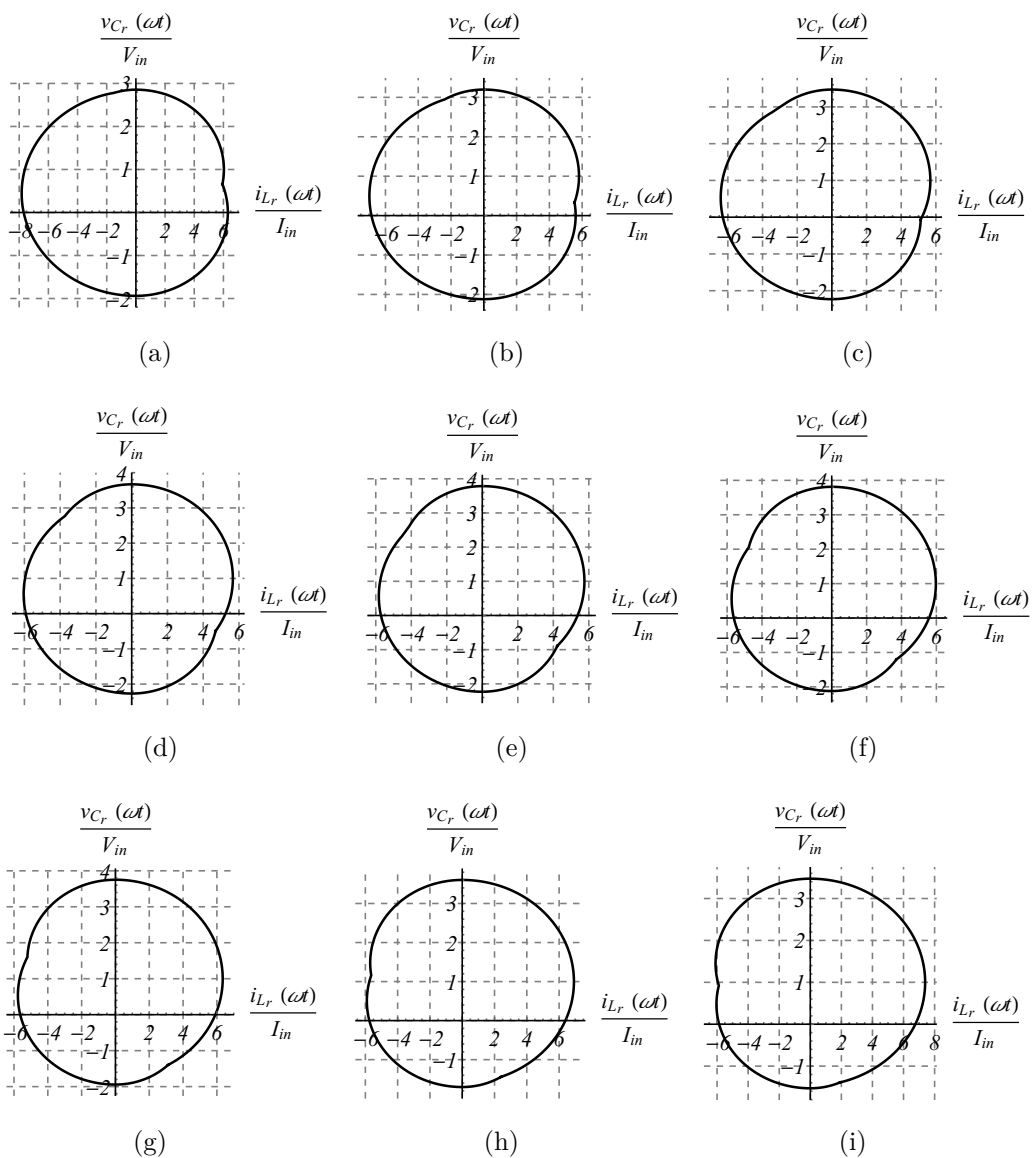
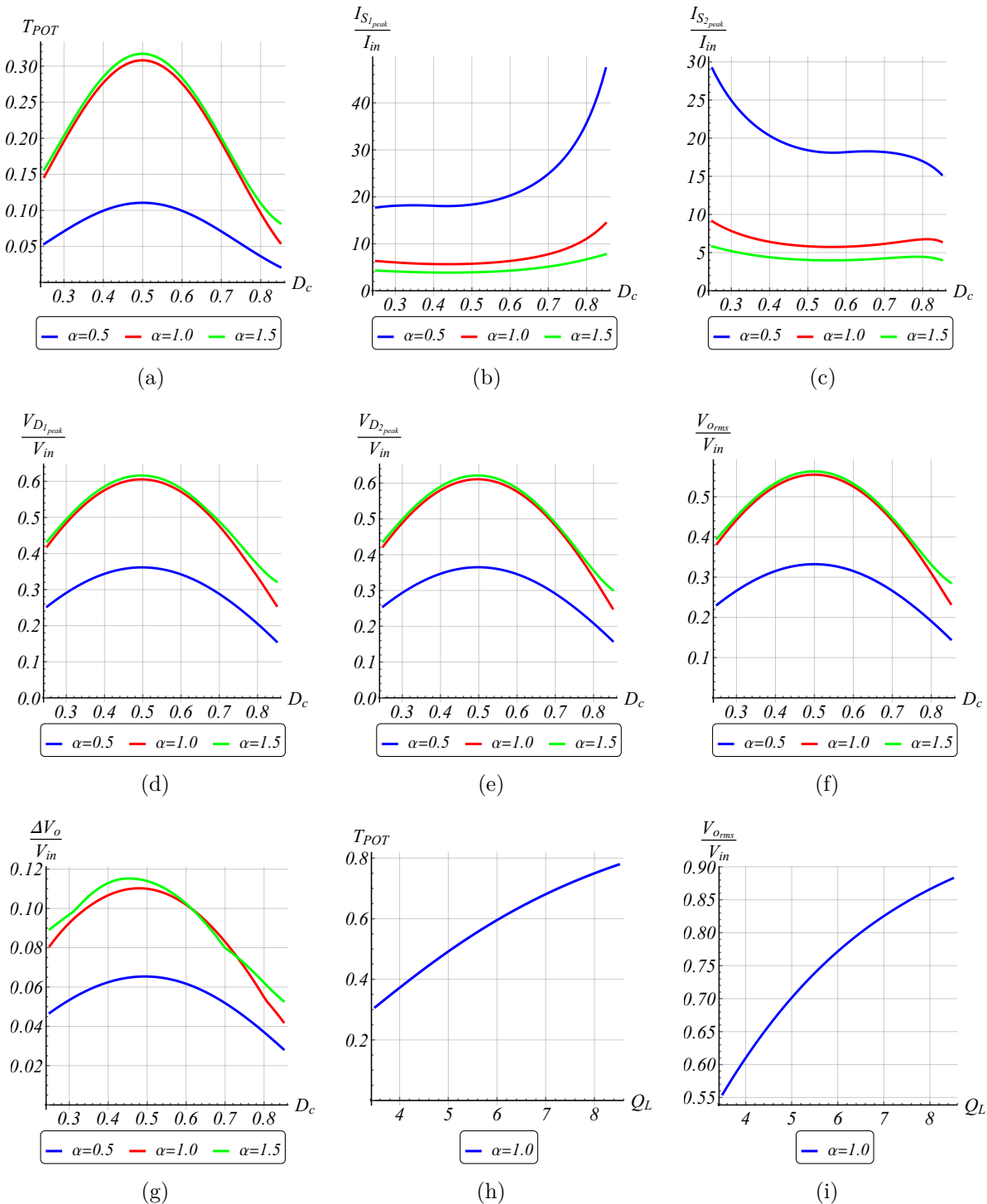


Figure C.12 – Normalized gain and component stress curves for the Class- $D^2$  converter: (a) Transfer power ratio  $T_{POT}$  as function of  $D_c$ . (b) Switch  $S_1$  peak current  $I_{S_{1peak}}/I_{in}$  as function of  $D_c$ . (c) Switch  $S_2$  peak current  $I_{S_{2peak}}/I_{in}$  as function of  $D_c$ . (d) Diode  $D_1$  peak voltage  $V_{D_{1peak}}/V_{in}$  as function of  $D_c$ . (e) Diode  $D_2$  peak voltage  $V_{D_{2peak}}/I_{in}$  as function of  $D_c$ . (f) Output voltage - rms  $V_{orms}/V_{in}$  as function of  $D_c$ . (g) Ripple in the output voltage  $\Delta V_o/V_{in}$  as function of  $D_c$ . (h) Transfer power ratio  $T_{POT}$  as function of  $Q_L$ . (i) Output voltage - rms  $V_{orms}/V_{in}$  as function of  $Q_L$ .



## Appendix D – Evolutionary Genetic Algorithm for Design of Cockcroft-Walton Circuits

### D.1 EVOLUTIONARY GENETIC ALGORITHM FOR DESIGN OF COCKCROFT-WALTON CIRCUITS

Genetic algorithm is a method for solving problems based on the biological evolution process. The main events of this method are the natural selection, crossover and mutation (MELANIE, 1999).

Although the method can be applied in several research areas, for each application it is necessary to adequate the method by considering the specifications, restrictions, complexity and required accuracy. In this work, the developed algorithm is applied for the topology shown in Figure 4.18. The algorithm can be considered as novelty in the literature regarding the design of the converter.

In order to design the Cockcroft-Walton AC-DC multiplier, an evolutionary genetic algorithm is proposed.

The algorithm main inputs are:

- Input voltage source peak value,  $V_{in}$ ;
- Input source frequency,  $f$ ;
- Output power,  $P_o$ ;
- Reference output voltage,  $V_o$ ;
- Diodes voltage drop,  $V_D$ ;
- Maximum allowed output voltage ripple,  $\delta V_{o_{max}}$ ;
- Maximum total capacitance,  $C_{TOT_{max}}$ ;
- Maximum number of stages,  $n_{max}$ .

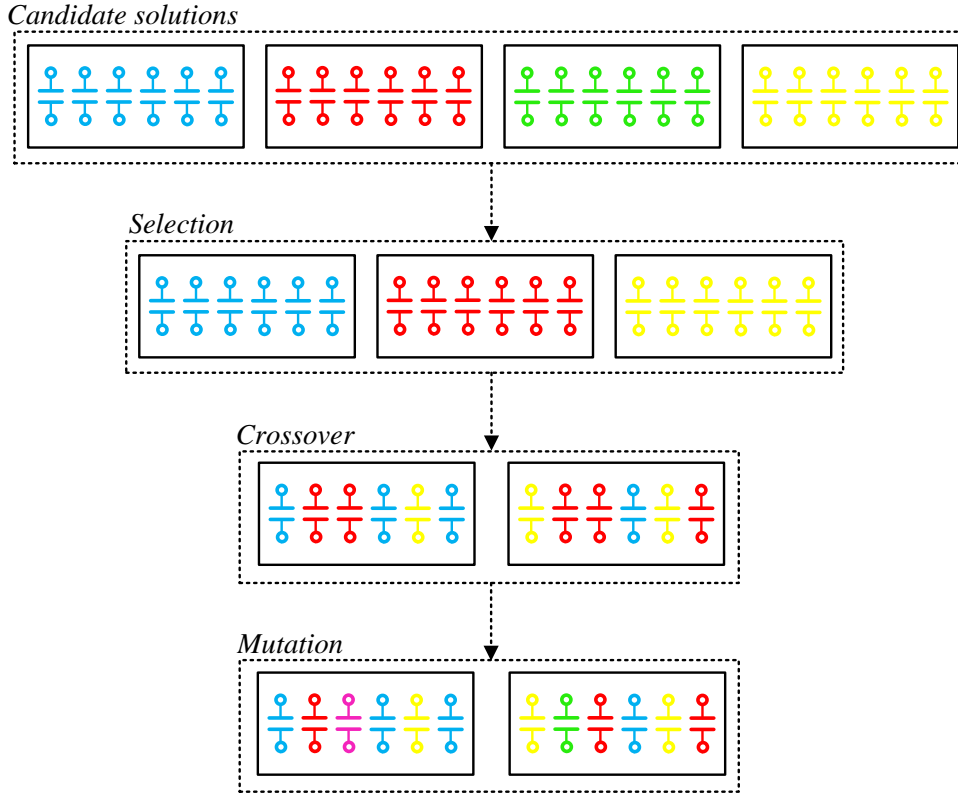
The idea is to generate several sets with random values for the capacitors. Each set is called *candidate solution* or *family* with genotype represented by the capacitors values. The analytical equations (4.94), (4.95) and (4.96) are evaluated for each candidate solution.

The main events of the genetic algorithm are represented in Figure D.1. It is shown four candidate solutions just for exemplification. In genetic algorithms, hundred or thousands of candidate solutions are used.

A fitness function should be evaluated in order to verify whether or not each candidate solution meets specifications. *Scores* or *weights* are given to the candidate solutions.

Subsequently, the *selection* process is developed. In this stage, a random choice based on the candidate solutions is performed. However, the weights given beforehand

Figure D.1 – Main events of the genetic algorithm.



Source: Author.

increase/decrease the chance that a candidate solution will be chosen.

The *crossover* mix the genotypes (capacitor values) to create new candidate solutions. Then, the process is repeated by a specific number of main iterations. Furthermore, the process is also repeated regarding the number of stages. In this case, starting from the minimum number (1) until a specific maximum allowed number of stages for the desirable application. By increasing the number of main iterations, candidate solutions and selection factor, there will be a wider range for finding a suitable solution. On the other hand, the computational effort is higher. Also, the narrower the specifications, the greater the need to increase the number of candidate solutions. These characteristics must be taken into account when setting the basis for the algorithm.

The basis for the algorithm are defined by: iterators are described by  $z$ ,  $m$ ,  $k$  and  $j$ ,  $n_C$  is the number of capacitors,  $ni$  is the number of main iterations,  $nf$  is the number of families for the first generation,  $\Xi$  is the selection factor,  $G_k$  is the genotype,  $w_1, \dots, w_{nf}$  represent the weights given by the fitness function,  $T_m$  is the set generated by the fitness function,  $T2_m$  is a set of capacitor values generated by a random choice based on  $T_m$  and  $T_{cv_m}$  is a set of capacitor values generated by a random sample based on  $T2_m$ .

The genetic algorithm was implemented in the mathematical software *Wolfram Mathematica 10*. The high-level of abstraction code is shown in Table D.1.

Table D.1 – Evolutionary genetic algorithm to design Cockcroft-Walton AC-DC multipliers.

Code
1. <b>Define</b> inputs: $V_{in}, f, P_o, V_o, V_D, \delta V_{o_{max}}, C_{TOT_{max}}, n_{max}$ ;
2. <b>Calculate</b> output load current: $I_o = \frac{P_o}{V_o}$ ;
3. <b>Calculate</b> AC-to-DC transfer function: $S = \frac{I_o}{V_{in}}$ ;
4. <b>For</b> $z = 1, z \leq n_{max}$ ;
5. $n = z$ ;
6. <b>Calculate</b> number of capacitors $n_C = 2n$ ;
7. <b>For</b> $m = 1, z \leq n_i$ ;
8. <b>For</b> $k = 1, k \leq n_f$ ;
9. <b>For</b> $j = 1, j \leq n_C$ ;
10. <b>Do</b> $t_j = [RandomReal_1, \dots, RandomReal_{n_C}]$ ;
11. <b>Do</b> Genotype, $G_k = RandomChoice[t_j]$ ;
12. $j++$ ;
13. $k++$ ;
14. <b>Do</b> $C_{k,j} = G_k[j, 1], k = \{1, n_f\}, j = \{1, n_C\}$ ;
15. <b>For</b> $k = n_f + Length[T_{cv_{m-2}}], k \leq n_f + Length[T_{cv_{m-1}}]$ ;
16. <b>Calculate</b> $\Delta V_{o_k} = \frac{S}{f} \left( \sum_{i=1}^n \frac{(n+1+i)^2}{C_{k,2i-1}} + \sum_{i=1}^{n-1} \frac{(n+1-i)(n-i)}{C_{k,2i}} \right) V_{in}$ ;
17. <b>Calculate</b> $\delta V_{o_k} = \frac{S}{f} \left( \sum_{i=1}^n \frac{(n+1-i)}{C_{k,2i}} \right) V_{in}$ ;
18. <b>Calculate</b> $V_{o_k} = \left( 2n - \frac{1}{V_{in}} \left( \Delta V_{o_k} + \frac{1}{2} \delta V_{o_k} \right) \right) V_{in} - 2nV_D$ ;
19. <b>Calculate</b> $C_{TOT_k} = \sum_{ci=1}^{n_C} C_{k,ci}$ ;
20. $k++$ ;
21. <b>Evaluate</b> Fitness function $f(\delta V_o, \Delta V_o, V_o, C_{TOT_{max}})$ ;
22. <b>Do</b> $T_m = [w_1 G_1, \dots, w_{n_f} G_n] f(\delta V_o, \Delta V_o, V_o, C_{TOT_{max}})$ ;
23. <b>For</b> $j = 1, j \leq \Xi$ ;
24. <b>Do</b> Selection, $T2_m = RandomChoice[T_m]$ ;
25. $\Xi++$ ;
26. <b>Do</b> Crossover, $T_{cv_m} = RandomSample[T2_m]$ ;
27. <b>Do</b> $G_{n_f+1} = T_{cv_m}[i], i = \{1, Length[T_{cv_m}]\}$ ;
28. <b>Go To</b> Line 14;
29. $m++$ ;
30. $z++$ ;

Source: Author.



## Appendix E – Discussion about the Practical Implementation of the Driving Circuits

### E.1 DISCUSSION ABOUT THE PRACTICAL IMPLEMENTATION OF THE DRIVING CIRCUITS

The use of resonant circuits as topological representation of piezoelectric transformers and contactless energy transfer system was also explored by Bisogno (2006), Alonso, Ordiz & Costa (2008), Engleitner (2011) and Nagashima et al. (2015). It is important to note that, there are some aspects that should be considered when implementing the driving circuits derived from the resonant topologies.

In inductive wireless power transfer systems, the analysis of the system based on resonant topologies is performed very similar to the one shown in this work for the Class-E<sup>2</sup> resonant DC-DC converter. For instance, the topology used in Nagashima et al. (2015) is the same shown in Fig. 4.2(a). However, in order to address the IPT system features, the transformation ratio is related to the distance between transmitter and receiver. In addition, the load quality factor in the inverter is high enough to generate a pure sinusoidal resonant current, which allows the analysis and design by separating the inverter and rectifier stages.

Even though the analysis of IPT systems is performed by setting several assumptions to achieve a simplified topology, it is well documented the need of including matching networks in the practical implementation (ZHAKSYLYK et al., 2020), (MUHARAM et al., 2020), (MIAO; LIU; GONG, 2017).

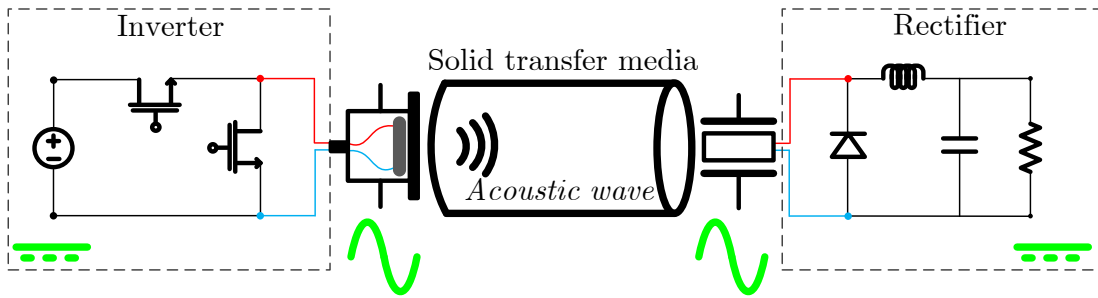
The same idea is applied for acoustic CET systems, piezoelectric energy harvesters and ultrasonic transducers. In other words, the mathematical analysis is usually performed by casting assumptions. However, in some cases, the practical implementation requires adjustments related to matching networks and circuits to drive the system.

One way to drive ultrasonic transducers based on piezoelectricity and piezoelectric transformers is to use an inverter, like as Half-bridge, Full-bridge, Class-D and Class-E topologies. The inverter is connected to the transmitter device and the mechanical parts of the piezoelectric components are tasked with the waveform shaping. This concept is depicted in Fig. E.1.

Another way is to build up the resonant tank by means of external electrical components. This concept requires extra components to be added. However, it is easier to ensure the correct operation of the driving circuits. For instance, inductors and capacitors can be used as resonant tank for the inverter in order to ensure that a sinusoidal wave is generated to supply the transmitter. In the same way, a matching circuit can be used to enhance the rectifier operation. This concept is shown in Fig. E.2.

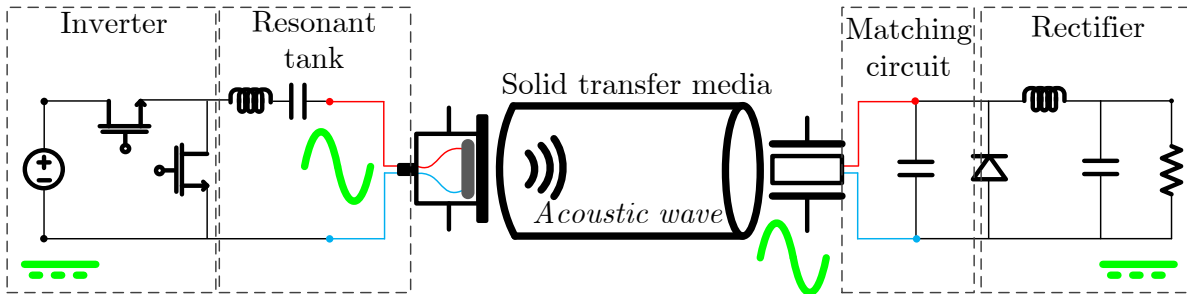
The third concept to be discussed is the use of a power amplifier with a wave-

Figure E.1 – Driving circuits considering the piezoelectric components as resonant tank.



Source: Author.

Figure E.2 – Driving circuits based on external electrical components.

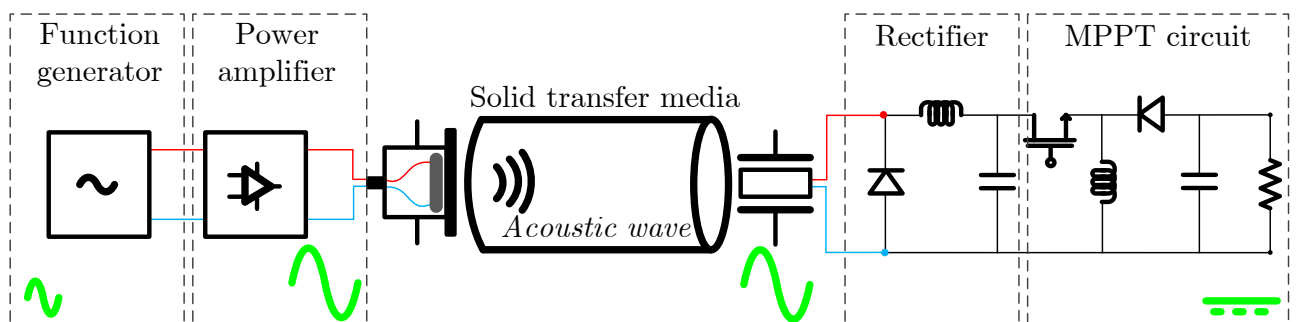


Source: Author.

form generator to supply the transmitter and a maximum power point tracking (MPPT) circuit cascaded with the rectifier. This idea ensures the proper driving circuit for the transmitter and it is useful for testing because it allows to use different frequencies and input source amplitudes. However, it requires equipments that are not suitable when considering a final product assembling. In addition, the MPPT circuit is mandatory when considering a practical application, such as battery charging. It is necessary that the AC-DC converter regulates its input voltage to gets the maximum power from the input. In the later Chapters, this concept is going to be used in the practical implementation of the power conversion circuitry for the electro-mechanical-acoustic CET system. The concept is shown in Fig. E.3.



Figure E.3 – Driving circuits based on function generator, power amplifier and MPPT circuit.



Source: Author.



## Appendix F – Automatic AC Model Construction Algorithm

### F.1 AUTOMATIC AC MODEL CONSTRUCTION ALGORITHM

Table F.1 – Automatic AC Model Construction Algorithm

	Code
1.	<b>Define</b> inputs: $k_{max}, n_o, i_c$ ;
2.	$nv = n_o + 2k_{max}n_o$ % number of state variables;
3.	<b>Define</b> symbolic switching function coefficient: $\langle s_1 \rangle_k = \frac{1}{2\pi} \left( \int_{D_c 2\pi} e^{-jk\tau} d\tau \right)$ ;
4.	<b>Define</b> symbolic switching function coefficient: $\langle s_2 \rangle_k = \frac{1}{2\pi} \left( \int_0^{T_1} e^{-jk\tau} d\tau + \int_{T_2}^{2\pi} e^{-jk\tau} d\tau \right)$ ;
5.	<b>For</b> ( $a = 1, b = 1$ ); $a \leq k_{max}$ ;
6.	<b>Do</b> Equations (5.50)-(5.70) % variables name definitions;
7.	$k++$ ;
8.	<b>For</b> $k = 0, k \leq k_{max}$ ;
9.	$\frac{d\langle i_{L_c} \rangle_k}{dt} = \frac{V_{in}}{L_c} - \sum_{i=-i_c}^{i_c} \frac{\langle s_1 \rangle_i \langle v_{C_1} \rangle_{k-i}}{L_c} - jk\omega_s \langle i_{L_c} \rangle_k$ ;
10.	$\frac{d\langle v_{C_1} \rangle_k}{dt} = \sum_{i=-i_c}^{i_c} \frac{\langle s_1 \rangle_i \langle i_{L_c} \rangle_{k-i}}{C_1} - \sum_{i=-i_c}^{i_c} \frac{\langle s_1 \rangle_i \langle i_{L_r} \rangle_{k-i}}{C_1} - jk\omega_s \langle v_{C_1} \rangle_k$ ;
11.	$\frac{d\langle i_{L_r} \rangle_k}{dt} = \sum_{i=-i_c}^{i_c} \frac{\langle s_1 \rangle_i \langle v_{C_1} \rangle_{k-i}}{L_r} - \frac{\langle v_{C_r} \rangle_k}{L_r} - \alpha \sum_{i=-i_c}^{i_c} \frac{\langle s_2 \rangle_i \langle v_{C_2} \rangle_{k-i}}{L_r} - jk\omega_s \langle i_{L_r} \rangle_k$ ;
12.	$\frac{d\langle v_{C_r} \rangle_k}{dt} = \frac{\langle i_{L_r} \rangle_k}{C_r} - jk\omega_s \langle v_{C_r} \rangle_k$ ;
13.	$\frac{d\langle v_{C_2} \rangle_k}{dt} = \alpha \sum_{i=-i_c}^{i_c} \frac{\langle s_2 \rangle_i \langle i_{L_r} \rangle_{k-i}}{C_2} - \sum_{i=-i_c}^{i_c} \frac{\langle s_2 \rangle_i \langle i_{L_f} \rangle_{k-i}}{C_2} - jk\omega_s \langle v_{C_2} \rangle_k$ ;
14.	$\frac{d\langle i_{L_f} \rangle_k}{dt} = \sum_{i=-i_c}^{i_c} \frac{\langle s_2 \rangle_i \langle v_{C_2} \rangle_{k-i}}{L_f} - \frac{\langle v_{C_f} \rangle_k}{L_f} - jk\omega_s \langle i_{L_f} \rangle_k$ ;
15.	$\frac{d\langle v_{C_f} \rangle_k}{dt} = \frac{\langle i_{L_f} \rangle_k}{C_f} - \frac{\langle v_{C_f} \rangle_k}{R_L C_f} - jk\omega_s \langle v_{C_f} \rangle_k$ ;
16.	$y_{vector} = [\mathbf{y}_1 \dots \mathbf{y}_{nv}]$ ;
17.	% it is necessary to isolate (collect) $y_{vector}$ in all differential equations;
18.	<b>Collect</b> $y_{vector}$ : $\frac{d\langle i_{L_c} \rangle_k}{dt}, \frac{d\langle v_{C_1} \rangle_k}{dt}, \frac{d\langle i_{L_r} \rangle_k}{dt}, \frac{d\langle v_{C_r} \rangle_k}{dt}, \frac{d\langle v_{C_2} \rangle_k}{dt}, \frac{d\langle i_{L_f} \rangle_k}{dt}, \frac{d\langle v_{C_f} \rangle_k}{dt}$ ;
19.	% next, real and imaginary parts should be separated;
20.	<b>Complex expand</b> : $\frac{d\langle i_{L_c} \rangle_k}{dt}, \frac{d\langle v_{C_1} \rangle_k}{dt}, \frac{d\langle i_{L_r} \rangle_k}{dt}, \frac{d\langle v_{C_r} \rangle_k}{dt}, \frac{d\langle v_{C_2} \rangle_k}{dt}, \frac{d\langle i_{L_f} \rangle_k}{dt}, \frac{d\langle v_{C_f} \rangle_k}{dt}$ ;
21.	$k++$ ;
22.	<b>Coefficient arrays</b> : $y_{vector}$ % creates array based on the terms that multiply $y_{vector}$ ;
23.	$\mathbf{A}_L = \mathbf{Array}[y_{vector}]$ ; % dynamic matrix based on terms that multiply $y_{vector}$ ;
24.	$\mathbf{B}_L = \mathbf{Array}[V_{in}]$ ; % input matrix based on terms that multiply $V_{in}$ ;

Source: Author.



## Appendix G – Large-Signal Model of the Class-E<sup>2</sup> Resonant Converter

### G.1 LARGE-SIGNAL MODEL OF THE CLASS-E<sup>2</sup> RESONANT CONVERTER

This Appendix details the terms of the state-space matrices for the large-signal model of the Class-E<sup>2</sup> resonant converter. Due to the size of the dynamic matrix  $\mathbf{A}_L$ , its terms are presented in a table format.

The terms are written as  $a_{i,j}$ , being  $i$  the matrix line and  $j$  the matrix column. Furthermore, the numbers of considered harmonics for each state variable are:

- Choke inductor  $L_c$  current,  $i_{L_c}$ :  $k = [0, 1, 2, 3, 4, 5]$ ;
- Capacitor  $C_1$  voltage,  $v_{C_1}$ :  $k = [0, 1, 2, 3, 4, 5]$ ;
- Resonant inductor  $L_r$  current,  $i_{L_r}$ :  $k = [0, 1]$ ;
- Resonant capacitor  $C_r$  voltage,  $v_{C_r}$ :  $k = [0, 1]$ ;
- Capacitor  $C_2$  voltage,  $v_{C_2}$ :  $k = [0, 1, 2, 3, 4, 5]$ ;
- Output filter inductor  $L_f$  current,  $i_{L_f}$ :  $k = [0, 1]$ ;
- Output filter capacitor  $C_f$  voltage,  $v_{C_f}$ :  $k = [0, 1]$ ;

The aforementioned number of considered harmonics are used only for the following table format representation of the matrices terms. In the results shown in Chapter 5, it was considered  $k = [0, 1, 2, 3, 4, 5]$  for all the state variables.

In this Appendix, some harmonics are not detailed into the terms of the matrices because they do not have huge impact in the dynamic model. For instance, resonant current  $i_{L_r}$  and resonant voltage  $v_{C_r}$  have predominant behavior related to harmonic  $k = 1$ . Furthermore, output filter variables  $i_{L_f}$  and  $v_{C_f}$  are DC variables with relatively small oscillations. So, by considering  $k = 0$  and  $k = 1$ , they can be modeled with good accuracy.

Input matrix  $\mathbf{B}_L$  is given by:

$$\mathbf{B}_{L77 \times 1} = \left[ \frac{1}{L_c}, 0, 0, \dots, 0 \right]^T. \quad (\text{G.1})$$

The matrices terms of dynamic matrix  $\mathbf{A}_L$  are shown in Tables G.1-G.9.

Table G.1 – Matrix  $\mathbf{A}_L$  elements - Pt. I.

Element	Term	Element	Term
$a_{1,12}$	$\frac{-1+D_c}{L_c}$	$a_{4,17}$	$\frac{\sin(D_c 2\pi)}{L_c 2\pi}$
$a_{1,13}$	$\frac{\sin(D_c 2\pi)}{L_c \pi}$	$a_{4,18}$	$\frac{-1+\cos(D_c 2\pi)}{L_c 2\pi}$
$a_{1,14}$	$\frac{-1+\cos(D_c 2\pi)}{L_c \pi}$	$a_{4,19}$	$\frac{\sin(D_c 4\pi)}{L_c 4\pi}$
$a_{1,15}$	$\frac{\sin(D_c 4\pi)}{L_c \pi}$	$a_{4,20}$	$\frac{-1+\cos(D_c 4\pi)}{L_c 4\pi}$
$a_{1,16}$	$\frac{-1+\cos(D_c 4\pi)}{L_c 2\pi}$	$a_{4,21}$	$\frac{\sin(D_c 6\pi)}{L_c 6\pi}$
$a_{1,17}$	$\frac{\sin(D_c 6\pi)}{L_c 3\pi}$	$a_{4,22}$	$\frac{-1+\cos(D_c 6\pi)}{L_c 6\pi}$
$a_{1,18}$	$\frac{-1+\cos(D_c 6\pi)}{L_c 3\pi}$	$a_{5,4}$	$-2\omega_s$
$a_{2,3}$	$\omega_s$	$a_{5,12}$	$\frac{-1+\cos(D_c 4\pi)}{L_c 4\pi}$
$a_{2,12}$	$\frac{\sin(D_c 2\pi)}{L_c 2\pi}$	$a_{5,13}$	$\frac{-2}{L_c 3\pi} + \frac{\cos(D_c 2\pi)}{L_c 2\pi} + \frac{\cos(D_c 6\pi)}{L_c 6\pi}$
$a_{2,13}$	$\frac{-1+D_c}{L_c} + \frac{\sin(D_c 4\pi)}{L_c 4\pi}$	$a_{5,14}$	$\frac{\sin(D_c 2\pi)}{L_c 2\pi} - \frac{\sin(D_c 6\pi)}{L_c 6\pi}$
$a_{2,14}$	$\frac{-1+\cos(D_c 4\pi)}{L_c 4\pi}$	$a_{5,16}$	$\frac{-1+D_c}{L_c}$
$a_{2,15}$	$\frac{\sin(D_c 2\pi)}{L_c 2\pi} + \frac{\sin(D_c 6\pi)}{L_c 6\pi}$	$a_{5,17}$	$\frac{1-\cos(D_c 2\pi)}{L_c 2\pi}$
$a_{2,16}$	$\frac{-2}{L_c 3\pi} + \frac{\cos(D_c 2\pi)}{L_c 2\pi} + \frac{\cos(D_c 6\pi)}{L_c 6\pi}$	$a_{5,18}$	$\frac{\sin(D_c 2\pi)}{L_c 2\pi}$
$a_{2,17}$	$\frac{\sin(D_c 4\pi)}{L_c 4\pi}$	$a_{5,19}$	$\frac{1-\cos(D_c 4\pi)}{L_c 4\pi}$
$a_{2,18}$	$\frac{-1+\cos(D_c 4\pi)}{L_c 4\pi}$	$a_{5,20}$	$\frac{\sin(D_c 4\pi)}{L_c 4\pi}$
$a_{2,19}$	$\frac{\sin(D_c 6\pi)}{L_c 6\pi}$	$a_{5,21}$	$\frac{1-\cos(D_c 6\pi)}{L_c 6\pi}$
$a_{2,20}$	$\frac{-1+\cos(D_c 6\pi)}{L_c 6\pi}$	$a_{5,22}$	$\frac{\sin(D_c 6\pi)}{L_c 6\pi}$
$a_{3,2}$	$-\omega_s$	$a_{6,7}$	$3\omega_s$
$a_{3,12}$	$\frac{-1+\cos(D_c 2\pi)}{L_c 2\pi}$	$a_{6,12}$	$\frac{-1+\cos(D_c 6\pi)}{L_c 6\pi}$
$a_{3,13}$	$\frac{-1+\cos(D_c 4\pi)}{L_c 4\pi}$	$a_{6,13}$	$\frac{-1+\cos(D_c 4\pi)}{L_c 4\pi}$
$a_{3,14}$	$\frac{-1+D_c}{L_c} - \frac{\sin(D_c 4\pi)}{L_c 4\pi}$	$a_{6,14}$	$\frac{\sin(D_c 4\pi)}{L_c 4\pi}$
$a_{3,15}$	$\frac{1}{L_c 3\pi} - \frac{\cos(D_c 2\pi)}{L_c 2\pi} + \frac{\cos(D_c 6\pi)}{L_c 6\pi}$	$a_{6,15}$	$\frac{-1+\cos(D_c 2\pi)}{L_c 2\pi}$
$a_{3,16}$	$\frac{\sin(D_c 2\pi)}{L_c 2\pi} - \frac{\sin(D_c 6\pi)}{L_c 6\pi}$	$a_{6,16}$	$\frac{\sin(D_c 2\pi)}{L_c 2\pi}$
$a_{3,17}$	$\frac{1-\cos(D_c 4\pi)}{L_c 4\pi}$	$a_{6,18}$	$\frac{-1+D_c}{L_c}$
$a_{3,18}$	$\frac{\sin(D_c 4\pi)}{L_c 4\pi}$	$a_{6,19}$	$\frac{1-\cos(D_c 2\pi)}{L_c 2\pi}$
$a_{3,19}$	$\frac{1-\cos(D_c 6\pi)}{L_c 6\pi}$	$a_{6,20}$	$\frac{\sin(D_c 2\pi)}{L_c 2\pi}$
$a_{3,20}$	$\frac{\sin(D_c 6\pi)}{L_c 6\pi}$	$a_{6,21}$	$\frac{1-\cos(D_c 4\pi)}{L_c 4\pi}$
$a_{4,5}$	$2\omega_s$	$a_{6,22}$	$\frac{\sin(D_c 4\pi)}{L_c 4\pi}$
$a_{4,12}$	$\frac{\sin(D_c 4\pi)}{L_c 4\pi}$	$a_{7,6}$	$-3\omega_s$
$a_{4,13}$	$\frac{\sin(D_c 2\pi)}{L_c 2\pi} + \frac{\sin(D_c 6\pi)}{L_c 6\pi}$	$a_{7,12}$	$\frac{-1+\cos(D_c 6\pi)}{L_c 6\pi}$
$a_{4,14}$	$\frac{1}{L_c 3\pi} - \frac{\cos(D_c 2\pi)}{L_c 2\pi} + \frac{\cos(D_c 6\pi)}{L_c 6\pi}$	$a_{7,13}$	$\frac{-1+\cos(D_c 4\pi)}{L_c 4\pi}$
$a_{4,15}$	$\frac{-1+D_c}{L_c}$	$a_{7,14}$	$\frac{\sin(D_c 4\pi)}{L_c 4\pi}$

Table G.2 – Matrix  $\mathbf{A}_L$  elements - Pt. II.

Element	Term	Element	Term
$a_{7,15}$	$\frac{-1+\cos(D_c 2\pi)}{L_c 2\pi}$	$a_{10,19}$	$\frac{\sin(D_c 2\pi)}{L_c 2\pi}$
$a_{7,16}$	$\frac{\sin(D_c 2\pi)}{L_c 2\pi}$	$a_{10,20}$	$\frac{1-\cos(D_c 2\pi)}{L_c 2\pi}$
$a_{7,18}$	$\frac{-1+D_c}{L_c}$	$a_{10,21}$	$\frac{-1+D_c}{L_c}$
$a_{7,19}$	$\frac{1-\cos(D_c 2\pi)}{L_c 2\pi}$	$a_{11,10}$	$-5\omega_s$
$a_{7,20}$	$\frac{\sin(D_c 2\pi)}{L_c 2\pi}$	$a_{11,15}$	$\frac{-1+\cos(D_c 6\pi)}{L_c 6\pi}$
$a_{7,21}$	$\frac{1-\cos(D_c 4\pi)}{L_c 4\pi}$	$a_{11,16}$	$\frac{\sin(D_c 6\pi)}{L_c 6\pi}$
$a_{7,22}$	$\frac{\sin(D_c 4\pi)}{L_c 4\pi}$	$a_{11,17}$	$\frac{-1+\cos(D_c 4\pi)}{L_c 4\pi}$
$a_{8,9}$	$4\omega_s$	$a_{11,18}$	$\frac{\sin(D_c 4\pi)}{L_c 4\pi}$
$a_{8,13}$	$\frac{\sin(D_c 6\pi)}{L_c 6\pi}$	$a_{11,19}$	$\frac{-1+\cos(D_c 2\pi)}{L_c 2\pi}$
$a_{8,14}$	$\frac{1-\cos(D_c 6\pi)}{L_c 6\pi}$	$a_{11,20}$	$\frac{\sin(D_c 2\pi)}{L_c 2\pi}$
$a_{8,15}$	$\frac{\sin(D_c 4\pi)}{L_c 4\pi}$	$a_{11,22}$	$\frac{-1+D_c}{L_c}$
$a_{8,16}$	$\frac{1-\cos(D_c 4\pi)}{L_c 4\pi}$	$a_{12,1}$	$\frac{1-D_c}{C_1}$
$a_{8,17}$	$\frac{\sin(D_c 2\pi)}{L_c 2\pi}$	$a_{12,2}$	$\frac{-\sin(D_c 2\pi)}{C_1 \pi}$
$a_{8,18}$	$\frac{1-\cos(D_c 2\pi)}{L_c 2\pi}$	$a_{12,3}$	$\frac{1-\cos(D_c 2\pi)}{C_1 \pi}$
$a_{8,19}$	$\frac{-1+D_c}{L_c}$	$a_{12,4}$	$\frac{-\sin(D_c 4\pi)}{C_1 2\pi}$
$a_{8,21}$	$\frac{\sin(D_c 2\pi)}{L_c 2\pi}$	$a_{12,5}$	$\frac{1-\cos(D_c 4\pi)}{C_1 2\pi}$
$a_{8,22}$	$\frac{-1+\cos(D_c 2\pi)}{L_c 2\pi}$	$a_{12,6}$	$\frac{-\sin(D_c 6\pi)}{C_1 3\pi}$
$a_{9,8}$	$-4\omega_s$	$a_{12,7}$	$\frac{1-\cos(D_c 6\pi)}{C_1 3\pi}$
$a_{9,13}$	$\frac{-1+\cos(D_c 6\pi)}{L_c 6\pi}$	$a_{12,23}$	$\frac{-1+D_c}{C_1}$
$a_{9,14}$	$\frac{\sin(D_c 6\pi)}{L_c 6\pi}$	$a_{12,24}$	$\frac{\sin(D_c 2\pi)}{C_1 \pi}$
$a_{9,15}$	$\frac{-1+\cos(D_c 4\pi)}{L_c 4\pi}$	$a_{12,25}$	$\frac{-1+\cos(D_c 2\pi)}{C_1 \pi}$
$a_{9,16}$	$\frac{\sin(D_c 4\pi)}{L_c 4\pi}$	$a_{12,26}$	$\frac{\sin(D_c 4\pi)}{C_1 2\pi}$
$a_{9,17}$	$\frac{-1+\cos(D_c 2\pi)}{L_c 2\pi}$	$a_{12,27}$	$\frac{-1+\cos(D_c 4\pi)}{C_1 2\pi}$
$a_{9,18}$	$\frac{\sin(D_c 2\pi)}{L_c 2\pi}$	$a_{12,28}$	$\frac{\sin(D_c 6\pi)}{C_1 3\pi}$
$a_{9,20}$	$\frac{-1+D_c}{L_c}$	$a_{12,29}$	$\frac{-1+\cos(D_c 6\pi)}{C_1 3\pi}$
$a_{9,21}$	$\frac{1-\cos(D_c 2\pi)}{L_c 2\pi}$	$a_{13,1}$	$\frac{-\sin(D_c 2\pi)}{C_1 2\pi}$
$a_{9,22}$	$\frac{\sin(D_c 2\pi)}{L_c 2\pi}$	$a_{13,2}$	$\frac{1-D_c}{C_1} - \frac{\sin(D_c 4\pi)}{C_1 4\pi}$
$a_{10,11}$	$5\omega_s$	$a_{13,3}$	$\frac{1-\cos(D_c 4\pi)}{C_1 4\pi}$
$a_{10,15}$	$\frac{\sin(D_c 6\pi)}{L_c 6\pi}$	$a_{13,4}$	$\frac{-\sin(D_c 2\pi)}{C_1 2\pi} - \frac{\sin(D_c 6\pi)}{C_1 6\pi}$
$a_{10,16}$	$\frac{1-\cos(D_c 6\pi)}{L_c 6\pi}$	$a_{13,5}$	$\frac{2}{C_1 3\pi} - \frac{\cos(D_c 2\pi)}{C_1 2\pi} - \frac{\cos(D_c 6\pi)}{C_1 6\pi}$
$a_{10,17}$	$\frac{\sin(D_c 4\pi)}{L_c 4\pi}$	$a_{13,6}$	$\frac{-\sin(D_c 4\pi)}{C_1 4\pi}$
$a_{10,18}$	$\frac{1-\cos(D_c 4\pi)}{L_c 4\pi}$	$a_{13,7}$	$\frac{1-\cos(D_c 4\pi)}{C_1 4\pi}$

Table G.3 – Matrix  $\mathbf{A}_L$  elements - Pt. III.

Element	Term	Element	Term
$a_{13,8}$	$\frac{-\sin(D_c 6\pi)}{C_1 6\pi}$	$a_{15,2}$	$\frac{-\sin(D_c 2\pi)}{C_1 2\pi} - \frac{-\sin(D_c 6\pi)}{C_1 6\pi}$
$a_{13,9}$	$\frac{1-\cos(D_c 6\pi)}{C_1 6\pi}$	$a_{15,3}$	$\frac{-1}{C_1 3\pi} + \frac{\cos(D_c 2\pi)}{C_1 2\pi} - \frac{\cos(D_c 6\pi)}{C_1 6\pi}$
$a_{13,14}$	$\omega_s$	$a_{15,4}$	$\frac{1-D_c}{C_1}$
$a_{13,23}$	$\frac{\sin(D_c 2\pi)}{C_1 2\pi}$	$a_{15,6}$	$\frac{-\sin(D_c 2\pi)}{C_1 2\pi}$
$a_{13,24}$	$\frac{-1+D_c}{C_1} + \frac{\sin(D_c 4\pi)}{C_1 4\pi}$	$a_{15,7}$	$\frac{1-\cos(D_c 2\pi)}{C_1 2\pi}$
$a_{13,25}$	$\frac{-1+\cos(D_c 4\pi)}{C_1 4\pi}$	$a_{15,8}$	$\frac{-\sin(D_c 4\pi)}{C_1 4\pi}$
$a_{13,26}$	$\frac{\sin(D_c 2\pi)}{C_1 2\pi} + \frac{\sin(D_c 6\pi)}{C_1 6\pi}$	$a_{15,9}$	$\frac{1-\cos(D_c 4\pi)}{C_1 4\pi}$
$a_{13,27}$	$\frac{-2}{C_1 3\pi} + \frac{\cos(D_c 2\pi)}{C_1 2\pi} + \frac{\cos(D_c 6\pi)}{C_1 6\pi}$	$a_{15,10}$	$\frac{-\sin(D_c 6\pi)}{C_1 6\pi}$
$a_{13,28}$	$\frac{\sin(D_c 4\pi)}{C_1 4\pi}$	$a_{15,11}$	$\frac{1-\cos(D_c 6\pi)}{C_1 6\pi}$
$a_{13,29}$	$\frac{-1+\cos(D_c 4\pi)}{C_1 4\pi}$	$a_{15,16}$	$2\omega_s$
$a_{13,30}$	$\frac{\sin(D_c 6\pi)}{C_1 6\pi}$	$a_{15,23}$	$\frac{\sin(D_c 4\pi)}{C_1 4\pi}$
$a_{13,31}$	$\frac{-1+\cos(D_c 6\pi)}{C_1 6\pi}$	$a_{15,24}$	$\frac{\sin(D_c 2\pi)}{C_1 2\pi} + \frac{\sin(D_c 6\pi)}{C_1 6\pi}$
$a_{14,1}$	$\frac{1-\cos(D_c 2\pi)}{C_1 2\pi}$	$a_{15,25}$	$\frac{1}{C_1 3\pi} - \frac{\cos(D_c 2\pi)}{C_1 2\pi} + \frac{D_c 6\pi}{C_1 6\pi}$
$a_{14,2}$	$\frac{1-\cos(D_c 4\pi)}{C_1 4\pi}$	$a_{15,26}$	$\frac{-1+D_c}{C_1}$
$a_{14,3}$	$\frac{1-D_c}{C_1} + \frac{\sin(D_c 4\pi)}{C_1 4\pi}$	$a_{15,28}$	$\frac{\sin(D_c 2\pi)}{C_1 2\pi}$
$a_{14,4}$	$\frac{-1}{C_1 3\pi} + \frac{\cos(D_c 2\pi)}{C_1 2\pi} - \frac{\cos(D_c 6\pi)}{C_1 6\pi}$	$a_{15,29}$	$\frac{-1+\cos(D_c 2\pi)}{C_1 2\pi}$
$a_{14,5}$	$\frac{-\sin(D_c 2\pi)}{C_1 2\pi} + \frac{\sin(D_c 6\pi)}{C_1 6\pi}$	$a_{15,30}$	$\frac{\sin(D_c 4\pi)}{C_1 4\pi}$
$a_{14,6}$	$\frac{-1+\cos(D_c 4\pi)}{C_1 4\pi}$	$a_{15,31}$	$\frac{-1+\cos(D_c 4\pi)}{C_1 4\pi}$
$a_{14,7}$	$\frac{-\sin(D_c 4\pi)}{C_1 4\pi}$	$a_{15,32}$	$\frac{\sin(D_c 6\pi)}{C_1 6\pi}$
$a_{14,8}$	$\frac{-1+\cos(D_c 6\pi)}{C_1 6\pi}$	$a_{15,33}$	$\frac{-1+\cos(D_c 6\pi)}{C_1 6\pi}$
$a_{14,9}$	$\frac{-\sin(D_c 6\pi)}{C_1 6\pi}$	$a_{16,1}$	$\frac{1-\cos(D_c 4\pi)}{C_1 4\pi}$
$a_{14,13}$	$-\omega_s$	$a_{16,2}$	$\frac{2}{C_1 3\pi} - \frac{\cos(D_c 2\pi)}{C_1 2\pi} - \frac{\cos(D_c 6\pi)}{C_1 6\pi}$
$a_{14,23}$	$\frac{-1+\cos(D_c 2\pi)}{C_1 2\pi}$	$a_{16,3}$	$-\frac{\sin(D_c 2\pi)}{C_1 2\pi} + \frac{\sin(D_c 6\pi)}{C_1 6\pi}$
$a_{14,24}$	$\frac{-1+\cos(D_c 4\pi)}{C_1 4\pi}$	$a_{16,5}$	$\frac{1-D_c}{C_1}$
$a_{14,25}$	$\frac{-1+D_c}{C_1} - \frac{\sin(D_c 4\pi)}{C_1 4\pi}$	$a_{16,6}$	$\frac{-1+\cos(D_c 2\pi)}{C_1 2\pi}$
$a_{14,26}$	$\frac{1}{C_1 3\pi} - \frac{\cos(D_c 2\pi)}{C_1 2\pi} + \frac{\cos(D_c 6\pi)}{C_1 6\pi}$	$a_{12,29}$	$\frac{-1+\cos(D_c 6\pi)}{C_1 3\pi}$
$a_{14,27}$	$\frac{\sin(D_c 2\pi)}{C_1 2\pi} - \frac{\sin(D_c 6\pi)}{C_1 6\pi}$	$a_{16,7}$	$\frac{-\sin(D_c 2\pi)}{C_1 2\pi}$
$a_{14,28}$	$\frac{1-\cos(D_c 4\pi)}{C_1 4\pi}$	$a_{16,8}$	$\frac{-1+\cos(D_c 4\pi)}{C_1 4\pi}$
$a_{14,29}$	$\frac{\sin(D_c 4\pi)}{C_1 4\pi}$	$a_{16,9}$	$\frac{-\sin(D_c 4\pi)}{C_1 4\pi}$
$a_{14,30}$	$\frac{1-\cos(D_c 6\pi)}{C_1 6\pi}$	$a_{16,10}$	$\frac{-1+\cos(D_c 6\pi)}{C_1 6\pi}$
$a_{14,31}$	$\frac{\sin(D_c 6\pi)}{C_1 6\pi}$	$a_{16,11}$	$\frac{-\sin(D_c 6\pi)}{C_1 6\pi}$
$a_{15,1}$	$\frac{-\sin(D_c 4\pi)}{C_1 4\pi}$	$a_{16,15}$	$-2\omega_s$



Table G.4 – Matrix  $\mathbf{A}_L$  elements - Pt. IV.

Element	Term	Element	Term
$a_{16,23}$	$\frac{-1+\cos(D_c4\pi)}{C_14\pi}$	$a_{18,2}$	$\frac{1-\cos(D_c4\pi)}{C_14\pi}$
$a_{16,24}$	$\frac{-2}{C_13\pi} + \frac{\cos(D_c2\pi)}{C_12\pi} + \frac{\cos(D_c6\pi)}{C_16\pi}$	$a_{18,3}$	$\frac{-\sin(D_c4\pi)}{C_14\pi}$
$a_{16,25}$	$\frac{\sin(D_c2\pi)}{C_12\pi} - \frac{\sin(D_c6\pi)}{C_16\pi}$	$a_{18,4}$	$\frac{1-\cos(D_c2\pi)}{C_12\pi}$
$a_{16,27}$	$\frac{-1+D_c}{C_1}$	$a_{18,5}$	$\frac{-\sin(D_c2\pi)}{C_12\pi}$
$a_{16,28}$	$\frac{1-\cos(D_c2\pi)}{C_12\pi}$	$a_{18,7}$	$\frac{1-D_c}{C_1}$
$a_{16,29}$	$\frac{\sin(D_c2\pi)}{C_12\pi}$	$a_{18,8}$	$\frac{-1+\cos(D_c2\pi)}{C_12\pi}$
$a_{16,30}$	$\frac{1-\cos(D_c4\pi)}{C_14\pi}$	$a_{18,9}$	$\frac{-\sin(D_c2\pi)}{C_12\pi}$
$a_{16,31}$	$\frac{\sin(D_c4\pi)}{C_14\pi}$	$a_{18,10}$	$\frac{-1+\cos(D_c4\pi)}{C_14\pi}$
$a_{16,32}$	$\frac{1-\cos(D_c6\pi)}{C_16\pi}$	$a_{18,11}$	$\frac{-\sin(D_c4\pi)}{C_14\pi}$
$a_{16,33}$	$\frac{\sin(D_c6\pi)}{C_16\pi}$	$a_{18,17}$	$-3\omega_s$
$a_{17,1}$	$\frac{-\sin(D_c6\pi)}{C_16\pi}$	$a_{18,23}$	$\frac{-1+\cos(D_c6\pi)}{C_16\pi}$
$a_{17,2}$	$\frac{-\sin(D_c4\pi)}{C_14\pi}$	$a_{18,24}$	$\frac{-1+\cos(D_c4\pi)}{C_14\pi}$
$a_{17,3}$	$\frac{-1+\cos(D_c4\pi)}{C_14\pi}$	$a_{18,25}$	$\frac{\sin(D_c4\pi)}{C_14\pi}$
$a_{17,4}$	$\frac{-\sin(D_c2\pi)}{C_12\pi}$	$a_{18,26}$	$\frac{-1+\cos(D_c2\pi)}{C_12\pi}$
$a_{17,5}$	$\frac{-1+\cos(D_c2\pi)}{C_12\pi}$	$a_{18,27}$	$\frac{\sin(D_c2\pi)}{C_12\pi}$
$a_{17,6}$	$\frac{1-D_c}{C_1}$	$a_{18,29}$	$\frac{-1+D_c}{C_1}$
$a_{17,8}$	$\frac{-\sin(D_c2\pi)}{C_12\pi}$	$a_{18,30}$	$\frac{1-\cos(D_c2\pi)}{C_12\pi}$
$a_{17,9}$	$\frac{1-\cos(D_c2\pi)}{C_12\pi}$	$a_{18,31}$	$\frac{\sin(D_c2\pi)}{C_12\pi}$
$a_{17,10}$	$\frac{-\sin(D_c4\pi)}{C_14\pi}$	$a_{18,32}$	$\frac{1-\cos(D_c4\pi)}{C_14\pi}$
$a_{17,11}$	$\frac{1-\cos(D_c4\pi)}{C_14\pi}$	$a_{18,33}$	$\frac{\sin(D_c4\pi)}{C_14\pi}$
$a_{17,18}$	$3\omega_s$	$a_{19,2}$	$\frac{-\sin(D_c6\pi)}{C_16\pi}$
$a_{17,23}$	$\frac{\sin(D_c6\pi)}{C_16\pi}$	$a_{19,3}$	$\frac{-1+\cos(D_c6\pi)}{C_16\pi}$
$a_{17,24}$	$\frac{\sin(D_c4\pi)}{C_14\pi}$	$a_{19,4}$	$\frac{-\sin(D_c4\pi)}{C_14\pi}$
$a_{17,25}$	$\frac{1-\cos(D_c4\pi)}{C_14\pi}$	$a_{19,5}$	$\frac{-1+\cos(D_c4\pi)}{C_14\pi}$
$a_{17,26}$	$\frac{\sin(D_c2\pi)}{C_12\pi}$	$a_{19,6}$	$\frac{-\sin(D_c2\pi)}{C_12\pi}$
$a_{17,27}$	$\frac{1-\cos(D_c2\pi)}{C_12\pi}$	$a_{19,7}$	$\frac{-1+\cos(D_c2\pi)}{C_12\pi}$
$a_{17,28}$	$\frac{-1+D_c}{C_1} - \frac{\sin(D_c6\pi)}{C_16\pi}$	$a_{19,8}$	$\frac{1-D_c}{C_1}$
$a_{17,30}$	$\frac{\sin(D_c2\pi)}{C_12\pi}$	$a_{19,10}$	$\frac{-\sin(D_c2\pi)}{C_12\pi}$
$a_{17,31}$	$\frac{-1+\cos(D_c2\pi)}{C_12\pi}$	$a_{19,11}$	$\frac{1-\cos(D_c2\pi)}{C_12\pi}$
$a_{17,32}$	$\frac{\sin(D_c4\pi)}{C_14\pi}$	$a_{19,20}$	$4\omega_s$
$a_{17,33}$	$\frac{-1+\cos(D_c4\pi)}{C_14\pi}$	$a_{19,24}$	$\frac{\sin(D_c6\pi)}{C_16\pi}$
$a_{18,1}$	$\frac{1-\cos(D_c6\pi)}{C_16\pi}$	$a_{19,25}$	$\frac{1-\cos(D_c6\pi)}{C_16\pi}$

Table G.5 – Matrix  $\mathbf{A}_L$  elements - Pt. V.

Element	Term	Element	Term
$a_{19,26}$	$\frac{\sin(D_c 4\pi)}{C_1 4\pi}$	$a_{21,10}$	$\frac{1-D_c}{C_1}$
$a_{19,27}$	$\frac{1-\cos(D_c 4\pi)}{C_1 4\pi}$	$a_{21,22}$	$5\omega_s$
$a_{19,28}$	$\frac{\sin(D_c 2\pi)}{C_1 2\pi}$	$a_{21,26}$	$\frac{\sin(D_c 6\pi)}{C_1 6\pi}$
$a_{19,29}$	$\frac{1-\cos(D_c 2\pi)}{C_1 2\pi}$	$a_{21,27}$	$\frac{1-\cos(D_c 6\pi)}{C_1 6\pi}$
$a_{19,30}$	$\frac{-1+D_c}{C_1}$	$a_{21,28}$	$\frac{\sin(D_c 4\pi)}{C_1 4\pi}$
$a_{19,32}$	$\frac{\sin(D_c 2\pi)}{C_1 2\pi}$	$a_{21,29}$	$\frac{1-\cos(D_c 4\pi)}{C_1 4\pi}$
$a_{19,33}$	$\frac{-1+\cos(D_c 2\pi)}{C_1 2\pi}$	$a_{21,30}$	$\frac{\sin(D_c 2\pi)}{C_1 2\pi}$
$a_{20,2}$	$\frac{1-\cos(D_c 6\pi)}{C_1 6\pi}$	$a_{21,31}$	$\frac{1-\cos(D_c 2\pi)}{C_1 2\pi}$
$a_{20,3}$	$\frac{-\sin(D_c 6\pi)}{C_1 6\pi}$	$a_{21,32}$	$\frac{-1+D_c}{C_1}$
$a_{20,4}$	$\frac{1-\cos(D_c 4\pi)}{C_1 4\pi}$	$a_{22,4}$	$\frac{1-\cos(D_c 6\pi)}{C_1 6\pi}$
$a_{20,5}$	$\frac{-\sin(D_c 4\pi)}{C_1 4\pi}$	$a_{22,5}$	$\frac{-\sin(D_c 6\pi)}{C_1 6\pi}$
$a_{20,6}$	$\frac{1-\cos(D_c 2\pi)}{C_1 2\pi}$	$a_{22,6}$	$\frac{1-\cos(D_c 4\pi)}{C_1 4\pi}$
$a_{20,7}$	$\frac{-\sin(D_c 2\pi)}{C_1 2\pi}$	$a_{22,7}$	$\frac{-\sin(D_c 4\pi)}{C_1 4\pi}$
$a_{20,9}$	$\frac{1-D_c}{C_1}$	$a_{22,8}$	$\frac{1-\cos(D_c 2\pi)}{C_1 2\pi}$
$a_{20,10}$	$\frac{-1+\cos(D_c 2\pi)}{C_1 2\pi}$	$a_{22,9}$	$\frac{-\sin(D_c 2\pi)}{C_1 2\pi}$
$a_{20,11}$	$\frac{-\sin(D_c 2\pi)}{C_1 2\pi}$	$a_{22,11}$	$\frac{1-D_c}{C_1}$
$a_{20,19}$	$-4\omega_s$	$a_{22,21}$	$-5\omega_s$
$a_{20,24}$	$\frac{-1+\cos(D_c 6\pi)}{C_1 6\pi}$	$a_{22,26}$	$\frac{-1+\cos(D_c 6\pi)}{C_1 6\pi}$
$a_{20,25}$	$\frac{\sin(D_c 6\pi)}{C_1 6\pi}$	$a_{22,27}$	$\frac{\sin(D_c 6\pi)}{C_1 6\pi}$
$a_{20,26}$	$\frac{-1+\cos(D_c 4\pi)}{C_1 4\pi}$	$a_{22,28}$	$\frac{-1+\cos(D_c 4\pi)}{C_1 4\pi}$
$a_{20,27}$	$\frac{\sin(D_c 4\pi)}{C_1 4\pi}$	$a_{22,29}$	$\frac{\sin(D_c 4\pi)}{C_1 4\pi}$
$a_{20,28}$	$\frac{-1+\cos(D_c 2\pi)}{C_1 2\pi}$	$a_{22,30}$	$\frac{-1+\cos(D_c 2\pi)}{C_1 2\pi}$
$a_{20,29}$	$\frac{\sin(D_c 2\pi)}{C_1 2\pi}$	$a_{22,31}$	$\frac{\sin(D_c 2\pi)}{C_1 2\pi}$
$a_{20,31}$	$\frac{-1+D_c}{C_1}$	$a_{22,33}$	$\frac{-1+D_c}{C_1 \pi}$
$a_{20,32}$	$\frac{1-\cos(D_c 2\pi)}{C_1 2\pi}$	$a_{23,12}$	$\frac{1-D_c}{L_r}$
$a_{20,33}$	$\frac{\sin(D_c 2\pi)}{C_1 2\pi}$	$a_{23,13}$	$\frac{-\sin(D_c 2\pi)}{L_r \pi}$
$a_{21,4}$	$\frac{-\sin(D_c 6\pi)}{C_1 6\pi}$	$a_{23,14}$	$\frac{1-\cos(D_c 2\pi)}{L_r \pi}$
$a_{21,5}$	$\frac{-1+\cos(D_c 6\pi)}{C_1 6\pi}$	$a_{23,34}$	$\frac{-1}{L_r}$
$a_{21,6}$	$\frac{-\sin(D_c 4\pi)}{C_1 4\pi}$	$a_{23,45}$	$\frac{-\alpha}{L_r} - \frac{-\alpha T_1}{L_r 2\pi} + \frac{\alpha T_2}{L_r 2\pi}$
$a_{21,7}$	$\frac{-1+\cos(D_c 4\pi)}{C_1 4\pi}$	$a_{23,46}$	$\frac{-\alpha \sin(T_1)}{L_r \pi} + \frac{\alpha \sin(T_2)}{L_r \pi}$
$a_{21,8}$	$\frac{-\sin(D_c 2\pi)}{C_1 2\pi}$	$a_{23,47}$	$\frac{-\alpha \cos(T_1)}{L_r \pi} + \frac{\alpha \cos(T_2)}{L_r \pi}$
$a_{21,9}$	$\frac{-1+\cos(D_c 2\pi)}{C_1 2\pi}$	$a_{24,12}$	$\frac{-\sin(D_c 2\pi)}{L_r 2\pi}$

Table G.6 – Matrix  $\mathbf{A}_L$  elements - Pt. VI.

Element	Term	Element	Term
$a_{24,13}$	$\frac{1-D_c}{L_r} - \frac{\sin(D_c 4\pi)}{L_r 4\pi}$	$a_{46,25}$	$\frac{\alpha(\cos(2T_1) - \cos(2T_2))}{C_2 4\pi}$
$a_{24,14}$	$\frac{1 - \cos(D_c 4\pi)}{L_r 4\pi}$	$a_{46,26}$	$\frac{\alpha(\sin(T_1) - \sin(T_2))}{C_2 2\pi} + \frac{\alpha(\sin(3T_1) - \sin(3T_2))}{C_2 6\pi}$
$a_{24,35}$	$-\frac{1}{L_r}$	$a_{46,27}$	$\frac{\alpha(\cos(T_1) - \cos(T_2))}{C_2 2\pi} + \frac{\alpha(\cos(3T_1) - \cos(3T_2))}{C_2 6\pi}$
$a_{24,45}$	$-\frac{\alpha \sin(T_1)}{L_r 2\pi} + \frac{\alpha \sin(T_2)}{L_r 2\pi}$	$a_{46,28}$	$\frac{\alpha(\sin(2T_1) - \sin(2T_2))}{C_2 4\pi}$
$a_{24,46}$	$\frac{-\alpha}{L_r} + \frac{\alpha(T_2 - T_1)}{L_r 2\pi} + \frac{\alpha(\sin(2T_2) - \sin(2T_1))}{L_r 4\pi}$	$a_{46,29}$	$\frac{\alpha(\cos(2T_1) - \cos(2T_2))}{C_2 4\pi}$
$a_{24,47}$	$\frac{\alpha(\cos(2T_2) - \cos(2T_1))}{L_r 4\pi}$	$a_{46,30}$	$\frac{\alpha(\sin(3T_1) - \sin(3T_2))}{C_2 6\pi}$
$a_{25,12}$	$\frac{1 - \cos(D_c 2\pi)}{L_r 2\pi}$	$a_{46,31}$	$\frac{\alpha(\cos(3T_1) - \cos(3T_2))}{C_2 6\pi}$
$a_{25,13}$	$\frac{1 - \cos(D_c 4\pi)}{L_r 4\pi}$	$a_{46,47}$	$\omega_s$
$a_{25,14}$	$\frac{1 - D_c}{L_r} + \frac{\sin(D_c 4\pi)}{L_r 4\pi}$	$a_{46,56}$	$\frac{\sin(T_2) - \sin(T_1)}{C_2 2\pi}$
$a_{25,36}$	$-\frac{1}{L_r}$	$a_{46,57}$	$-\frac{1}{C_2} + \frac{T_2 - T_1}{C_2 2\pi} + \frac{\sin(2T_2) - \sin(2T_1)}{C_2 4\pi}$
$a_{25,45}$	$-\frac{\alpha \cos(T_1)}{L_r 2\pi} + \frac{\alpha \cos(T_2)}{L_r 2\pi}$	$a_{46,58}$	$\frac{\cos(2T_2) - \cos(2T_1)}{C_2 4\pi}$
$a_{25,46}$	$-\frac{\alpha \cos(2T_1)}{L_r 4\pi} + \frac{\alpha \cos(2T_2)}{L_r 4\pi}$	$a_{46,59}$	$\frac{\sin(T_2) - \sin(T_1)}{C_2 2\pi} + \frac{\sin(3T_2) - \sin(3T_1)}{C_2 6\pi}$
$a_{25,47}$	$\frac{-\alpha}{L_r} + \frac{\alpha(T_2 - T_1)}{L_r 2\pi} + \frac{\alpha(\sin(2T_1) - \sin(2T_2))}{L_r 4\pi}$	$a_{46,60}$	$\frac{\cos(T_2) - \cos(T_1)}{C_2 2\pi} + \frac{\cos(3T_2) - \cos(3T_1)}{C_2 6\pi}$
$a_{34,23}$	$\frac{1}{C_r}$	$a_{46,61}$	$\frac{\sin(2T_2) - \sin(2T_1)}{C_2 4\pi}$
$a_{34,24}$	$\frac{1}{C_r}$	$a_{46,62}$	$\frac{\cos(2T_2) - \cos(2T_1)}{C_2 4\pi}$
$a_{34,25}$	$\frac{1}{C_r}$	$a_{46,63}$	$\frac{\sin(3T_2) - \sin(3T_1)}{C_2 6\pi}$
$a_{45,23}$	$\frac{\alpha}{C_2} + \frac{\alpha(T_1 - T_2)}{C_2 2\pi}$	$a_{46,64}$	$\frac{\cos(3T_2) - \cos(3T_1)}{C_2 6\pi}$
$a_{45,24}$	$\frac{\alpha(\sin(T_1) - \sin(T_2))}{C_2 \pi}$	$a_{47,23}$	$\frac{\alpha(\cos(T_1) - \cos(T_2))}{C_2 2\pi}$
$a_{45,25}$	$\frac{\alpha(\cos(T_1) - \cos(T_2))}{C_2 \pi}$	$a_{47,24}$	$\frac{\alpha(\cos(2T_1) - \cos(2T_2))}{C_2 4\pi}$
$a_{45,26}$	$\frac{\alpha(\sin(2T_1) - \sin(2T_2))}{C_2 2\pi}$	$a_{47,25}$	$\frac{\alpha}{C_2} + \frac{\alpha(T_1 - T_2)}{C_2 2\pi} + \frac{\alpha(\sin(2T_2) - \sin(2T_1))}{C_2 4\pi}$
$a_{45,27}$	$\frac{\alpha(\cos(2T_1) - \cos(2T_2))}{C_2 2\pi}$	$a_{47,26}$	$\frac{\alpha(\cos(T_2) - \cos(T_1))}{C_2 2\pi} + \frac{\alpha(\cos(3T_1) - \cos(3T_2))}{C_2 6\pi}$
$a_{45,28}$	$\frac{\alpha(\sin(3T_1) - \sin(3T_2))}{C_2 3\pi}$	$a_{47,27}$	$\frac{\alpha(\sin(T_1) - \sin(T_2))}{C_2 2\pi} + \frac{\alpha(\sin(3T_2) - \sin(3T_1))}{C_2 6\pi}$
$a_{45,29}$	$\frac{\alpha(\cos(3T_1) - \cos(3T_2))}{3C_2 \pi}$	$a_{47,28}$	$\frac{\alpha(\cos(2T_2) - \cos(2T_1))}{C_2 4\pi}$
$a_{45,56}$	$-\frac{1}{C_2} + \frac{T_2 - T_1}{C_2 2\pi}$	$a_{47,29}$	$\frac{\alpha(\sin(2T_1) - \sin(2T_2))}{C_2 4\pi}$
$a_{45,57}$	$-\frac{\sin(T_1) + \sin(T_2)}{C_2 \pi}$	$a_{47,30}$	$\frac{\alpha(\cos(3T_2) - \cos(3T_1))}{C_2 6\pi}$
$a_{45,58}$	$-\frac{\cos(T_1) + \cos(T_2)}{C_2 \pi}$	$a_{47,31}$	$\frac{\alpha(\sin(3T_1) - \sin(3T_2))}{C_2 6\pi}$
$a_{45,59}$	$-\frac{\sin(2T_1) + \sin(2T_2)}{C_2 2\pi}$	$a_{47,46}$	$-\omega_s$
$a_{45,60}$	$-\frac{\cos(2T_1) + \cos(2T_2)}{C_2 2\pi}$	$a_{47,56}$	$\frac{(\cos(T_2) - \cos(T_1))}{C_2 2\pi}$
$a_{45,61}$	$-\frac{\sin(3T_1) + \sin(3T_2)}{C_2 3\pi}$	$a_{47,57}$	$\frac{(\cos(2T_2) - \cos(2T_1))}{C_2 4\pi}$
$a_{45,62}$	$-\frac{\cos(3T_1) + \cos(3T_2)}{C_2 3\pi}$	$a_{47,58}$	$-\frac{1}{C_2} + \frac{T_2 - T_1}{C_2 2\pi} + \frac{(\sin(2T_1) - \sin(2T_2))}{C_2 4\pi}$
$a_{46,23}$	$\frac{\alpha(\sin(T_1) - \sin(T_2))}{C_2 2\pi}$	$a_{47,59}$	$\frac{(\cos(T_1) - \cos(T_2))}{C_2 2\pi} + \frac{(\cos(3T_2) - \cos(3T_1))}{C_2 6\pi}$
$a_{46,24}$	$\frac{\alpha}{C_r} + \frac{\alpha(T_1 - T_2)}{C_r 2\pi} + \frac{\alpha(\sin(2T_1) - \sin(2T_2))}{C_2 4\pi}$	$a_{47,60}$	$\frac{(\sin(T_2) - \sin(T_1))}{C_2 2\pi} + \frac{(\sin(3T_1) - \sin(3T_2))}{C_2 6\pi}$

Table G.7 – Matrix  $\mathbf{A}_L$  elements - Pt. VII.

Element	Term	Element	Term
$a_{47,61}$	$\frac{(\cos(2T_1) - \cos(2T_2))}{C_2 4\pi}$	$a_{49,29}$	$\frac{\alpha(\sin(T_1) - \sin(T_2))}{C_2 2\pi}$
$a_{47,62}$	$\frac{(\sin(2T_2) - \sin(2T_1))}{C_2 4\pi}$	$a_{49,30}$	$\frac{\alpha(\cos(2T_2) - \cos(2T_1))}{C_2 4\pi}$
$a_{47,63}$	$\frac{(\cos(3T_1) - \cos(3T_2))}{C_2 6\pi}$	$a_{49,31}$	$\frac{\alpha(\sin(2T_1) - \sin(2T_2))}{C_2 4\pi}$
$a_{47,64}$	$\frac{(\sin(3T_2) - \sin(3T_1))}{C_2 6\pi}$	$a_{49,32}$	$\frac{\alpha(\cos(3T_2) - \cos(3T_1))}{C_2 6\pi}$
$a_{48,23}$	$\frac{\alpha(\sin(2T_1) - \sin(2T_2))}{C_2 4\pi}$	$a_{49,33}$	$\frac{\alpha(\sin(3T_1) - \sin(3T_2))}{C_2 6\pi}$
$a_{48,24}$	$\frac{\alpha(\sin(2T_1) - \sin(2T_2))}{C_2 2\pi} + \frac{\alpha(\sin(3T_1) - \sin(3T_2))}{C_2 6\pi}$	$a_{49,48}$	$-2\omega_s$
$a_{48,25}$	$\frac{\alpha(\cos(2T_2) - \cos(2T_1))}{C_2 2\pi} + \frac{\alpha(\cos(3T_1) - \cos(3T_2))}{C_2 6\pi}$	$a_{49,56}$	$\frac{\cos(2T_2) - \cos(2T_1)}{C_2 4\pi}$
$a_{48,26}$	$\frac{\alpha}{C_2} + \frac{\alpha(T_1 - T_2)}{C_2 2\pi}$	$a_{49,57}$	$\frac{\cos(T_2) - \cos(T_1)}{C_2 2\pi} + \frac{\cos(3T_2) - \cos(3T_1)}{C_2 6\pi}$
$a_{48,28}$	$\frac{\alpha(\sin(2T_1) - \sin(2T_2))}{C_2 2\pi}$	$a_{49,58}$	$\frac{\sin(T_2) - \sin(T_1)}{C_2 2\pi} + \frac{\sin(3T_1) - \sin(3T_2)}{C_2 6\pi}$
$a_{48,29}$	$\frac{\alpha(\cos(T_1) - \cos(T_2))}{C_2 2\pi}$	$a_{49,60}$	$\frac{-1}{C_2} + \frac{T_2 - T_1}{C_2 2\pi}$
$a_{48,30}$	$\frac{\alpha(\sin(2T_1) - \sin(2T_2))}{C_2 4\pi}$	$a_{49,61}$	$\frac{\cos(T_1) - \cos(T_2)}{C_2 2\pi}$
$a_{48,31}$	$\frac{\alpha(\cos(2T_1) - \cos(2T_2))}{C_2 4\pi}$	$a_{49,62}$	$\frac{\sin(T_2) - \sin(T_1)}{C_2 2\pi}$
$a_{48,32}$	$\frac{\alpha(\sin(3T_1) - \sin(3T_2))}{C_2 6\pi}$	$a_{49,63}$	$\frac{\cos(2T_1) - \cos(2T_2)}{C_2 4\pi}$
$a_{48,33}$	$\frac{\alpha(\cos(3T_1) - \cos(3T_2))}{C_2 6\pi}$	$a_{49,64}$	$\frac{\sin(2T_2) - \sin(2T_1)}{C_2 4\pi}$
$a_{48,49}$	$2\omega_s$	$a_{49,65}$	$\frac{\cos(3T_1) - \cos(3T_2)}{C_2 6\pi}$
$a_{48,56}$	$\frac{(\sin(2T_2) - \sin(2T_1))}{C_2 4\pi}$	$a_{49,66}$	$\frac{\sin(3T_2) - \sin(3T_1)}{C_2 6\pi}$
$a_{48,57}$	$\frac{(\sin(2T_2) - \sin(2T_1))}{C_2 2\pi} + \frac{(\sin(3T_2) - \sin(3T_1))}{C_2 6\pi}$	$a_{50,23}$	$\frac{\alpha(\sin(3T_1) - \sin(3T_2))}{C_2 6\pi}$
$a_{48,58}$	$\frac{(\cos(T_1) - \cos(T_2))}{C_2 2\pi} + \frac{(\cos(3T_2) - \cos(3T_1))}{C_2 6\pi}$	$a_{50,24}$	$\frac{\alpha(\sin(2T_1) - \sin(2T_2))}{C_2 4\pi}$
$a_{48,59}$	$\frac{-1}{C_2} + \frac{T_2 - T_1}{C_2 2\pi}$	$a_{50,25}$	$\frac{\alpha(\cos(2T_2) - \cos(2T_1))}{C_2 4\pi}$
$a_{48,60}$	$\frac{\alpha(\sin(2T_1) - \sin(2T_2))}{C_2 2\pi}$	$a_{50,26}$	$\frac{\alpha(\sin(T_1) - \sin(T_2))}{C_2 2\pi}$
$a_{48,61}$	$\frac{(\sin(T_2) - \sin(T_1))}{C_2 2\pi}$	$a_{50,27}$	$\frac{\alpha(\cos(T_2) - \cos(T_1))}{C_2 2\pi}$
$a_{48,62}$	$\frac{(\cos(T_2) - \cos(T_1))}{C_2 2\pi}$	$a_{50,28}$	$\frac{\alpha}{C_2} + \frac{\alpha(T_1 - T_2)}{C_2 2\pi}$
$a_{48,63}$	$\frac{(\sin(2T_2) - \sin(2T_1))}{C_2 4\pi}$	$a_{50,30}$	$\frac{\alpha(\sin(T_1) - \sin(T_2))}{C_2 2\pi}$
$a_{48,64}$	$\frac{(\cos(2T_2) - \cos(2T_1))}{C_2 4\pi}$	$a_{50,31}$	$\frac{\alpha(\cos(T_1) - \cos(T_2))}{C_2 2\pi}$
$a_{48,65}$	$\frac{(\sin(3T_2) - \sin(3T_1))}{C_2 6\pi}$	$a_{50,32}$	$\frac{\alpha(\sin(2T_1) - \sin(2T_2))}{C_2 4\pi}$
$a_{48,66}$	$\frac{(\cos(3T_2) - \cos(3T_1))}{C_2 6\pi}$	$a_{50,33}$	$\frac{\alpha(\cos(2T_1) - \cos(2T_2))}{C_2 4\pi}$
$a_{49,23}$	$\frac{\alpha(\cos(2T_1) - \cos(2T_2))}{C_2 4\pi}$	$a_{50,51}$	$3\omega_s$
$a_{49,24}$	$\frac{\alpha(\cos(T_1) - \cos(T_2))}{C_2 2\pi} + \frac{\alpha(\cos(3T_1) - \cos(3T_2))}{C_2 6\pi}$	$a_{50,56}$	$\frac{(\sin(3T_2) - \sin(3T_1))}{C_2 6\pi}$
$a_{49,25}$	$\frac{\alpha(\sin(T_1) - \sin(T_2))}{C_2 2\pi} + \frac{\alpha(\sin(3T_2) - \sin(3T_1))}{C_2 6\pi}$	$a_{50,57}$	$\frac{(\sin(2T_2) - \sin(2T_1))}{C_2 4\pi}$
$a_{49,26}$	$\frac{-\cos(3T_1) + \cos(3T_2)}{C_2 3\pi}$	$a_{50,58}$	$\frac{(\cos(2T_1) - \cos(2T_2))}{C_2 4\pi}$
$a_{49,27}$	$\frac{\alpha}{C_2} + \frac{\alpha(T_1 - T_2)}{C_2 2\pi}$	$a_{50,59}$	$\frac{(\sin(T_2) - \sin(T_1))}{C_2 2\pi}$
$a_{49,28}$	$\frac{\alpha(\cos(T_2) - \cos(T_1))}{C_2 2\pi}$	$a_{50,60}$	$\frac{(\cos(T_1) - \cos(T_2))}{C_2 2\pi}$

Table G.8 – Matrix  $\mathbf{A}_L$  elements - Pt. VIII.

Element	Term	Element	Term
$a_{50,61}$	$\frac{-1}{C_2} + \frac{T_2-T_1}{C_2 2\pi}$	$a_{52,29}$	$\frac{\alpha(\cos(T_2)-\cos(T_1))}{C_2 2\pi}$
$a_{50,63}$	$\frac{(\sin(T_2)-\sin(T_1))}{C_2 2\pi}$	$a_{52,30}$	$\frac{\alpha}{C_2} + \frac{\alpha(T_1-T_2)}{C_2 2\pi}$
$a_{50,64}$	$\frac{(\cos(T_2)-\cos(T_1))}{C_2 2\pi}$	$a_{52,32}$	$\frac{\alpha(\sin(T_1)-\sin(T_2))}{C_2 2\pi}$
$a_{50,65}$	$\frac{(\sin(2T_2)-\sin(2T_1))}{C_2 4\pi}$	$a_{52,33}$	$\frac{\alpha(\cos(T_1)-\cos(T_2))}{C_2 2\pi}$
$a_{50,66}$	$\frac{(\cos(2T_2)-\cos(2T_1))}{C_2 4\pi}$	$a_{52,53}$	$4\omega_s$
$a_{51,23}$	$\frac{\alpha(\cos(3T_1)-\cos(3T_2))}{C_2 6\pi}$	$a_{52,57}$	$\frac{\sin(3T_2)-\sin(3T_1)}{C_2 6\pi}$
$a_{51,24}$	$\frac{\alpha(\cos(2T_1)-\cos(2T_2))}{C_2 4\pi}$	$a_{52,58}$	$\frac{\cos(3T_1)-\cos(3T_2)}{C_2 6\pi}$
$a_{51,25}$	$\frac{\alpha(\sin(2T_1)-\sin(2T_2))}{C_2 4\pi}$	$a_{52,59}$	$\frac{\sin(2T_2)-\sin(2T_1)}{C_2 4\pi}$
$a_{51,26}$	$\frac{\alpha(\cos(T_1)-\cos(T_2))}{C_2 2\pi}$	$a_{52,60}$	$\frac{\cos(2T_1)-\cos(2T_2)}{C_2 4\pi}$
$a_{51,27}$	$\frac{\alpha(\sin(T_1)-\sin(T_2))}{C_2 2\pi}$	$a_{52,61}$	$\frac{\sin(T_2)-\sin(T_1)}{C_2 2\pi}$
$a_{51,29}$	$\frac{\alpha}{C_2} + \frac{\alpha(T_1-T_2)}{C_2 2\pi}$	$a_{52,62}$	$\frac{\cos(T_1)-\cos(T_2)}{C_2 2\pi}$
$a_{51,30}$	$\frac{\alpha(\cos(T_2)-\cos(T_1))}{C_2 2\pi}$	$a_{52,63}$	$\frac{-1}{C_2} + \frac{T_2-T_1}{C_2 2\pi}$
$a_{51,31}$	$\frac{\alpha(\sin(T_1)-\sin(T_2))}{C_2 2\pi}$	$a_{52,65}$	$\frac{\sin(T_2)-\sin(T_1)}{C_2 2\pi}$
$a_{51,32}$	$\frac{\alpha(\cos(2T_2)-\cos(2T_1))}{C_2 4\pi}$	$a_{52,66}$	$\frac{\cos(T_2)-\cos(T_1)}{C_2 2\pi}$
$a_{51,33}$	$\frac{\alpha(\sin(2T_1)-\sin(2T_2))}{C_2 4\pi}$	$a_{53,24}$	$\frac{\alpha(\cos(3T_1)-\cos(3T_2))}{C_2 6\pi}$
$a_{51,50}$	$-3\omega_s$	$a_{53,25}$	$\frac{\alpha(\sin(3T_1)-\sin(3T_2))}{C_2 6\pi}$
$a_{51,56}$	$\frac{(\cos(3T_2)-\cos(3T_1))}{C_2 6\pi}$	$a_{53,26}$	$\frac{\alpha(\cos(2T_1)-\cos(2T_2))}{C_2 4\pi}$
$a_{51,57}$	$\frac{(\cos(2T_2)-\cos(2T_1))}{C_2 4\pi}$	$a_{53,27}$	$\frac{\alpha(\sin(2T_1)-\sin(2T_2))}{C_2 4\pi}$
$a_{51,58}$	$\frac{(\sin(2T_2)-\sin(2T_1))}{C_2 4\pi}$	$a_{53,28}$	$\frac{\alpha(\cos(T_1)-\cos(T_2))}{C_2 2\pi}$
$a_{51,59}$	$\frac{\alpha(\cos(T_2)-\cos(T_1))}{C_2 2\pi}$	$a_{53,29}$	$\frac{\alpha(\sin(T_1)-\sin(T_2))}{C_2 2\pi}$
$a_{51,60}$	$\frac{(\sin(T_2)-\sin(T_1))}{C_2 2\pi}$	$a_{53,31}$	$\frac{\alpha}{C_2} + \frac{\alpha(T_1-T_2)}{C_2 2\pi}$
$a_{51,61}$	$\frac{(\cos(T_2)-\cos(T_1))}{C_2 2\pi}$	$a_{53,32}$	$\frac{\alpha(\cos(T_2)-\cos(T_1))}{C_2 2\pi}$
$a_{51,62}$	$\frac{-1}{C_2} + \frac{T_2-T_1}{C_2 2\pi}$	$a_{53,33}$	$\frac{\alpha(\sin(T_1)-\sin(T_2))}{C_2 2\pi}$
$a_{51,63}$	$\frac{(\cos(T_1)-\cos(T_2))}{C_2 2\pi}$	$a_{53,52}$	$-4\omega_s$
$a_{51,64}$	$\frac{(\sin(T_2)-\sin(T_1))}{C_2 2\pi}$	$a_{53,57}$	$\frac{(\cos(3T_2)-\cos(3T_1))}{C_2 6\pi}$
$a_{51,65}$	$\frac{(\cos(2T_1)-\cos(2T_2))}{C_2 4\pi}$	$a_{53,58}$	$\frac{(\sin(3T_2)-\sin(3T_1))}{C_2 6\pi}$
$a_{51,66}$	$\frac{(\sin(2T_2)-\sin(2T_1))}{C_2 4\pi}$	$a_{53,59}$	$\frac{(\cos(2T_2)-\cos(2T_1))}{C_2 4\pi}$
$a_{52,24}$	$\frac{\alpha(\sin(3T_1)-\sin(3T_2))}{C_2 6\pi}$	$a_{53,60}$	$\frac{(\sin(2T_2)-\sin(2T_1))}{C_2 4\pi}$
$a_{52,25}$	$\frac{\alpha(\cos(3T_2)-\cos(3T_1))}{C_2 6\pi}$	$a_{53,61}$	$\frac{(\cos(T_2)-\cos(T_1))}{C_2 2\pi}$
$a_{52,26}$	$\frac{\alpha(\sin(2T_1)-\sin(2T_2))}{C_2 4\pi}$	$a_{53,62}$	$\frac{(\sin(T_2)-\sin(T_1))}{C_2 2\pi}$
$a_{52,27}$	$\frac{\alpha(\cos(2T_2)-\cos(2T_1))}{C_2 4\pi}$	$a_{53,64}$	$\frac{-1}{C_2} + \frac{T_2-T_1}{C_2 2\pi}$
$a_{52,28}$	$\frac{\alpha(\sin(T_1)-\sin(T_2))}{C_2 2\pi}$	$a_{53,65}$	$\frac{(\cos(T_1)-\cos(T_2))}{C_2 2\pi}$

Table G.9 – Matrix  $\mathbf{A}_L$  elements - Pt. IX.

Element	Term	Element	Term
$a_{53,66}$	$\frac{(\sin(T_2) - \sin(T_1))}{C_2 2\pi}$	$a_{56,46}$	$\frac{\sin(T_1) - \sin(T_2)}{L_f \pi}$
$a_{54,26}$	$\frac{\alpha(\sin(3T_1) - \sin(3T_2))}{C_2 6\pi}$	$a_{56,47}$	$\frac{\cos(T_1) - \cos(T_2)}{L_f \pi}$
$a_{54,27}$	$\frac{\alpha(\cos(3T_2) - \cos(3T_1))}{C_2 6\pi}$	$a_{56,67}$	$\frac{-1}{L_f}$
$a_{54,28}$	$\frac{\alpha(\sin(2T_1) - \sin(2T_2))}{C_2 4\pi}$	$a_{57,45}$	$\frac{\sin(T_1) - \sin(T_2)}{L_f 2\pi}$
$a_{54,29}$	$\frac{\alpha(\cos(2T_2) - \cos(2T_1))}{C_2 4\pi}$	$a_{57,46}$	$\frac{1}{L_f} + \frac{T_1 - T_2}{L_f 2\pi} + \frac{\sin(2T_1) - \sin(2T_2)}{L_f 4\pi}$
$a_{54,30}$	$\frac{\alpha(\sin(T_1) - \sin(3T_2))}{C_2 2\pi}$	$a_{57,58}$	$\omega_s$
$a_{54,31}$	$\frac{\alpha(\cos(T_2) - \cos(T_1))}{C_2 2\pi}$	$a_{57,68}$	$\frac{-1}{L_f}$
$a_{54,32}$	$\frac{\alpha}{C_2} + \frac{\alpha(T_1 - T_2)}{C_2 2\pi}$	$a_{58,45}$	$\frac{\cos(T_1) - \cos(T_2)}{L_f 2\pi}$
$a_{54,55}$	$5\omega_s$	$a_{58,46}$	$\frac{\cos(2T_1) - \cos(2T_2)}{L_f 4\pi}$
$a_{54,59}$	$\frac{\sin(3T_2) - \sin(3T_1)}{C_2 6\pi}$	$a_{58,47}$	$\frac{1}{L_f} + \frac{T_1 - T_2}{L_f 2\pi} + \frac{\sin(2T_2) - \sin(2T_1)}{L_f 4\pi}$
$a_{54,60}$	$\frac{\cos(3T_1) - \cos(3T_2)}{C_2 6\pi}$	$a_{58,57}$	$-\omega_s$
$a_{54,61}$	$\frac{\sin(2T_2) - \sin(2T_1)}{C_2 4\pi}$	$a_{58,69}$	$\frac{-1}{L_f}$
$a_{54,62}$	$\frac{\cos(2T_1) - \cos(2T_2)}{C_2 4\pi}$	$a_{67,56}$	$\frac{1}{C_f}$
$a_{54,63}$	$\frac{\sin(T_2) - \sin(T_1)}{C_2 2\pi}$	$a_{67,67}$	$\frac{-1}{R_L C_f}$
$a_{54,64}$	$\frac{\cos(T_1) - \cos(T_2)}{C_2 2\pi}$	$a_{68,57}$	$\frac{1}{C_f}$
$a_{54,65}$	$\frac{-1}{C_2} + \frac{T_2 - T_1}{C_2 2\pi}$	$a_{68,68}$	$\frac{-1}{R_L C_f}$
$a_{55,26}$	$\frac{\alpha(\cos(3T_1) - \cos(3T_2))}{C_2 6\pi}$	$a_{68,69}$	$\omega_s$
$a_{55,27}$	$\frac{\alpha(\sin(3T_1) - \sin(3T_2))}{C_2 6\pi}$	$a_{69,58}$	$\frac{1}{C_f}$
$a_{55,28}$	$\frac{\alpha(\cos(2T_1) - \cos(2T_2))}{C_2 4\pi}$	$a_{69,68}$	$-\omega_s$
$a_{55,29}$	$\frac{\alpha(\sin(2T_1) - \sin(2T_2))}{C_2 4\pi}$	$a_{69,69}$	$\frac{-1}{R_L C_f}$
$a_{55,30}$	$\frac{\alpha(\cos(T_1) - \cos(T_2))}{C_2 2\pi}$		
$a_{55,31}$	$\frac{\alpha(\sin(T_1) - \sin(T_2))}{C_2 2\pi}$		
$a_{55,33}$	$\frac{\alpha}{C_2} + \frac{\alpha(T_1 - T_2)}{C_2 2\pi}$		
$a_{55,54}$	$-5\omega_s$		
$a_{55,59}$	$\frac{(\cos(3T_2) - \cos(3T_1))}{C_2 6\pi}$		
$a_{55,60}$	$\frac{(\sin(3T_2) - \sin(3T_1))}{C_2 6\pi}$		
$a_{55,61}$	$\frac{(\cos(2T_2) - \cos(2T_1))}{C_2 4\pi}$		
$a_{55,62}$	$\frac{(\sin(2T_2) - \sin(2T_1))}{C_2 4\pi}$		
$a_{55,63}$	$\frac{(\cos(T_2) - \cos(T_1))}{C_2 2\pi}$		
$a_{55,64}$	$\frac{(\sin(T_2) - \sin(T_1))}{C_2 2\pi}$		
$a_{55,66}$	$\frac{-1}{C_2} + \frac{T_2 - T_1}{C_2 2\pi}$		
$a_{56,45}$	$\frac{1}{L_f} + \frac{T_1 - T_2}{L_f 2\pi}$		

## Appendix H – Small-Signal Model of the Class-E<sup>2</sup> Resonant Converter

### H.1 SMALL-SIGNAL MODEL OF THE CLASS-E<sup>2</sup> RESONANT CONVERTER

This Appendix details the terms of the input matrix for the small-signal model of the Class-E<sup>2</sup> resonant converter. Due to the size of the input matrix  $\mathbf{B}_S$ , its terms are presented in a table format.

The terms are written as  $b_{i,j}$ , being  $i$  the matrix line and  $j$  the matrix column. The matrices terms of the input matrix  $\mathbf{B}_S$  are shown in Table H.1.

Most of the terms shown in Table H.1 have  $Y_i$ , which is the equilibrium solution of the large-signal model. The subscript  $i$  indicates the line that was used to solve the dynamic matrix from the large-signal model.

Table H.1 – Matrix  $\mathbf{B}_S$  elements.

Element	Term	Element	Term	Element	Term
$b_{2,1}$	$Y_3$	$b_{37,1}$	$2Y_{38}$	$b_{72,1}$	$3Y_{73}$
$b_{3,1}$	$-Y_2$	$b_{38,1}$	$-2Y_{37}$	$b_{73,1}$	$-3Y_{72}$
$b_{4,1}$	$2Y_5$	$b_{39,1}$	$3Y_{40}$	$b_{74,1}$	$4Y_{75}$
$b_{5,1}$	$-2Y_4$	$b_{40,1}$	$-3Y_{39}$	$b_{75,1}$	$-4Y_{74}$
$b_{6,1}$	$3Y_7$	$b_{41,1}$	$4Y_{42}$	$b_{76,1}$	$5Y_{77}$
$b_{7,1}$	$-3Y_6$	$b_{42,1}$	$-4Y_{41}$	$b_{77,1}$	$-5Y_{76}$
$b_{8,1}$	$4Y_9$	$b_{43,1}$	$5Y_{44}$	$b_{1,2}$	$\frac{1}{L_c}$
$b_{9,1}$	$-4Y_8$	$b_{44,1}$	$-5Y_{43}$	$b_{2,2}$	$\frac{1}{L_c}$
$b_{10,1}$	$5Y_{11}$	$b_{46,1}$	$Y_{47}$	$b_{4,2}$	$\frac{1}{L_c}$
$b_{11,1}$	$-5Y_{10}$	$b_{47,1}$	$-Y_{46}$	$b_{6,2}$	$\frac{1}{L_c}$
$b_{13,1}$	$Y_{14}$	$b_{48,1}$	$2Y_{49}$	$b_{8,2}$	$\frac{1}{L_c}$
$b_{14,1}$	$-Y_{13}$	$b_{49,1}$	$-2Y_{48}$	$b_{10,2}$	$\frac{1}{L_c}$
$b_{15,1}$	$2Y_{16}$	$b_{50,1}$	$3Y_{51}$		
$b_{16,1}$	$-2Y_{15}$	$b_{51,1}$	$-3Y_{50}$		
$b_{17,1}$	$3Y_{18}$	$b_{52,1}$	$4Y_{53}$		
$b_{18,1}$	$-3Y_{17}$	$b_{53,1}$	$-4Y_{52}$		
$b_{19,1}$	$4Y_{20}$	$b_{54,1}$	$5Y_{55}$		
$b_{20,1}$	$-4Y_{19}$	$b_{55,1}$	$-5Y_{54}$		
$b_{21,1}$	$5Y_{22}$	$b_{57,1}$	$Y_{58}$		
$b_{22,1}$	$-5Y_{21}$	$b_{58,1}$	$-Y_{57}$		
$b_{24,1}$	$Y_{25}$	$b_{59,1}$	$2Y_{60}$		
$b_{25,1}$	$-Y_{24}$	$b_{60,1}$	$-2Y_{59}$		
$b_{26,1}$	$2Y_{27}$	$b_{61,1}$	$3Y_{62}$		
$b_{27,1}$	$-2Y_{26}$	$b_{62,1}$	$-3Y_{61}$		
$b_{28,1}$	$3Y_{29}$	$b_{63,1}$	$4Y_{64}$		
$b_{29,1}$	$-3Y_{28}$	$b_{64,1}$	$-4Y_{63}$		
$b_{30,1}$	$4Y_{31}$	$b_{65,1}$	$5Y_{66}$		
$b_{31,1}$	$-4Y_{30}$	$b_{66,1}$	$-5Y_{65}$		
$b_{32,1}$	$5Y_{33}$	$b_{68,1}$	$Y_{69}$		
$b_{33,1}$	$-5Y_{32}$	$b_{69,1}$	$-Y_{68}$		
$b_{35,1}$	$Y_{36}$	$b_{70,1}$	$2Y_{71}$		
$b_{36,1}$	$-Y_{35}$	$b_{71,1}$	$-2Y_{70}$		